

# Mimicking the active site of Lytic Polysaccharides Monooxygenases (LPMO) enzymes for catalysis

*Synthesis and Characterization*

Atiqa Ambrin Ansar



Thesis submitted for a Master's degree in Chemistry  
60 credits

Department of Chemistry  
Faculty of Mathematics and Natural Sciences

UNIVERSITY OF OSLO

Spring 2023

© Atiqa Ambrin Ansar

2023

Mimicking the active site of Lytic Polysaccharides Monooxygenases (LPMO) enzymes for catalysis

Atiqa Ambrin Ansar

<http://www.duo.uio.no/>

Printing: Repräsentralen, Universitetet i Oslo

# Acknowledgements

Firstly, I would like to thank my supervisor, Mohamed Amedjkouh, for giving me the opportunity of working on this project, and for the valuable guidance and help you have provided over the past few years. Being a member of your group has been an incredible journey and has made me grow as a chemist. I would also like to thank everyone who provided invaluable assistance in the lab, making numerous tasks much easier through your helpful tips and guidance. I want to thank Rafael Cortez Sgroi Pupo for always finding time to help me with NMR and throughout my time in lab. I want to thank Isabelle Gerz for guiding me through the whole project, and I really appreciate your valuable feedback. Your insights and constructive criticism have been influential on me. I would also like to thank all the members of the CUBE project and the homogeneous group for giving me feedback throughout my journey. Lastly, I am grateful to my friends and family for their support and encouragement throughout this academic endeavor. Their belief in my abilities and their constant motivation have been a driving force behind me being persistent.





# Abstract

This study focuses on synthesizing and characterizing new metal complexes designated to mimic the active site of a copper containing enzyme, Lytic Polysaccharide Monooxygenase (LPMO).<sup>1</sup> The aim was to design synthetic routes towards synthesizing ligands incorporating functional groups that are present in the active site of the enzyme. The direct, selective oxidation of methane to methanol, C-H activation, has long been a dream reaction.<sup>2, 3</sup> These complexes are aimed for catalytic testing for selective oxidation by C-H activation of light alkanes to alcohols.

Previously in the group, copper complexes coordinated to only nitrogen atoms have been synthesized and characterized. In this study, novel ligands comprising not only nitrogen atoms but also oxygen atoms were synthesized. The synthesized ligands were metalated with both copper(I)- and copper(II)-salt. The synthesized compounds were investigated with nuclear magnetic resonance (NMR), mass spectrometry (MS), UV-Vis spectroscopy, Fourier-transform infrared spectroscopy (FTIR) and Single Crystal X-ray Diffraction (SC-XRD).

The strategy of synthesizing ligands also includes a carboxylate precursor for their incorporation into Metal-Organic Frameworks (MOF). The purpose of synthesizing copper-complexes is twofold, to serve as a catalyst on their own, and to also be incorporated into MOF and function as a catalyst there.



# Abbreviations

<b>aq.</b>	Aqueous
<b>br</b>	Broad (NMR)
<b>Cat.</b>	Catalyzed
<b>COSY</b>	Correlation spectroscopy (NMR)
<b>conc.</b>	Concentrated
<b>d</b>	Doublet (NMR)
<b>dd</b>	Double of Doublets (NMR)
<b>DEPT</b>	Distortionless Enhancement by Polarization Transfer
<b>ESI</b>	Electrospray ionization
<b>Equiv.</b>	Equivalent(s)
<b>FTIR</b>	Fourier-transform infrared spectroscopy
<b>HRMS</b>	High resolution mass spectrometry
<b>HSQC</b>	Heteronuclear single quantum coherence (NMR)
<b>HMBC</b>	Heteronuclear multiple bond correlation (NMR)
<b>Hz</b>	Hertz
<b>m</b>	multiplett (NMR)
<b>MS</b>	Mass spectrometry
<b>m/z</b>	Mass to ratio charge (MS)
<b>MHz</b>	Megahertz
<b>MOF</b>	Metal-organic framework
<b>NOESY</b>	Nuclear Overhauser effect spectroscopy (NMR)
<b>NMR</b>	Nuclear magnetic resonance
<b>OTf</b>	Trifluoromethanesulfonate
<b>ORTEP</b>	Oak Ridge Thermal Ellipsoid
<b>r.t.</b>	Room temperature
<b>ROESY</b>	Rotating-frame nuclear Overhauser effect spectroscopy (NMR)
<b>s</b>	Singlet (NMR)
<b>Sat.</b>	Saturated
<b>SC-XRD</b>	Single Crystal X-ray Diffraction

**TOCSY**

Total Correlation Spectroscopy

**UV-Vis**

Ultraviolet-Visible Spectroscopy

**XAS**

X-ray Absorption Spectroscopy

**XANES**

X-ray Absorption Near-Edge Structure

**EXAFS**

X-ray absorption fine structure

# Contents

Acknowledgements.....	iii
Abstract.....	v
Abbreviations.....	vii
1 Introduction .....	1
1.1 Motivation for this work .....	1
1.2 Inspiration derived from nature .....	2
1.3 Ligand design strategy .....	4
1.4 Oxidation states and coordination numbers of Copper .....	6
1.5 Synthetic methods .....	7
1.5.1 Suzuki-Miyaura Cross-Coupling reaction .....	7
1.5.2 Schiff Base synthesis .....	8
1.5.3 Reductive amination .....	9
1.6 Spectroscopic Techniques.....	10
1.6.1 Nuclear Magnetic Resonance Spectroscopy (NMR) .....	10
i. <sup>1</sup> H NMR and <sup>13</sup> C NMR.....	10
ii. COSY and TOCSY.....	10
iii. HSQC and HMBC .....	11
iv. NOESY.....	11
1.6.2 X-ray Absorption Spectroscopy (XAS) .....	12
i. X-ray Absorption Near-Edge Structure (XANES) .....	13
2 Discussion.....	14
2.1 LPMO active site: An Approach for Ligand Design .....	14
2.2 Ligand Synthesis Strategies.....	15
2.2.1 Synthesis Route towards Ligand (3).....	16
2.2.2 Synthesis Route towards Ligand (8).....	18
2.2.3 Attempted Reduction of Ligand (8) .....	24
2.2.4 Synthesis Route towards Ligand (14).....	27
2.2.5 Reaction optimization for compound 13 .....	29
2.3 Metalation.....	30
2.3.1 Metalation of Ligand 3 .....	30
2.3.2 Metalation of Ligand 8 .....	36
2.3.3 XANES measurements.....	42
2.3.4 One-pot Synthesis: Copper Complex (15).....	44
2.4 Miscellaneous .....	46

3	Experimental .....	47
3.1	General Considerations.....	47
3.2	Experimental: X-ray absorption measurements.....	48
3.3	Synthesis of (1).....	49
3.4	Synthesis of (2).....	50
3.5	Synthesis of Ligand (3) .....	51
3.6	Synthesis of Complex (4).....	52
3.7	Synthesis of Complex (5).....	53
3.8	Synthesis of (6).....	54
3.8.1	Sideproduct (6a).....	55
3.9	Synthesis of (7).....	56
3.10	Synthesis of Ligand (8) .....	58
3.11	Synthesis of Complex (9).....	59
3.12	Synthesis of Complex (10).....	60
3.13	Synthesis of (11).....	61
3.14	Synthesis of (12).....	62
3.15	Synthesis of (13).....	63
3.16	Synthesis of Ligand (14) .....	64
3.17	Synthesis of Complex (15).....	66
3.18	Synthesis of (16).....	67
3.19	Synthesis of (17).....	68
3.20	Synthesis of (18).....	69
3.21	Synthesis of (19).....	70
4	Conclusion .....	71
5	Bibliography .....	72
6	Appendix .....	80
6.1	A.1 NMR data .....	80
6.2	A.2 UV-Vis data .....	130
6.3	IR data .....	143
6.4	SC-XRD data .....	145

# 1 Introduction

According to United Nations Environment Programme (UNEP), methane is responsible for more than 25% of the global warming we are experiencing today, and it is ten times more powerful than carbon dioxide at warming the atmosphere.<sup>4, 5</sup> Since methane is a potent greenhouse gas, it is crucial to find ways to convert methane into other useful products, such as methanol. By doing so will it not only mitigate methane's impact on the environment, but also generates valuable fuel source and chemicals for further industrial applications.<sup>6</sup>

Methane to methanol is considered the holy grail of catalysis, and currently, the conversion of methane to methanol is performed through a method called steam reforming, which is an energy demanding method that requires high temperatures and pressures.<sup>6, 7</sup> Search for more efficient catalysts have been ongoing among chemists towards this aim, methane to methanol, with catalysts making this conversion much faster and economical.<sup>8</sup>

## 1.1 Motivation for this work

The long-term goal of this project is to develop Copper-based catalyst for C-H activation. The pursuit of selective C-H activation has been ongoing over many years across various fields, including homogeneous, heterogeneous, and biological catalysis.<sup>9, 10, 11</sup> However, progress has been moderate due to limited cross-fertilization among these fields. In this study, by taking inspiration from biological catalysts, enzymes, homogeneous catalyst were synthesized. Synthetic designs were used ensuring their suitability for incorporation into heterogeneous catalysts, Metal-Organic Framework (MOF). Therefore, the aim of this work is to mimic the structure of the active site of a copper-containing enzyme, Lytic Polysaccharide Monooxygenase (LPMO), and synthesize new Cu-containing catalysts.

## 1.2 Inspiration derived from nature

Lytic Polysaccharide Monooxygenase (LPMO) enzymes are a class of copper containing enzymes that is crucial for breaking down complex carbohydrates, such as cellulose and chitin.<sup>12</sup> LPMO enzymes generate oxidized products that can be more efficiently degraded by other enzymes. These enzymes are major contributors in the carbon recycling process in nature and are utilized in biorefinery industry.<sup>13</sup>

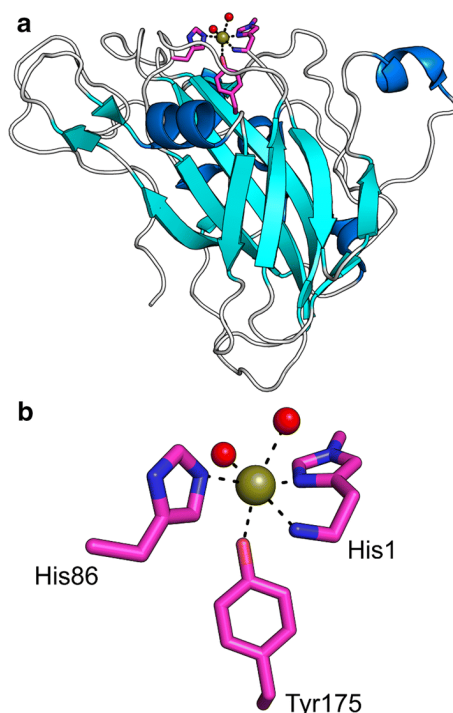


Figure 1:**a**: Figure shows three-dimensional structure of the AA9 LPMO enzyme in a cartoon form **b**: Stick visualization of the catalytic center is depicted in pink-colored sticks, while the copper atom is shown as a golden sphere. Additionally, there are two water molecules that are coordinated by the copper atom, shown as red-colored spheres. PDB ID: 2YET. Figures were retrieved from reference.<sup>1</sup>

As shown above (Figure 1), the active site of the LPMO enzyme consists of two histidine residues that encircle the copper atom. The copper atom is ligated to three nitrogen atoms from the two surrounding histidine ligands in such a manner that from one histidine brace (His1, Figure 1b) both the N-terminal and the side-chain imidazole nitrogen are coordinated to the metal. From the other histidine brace (His86, Figure 1a), the side-chain imidazole nitrogen is coordinated to the metal.<sup>1</sup> Furthermore there is a tyrosine moiety (Tyr175, Figure 1b) present in close proximity to the copper. Recent studies suggest that this tyrosine residue might play a role in regulating the reactivity of the copper ion in the active site, and protect the active site



against oxidative damage.<sup>14, 15</sup> While some studies have proposed that the Tyrosine might have a direct interaction with copper or participate in electron transfer reactions.<sup>16</sup>

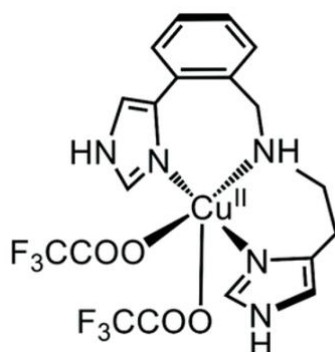


Figure 2: A biomimetic mononuclear copper(II) complex bearing a histidine brace.<sup>17</sup>

Biomimetic chemistry is focused on building models that imitate enzyme activity and specificity.<sup>18</sup> Transition metal complexes serve as valuable models for active sites in enzymes.<sup>19</sup> A biomimetic mononuclear copper(II) complex (Figure 2) is characterized as an active-site model of monooxygenases such as LPMO and particulate methane monooxygenase (pMMO), with similar functional and structural features to the active sites of the enzymes.<sup>17</sup>

## 1.3 Ligand design strategy

Heterogenization of catalyst refers to attaching the catalyst onto a solid support such as zeolites or metal-organic frameworks (MOF).<sup>20</sup> Zeolites and MOFs are porous materials utilized in a range of applications, such as catalysis and gas separation.<sup>21, 22, 23</sup> Zeolites are crystalline microporous aluminosilicates that possess distinctive properties including high surface area, shape selectivity and acidity, making them a valuable material in a wide range of industrial applications.<sup>21</sup> On the other hand, MOFs are a newer class of porous crystalline materials with frameworks consisting of inorganic building units, metal ions or clusters, which are connected by organic linkers.<sup>22</sup> MOFs have tunable properties, including pore size, shape, and functionality, which makes them attractive for gas storage, separation, and catalysis.<sup>12, 15</sup>

Ligand robustness is a general problem in organometallic chemistry and there are various ways in which a homogeneous catalyst can decompose. Including them is decomposition of metal, ligand decomposition, reaction with impurities, dimer formation, and reaction of the metal center with the ligand.<sup>25, 26</sup> Metal-organic frameworks have emerged as excellent tools for converting homogeneous catalysts into heterogeneous catalyst. This approach reaps benefits of both the organometallic compound and the MOF constituents. As heterogeneous catalysts are more easily separable and reusable, and homogeneous catalysts can be more selective and efficient due to their ability to interact more closely with the reactants.<sup>20, 27, 28, 29</sup> The primary difference between heterogeneous and homogeneous catalysts is their interaction with the reactants and their physical state. For organic linkers to effectively function both as structural elements and as a functionalized part of the MOF, they require to coordinate to two or more metal clusters through functional groups, such as carboxylic acid, amino and pyridine groups. The linker molecule should have a rigid structure, to retain porosity of the material and prevent collapsing of the framework.<sup>30, 31</sup>

UiO based MOFs, including UiO-66, UiO-67, UiO-68, are zirconium-based MOFs, where zirconium metal nodes are coordinated to organic linkers (Figure 3).<sup>32</sup> They possess high stability, tunability, porosity and functions.<sup>33</sup> The structure of organic linkers in UiO-MOFs can be controlled.<sup>32</sup> Additional functionality can be introduced into MOF by introducing specific properties or modifying the structure of the linker.

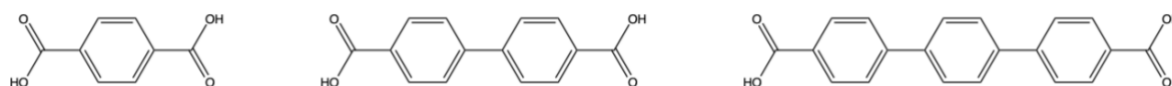
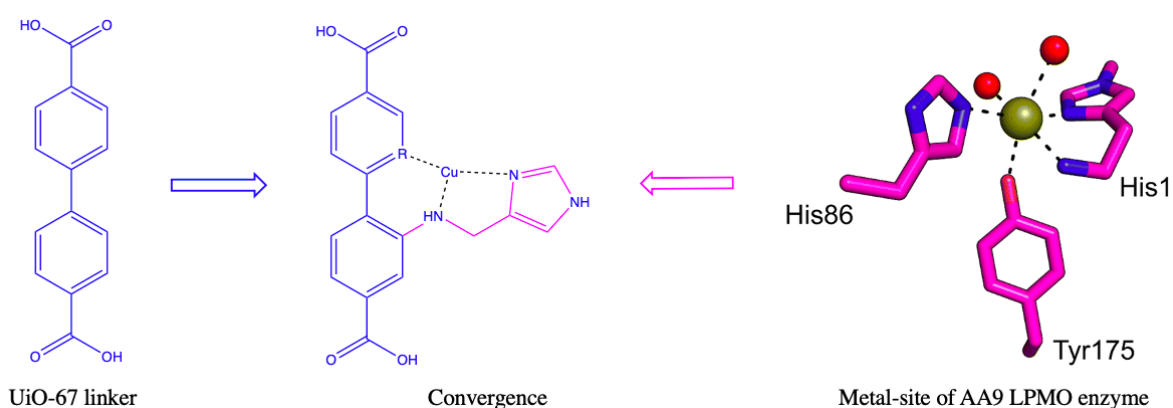


Figure 3: From left: aromatic dicarboxylic acids used as linkers for the respective MOFs, UiO-66, UiO-67, UiO-68.

By mimicking the active site of the enzyme, certain key features are borrowed, including functional motifs, catalytic residues or structural elements.<sup>34</sup> Functionalization of the organic linker and selectively choosing and incorporating a metal center can target specific reactions.<sup>34</sup> In this case (Scheme 1), by combining the UiO-67 linker as the backbone with LPMO-inspired ligand, expectantly the enzyme's reactivity can be induced into the complex.<sup>12</sup>



Scheme 1: Convergence of UiO-67 linker and active site of LPMO enzyme to create a novel arrangement.<sup>1, 32</sup>

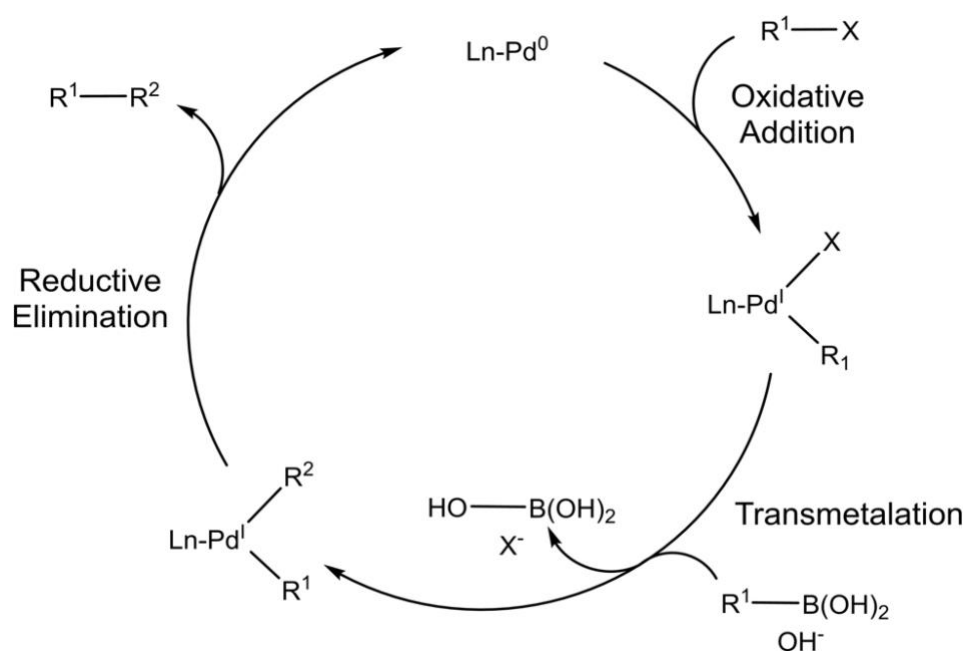
## 1.4 Oxidation states and coordination numbers of Copper

Copper is one of the most abundant transition metals that exhibits four oxidation states,  $\text{Cu}^0$ ,  $\text{Cu}^{\text{I}}$ ,  $\text{Cu}^{\text{II}}$  and  $\text{Cu}^{\text{III}}$ .  $\text{Cu}^{\text{I}}$  and  $\text{Cu}^{\text{II}}$  are the two most prominent oxidation states, and have a accessible +1/+2 redox couple.<sup>35, 36</sup> Copper participates in a diverse variety of roles in nature, such as it act as a cofactor in various enzymes and performs essential roles in photosynthesis.<sup>37, 38</sup> Copper in its +2 oxidation state has a  $d^9$  configuration, since it loses two electrons. Due to one unpaired electron in the 3d orbital, copper(II) have paramagnetic properties, making it not observed by NMR.<sup>39</sup> Therefore, other techniques like UV-vis, MS, IR and EPR can be useful for analyzing compounds containing paramagnetic materials.<sup>40</sup> In UV-vis for instance, presence of copper(II) can be observed due to d-d transition, electronic transition between molecular orbitals in open d-shell.<sup>41, 42</sup> On the other hand copper(I) have its 3d orbital filled with  $d^{10}$  configuration, making it diamagnetic due to no unpaired electrons.<sup>39</sup> These oxidation states of copper play a vital role in determining both physical and chemical properties of it. For instance, copper(I) (cuprous) compounds are air sensitive, and easily oxidizes to copper(II) and thus need to be stored and handled in an inert atmosphere. The coordination number (CN) of copper depends on the ligand and the oxidation state of the copper.<sup>43</sup> Copper(I) usually have linear structure, CN = 2, or tetrahedral, CN = 4, whereas Copper(II) prefer higher coordination numbers, 4, 5 and 6.<sup>43</sup>

## 1.5 Synthetic methods

### 1.5.1 Suzuki-Miyaura Cross-Coupling reaction

Cross-coupling reactions are considered to be among the most important reactions in chemistry, and have had a profound impact in organic synthesis.<sup>44</sup> It is a widely used reaction for carbon-carbon formation, and among other coupling reactions, the Suzuki-Miyaura cross-coupling reaction is one of the most widely utilized reactions to obtain biaryls and functionalized aromatic molecules.<sup>45</sup>



Scheme 2: General Scheme for Palladium-catalyzed Suzuki Miyaura cross-coupling reaction.<sup>45</sup>

Palladium-catalyzed Suzuki-Miyaura cross-coupling reaction involves coupling of an organoboron ( $\text{R}^2\text{-B(OH)}_2$ ) with an organic halide ( $\text{R}^1\text{-X}$ ), and consists of three steps: oxidative addition, transmetalation and reductive elimination (Scheme 2). In the first step, oxidative addition, bond between an organic electrophile ( $\text{R}^1\text{-X}$ ) breaks as addition of  $\text{L}_n\text{Pd}$  occurs, this leads to oxidation of the  $\text{Pd}^0$  to  $\text{Pd}^{\text{II}}$ . In the second step, transmetalation, the organometallic nucleophile ( $\text{R}^2\text{-B(OH)}_2$ ) reacts with the  $\text{Pd}^{\text{II}}$ -intermediate, and the organic group ( $\text{R}^2$ ) is transferred from boron to palladium. The last step, reductive elimination, involves breaking of the two bonds on the palladium and formation a new carbon-carbon bond ( $\text{R}^1\text{-R}^2$ ), this regenerates the Pd-catalyst back to  $\text{Pd}^0$ .<sup>45, 46, 47</sup>

## 1.5.2 Schiff Base synthesis

Schiff bases are a class of organic compounds that are characterized by the presence of a double bond linking a carbon and a nitrogen atom.<sup>48</sup> Schiff bases are named after a German chemist Hugo Schiff, who first reported this class of compounds in 1864.<sup>48</sup> Schiff bases have wide variety application in various fields, such as medical and pharmaceutical fields,<sup>49</sup> and dye industry.<sup>50</sup> Schiff bases are common ligands in coordination chemistry.<sup>51</sup> Jacobsen's catalyst (Figure 4), which incorporate two Schiff bases as part of its structure, is a popular reagent for enantioselective epoxidation of alkene.<sup>52</sup>

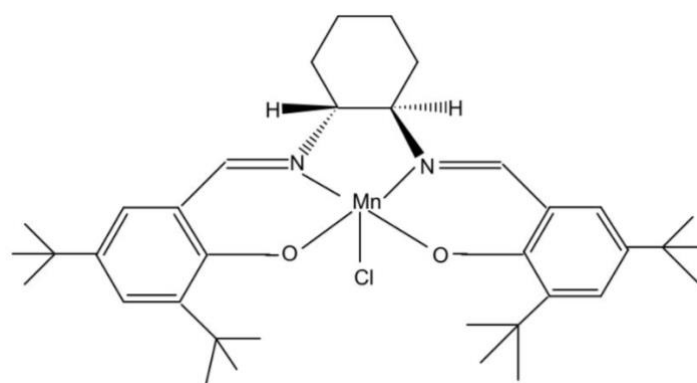
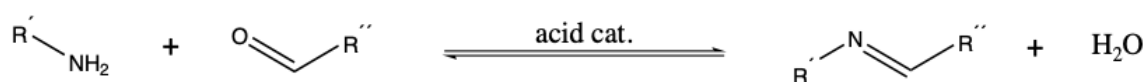


Figure 4: Jacobsen's catalyst.<sup>53</sup>

Schiff bases, also known as imines, are aldehyde- or ketone-like compounds, and derive from an amino and carbonyl compound.<sup>54</sup> Schiff bases have extensive uses across various industries, e.g., catalysis, biological activities, analytical chemistry and agrochemical activities.<sup>55</sup> In addition, Schiff base ligands have the ability to form stable metal complexes with a wide range of transition metals.<sup>56</sup>

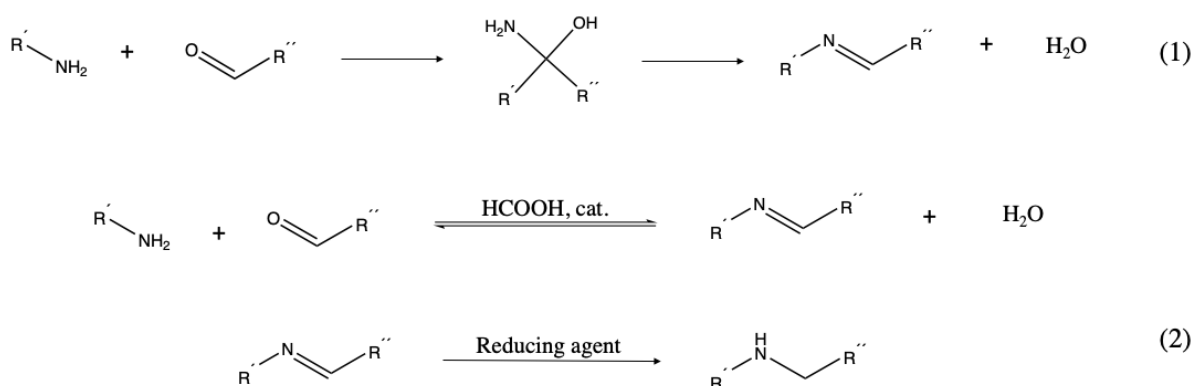


Scheme 3: General Scheme for Schiff base synthesis.

Condensation of a primary amine with a carbonyl yield in a Schiff base (Scheme 3), a more detailed description on formation of Schiff base is given below in Section 1.5.3.

### 1.5.3 Reductive amination

Reductive amination is a form of amination, which proceeds in two steps (Scheme 4). In the first step, an amine and a carbonyl compound react to form a hemiaminal specie, a functional group with a hydroxyl- and amino-group attached to the same carbon (reaction (1), Scheme 4).<sup>57</sup> Hemiaminal are presented only as short-lived reaction intermediates,<sup>57</sup> which form Schiff base (imine) as a result of water elimination.<sup>58</sup> Formation of imine is facilitated by presence of an acid catalyst, e.g. formic acid, through protonation of the carbonyl and making it more prone to nucleophilic attack.<sup>59</sup> Reaction between the carbonyl/amine and imine is in equilibrium and can be shifted towards imine by removal of the formed water. In the second step of reductive amination (reaction (2), Scheme 4), the formed imine (intermediate) is reduced to its corresponding amine by using a reducing agent, such as sodium borohydride (NaBH<sub>4</sub>). Both steps occur sequentially in the same reaction pot (one-pot synthesis).



Scheme 4: General Scheme for reductive amination (one-pot synthesis) of a primary amine with a carbonyl compound.

## 1.6 Spectroscopic Techniques

### 1.6.1 Nuclear Magnetic Resonance Spectroscopy (NMR)

Nuclear Magnetic Resonance (NMR) spectroscopy is a technique used for determining the molecular structure, chemical environment and dynamics of molecule.<sup>60, 61</sup> NMR is extensively utilized in various domains, such as biochemistry,<sup>62</sup> organic chemistry and pharmaceutical development.<sup>63</sup> The principle behind NMR is that many nuclei when entering an external field align itself either with or oppose the field. The nuclear magnetic resonance phenomenon occurs when nuclei aligned with an applied field are induced to absorb energy and change their spin orientation with respond to the applied field. By applying radiofrequency pulses and measuring the response of the nuclei, the resulting signal is known as a Free Induction Decay (FID). Using a Fourier transform, the different frequency components of a signal can be determined.<sup>64, 65</sup> The discussion in this thesis incorporate several 1D and 2D NMR techniques, briefly explained below.

#### i. $^1\text{H}$ NMR and $^{13}\text{C}$ NMR

Proton Nuclear Magnetic Resonance ( $^1\text{H}$  NMR) is the application of nuclear magnetic resonance in NMR spectroscopy with respect to hydrogen-1 nuclei in the molecule, to determine the structure of the molecule. The  $^1\text{H}$  NMR experiment gives information about integrals (number of protons), chemical shift, multiplicity and coupling constants.<sup>65</sup> In contrast with  $^1\text{H}$  (natural abundance of 99.98%),<sup>65</sup>  $^{13}\text{C}$ -isotope is less abundant in nature, approximately 1.108%.<sup>65</sup> Consequently,  $^{13}\text{C}$  NMR experiments require longer acquisition times and higher sensitivity compared to  $^1\text{H}$  NMR. Most  $^{13}\text{C}$  NMR experiments are decoupled meaning there is no signal splitting effect (multiplicity).<sup>64</sup>

#### ii. COSY and TOCSY

The Homonuclear Correlation Spectroscopy (COSY) is a useful method for determining which signals arise from neighboring protons, it's a 2D NMR experiment which gives  $^1\text{H}$ - $^1\text{H}$  correlation. Correlation appears when there is spin-spin coupling between protons. COSY experiments identify those nuclei that share a J coupling, which, for protons, operate typically over 2–3 bonds. Total Correlation Spectroscopy (TOCSY) is also a 2D NMR which creates correlations between all protons within a given system, not just between geminal or vicinal



protons as in COSY. A TOCSY spectrum displays an entire chain of protons, each of which is coupled to the next.<sup>64, 65</sup>

### **iii. HSQC and HMBC**

Heteronuclear Single Quantum Correlation spectroscopy (HSQC) is a 2D NMR experiment to determine  $^1\text{H}$ - $^{13}\text{C}$  single bond correlations. Whereas Heteronuclear Multiple Bond Correlation (HMBC) provides a wealth of information on the skeleton of the molecule and can be used to determine long range heteronuclear couplings with proton observation. HMBC gives  $^1\text{H}$ - $^{13}\text{C}$  bond correlations, typically over 2 or 3 bonds, but in certain cases, they can also extend over 4-5 bonds. In HMBC, the  $^1\text{H}$ - $^{13}\text{C}$  signal over one bond are filtered out but can breakthrough-appear as  $^1\text{J}_{\text{CH}}$ .<sup>64, 65</sup>  $^{15}\text{N}$  NMR can provide valuable information about coordination of nitrogen atom in a compound, but since  $^{15}\text{N}$  has low natural abundance of 0.366%, the indirect detection technique of  $^{15}\text{N}$ - $^1\text{H}$  HMBC can be used.<sup>66</sup>  $^{15}\text{N}$ - $^1\text{H}$  HMBC leverages the sensitivity of  $^1\text{H}$  NMR signals to overcome the difficulties that have typically been associated with direct  $^{15}\text{N}$  NMR.<sup>66</sup>

### **iv. NOESY**

Nuclear Overhauser Effect Spectroscopy (NOESY) is a 2D NMR experiment, where the pulse sequence is optimized to detect coupling through space correlations. In other words, it is useful for determining which signals arise from protons that are close to each other in space even if they are not chemically bonded.<sup>64</sup> NOESY takes advantage of nuclear Overhauser effect.<sup>67</sup>  $^1\text{H}$  nuclei that interact with another  $^1\text{H}$  nuclei through a dipolar relaxation process will appear as cross peaks in NOESY spectrum.<sup>65</sup>

## 1.6.2 X-ray Absorption Spectroscopy (XAS)

X-ray Absorption Spectroscopy (XAS) is a technique used to study the chemical nature and environment of atoms in molecule.<sup>68</sup> Over the last three decades, XAS has made major contributions to numerous areas of biochemical research topics.<sup>68, 69</sup> It has played an essential role in exploring the correlation between structure and function of the metal sites in metalloprotein.<sup>69</sup> Both *in situ* and *operando* characterization by XAS have significantly contributed to the understanding of how heterogeneous and homogeneous catalysts functions.<sup>70, 71, 72</sup>

The principle of XAS is based on transitions of core electrons from the ground state to excited states by interaction of matter with X-rays.<sup>68</sup> The choice of the energy of the X-rays that are used, determines the specific element being probed, making XAS element-selective.<sup>68, 73</sup>

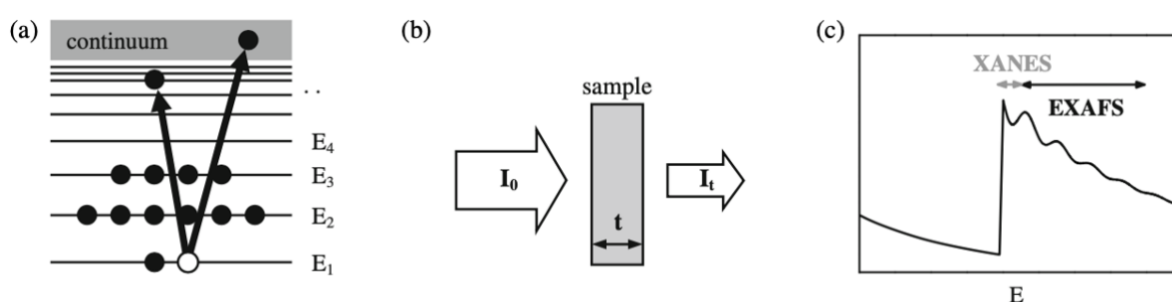


Figure 5: (a) Schematic Schematic of the absorption process, (b) Schematic of incident and transmitted X-ray beam and (c) absorption coefficient  $\mu(E)$  versus photon energy  $E$  including the fine structure above the edge divided into the XANES and EXAFS regions.<sup>74</sup>

Upon interaction of X-ray with an atom, core electron of the atom is either excited to lowest unoccupied molecular orbital (LUMO) or to the continuum (Figure 5, (a)), thus producing a photoelectron.<sup>65</sup> An X-ray absorption spectrum is acquired by measuring the ratio of the beam intensities before and after passing through the absorber, while the photon energy is tuned (Figure 5, (b, c)).<sup>74, 75</sup> XAS involves study of two main regions; X-ray absorption near-edge structure (XANES) and X-ray absorption fine structure (EXAFS). This thesis solely concentrates on XANES spectra of the synthesized complexes.

### **i. X-ray Absorption Near-Edge Structure (XANES)**

X-ray absorption Near-Edge Structure (XANES) spectra provide detailed information about the oxidation state and coordination environment of the metal atoms.<sup>68</sup> The XANES region of the spectrum is divided into two sections: the pre-edge and the rising-edge. As the photon energy reaches a value that is capable of exciting an electron from a strongly bound core level to a higher unoccupied state, a pre-edge is observed.<sup>75</sup> With increasing energy of the photon, the core electron get ionized and get ejected out of the molecule into the continuum state, giving rise to the edge in XANES spectrum.<sup>75</sup> Each edge has a typical energy, mainly depending on the atomic number of the absorbing atom.<sup>73</sup> The edges K-, L- and M- corresponds to which core the electron is excited from,  $n = 1, 2$  and  $3$ , respectively.<sup>68</sup> Transition metals with higher oxidation states have position of the absorption edge at higher energies.<sup>76</sup>

## 2 Discussion

### 2.1 LPMO active site: An Approach for Ligand Design

The ideal strategy for modelling LPMO's active site relies on the synthesis of copper-complexes with polydentate ligands, with nitrogen and/or oxygen atoms that can coordinate to the copper ion, analogous to the histidine and tyrosine residues present at the active site of the enzyme.

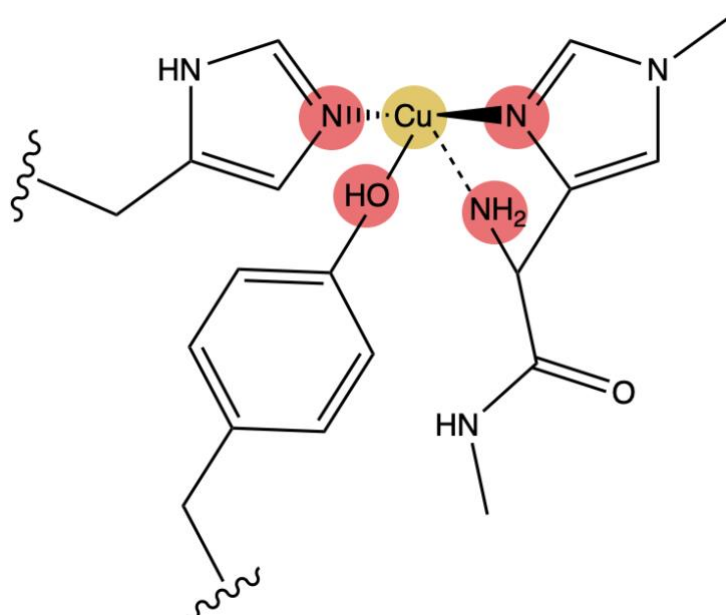


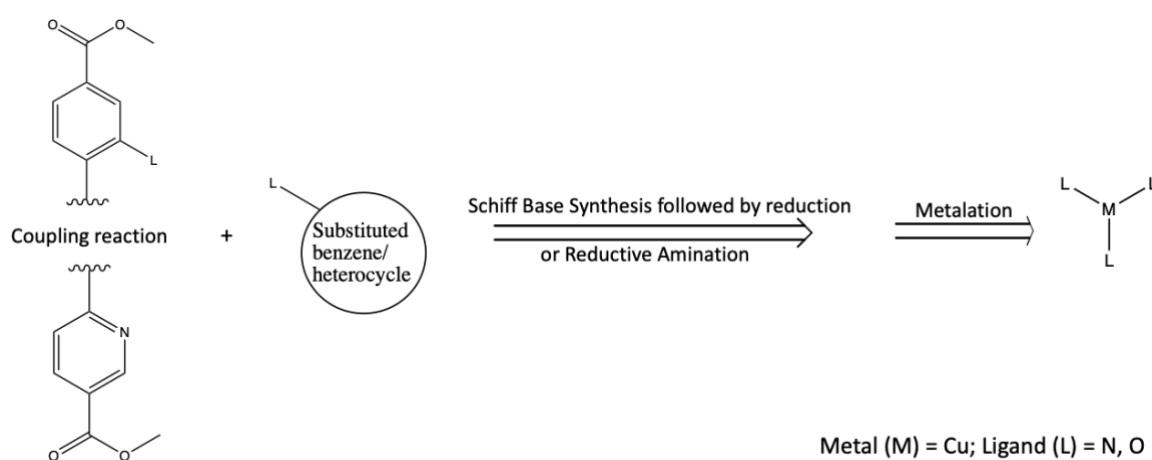
Figure 6: Structure of the metal-site of AA9 LPMO enzyme. Metal ion (Copper) in gold, ligated by nitrogen and oxygen atoms (red).

As depicted above (Figure 6), there are two  $sp^2$  hybridized nitrogen atoms and one  $sp^3$  hybridized nitrogen atom, coordinated to the metal. To introduce these ligated atoms, heterocyclic compounds like imidazole and pyridine, and aromatic rings containing hydroxy- and amino-group were chosen, as they hold similar properties.

Previously in the group, copper complexes bearing bidentate, tridentate and tetradentate N-ligands have been synthesized.<sup>77</sup> In this thesis, to imitate the metal-center as best as possible, copper complexes that involve coordination with nitrogen and oxygen ligands have been synthesized and characterized.

## 2.2 Ligand Synthesis Strategies

Considering the potential for the synthesized complexes to be incorporated into MOFs in the future, the ligands were designed to have ester groups attached to them. The ester groups after conversion to their corresponding diacids by hydrolysis, forms linkers for MOFs. The ester group serves as a protecting group during synthesis and also increases solubility of the compound. To obtain crystalline MOFs, it is crucial to have rigid linkers. Therefore, to ensure a rigid structure of the ligand, it is crucial to have two aromatic rings as the backbone of the ligand, such as phenyl- or pyridyl scaffolds. Aromatic rings are planar because of the  $sp^2$ -hybridization, which increases both the stability and rigidity of the ligand.



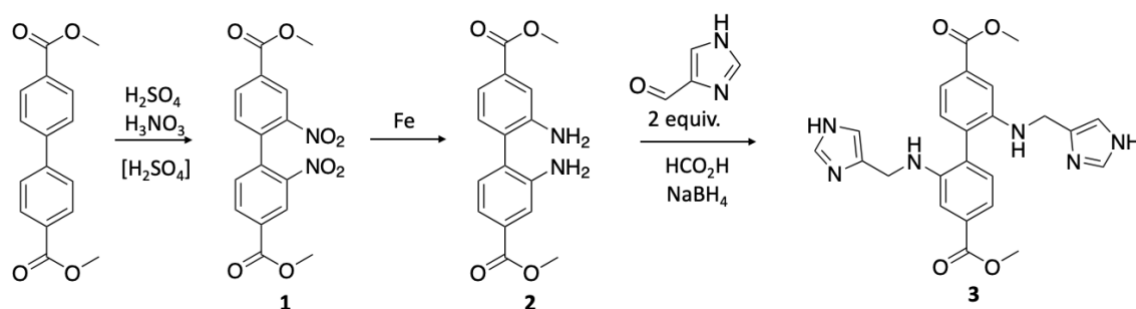
Scheme 5: Synthetic strategy towards incorporating functional groups (including nitrogen and oxygen) to facilitate metalation.

For introducing different functional groups containing nitrogen and oxygen atoms, metal catalyzed cross-coupling reaction, more specifically Suzuki-Miyaura coupling reaction, can be a suitable choice for carbon-carbon bond formation.<sup>78</sup> As depicted above (Scheme 5), by cross-coupling reaction, different functional groups can be effectively incorporated into the ligand structure, providing new coordination sites for the metal (Cu). One approach involves coupling reaction between two nitrogen bearing phenyls, for example between a pyridine and a nitro-bearing phenyl, which after reduction can further react in a Schiff base synthesis with a phenyl containing a hydroxy group. Another alternative approach can be coupling reaction between two phenyl groups, one containing a hydroxy, and the other containing amino group which further can take part in Schiff base synthesis and introducing another nitrogen in form of a pyridine/imidazole for instance. Therefore, by strategically varying and selecting the

substituents for Suzuki-Miyaura cross-coupling reaction and Schiff base synthesis, it is possible to form the desired functionalized ligands.

### 2.2.1 Synthesis Route towards Ligand (3)

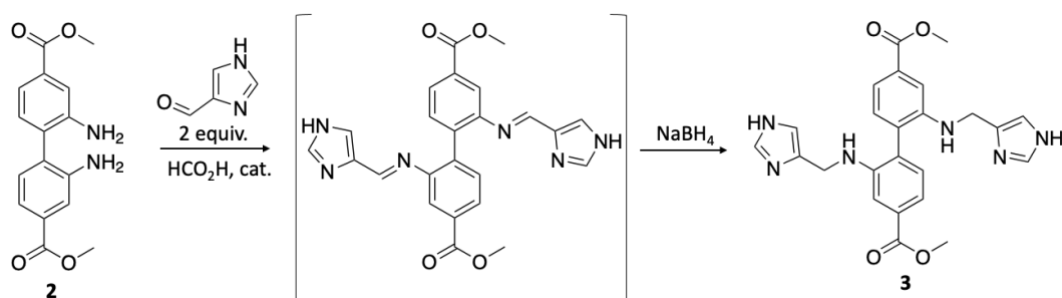
The synthesis route of ligand **3** consisted of three sequential steps, as shown below (Scheme 6), which includes nitration, followed by reduction and reductive amination in a one-pot manner.



Scheme 6: Nitration, followed by reduction and one-pot synthesis to form **3**.

The first step involves nitration of commercially available Dimethylbiphenyl-4,4'-dicarboxylate. The reaction was carried out using nitric acid as a nitrating agent, and sulfuric acid as a protonating agent. The reaction was proceeded according to literature.<sup>79</sup> Since nitration reaction is generally an exothermic reaction, the reactants are added at low temperatures (around 1-5 °C). After recrystallization from acetonitrile, product **1** was obtained as yellow cube-shaped crystals at a yield of 68%.

The second step in the synthesis route is reduction of the nitrated compound **1** to compound **2**.<sup>80</sup> Iron was used as a reducing agent along with acetic acid. The acid serves to protonate the nitro-group and activates it for reduction by iron. The crude product was recrystallized from toluene, resulting in a yield of 84%. The formation of **2** was observed by appearance of amine signal at 4.99 ppm in  $^1\text{H}$  NMR, integrating 2 hydrogens, and the rest of the spectroscopic data was in accordance with that reported in the literature.<sup>80</sup>



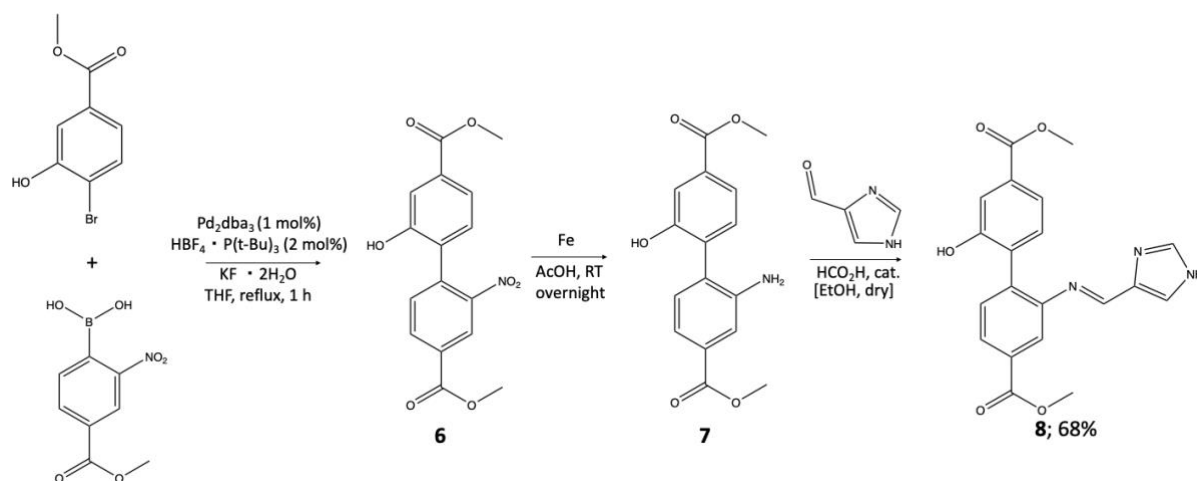
Scheme 7: Reductive amination of **2** in presence of formic acid, forming ligand **3**. Reaction procedure adapted from reference.<sup>77</sup>

Previously in the group,<sup>77</sup> the imine form of the Ligand **3**, the intermediate in this reaction (Scheme 7), has been synthesized and metalized with Cu(OTf), with all four of the sp<sup>2</sup> hybridized nitrogen atoms coordinated to the copper ion. After analyzing the structure of the active site of the LPMO enzyme, along with two sp<sup>2</sup> hybridized nitrogen atoms, there is also one amino group (sp<sup>3</sup>-hybridized) coordinated to the metal. Therefore, the inclusion of amino groups in the ligand, which might have the ability to coordinate with copper, was chosen, enhancing its resemblance to the active site.

To obtain the desired ligand **3**, the final step involved a one-pot synthesis which consists of Schiff base synthesis, followed by reduction (reductive amination), to convert the initially formed imine to the desired amine (Scheme 7). The Schiff base reaction is an acid-catalyzed condensation, and formic acid was used as the catalyst. The crude product was purified by recrystallization from acetonitrile, resulting in a yellow solid with a yield of 24%. The yield was lower than the reported yield of 30%,<sup>77</sup> this could likely be the result of the work-up procedure and recrystallization as the purification method. Despite the significant loss of material, the remaining product was pure by NMR and MS. The presence of terminal imidazole groups was identified by <sup>1</sup>H NMR with the characteristic signal of NH (imidazole) at 11.9 ppm, and formation of CH<sub>2</sub> was observed at 4.23 ppm. The rest of the signals were assigned with the help of 2D NMR, and the overall spectroscopic data fitted well with that reported in literature.<sup>77</sup> Additionally, the ligand was also studied by FTIR and UV-Vis (Section 2.3.1) in order to draw a comprehensive comparison with this corresponding copper(II) complex **5**.

## 2.2.2 Synthesis Route towards Ligand (8)

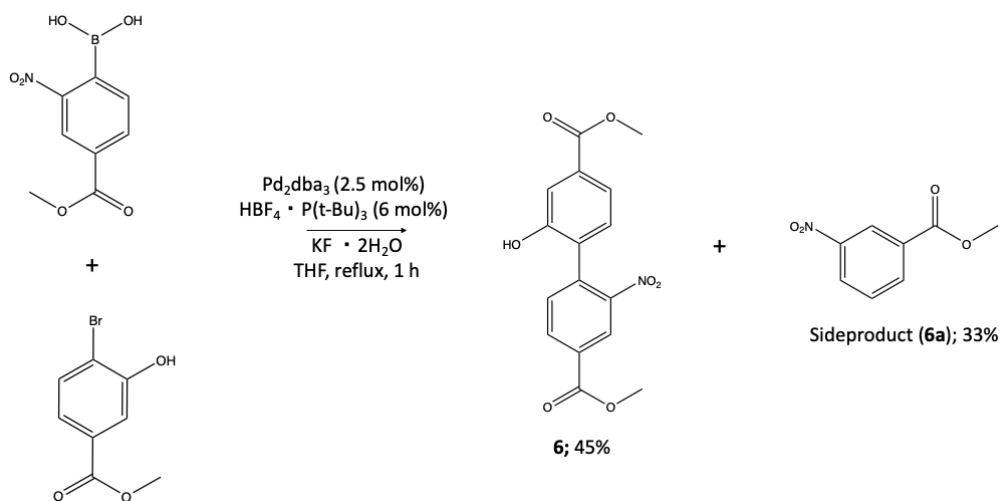
To functionalize the backbone of the linker, palladium catalyzed Suzuki-Miyaura cross-coupling reaction was employed. In this case to introduce a hydroxy and imine group in the system, cross-coupling was conducted involving derivatives of hydroxy and nitro groups. The synthesis route of ligand **8** is shown below (Scheme 8), which consists of three sequential steps, Suzuki-Miyaura cross-coupling reaction, reduction, and Schiff base synthesis.



Scheme 8: Synthesis route to ligand **8**, Suzuki-Miyaura cross-coupling reaction, followed by reduction and Schiff base synthesis.

The first step towards synthesizing ligand **8** was Suzuki-Miyaura cross-coupling reaction between commercially available reactants methyl 4-bromo-3-hydroxybenzoate and (4-(methoxycarbonyl)-2-nitrophenyl) boronic acid. The reaction was conducted by using  $\text{Pd}_2\text{dba}_3$  as the primary catalyst,  $\text{HBF}_4 \cdot \text{P}(\text{t-Bu})_3$  as a co-catalyst, and  $\text{KF} \cdot 2\text{H}_2\text{O}$  as a base in THF as the solvent. The reaction procedure was adapted from reference.<sup>81</sup> Flash chromatography was used to purify the crude, and the resulting product was further purified by recrystallization from toluene, resulting in yellow/green crystals with a yield of 45%. The reported yield in the literature was higher, 69%.<sup>81</sup> The relatively low yield is due to the unreacted starting material, as identified through crude NMR spectrum.





Scheme 9: Palladium-catalyzed Suzuki-Miyaura cross-coupling reaction, forming **6** and the sideproduct **6a**.

During the Suzuki-Miyaura cross-coupling reaction (Scheme 9), an unintended sideproduct **6a** was observed, the aryl boronic acid was found to decompose to the parent arene. The sideproduct (**6a**) was isolated by flash chromatography (gradient: first: half DCM / half 5% EtOAc in Hexane, then: half DCM / half 15% EtOAc in Hexane) with a yield of 33%, and fully characterized by NMR. The Suzuki-Miyaura reaction is a widely used organic reaction for synthesis of C-C bonds between aryl/vinyl boronic acids and aryl/vinyl halides. However, one of the challenges accompanying this reaction is the decomposition of boronic acids under certain reaction conditions. Transition metal catalysts, bases, and elevated temperatures can compromise the stability of the boronic acid.<sup>82, 83</sup> Formation of this sideproduct has also been observed in similar reactions, employing the same boronic acid but varying aryl/vinyl halide.<sup>81</sup> The precise cause of the decomposition is uncertain, it could either be the metal catalyst, the base, reaction temperature or a combination of these factors. Further investigation is required to gain a more detailed understanding of the factors leading to the decomposition of the aryl boronic acid.

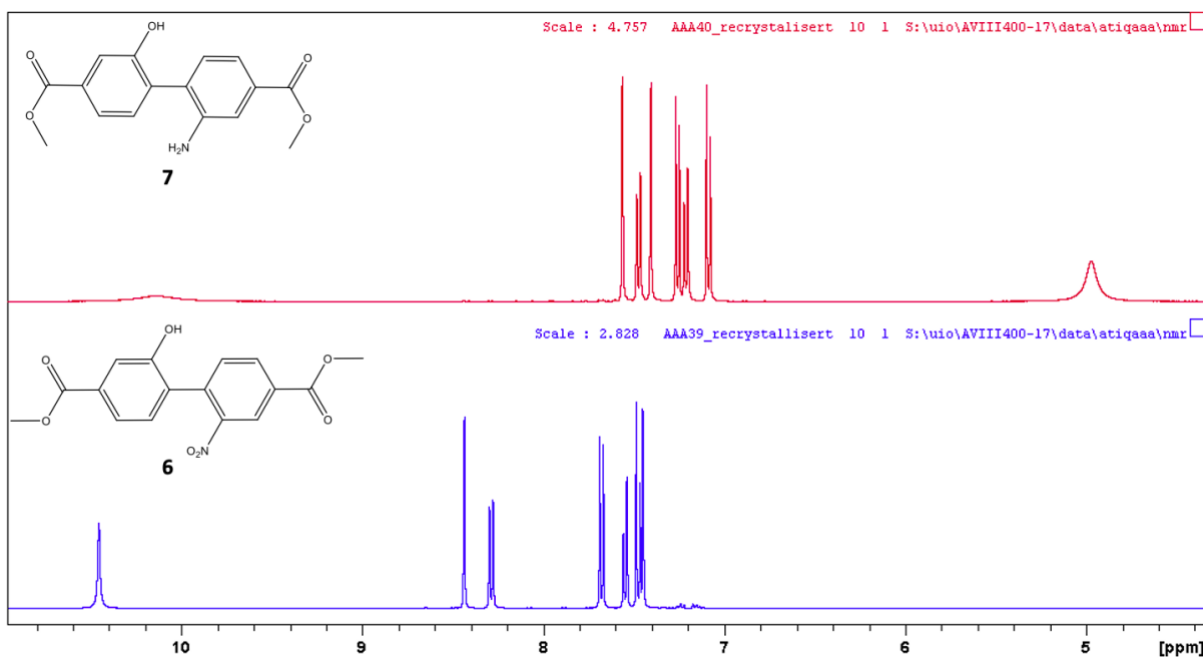
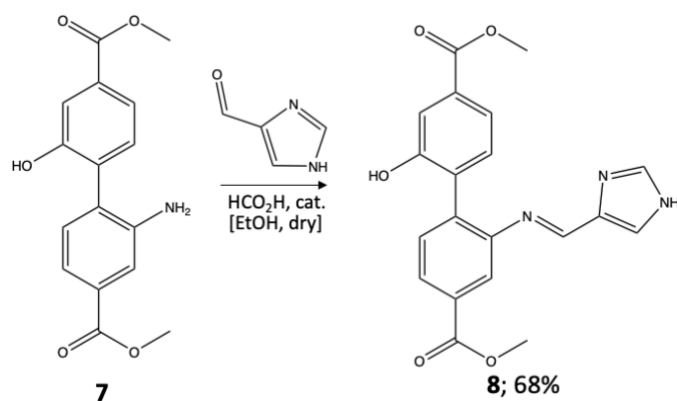


Figure 7: Comparison of <sup>1</sup>H NMR (400MHz, DMSO-d<sub>6</sub>) spectrum of compound **6** (below) and **7** (above).

The second step in the synthesis route is reduction of the nitro-group present in compound **6**. Iron was used as a reducing agent along with acetic acid. The reaction was proceeded as expected, and after recrystallization from acetonitrile a yellow solid **7** was obtained with a yield of 46%. The formation of amino group was observed by appearance of a broad singlet at 4.97 ppm (Figure 7), integrating 2 hydrogens. In addition, the signals at the aromatic region shifted more downfield for compound **7**, compared to the signals of compound **6**. Another noteworthy observation was broadening of hydroxy signal (Figure 3) after the reduction. There are several factors that can lead to broadening of signals in nuclear magnetic resonance (NMR). In this case, it could be rapid molecular motion (dynamic in the molecule), which can broaden the NMR signals due to averaging of different magnetic environments experienced by the nuclei. The torsion angle between two phenyl rings (biphenyl) is sensitive to its chemical and macroscopic environment.<sup>84</sup> In a study,<sup>85</sup> barriers to rotation have been determined by dynamic NMR spectroscopy for a series of biphenyl compounds, and the variation in steric size has been identified as the primary contributor in rotation barrier. To conclude, the increased dynamism results in greater signal broadening. Therefore, since compound **6**, containing a nitro-group is bulkier than the amino-group in compound **7**, the signal OH-signal for **6** is sharper due to reduced rotational freedom as in for **7**.



Scheme 10: Synthesis of ligand **8**, through acid catalyzed Schiff base synthesis.

The final step towards synthesizing the desired ligand **8** involves Schiff base synthesis, a condensation reaction between an aldehyde (1H-imidazole-4-carbaldehyde) and amine **7**, with formic acid as a catalyst promoting the condensation reaction (Scheme 10). It was an overnight reaction which resulted in an airy/puffy white solid after recrystallization from acetonitrile, with a yield of 68%. After recrystallization, the isolated compound **8** was dried in vacuum oven (60 °C, overnight). However, there was still detectable traces of acetonitrile present in the sample, observed by NMR. Despite making another attempt on drying the compound by the vacuum oven, no change was observed.

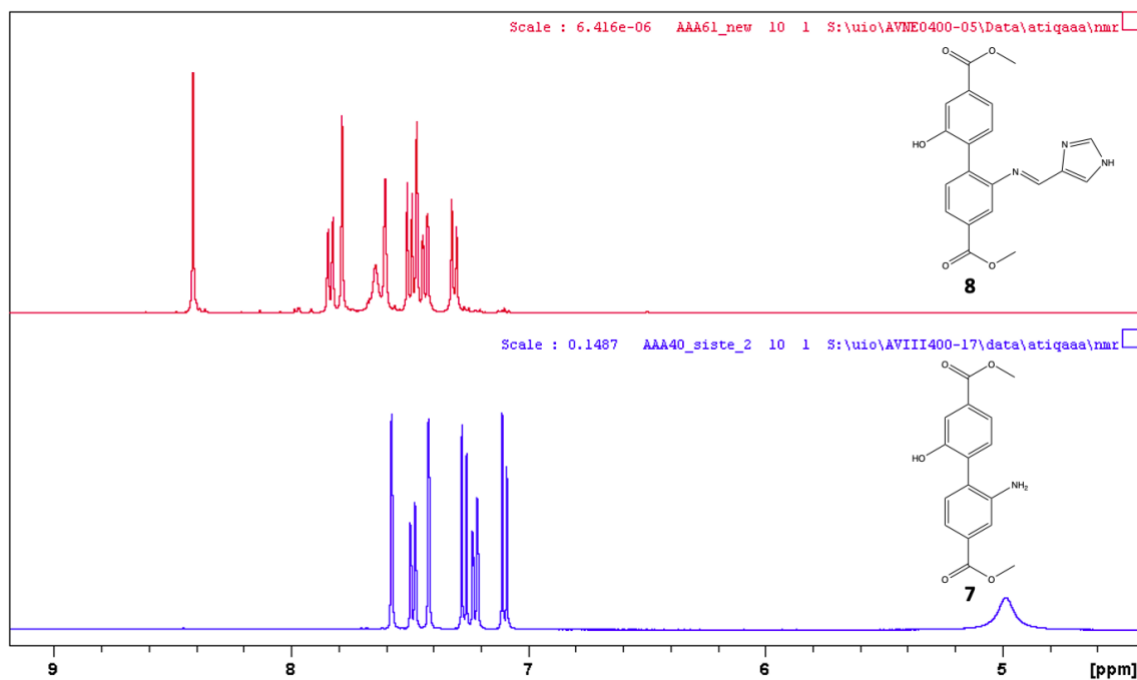


Figure 8: Comparison of  $^1\text{H}$  NMR (400MHz,  $\text{DMSO-d}_6$ ) spectrum of compound **7** (below) and **8** (above).

Ligand **8** was characterized by NMR and HRMS. Formation of the Schiff base **8** was observed by disappearance of amine signal at 4.97 ppm (Figure 8, below), accompanied by the appearance of a characteristic signal at 8.41 ppm for the imine, integrating 1 hydrogen, (Figure 8, above). Furthermore, the signals at the aromatic region exhibited a more downfield shift.

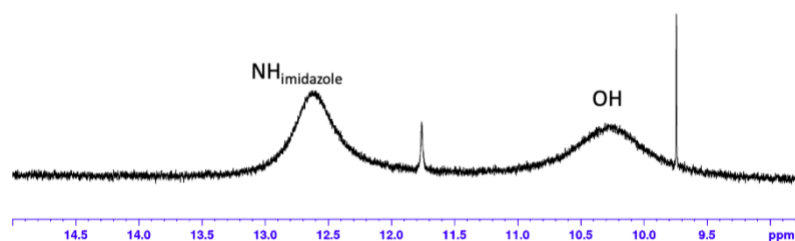


Figure 9:  $^1\text{H}$  NMR (400MHz,  $\text{DMSO-d}_6$ ) spectrum of ligand **8**.

Moreover, the typical broad signals for hydroxy- and NH (imidazole)-group were observed at 10.25 and 12.62 ppm respectively (Figure 9). In addition to these two signals, there were two more signals next to hydroxy- and NH (imidazole)- signal, at 9.75 and 11.75 ppm, possibly dynamic-induced signals, with relatively low intensity compared to other signals in the spectrum.

The NMR signals shown above (Figure 9) suggests that the compound **8** is in a state of dynamic equilibrium. In imidazole, there is lone pair of electrons at N-atom which is not involved in the aromaticity of the heterocycle,<sup>86</sup> making imidazole act as a weak base. In addition, the resonance forms of imidazole (Figure 10) also make this nitrogen atom more nucleophile, allowing the nitrogen atom to undergo electrophilic reactions

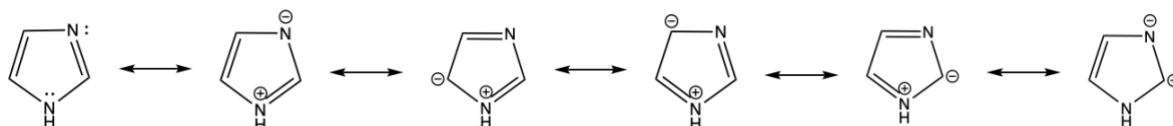


Figure 10: Resonance forms of imidazole.<sup>25</sup>

The hydroxy group can act both as a proton donor and proton acceptor depending on its environment. Given the circumstances, it is likely that nitrogen with the lone pair acts as a nucleophile and abstracts the hydrogen in the OH-group, resulting in intra-molecular hydrogen transfer, forming a zwitterion with an imidazolium ion and phenolate (Figure 11).

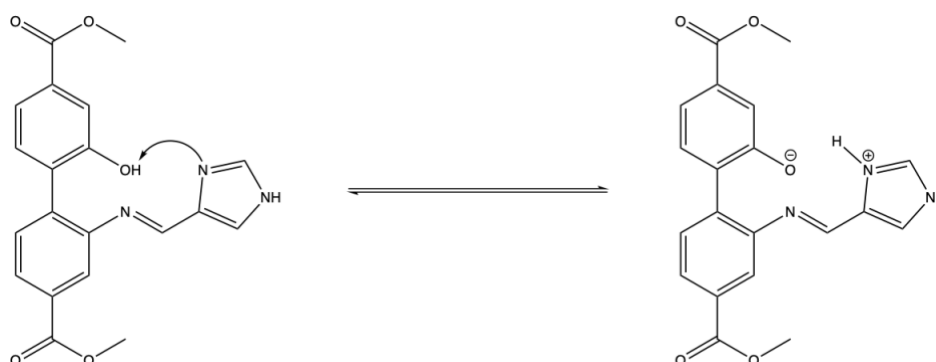
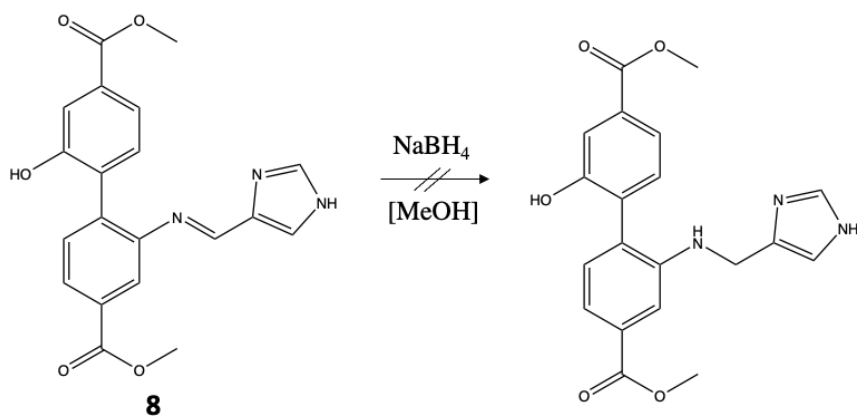


Figure 11: Possible zwitterion formation of **8**, resulting in multiple NMR resonances.

### 2.2.3 Attempted Reduction of Ligand (8)

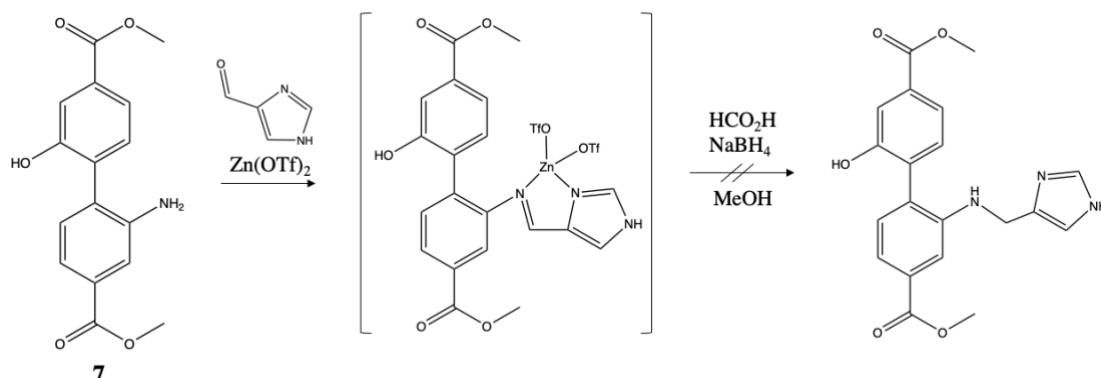
To enhance the resemblance of the potential complex to the active site of LPMO enzyme, reduction of imine in ligand **8** was attempted. Since in **8**, there are two  $sp^2$ -hybridized nitrogen atoms for coordination, whereas at the active site there are both  $sp^3$ - and  $sp^2$ -hybridized nitrogen atoms coordinated to the metal. Therefore, it was attempted to reduce the Schiff base (imine) to a  $sp^3$ -hybridized nitrogen.



Scheme 11: Attempted reduction of schiff base **8** with sodium borohydride to yield secondary amine.

Sodium borohydride ( $\text{NaBH}_4$ ) is a mild reducing agent, and is common for reduction of Schiff bases to yield secondary amine.<sup>87, 88</sup> The reduction of imine present in ligand **8** was attempted using 5 equivalent of  $\text{NaBH}_4$  in dry methanol (Scheme 11). The crude was studied by NMR, the imine signal remained unaffected, and there was no emergence of a secondary amine signal. Additionally, the aromatic- and methyl-signals exhibited no change, confirming the reaction did not proceed as expected. Despite increasing the reductant amount, from doubling it to 10 equiv., then having it in an excess amount, the reaction did not achieve intended outcome.

A different strategy was opted for reduction, namely via a zinc complex. A zinc(II) Schiff base complex was synthesized (Scheme 12) from **7**, and then subsequently reduced using NaBH<sub>4</sub> to obtain the corresponding amine.



Scheme 12: Attempted reduction of imine **8** to amine via zinc complex. Procedure adapted from reference.<sup>77</sup>

As observed by NMR (Figure 12), synthesis of the zinc(II) Schiff base proceeded as expected. A distinct shift is evident upon comparing the methyl signals of **7** and the Zn-complex, and majority of **7** has reacted, just a small portion of **7** remained unreacted as traces of it can be seen in the complex's NMR spectrum. Furthermore, signals in the aromatic region also exhibited shift, along with broadening of signals. The formation of Schiff base was identified by appearance of a signal at 8.4 ppm, which is characteristic for imine.

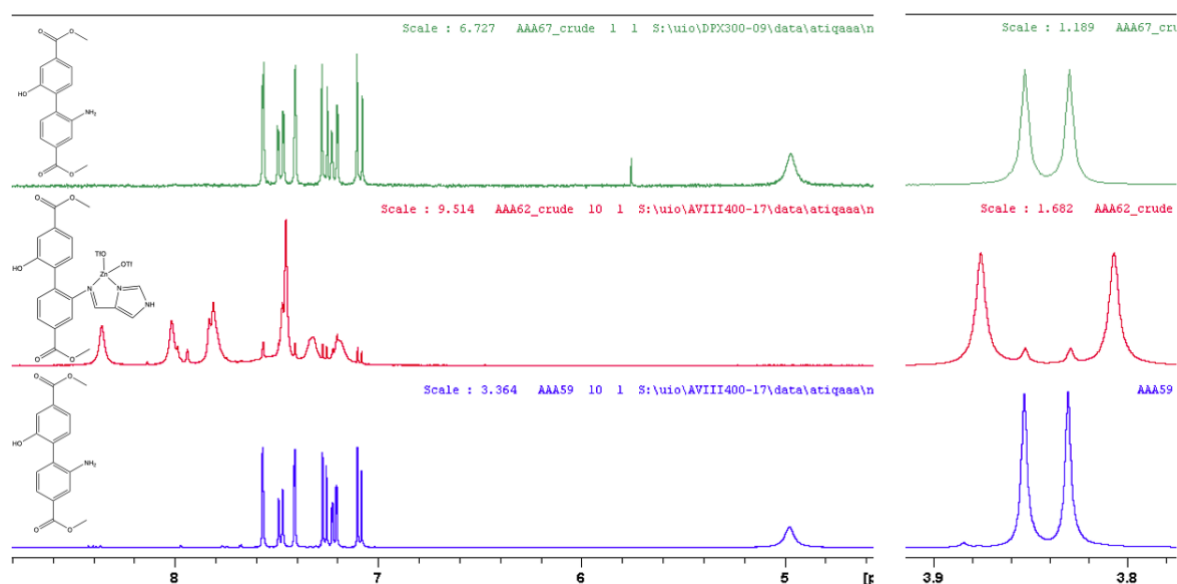


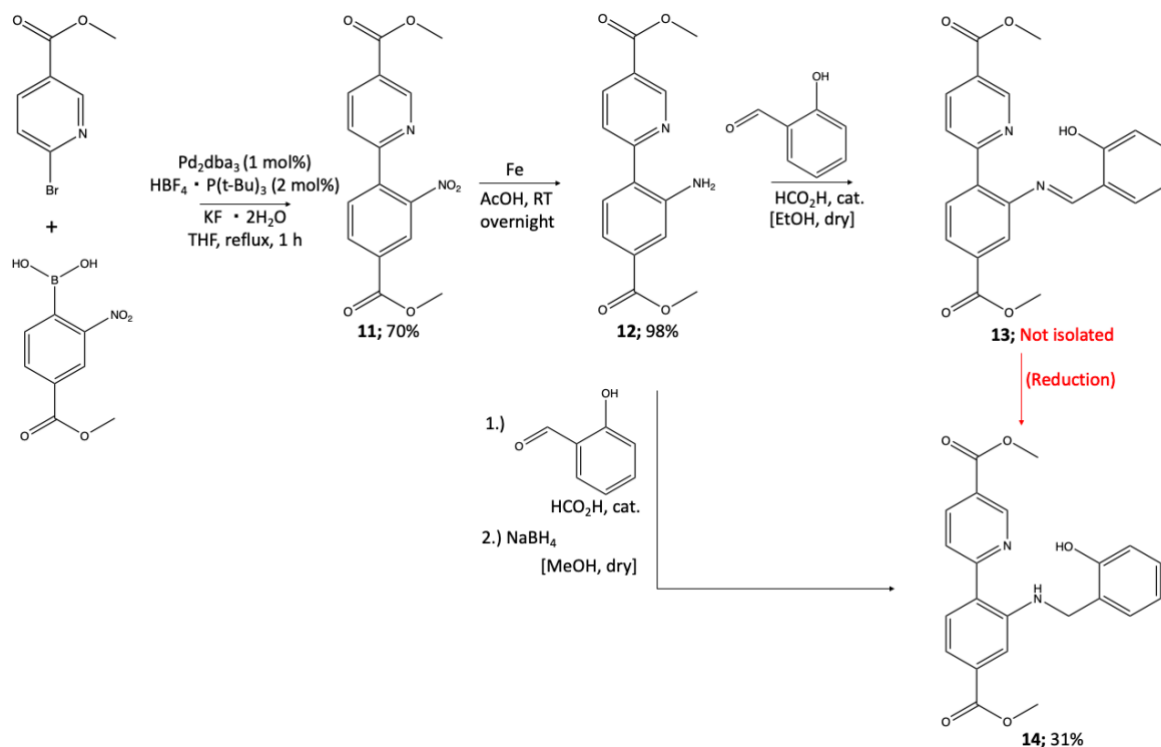
Figure 12: Comparison of <sup>1</sup>H NMR (400MHz, DMSO-d<sub>6</sub>) spectra of starting material **12** (bottom), zinc complex **intermediate** (middle), and (300 MHz, DMSO-d<sub>6</sub>) spectrum of crude (top) after reduction with NaBH<sub>4</sub>.

Following reduction with  $\text{NaBH}_4$ , the reaction failed to yield the expected compound, a ligand containing a secondary amine. Instead, after the workup, starting material from previous step, **7**, was collected in the organic phase. The workup consisted of neutralizing  $\text{NaBH}_4$  with  $\text{NaHCO}_3$ , and then removal of metal ion with  $\text{Na}_2\text{EDTA}$ . The peculiarity lied in the absence of aldehyde in the crude NMR, only compound **7** was observed, while the presence of the aldehyde was not detected. It is possible that the aldehyde might have retained in the aqueous phase during the workup. This reaction has not been repeated, but repetition of this reaction and a thorough investigation is necessary for better understanding of the outcome.



## 2.2.4 Synthesis Route towards Ligand (14)

The third ligand design was proposed to introduce yet again both  $sp^3$ - and  $sp^2$ -hybridized nitrogen atoms and an oxygen atom, with the aim of closely imitating the active site of the LPMO enzyme.



Scheme 13: Two synthetic strategies for ligand **14**.

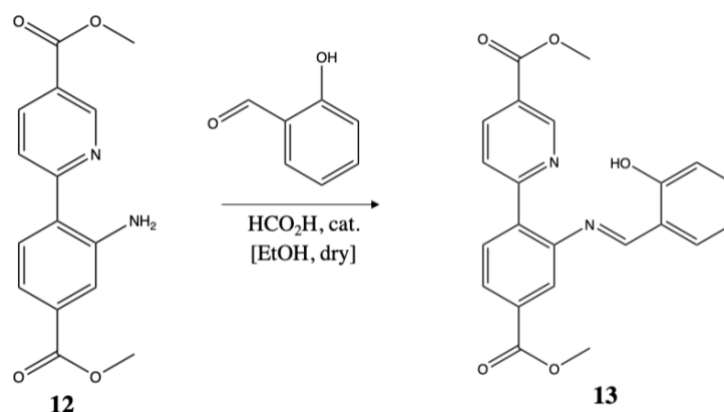
Two approaches were made to obtain ligand **14** (Scheme 13). The first approach consisted of four steps: a Suzuki Miyaura cross-coupling reaction, followed by reduction, Schiff base synthesis and then reduction of the Schiff base. After successfully completing the first two steps, coupling reaction forming **11**, followed by reduction to **12**, the product **13** from the third reaction was not isolatable as a pure compound. Different eluent systems had been tested for isolating **13** by flash chromatography, along with different solvents for recrystallization, but none gave the desired outcome. Therefore, an alternate synthetic strategy was used as a substitute for the third reaction in the first approach. A one-pot synthesis, formation of imine *in situ* and reduction to secondary amine, was conducted and proved to be successful. The one-pot synthesis route was not initially chosen due to the intention of metalating both **13** and **14**.

Synthesis of ligand **14** begins with a Suzuki Miyaura cross-coupling reaction between commercially available Methyl 6-Bromo-3-pyridine carboxylate and 4-methoxycarbonyl-2-nitrophenylboronic acid to form **11** (Scheme 13). The reaction was conducted by using Pd<sub>2</sub>dba<sub>3</sub> as the primary catalyst, HBF<sub>4</sub> • P(t-Bu)<sub>3</sub> as a co-catalyst, and KF • 2H<sub>2</sub>O as a base in THF as the solvent. The reaction procedure was adapted from literature.<sup>81</sup> The crude was purified with flash chromatography, resulting in a yield of 70%, whereas the reported yield in the literature is 95%.<sup>81</sup> The relatively low yield is due to a combination of both unreacted reactants and loss of some material in the purification step. The formation of **11** was characterized by NMR and MS. The NMR spectrum of the product **11** exhibited shifts for all the signals in the aromatic region and the methyl signals.

The second step in the synthesis route is reduction of the nitro-group present in compound **11**. Iron was used as a reducing agent along with acetic acid. The reaction was proceeded as expected with a yield of 98%, and no purification step was required as the crude was clean by NMR. The reduction of nitro-group and formation of **12** was confirmed by NMR by the appearance of a singlet at 6.02 ppm, integrating 2 protons.

The final step towards synthesizing the desired ligand **14** involves a one-pot synthesis, reductive amination, Schiff base synthesis and reduction in one step. The crude NMR of **14** showed ca. 50% conversion to the product. There were no traces of imine (**13**) detected in the crude NMR, just unreacted **12** was observed. Hence, it is safe to conclude that all the formed imine was effectively reduced to **14**. Flash chromatography (gradient: first: 20% EtOAc / 80% Hexane, then: 50% EtOAc / 50% Hexane) was used to purify the crude, which resulted in a yield of 31%. There was trace amount of **12** present in the final product, but due to time limitation it was not further purified.

## 2.2.5 Reaction optimization for compound **13**



Scheme 14: Schiff base synthesis to form **13**.

Despite numerous attempts, both by flash chromatography and recrystallization, isolating **13** (Scheme 14) was not achieved. Therefore, reaction optimization strategy was employed to maximize the yield and eventually facilitate isolating the product.

Table 1: Attempted synthesis of **13** under different reaction conditions.

Attempt	Aldehyde equiv	Reaction time	Formic acid	Conversion
1	1.1 equiv.	1 day	2 drops	75% (Molar ratio after workup)
2	1.1 equiv.	1 day	3 drops	65% (Molar ratio after workup)
3	1.1 equiv.	2 days	3 drops	52%
4	1.1 equiv.	3 days	3 drops	63%

The amount of formic acid and reaction time were modified in subsequent attempts to increase the yield of **13**. Salicylaldehyde was present in excess (1.1 equiv.), since it is in liquid form in contrast to the other reactant **12** and the product **13**, which are in solid state, thereby easier to remove. As shown above (Table 1), the conversion from first two attempts were calculated after the workup procedure, while conversion for the last two attempts were determined prior to workup, i.e. taken right from the reaction mixture. Therefore, direct comparison between the two sets, the first two with the bottom two, are not feasible. In the first two attempts, the reaction time was kept the same (1 day), while the quantity of formic acid was altered (from 2 to 3 drops). Increasing the amount of formic acid in the reaction mixture showed deterioration in the conversion. Furthermore, reaction time was also a factor in the improvement of the conversion. By comparing the last two reaction attempts, increasing the reaction time (from 2 to 3 days) resulted in increased conversion.

## 2.3 Metalation

Due to the paramagnetic property of Copper (II) complexes, the synthesized ligands were metalated with both Copper (I)- and Copper (II)-salts in order to obtain a more comprehensive understanding of the complexes. In contrary to  $\text{Cu}^{2+}$  ion,  $\text{Cu}^+$  ion is diamagnetic, thereby allowing us to conduct NMR analysis on Copper(I) containing compounds. The Copper (II) complexes were analyzed by using MS, UV-Vis and FTIR.

### 2.3.1 Metalation of Ligand 3

As shown below (Figure 13), Ligand **3** was metalated with both copper(I)- and copper(II)trifluorometanesulfonate, forming complex **4** and **5**, respectively. After workup, complex(I)complex **4** yielded in a turquoise solid (98%) and complex **5** yielded in a dark green powder (94%).

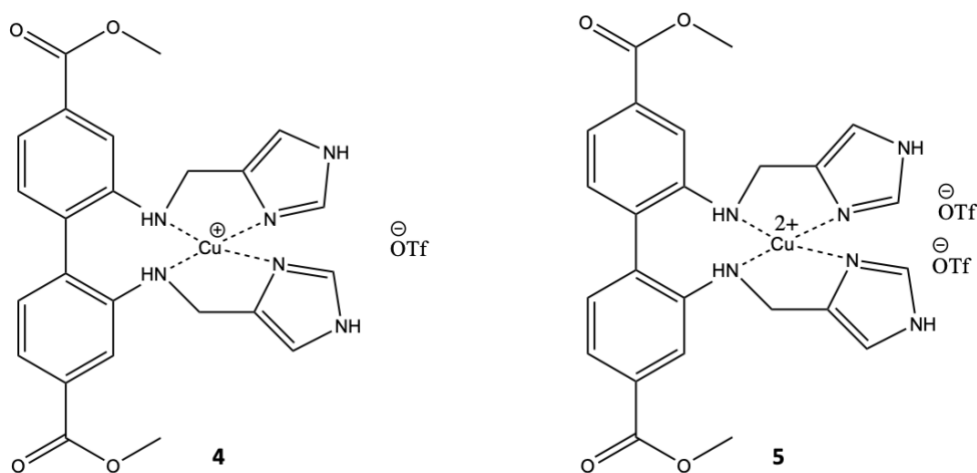


Figure 13: The synthesized copper (I)- (**4**) and copper (II)-complexes (**5**).

Complex **4** exhibited significant instability, it was easily oxidized even when stored in an inert atmosphere (glovebox). Consequently, the complex was characterized short after the workup, despite presence of some residual solvents.

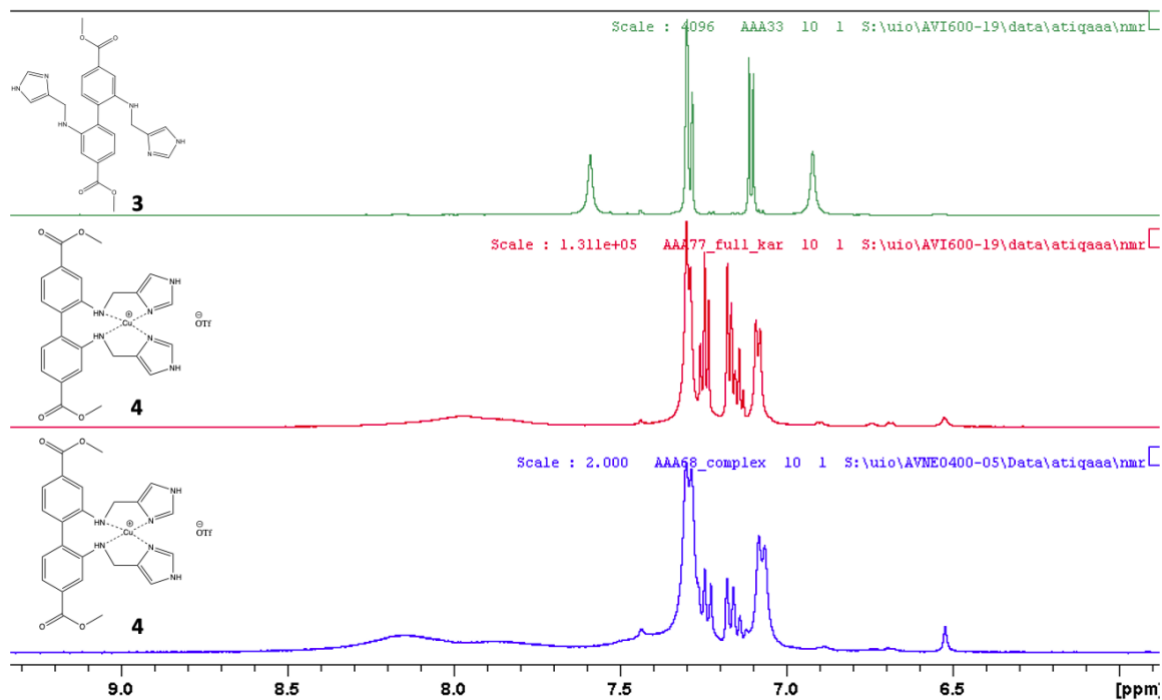


Figure 14: Comparison of  $^1\text{H}$  NMR (600MHz,  $\text{DMSO-d}_6$ ) spectrum of ligand **3** (top) and complex **4** from two different batches, measured shortly after workup (middle), and measured after couple of days (bottom).

As shown above (Figure 14), after metalation of ligand **3**, the aromatic signals exhibited a significant shift and slight broadening of the signals. The NH (imidazole) signal also exhibited a slight shift. Furthermore, there was a broad signal observed at 8.00 ppm, integrating 4 hydrogens. This signal showed no correlation to other signals, as investigated by 2D NMR. The cause of the observed broad signal at 8.00 ppm is uncertain whether it is attributed to the presence of solvent or the process of the complex's oxidation. As shown above (Figure 14),  $^1\text{H}$  NMR of complex **4** from a different batch, measured after a few days of synthesizing it, shows more oxidized sample, even when store in an inert atmosphere.

Obtaining a high-quality single crystal for Single Crystal X-Ray Diffraction has been a challenge for the synthesized complexes in this thesis. However, after numerous attempts with different solvents, a green-colored single crystal for complex **5** was obtained by vapor diffusion technique using pentane and dichloromethane. Although the crystal obtained was not of high-quality, displaying "Level A Alerts", it still is a good first estimate of how the structure looks like. The structure (Figure 15) revealed that the compound was a copper complex, with the ligand surrounding it forming a chelate complex, as expected (Figure 13).

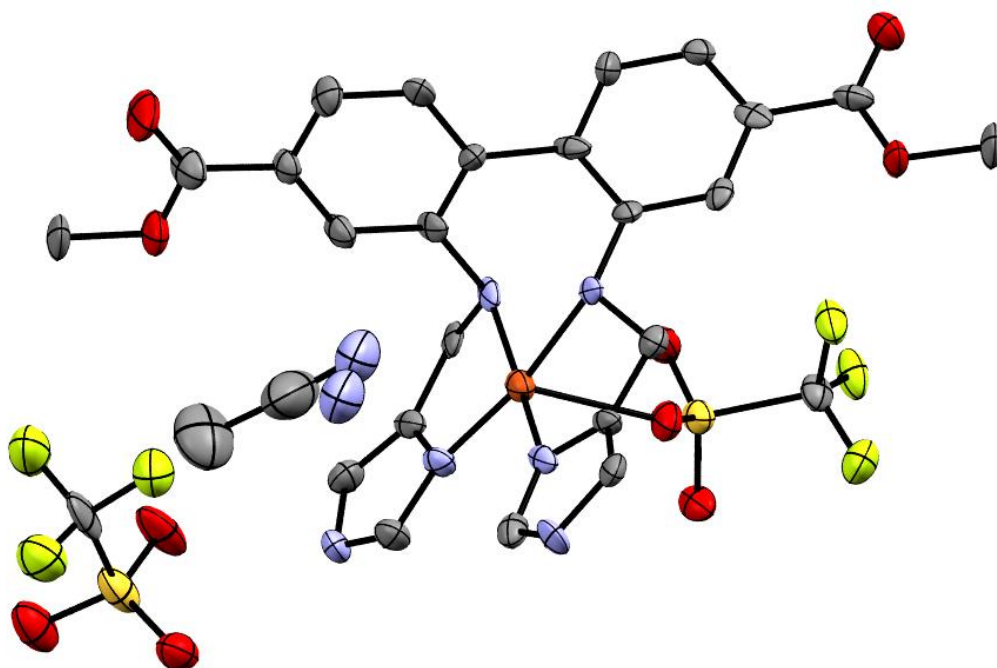


Figure 15: Single crystal XRD structure of **5** with ellipsoids drawn at the 50% probability level. Hydrogen bonds have been removed for clarity.

As shown in the SC-XRD structure above (Figure 15), the Copper(II) consists within a five-coordinate environment. It is coordinated with two  $sp^2$ -hybridized nitrogen atoms deriving from the imidazole residues, two  $sp^3$ -hybridized nitrogen atoms, and one oxygen atom from one of the two counter-anions, trifluoromethanesulfonate (OTf). The co-crystallized acetonitrile exhibited significant distortion; therefore two nitrogen atoms are shown.

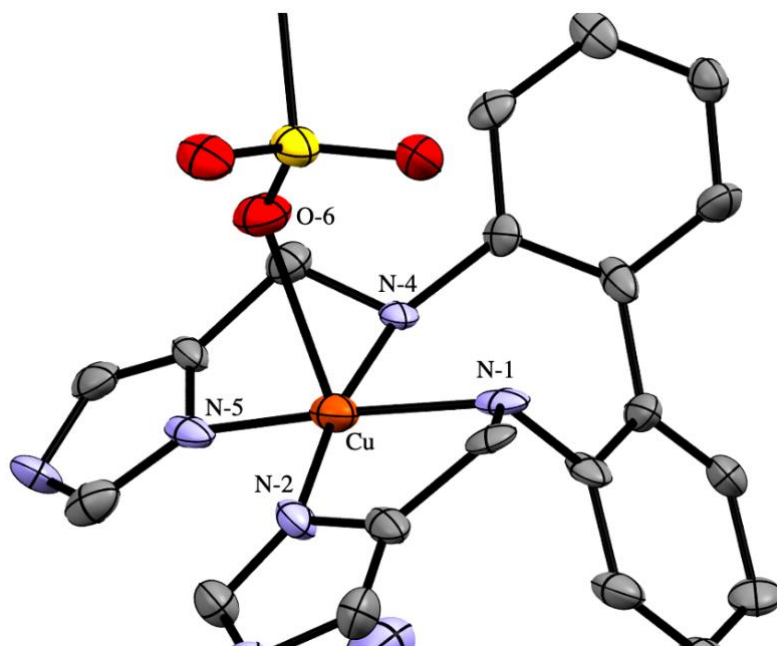


Figure 16: Close up on the metal center in the SC-XRD of complex **5**. Coordination bond lengths [Å]: Cu-N1: 2.056(8), Cu-N2: 1.958(9), Cu-N4: 2.082 (9), Cu-N5: 1.942(9), Cu-O6: 2.395(6)

The Cu-N<sub>imidazole</sub> coordination bonds are 1.95 Å and 1.94 Å, which align with the typical Cu-N<sub>imidazole</sub> bond (1.99 Å).<sup>89</sup> The Cu-N<sub>amine</sub> coordination bonds are longer than Cu-N<sub>imidazole</sub>, 2.08 Å and 2.39 Å, which sits also well with that listed in literature (2.03 Å).<sup>89</sup> Furthermore, the Cu-O<sub>triflate</sub> coordination bond is 2.39 Å, this deviates slightly from a typical Cu-O bond (1.92 Å). There is also an acetonitrile that has co-crystallized with the complex, but it does not coordinate to the copper. The distance between nitrogen on the acetonitrile and copper is 3.00 Å, this does not align with the range of the other coordination bond lengths of the complex. Moreover, the two phenyl rings are not in plane, they are significantly twisted by 55°.

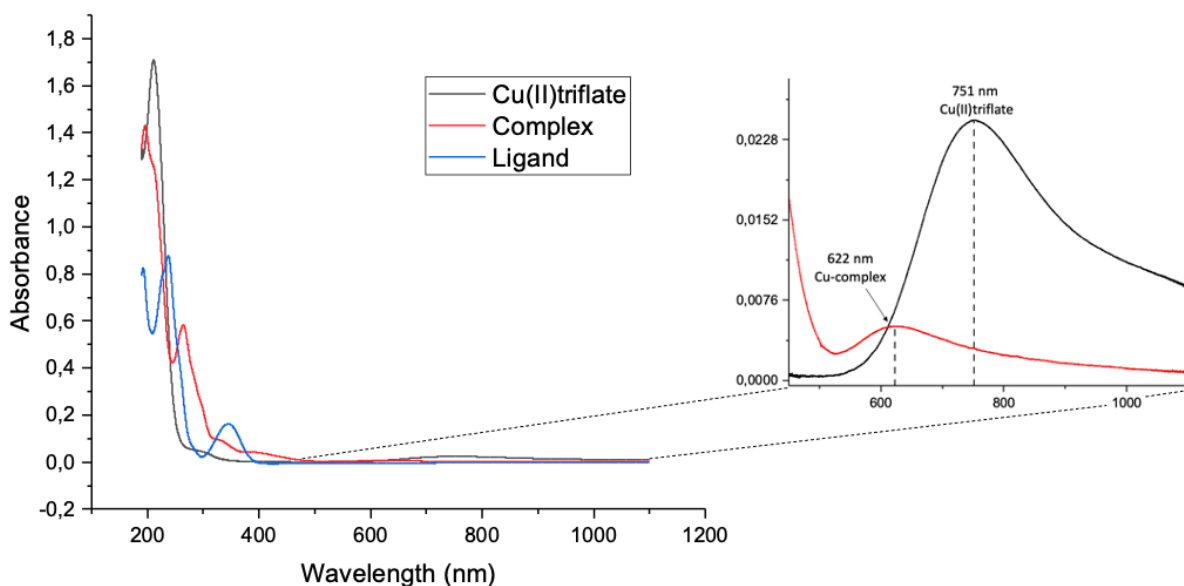


Figure 17: UV-vis spectra of complex **5**, ligand **3** and Cu(OTf)<sub>2</sub>. Due to the intensity difference between the triflate, and the complex and ligand, the spectra had to be recorded at two different concentrations.

Spectra of ligand **3**, complex **5**, and Cu(OTf)<sub>2</sub> were recorded in acetonitrile solutions. As shown above (Figure 17), a comparison of UV-vis spectra of complex **5** and ligand **3** in the UV-region (ca. 200-400 nm) displays a red shift for the complex, from  $\lambda_{\text{max}}$  240 (ligand **3**) to  $\lambda_{\text{max}}$  264 (complex **5**). Band observed for the ligand (**3**) at 343 nm is not present for the complex (**5**). Furthermore, in the visible region, d-d transition was observed for both Cu(OTf)<sub>2</sub> and copper(II)complex **5**. A blue shift is apparent for the d-d transition of the complex. This confirms both the presence of copper(II) in **5** and that it has a different ligand environment than the Cu(OTf)<sub>2</sub>.



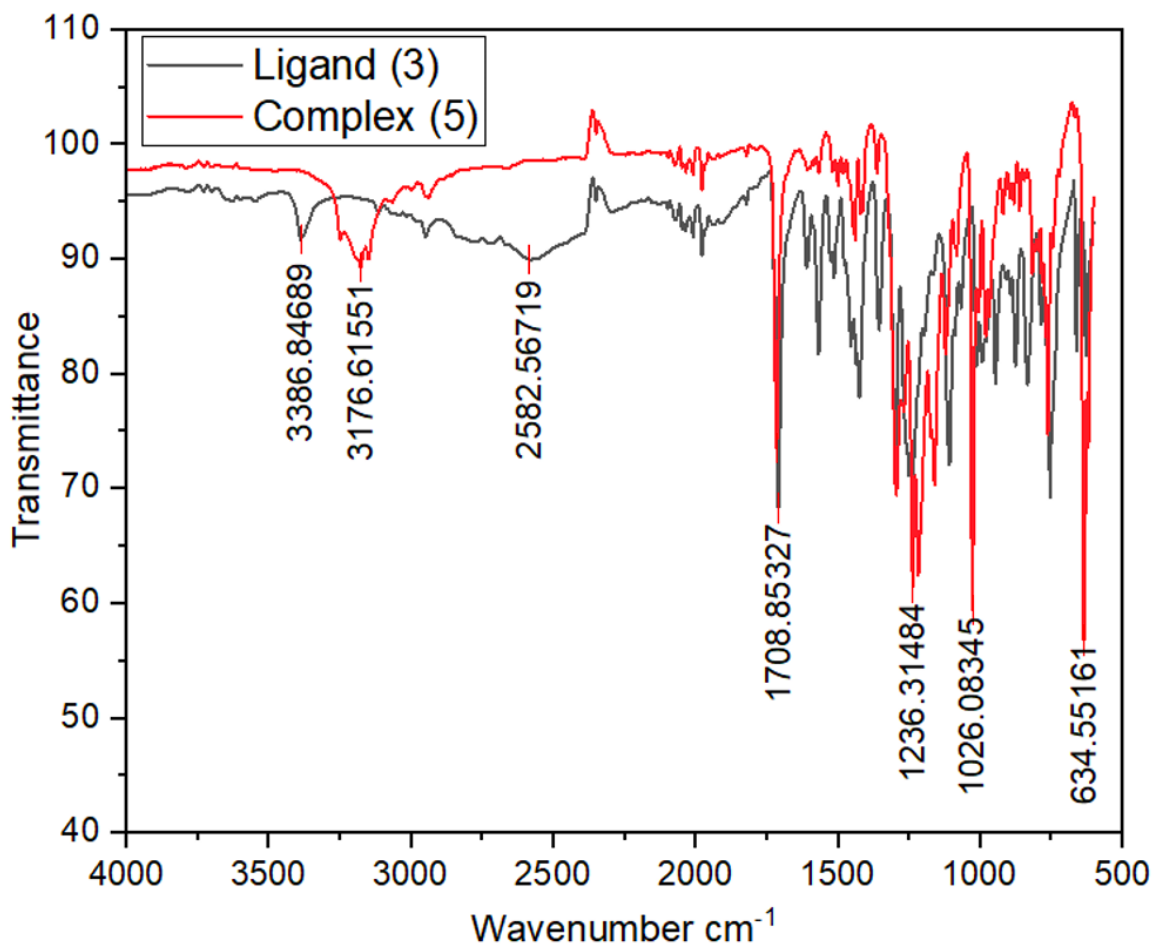


Figure 18: Comparison of FTIR spectra of complex **5** and ligand **3**.

FTIR experiment was conducted prior to obtaining a single crystal for SC-XRD. This technique was utilized with the purpose of proposing the coordination structure of complex **5**. A comparison of FTIR spectra (Figure 18) of complex **5** and ligand **3** is shown above. IR frequencies are cross-referenced with frequency range provided in the literature.<sup>90</sup> IR transmittance at 3386 cm<sup>-1</sup> for the ligand (**3**) corresponds to N-H bending in a secondary amine. This N-H bending is also present for the complex (**5**) with a shift, at 3176 cm<sup>-1</sup>. Furthermore, at around 1236 cm<sup>-1</sup>, IR transmittance is present for both the ligand (**3**) and the complex (**5**), but comparatively higher transmittance for the complex. Around this region, frequencies for aromatic amines are observed. By comparing the two spectra, the FTIR supplements the proposed coordination of the complex.

### 2.3.2 Metalation of Ligand 8

As shown below (Figure 19), Ligand **8** was metalated with both copper(I)- and copper(II)-trifluoromethanesulfonate, forming complex **9** and **10**, respectively.

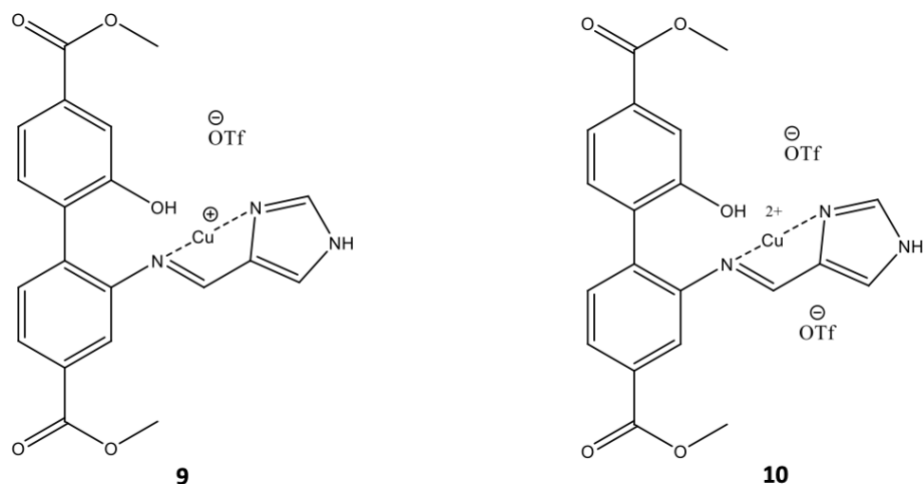


Figure 19: The synthesized copper (I)- (**9**) and copper (II)-complexes (**10**).

After workup, copper(I)-complex **9** yielded in a brown/red solid and complex **10** yielded in a black solid. The color of copper(II) complexes are commonly associated with a blue/green hue, but for this particular complex **10**, it deviated from the norm and had a black color. The green color stems from d-d transition, which can be measured by UV-vis spectroscopy in the visible range.

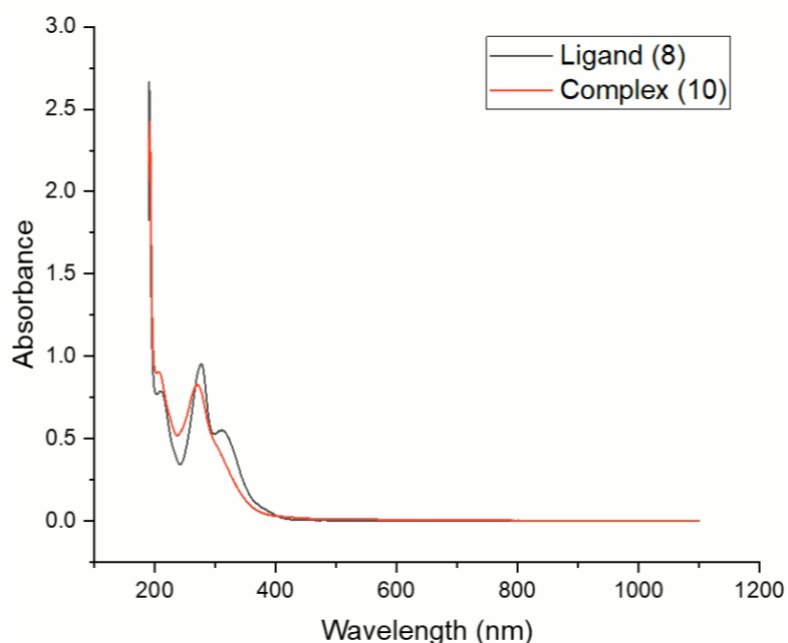


Figure 20: UV-vis spectra of ligand **8** and complex **10**.

UV-vis experiment was conducted to observe the occurrence of d-d transition within complex **10**, since it features a copper(II) metal atom. However, there was no d-d transition evident in the spectrum. Spectra of ligand **8** and its corresponding copper(II) complex (**10**) were recorded in acetonitrile solutions with a concentration of 30  $\mu\text{M}$ . A comparison of UV-vis spectra of ligand **8** and complex **10** is shown above (Figure 20). In the ultraviolet (UV) region, the band observed at 311 nm for the ligand (**8**) is not present for the complex (**10**). In addition, the band observed at 276 nm for the ligand (**8**) is also observed for the complex (**10**), however with a lower absorbance.

Since the complex show no d-d transition, in order to address doubts regarding the potential reduction of the copper(II) complex, NMR was employed to analyze the sample. The NMR spectrum showed immensely broad resonances, confirming the compound being paramagnetic.

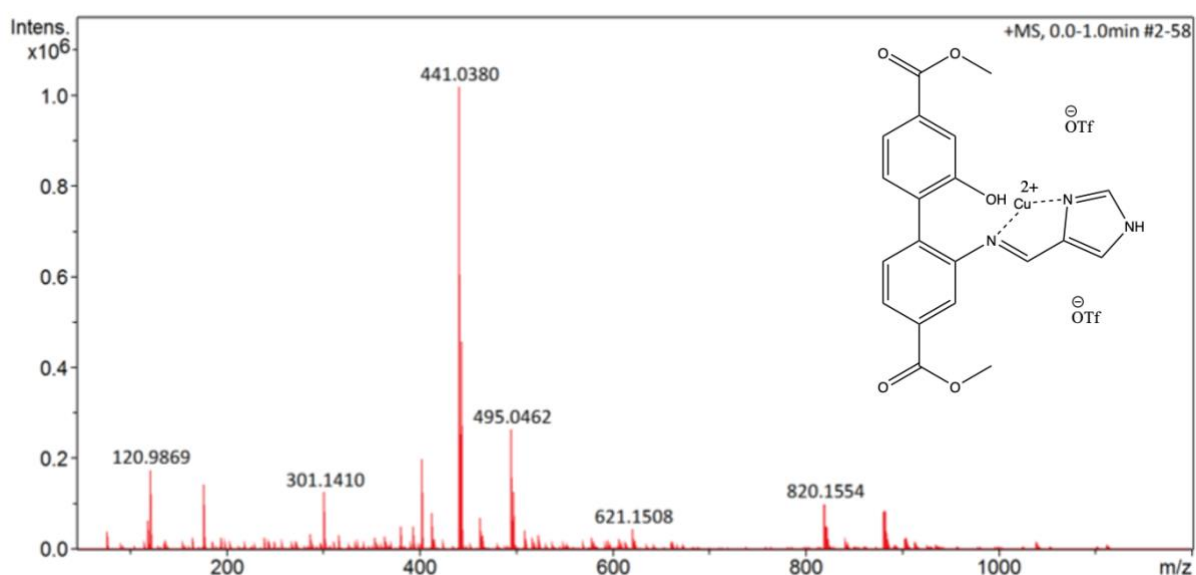


Figure 21: ESI-MS spectrum of complex **10**.

Complex **10** was further analyzed by ESI-MS and XANES (Section 2.3.3). MS spectrum of **10** (Figure 21) showed base peak at 441.0380  $m/z$  which corresponds to the deprotonated molecular cation  $[\text{M}-\text{H}]^+$ . Furthermore, MS-data confirmed presence of copper in the molecule. This confirmation was achieved by identifying isotopes for copper present within the molecule. Copper has two naturally occurring stable isotopes,  $^{63}\text{Cu}$  and  $^{65}\text{Cu}$ , with a natural abundance of 69.17% and 30.83%, respectively.<sup>91</sup> The mass spectrum exhibit base peak at 441.0380  $m/z$  with intensity of 100%, and a peak at 443.0365  $m/z$   $[\text{M}+2]$  with an intensity of 45%, confirming presence of copper.

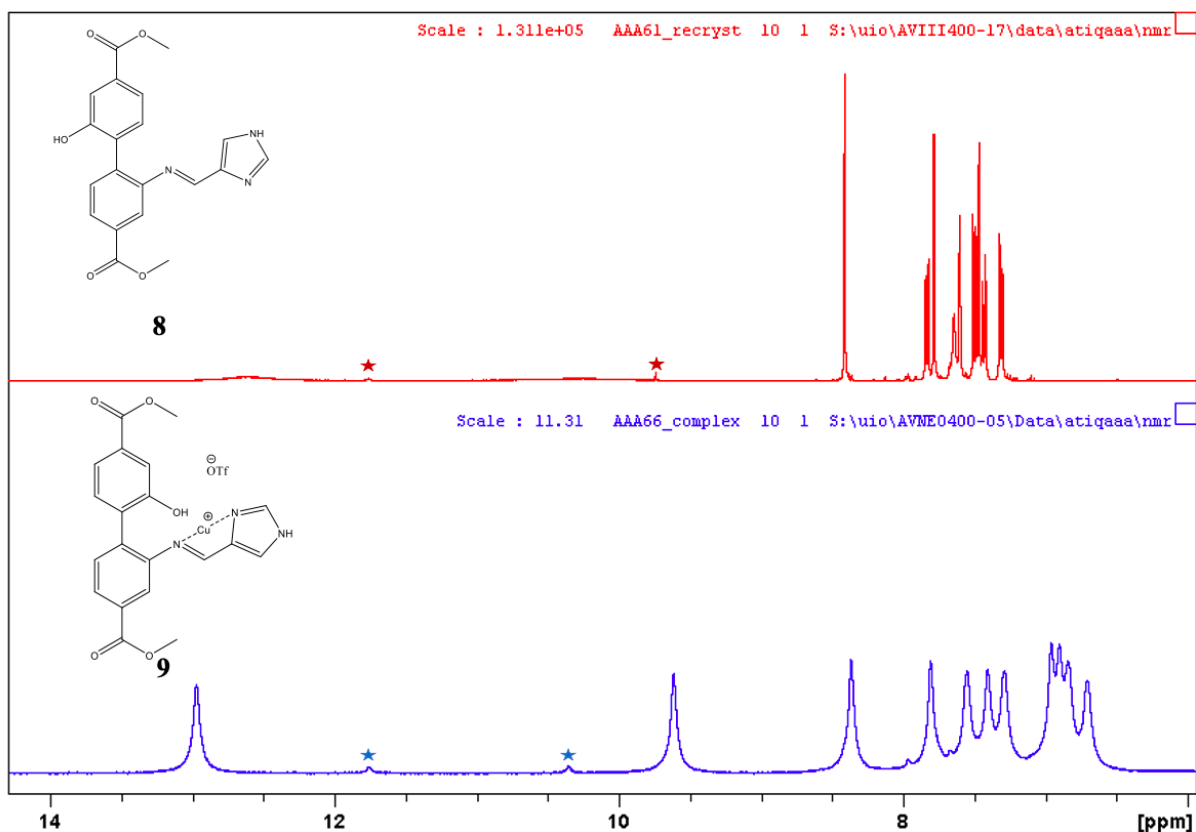


Figure 22: Comparison of <sup>1</sup>H NMR (400MHz, DMSO-d<sub>6</sub>) spectra of ligand **8** with its corresponding complex **9**.

Ligand **8** was successfully metalated to complex **9** as studied by NMR and MS results. A comparison of <sup>1</sup>H NMR of the complex **9** and the ligand **8** is shown above (Figure 22). The first observation that serves as confirmation of the metalation is broadening of signals. This has also been previously observed in other imidazole-bearing complexes in the group.<sup>77</sup> The signals were too broadened to display fine structure, the signals were assigned using 2D NMR techniques. Furthermore, the signals at the aromatic region and the imine signal exhibited a significant shift, and the aromatic signals were wider apart compared to the signals of the ligand **8**. As previously discussed (Section 2.2.2), due to intramolecular bond formation and dynamic equilibrium of the ligand, signals with relatively low intensity compared to other signals were also observed for the complex (marked with stars).

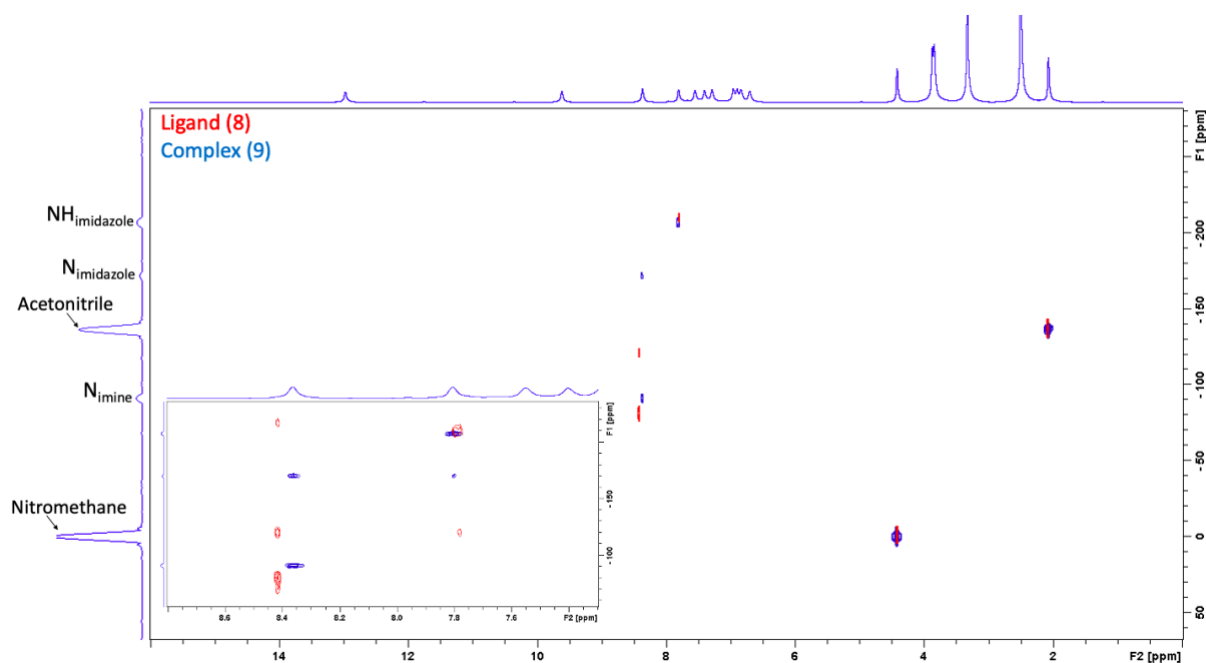


Figure 23: Comparison of  $^{15}\text{N}$ - $^1\text{H}$  HMBC (400 MHz,  $\text{DMSO-d}_6$ ) spectra of Cu(I) complex **(9)** (blue) and the corresponding ligand **(8)** (red). Nitromethane was used as an external standard.

As shown above (Figure 23),  $^{15}\text{N}$ - $^1\text{H}$  HMBC spectra of the ligand **8** and its corresponding complex **9** were obtained. A significant shift is observed for both the  $\text{sp}^2$ -hybridized nitrogen atom on the imidazole and the imine. Although the imine shift is of lesser magnitude, it is still a good descriptor that the imine might be coordinated to the metal. The magnitude of the shifts suggests that the Cu-imidazole bond is stronger than the Cu-imine bond. A notable shift was also observed for the  $\text{sp}^3$ -hybridized nitrogen in imidazole, but the magnitude of the shift is insignificant, therefore it supplements the proposed structure/coordination of the complex. Presence of acetonitrile was observed both in the ligand **8** and the complex **9** by NMR. Acetonitrile was used for recrystallization of the ligand **8**, but despite a lot of attempts on drying by vacuum oven, the solvent seemed to be trapped. Although, acetonitrile was not used in the metalation reaction, the presence of acetonitrile persisted. Coordination of acetonitrile to copper-metal is common,<sup>92</sup> however the acetonitrile correlation does not exhibit a shift, and without a crystal-structure of the complex it is not feasible to comment on acetonitrile's coordination.

The  $^{15}\text{N}$  NMR coordination shift is defined as the difference between the chemical shift of the ligand in its complex and that of the free ligand (equation 3).<sup>77, 93</sup>

$$\Delta ^{15}\text{N}_{\text{coordination shift}} = \delta ^{15}\text{N}_{\text{complex}} - \delta ^{15}\text{N}_{\text{ligand}} \quad (3)$$

It is typical for nitrogen atoms coordinated to metal centers ( $\delta ^{15}\text{N}_{\text{complex}}$ ) to appear at lower chemical shift as compared with their non-coordinated state ( $\delta ^{15}\text{N}_{\text{ligand}}$ ),<sup>94</sup> as this is also the case here.

$$\Delta \text{N}_{\text{imidazole}} = -170 - (118) = -52 \text{ [-55]}$$

$$\Delta \text{N}_{\text{imine}} = -91 - (-79) = -12 \text{ [-16]}$$

A similar complex has been synthesized in the group (Figure 24),<sup>77</sup> with a  $\text{ML}_2$  type coordination involving a copper atom coordinated to four nitrogen atoms. This complex is suitable for comparison with complex **9**, due to its similar structure, Schiff base ligand bearing 1-H imidazole. For complex **9**, the  $^{15}\text{N}$  coordination shifts are calculated above, and the shifts from literature are shown in brackets. The  $^{15}\text{N}$  coordination shifts of complex **9** and the complex from the literature, are in accordance.

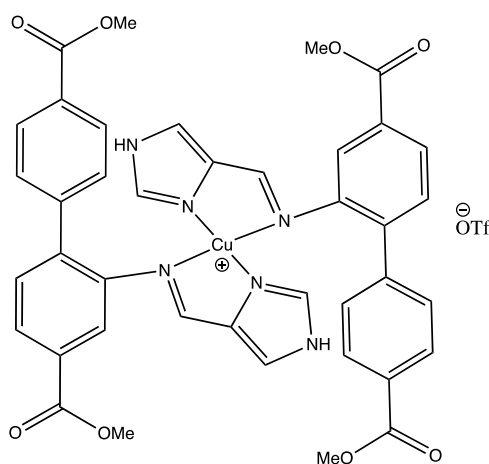


Figure 24:  $\text{ML}_2$  type copper(I) complex, assigned as **2** in the paper.<sup>77</sup>

Furthermore, to investigate the coordination of the hydroxy group to the metal, the carbon carrying the functional group was examined by  $^{13}\text{C}$  NMR. The carbon signals adjacent to the hydroxy group were observed at 154.8 and 154.2 ppm, for the ligand and the complex, respectively. The observed shift is small, suggesting no coordination of the oxygen to the metal.

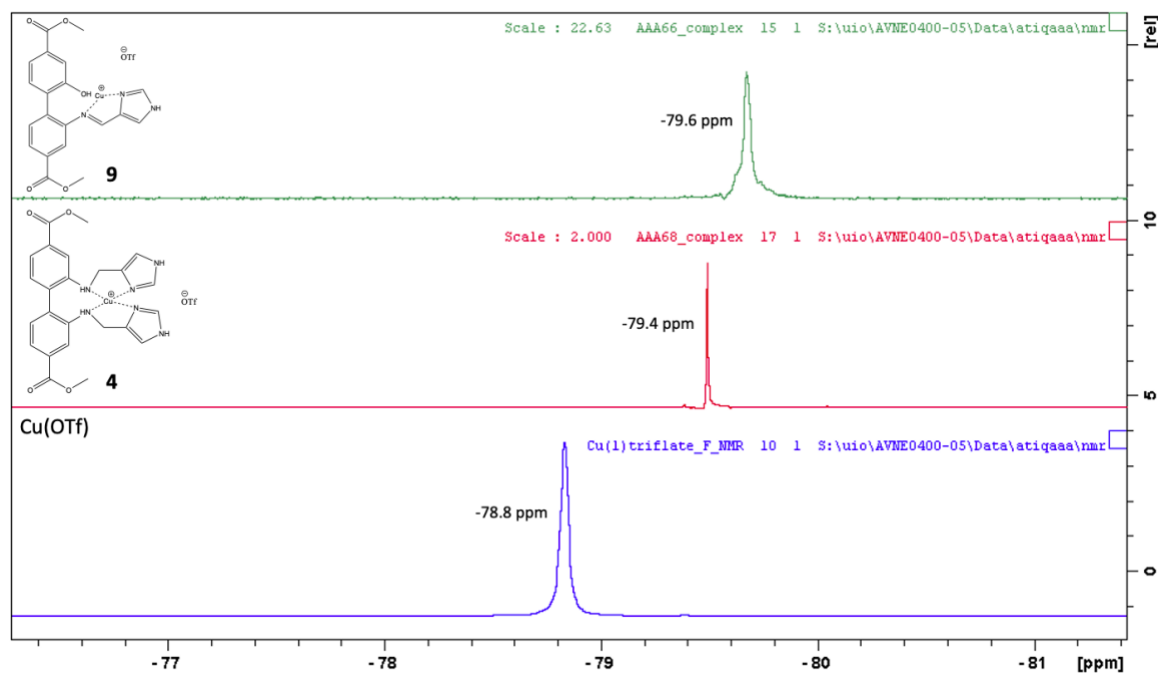


Figure 25: Comparison of  $^{19}\text{F}$  NMR (400 MHz,  $\text{DMSO-d}_6$ ) spectra of complexes **9** and **4**, along with copper(I)trifluorometanesulfonate. Hexafluorobenzene was used as an external standard.

As the counter anion, trifluorometanesulfonate ( $\text{CF}_3\text{O}_3\text{S}^-$ ), of the synthesized complexes contain fluorine,  $^{19}\text{F}$  NMR was conducted to observe any variation from the reactant,  $\text{Cu}(\text{OTf})$ . A comparison of  $^{19}\text{F}$  NMR of copper(I)complexes **4** and **9** with  $\text{Cu}(\text{OTf})$  is shown above (Figure 25).  $^{19}\text{F}$ -signal for both the complexes exhibited an upfield shift compared to  $^{19}\text{F}$ -signal for  $\text{Cu}(\text{OTf})$ , indicating change in the chemical environment surrounding the counter anions for both the complexes.

### 2.3.3 XANES measurements

XANES spectra of complexes **4**, **5** (synthesized as Cu(I) and Cu(II) complexes of ligand **3**) and complexes **9**, **10** (synthesized as Cu(I) and Cu(II) complexes of ligand **8**) were collected at the MPI CEC in Mülheim, Germany by collaborators in the CUBE project. For the purpose of comparison, the spectra of two previously synthesized complexes are also shown.<sup>77</sup> Their ligand resembles the tetradentate ligand **3**, but the secondary amine is replaced by an imine.

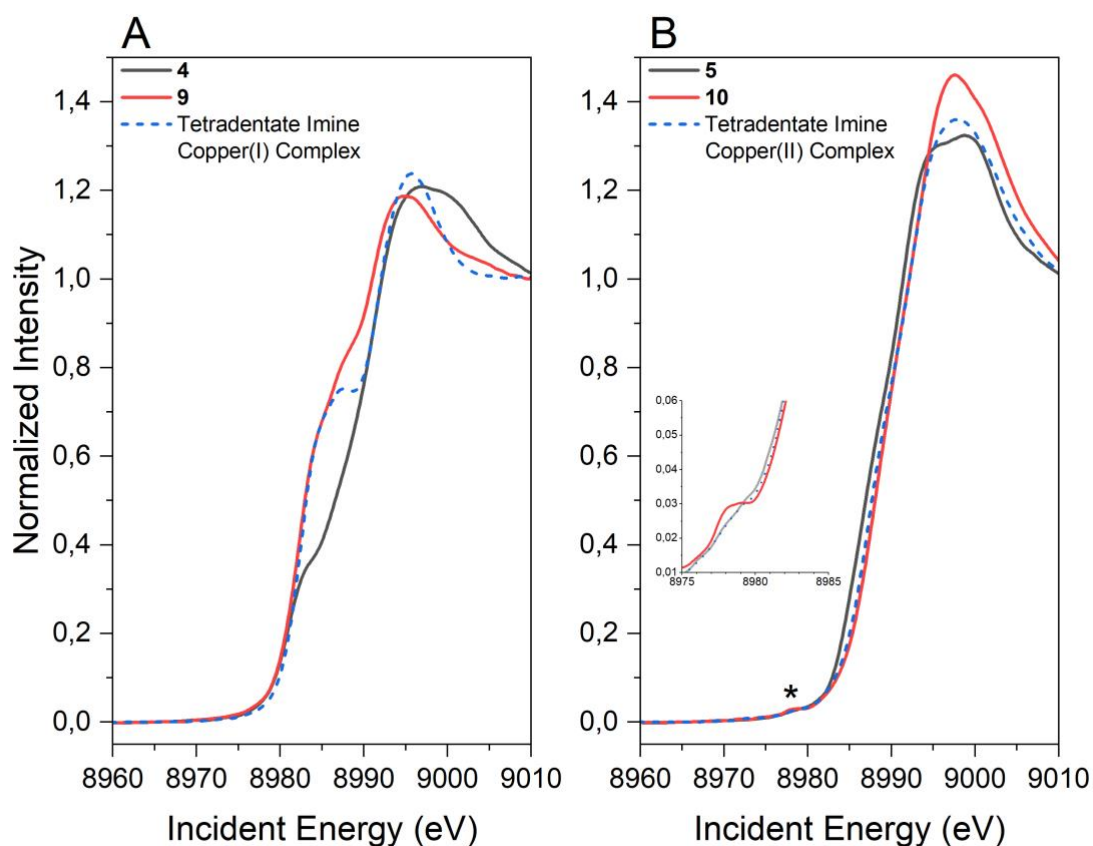


Figure 26: Cu K-edge XANES spectra of complexes **4**, **5**, **9**, and **10**. In addition, the XANES spectra of related tetradentate imine copper complexes are displayed. **A**. Copper(I) complexes. **B**. Copper(II) complexes. The pre-edge feature is marked with an asterisk.

The edge position  $E_0$  was determined as the first inflection point of the spectrum. The copper(I) species have a red-shifted  $E_0$  compared to the copper(II) species (Figure 26), which is in agreement with literature.<sup>76</sup> Nevertheless, complex **4** seems to be a mixture of a copper(I) and a copper(II) species. Oxidation has occurred, as the batch showed a greenish tint and additional, broadened resonances were observed in the  $^1\text{H}$  NMR spectrum. All copper(I) complexes have a distinct rising edge shoulder originating from the  $1s\text{-}4p$  transition. The intensity depends on the coordination number and geometry,<sup>95, 96, 77</sup> making it difficult to estimate the degree of

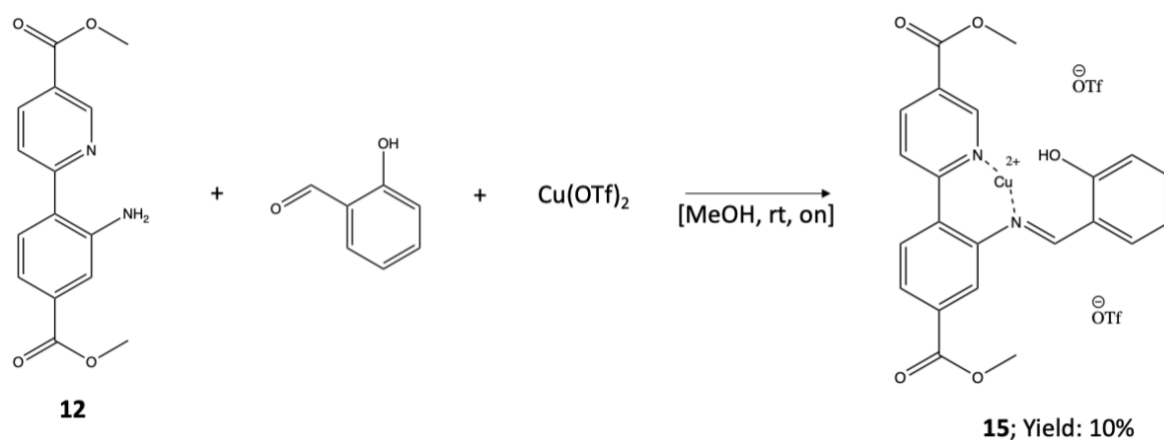


oxidation in **4** from the relative intensity of the transition to that in the reference complex and **9**.

There is a strong resemblance in the features of complexes **9** and **10** and the previously reported imine copper complexes (dashed lines in Figure 26). This may be rationalized with the Schiff-base coordination and is further supported by the good agreement of the  $^{15}\text{N}$  NMR coordination shifts between these copper(I) complexes (see Section 2.3.2).

A faint pre-edge feature is observable for all copper(II) complexes (8978-8979 eV, asterisk in Figure 26B), stemming from the 1s-3d transition in the cupric species.<sup>97</sup> Again, the complex of ligand **3**, compound **5** is the one with the stronger distinction from the reference complex. The edge is slightly shifted to lower energies and the white line is less sharp, with two close-by features. A similar white line shape has been reported for multinuclear copper complexes where one of the copper sites had a square pyramidal geometry.<sup>98</sup> This is in good agreement with the preliminary crystal structure of **5**.

### 2.3.4 One-pot Synthesis: Copper Complex (15)



Scheme 15: One-pot synthesis reaction forming a copper(II)-complex **15**.

After many unsuccessful attempts on isolating the ligand **13** for further reduction to **14** following a metalation, it was decided to move on with a different approach. Earlier in the group,<sup>77</sup> a series of copper-complexes have been synthesized by a one-pot synthesis reaction, with good yields. Therefore, one-pot synthesis with Schiff base synthesis and metalation in one step was employed (Scheme 15). Complex **15** was obtained as a green solid with a yield of 10%. The low yield could be due to the fact that the reaction was conducted on a small scale, on 0.6 mmol scale.

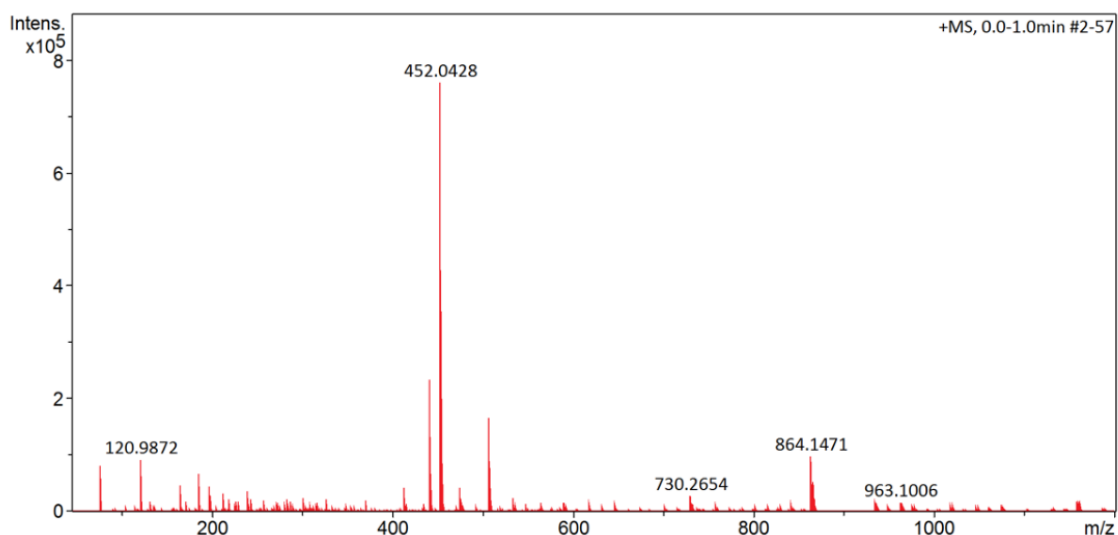


Figure 27: ESI-MS spectrum of complex **15**.

The complex was analyzed by ESI-MS. MS spectrum of **15** (Figure 27) showed base peak at 452.0428 m/z which corresponds to the deprotonated molecular cation  $[M-H]^+$ . Furthermore, MS-data confirmed presence of copper in the molecule as it showed copper's isotopic signature. The mass spectrum exhibits base peak at 452.0428 m/z with intensity of 100%, and a peak at 454.0413 m/z  $[M+2]$  with an intensity of 46%, confirming presence of copper.

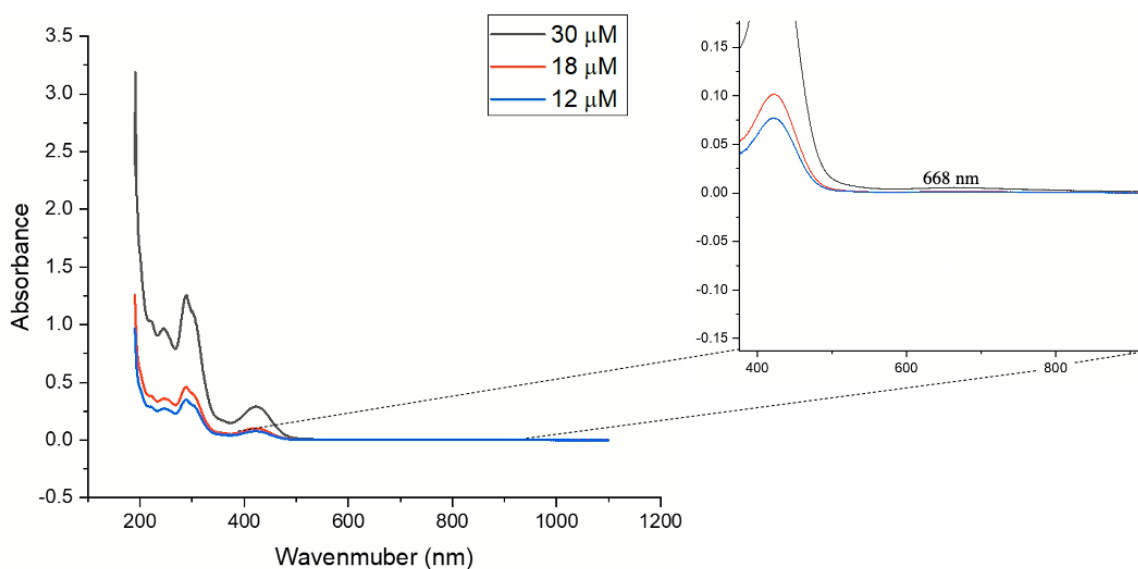
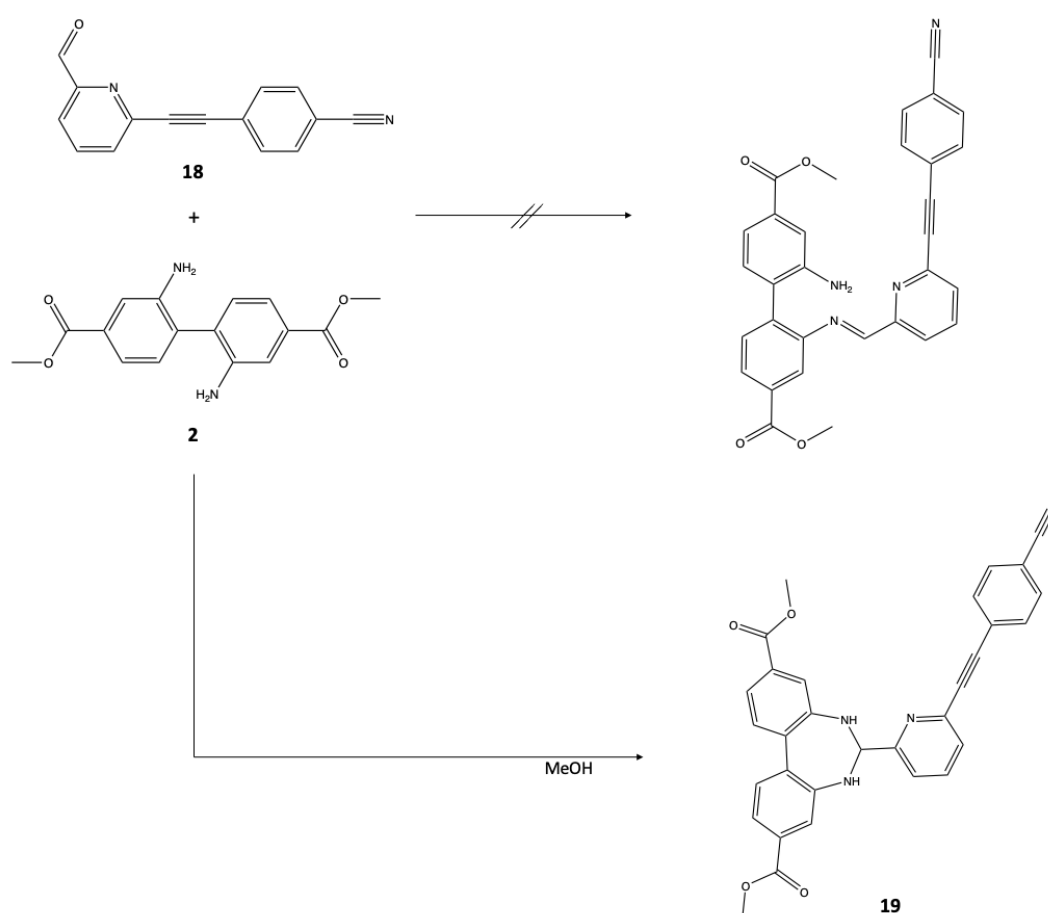


Figure 28: UV-vis spectrum of complex **15**, at different concentrations in MeCN.

UV-vis experiment was conducted to observe the occurrence of d-d transition within complex **15**, since it features a copper(II) metal atom. As shown above (Figure 28), in the visible region d-d transition band is observed at 668 nm for the complex.

## 2.4 Miscellaneous

Previously in the group,<sup>77</sup> in certain situations under metalation of ligands, formation of  $ML_2$  type complexes has been observed, i.e. two ligands per copper atom. This hinders the resemblance of the synthesized complex to the enzymes active site. To prevent formation of the undesired  $ML_2$  type complexes, a strategy involving incorporation of elongated pi-system was employed to create steric hinderance. The initial assumption was that by incorporating a bulky group, it would lead to formation of an imine (Scheme 16), but the outcome yielded a diazepine (**19**). Based on prior research in the group,<sup>77</sup> the outcome of a reaction between an amine and an aldehyde is influenced by the substituent on the utilized aldehyde.



Scheme 16: Synthesis of diazepine (**19**).

This side project was pursued alongside the main project, however due to a redirection of priorities, the project did not progress further

# 3 Experimental

## 3.1 General Considerations

The synthesis of all Cu(I) species was conducted inside an Ar-filled UNIlab pro glovebox from MBraun. All solvents that were utilized for synthesis of Cu(I) species underwent degassing with the freeze-pump-thaw technique (3 cycles). The procedure for preparing NMR samples of copper-containing compounds involved using an adapter and commercial 9-inch NMR tubes. The samples were prepared inside the glovebox and then transferred using the adapter to NMR tube. The tube was then connected to a vacuum line, and the solvent was frozen with liquid nitrogen. Finally, the tube was flame sealed under vacuum to prevent oxidation of the copper-containing compound.

NMR spectra were recorded on the following Bruker instruments: AVIIIHD800, AVI600, AVIII400 and AVNEO400.  $^{15}\text{N}$  NMR and  $^{19}\text{F}$  NMR signals are referred to an external standard, nitromethane and hexafluorobenzene respectively. To prepare the external standard, 1  $\mu\text{L}$  of each reference was mixed with 35  $\mu\text{L}$  of the respective NMR solvent. The resulting solution was then transferred into a capillary, flame sealed, and then placed in the NMR tube. Nitromethane was calibrated to 0 ppm ( $^1\text{H}$ - $^{15}\text{N}$  HMBC), and hexafluorobenzene was calibrated to -164.5 ppm ( $^{19}\text{F}$  NMR).

Chemicals were used as received from commercial suppliers, unless noted otherwise.

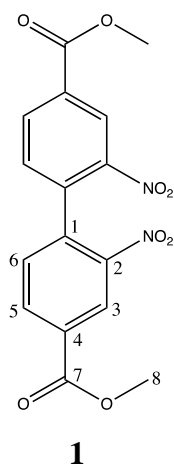
Single crystal diffraction data were acquired on Bruker D8 Venture equipped with a Photon 100 detector and using Mo  $K\alpha$  radiation ( $\lambda = 0.71073 \text{ \AA}$ ) from an Incoatec  $i\mu\text{S}$  microsource. Data reduction was performed with Bruker Apex3 Suite, the structures were solved with ShelXT and refined with ShelXL. Olex2 was used as user interface. The cif files were edited with encipher v.1.4 and Mercury v.4.2.0 was used to produce molecular graphics.

The UV-Visible measurements were performed on a Specord 200 Plus instrument. All molar extinction coefficients were calculated by linear regression of the absorbance vs concentration.

## 3.2 Experimental: X-ray absorption measurements

XAS spectra were collected with an easyXES100-extended laboratory spectrometer (easyXAFS, LLC, Seattle, USA) using a Varex® VF-80JM 100 W palladium cathode source operating at 25 kV accelerating potential and 2 mA of tube current creating 50 W of output.<sup>99, 100</sup> An aluminium slit aperture of 1 mm width was placed in front of the source to improve resolution and decrease divergence and thereby noise. A helium flight path within the Rowland circle area was used to reduce the X-ray attenuation in air. A spherical crystal analyzer (Si 553), with 1 m bending radius was used as the instrument's monochromator. The samples were prepared in an N<sub>2</sub>-Glovebox and diluted to mass fractions ranging of about 5% copper in Hoechst Wax® (tableting aid for X-ray sample prep), ground, pelletized and placed in a custom air-tight sample cell (13 mm pellet diameter, 10 mm diameter effective sample area, 1 mm thickness). The transmitted photons in the 8940–9100 eV range were detected by a Vortex®60-EX SDD. A hundred scans were acquired consecutively with 0.2 eV step across Cu K-edge region and several spaced data points before and after for normalization. The first and last ten scans were compared to assess radiation damage and potential air oxidation in the Cu(I) case. Before averaging, every scan was inspected individually. The incident flux ( $I_0$ ) was measured in the same cell without sample. The energy axes of all spectra were calibrated versus the first inflection point of copper foil spectrum at 8980.3 eV measured in the same conditions. The final spectra were obtained with the  $\ln(I_0/I_1)$  relationship and normalized in the Athena software. A three-point smoothing was applied to improve clarity, without introducing or suppressing spectral features.

### 3.3 Synthesis of (1)



#### Procedure:

The compound was prepared as reported by Hylland *et al.*<sup>78</sup>

A three-necked round bottom flask containing conc. H<sub>2</sub>SO<sub>4</sub> (120 mL) was cooled down to around 2 °C in an ice bath. Dimethylbiphenyl-4,4'-dicarboxylate (10g, 37 mmol, 1.0 equiv.) was added in portions over 25 min.

To the resulting solution, a mixture of conc. HNO<sub>3</sub> (5.9 mL, 133 mmol, 3.6 equiv.) and conc. H<sub>2</sub>SO<sub>4</sub> (7.8 mL, 144 mmol, 3.9 equiv.) was added dropwise over 40-60 min, maintaining the temperature below 5 °C. the ice bath was removed, and the reaction was left to stir for 30 min.

The reaction mixture was poured into 1.2 l of ice slush and the precipitate was filtered, washed with water, and dried on air overnight. The precipitate was dissolved in ethyl acetate (740 mL) and washed with sat. NaHCO<sub>3</sub> (2×200 mL) and sat. NaCl (2×200 mL) and dried with Na<sub>2</sub>SO<sub>4</sub>. The solvent was removed under reduce pressure and the crude product was recrystallized from acetonitrile, resulting in cube-shaped yellow crystals.

Yield: 9.25 g, 25.6 mmol, 68%

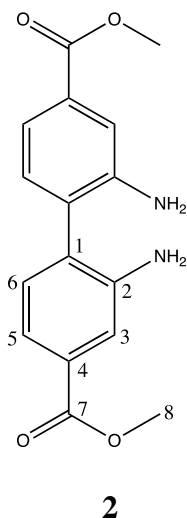
**<sup>1</sup>H NMR (400MHz, CDCl<sub>3</sub>):** δ 3.98 (s, 6H, H-8), 7.36 (d, 2H, J = 7.96 Hz, H-6), 8.33 (dd, 2H, J = 1.68 and 7.96 Hz, H-5), 8.86 (d, 2H, J = 1.56 Hz, H-3)

**<sup>13</sup>C NMR (400 MHz, CDCl<sub>3</sub>):** δ 52.9 (C-8), 126.0 (C-3), 130.9 (C-6), 131.9 (C-1), 134.2 (C-5), 137.6 (C-4), 146.8 (C-2), 164.5 (C-7)

**HRMS (ESI) *m/z* [M+Na<sup>+</sup>]** (C<sub>16</sub>H<sub>12</sub>N<sub>2</sub>O<sub>8</sub> + Na<sup>+</sup>) Calcd: 383.0486; Found: 383.0485

The compound is in accordance with the spectroscopic data found in literature.<sup>78</sup>

### 3.4 Synthesis of (2)



#### Procedure:

A modified literature procedure was used.<sup>80</sup>

Dimethyl 2,2'-dinitrophenyl-4,4'-dicarboxylate (8.44 g, 23.4 mmol, 1.0 equiv.) and subsequently Fe (20.9 g, 374 mmol, 16 equiv.) were added to a flask containing acetic acid (240 mL). The mixture was stirred under a stream of Argon. After 30 min an exothermic reaction started. The reaction mixture remained stirring under argon for an additional 21 hours at room temperature.

The suspension was then transferred to a beaker containing water (2.2 L) and stirred for 15 min. The solids were filtered off and washed with water (3×200 mL). The solids were dissolved in ethyl acetate (600 mL) and filtered through celite, which was subsequently washed with ethyl acetate (3×100 mL). The filtrate was dried with Na<sub>2</sub>SO<sub>4</sub> and the solvent was removed under reduced pressure. The crude product was recrystallized from toluene.

Yield = 5.92 g, 19.7 mmol, 84%

**<sup>1</sup>H NMR** (400MHz, DMSO-*d*<sub>6</sub>): δ 3.83 (s, 6H, H-8), 4.99 (s, 4H, NH<sub>2</sub>), 7.07 (d, J = 7.8 Hz, 2H, H-6), 7.23 (dd, J = 7.8 and 1.6 Hz, 2H, H-5), 7.44 (d, J = 1.6 Hz, 2H, H-3)

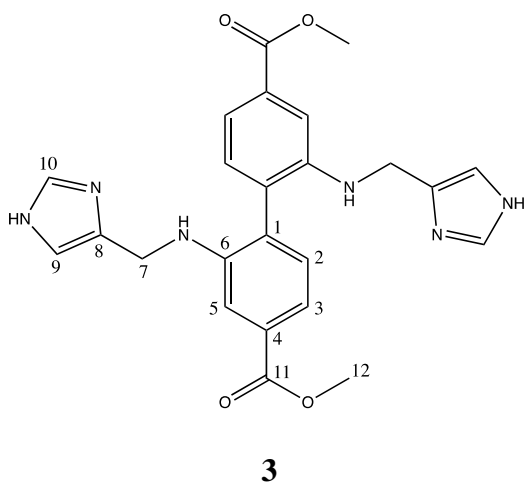
**<sup>13</sup>C NMR** (400MHz, DMSO-*d*<sub>6</sub>): δ 51.9, 115.8, 117.1, 127.5, 129.6, 130.7, 145.5, 166.5

**HRMS (ESI) *m/z* [M+Na<sup>+</sup>]** (C<sub>16</sub>H<sub>16</sub>N<sub>2</sub>O<sub>4</sub> + Na<sup>+</sup>) Calcd: 323.1002; Found: 323.1002

The spectroscopic data is in accordance with that reported in the literature.<sup>80</sup>



### 3.5 Synthesis of Ligand (3)



#### Procedure:

A mixture of dimethyl 2,2'-diamino-[1,1'-biphenyl]-4,4'-dicarboxylate (**2**) (782.8g, 2.6 mol, 1.00 equiv.), 1H-imidazole-4-carbaldehyde (502.9 mg, 5.23 mmol, 2.0 equiv.) and five drops of formic acid were stirred in dry methanol overnight. The reaction mixture was cooled with an ice bath. NaBH<sub>4</sub> (984.4 mg, 26.0 mmol, 9.98 equiv.) was added portion wise over the course of 10 minutes. The ice bath was then removed, and the reaction was stirred at ambient temperature for 2 more hours. The reaction was diluted in 50 mL NaHCO<sub>3</sub> (aq., sat.). The aqueous phase was extracted with 100 mL dichloromethane (3×100mL). The combined organic phases were dried over NaSO<sub>4</sub>. The solvent was removed under reduced pressure. After recrystallization from acetonitrile a yellow solid was obtained.

Yield: 284mg, 0.617 mmol, 24%

**<sup>1</sup>H NMR (400MHz, DMSO-d<sub>6</sub>):** δ 3.82 (s, 6H, H-12), 4.23 (s, 4H, H-7), 5.02 (t, J = 5.2 Hz, 2H, sec. amine), 6.92 (s, 2H, H-9), 7.1 (d, J = 7.7 Hz, 2H, H-2), 7.28 (dd, J = 7.3 and 1.4 Hz, 2H, H-3), 7.30 (d, J = 1.2 Hz, 2H, H-5), 7.59 (s, 2H, H-10), 11.9 (s (br), 2H, NH from imidazole).

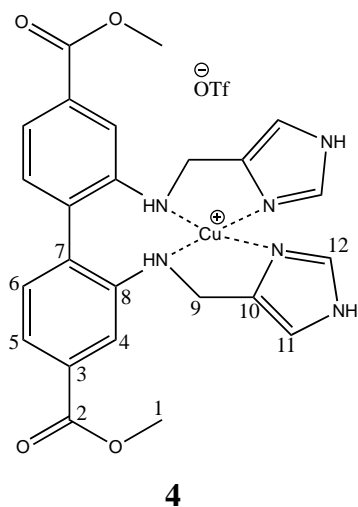
**<sup>13</sup>C NMR (400 MHz, DMSO-d<sub>6</sub>):** δ 40.2 (from HSQC) (C-7), 52.0 (C-12), 111.0 (C-5), 117.3 (C-3), 128.1 (C-1), 130.0 (C-8), 130.8 (C-2), 135.2 (C-10), 145.3 (C-6), 166.5 (C-11). C-9 and C-4 signals are missing.

**HRMS (ESI) *m/z* [M+H<sup>+</sup>]** (C<sub>16</sub>H<sub>15</sub>NO<sub>5</sub> + H<sup>+</sup>): Calcd: 461.1932; Found: 461.1931

**UV/Vis (ε [μM<sup>-1</sup>cm<sup>-1</sup>] CH<sub>2</sub>Cl<sub>2</sub>):** λ<sub>max</sub> (240): 0.043 ± 0.002; λ<sub>sh</sub> (281): 0.0133 ± 0.0004;

λ<sub>max</sub> (343): 0.0087 ± 0.0004

## 3.6 Synthesis of Complex (4)



### Procedure:

A mixture of **3** (95 mg, 0.20 mmol, 1.0 equiv.) and CuOTf (43 mg, 0.20 mmol, 1.0 equiv.) were stirred in toluene (2 mL) overnight. Reaction mixture was precipitated with diethylether (2 mL). The solid was collected through filtration and washed with diethyl ether (4 mL). Residual solvent was left to evaporate overnight to yield as a turquoise solid.

Yield: 133 mg, 0.19 mmol, 98%

**<sup>1</sup>H NMR (600MHz, DMSO-*d*<sub>6</sub>):** δ 3.82 (s, 6H, H-1), 4.23 (s(br), 4H, H-9), 5.22 (s(br), 2H, NH), 7.08 (d, J = 7.38 Hz, 2H, H-5), 7.17 (d, J = 7.56 Hz, 2H, H-12), 7.24 (d, J = 7.56 Hz, 2H, H-6), 7.29 (s, 2H, H-4), 7.30 (s, 2H, H-11), 7.97 (s(br), 4H), 12.51 (s(br), 4H)

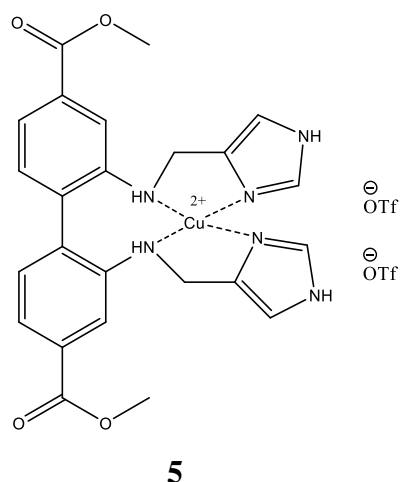
**<sup>13</sup>C NMR (600 MHz, DMSO-*d*<sub>6</sub>):** δ 40.0 (found from HSQC, C-9), 52.0 (C-1), 110.8 (C-11), 117.5 (C-4), 128.1 (C-6), 128.3 (C-12), 130.1 (C-3), 130.8 (C-5), 145.3 (C-8), 166.5 (C-2)

Signals C-7 and C-10 are missing

**<sup>19</sup>F NMR (400 MHz, DMSO-*d*<sub>6</sub>):** δ -79.4 (CF<sub>3</sub>)

**HRMS (ESI) *m/z* [M<sup>+</sup>]** (C<sub>24</sub>H<sub>24</sub>CuN<sub>6</sub>O<sup>+</sup>): Calcd: 523.1150; Found: 523.1147

### 3.7 Synthesis of Complex (5)



#### Procedure:

A mixture of 3 (143.3 mg, 0.31 mmol, 1.00 equiv.) and Cu(OTf)<sub>2</sub> (112.4 mg, 0.31, 1.00 equiv.) were stirred in acetonitrile (6 mL) overnight. The solvent was removed under reduced pressure. After drying in vacuum oven at 50 °C overnight, a dark green powder was obtained.

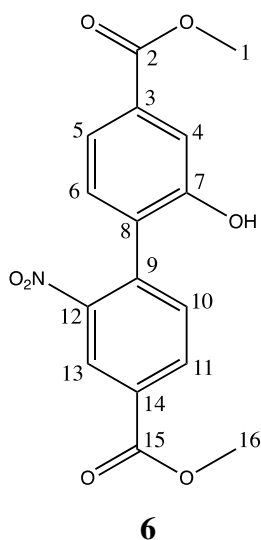
Yield: 241 mg, 0.29 mmol, 94%

**HRMS (ESI)  $m/z$  [ $M^{2+}$ ] ( $C_{24}H_{24}CuN_6O_4^{2+}$ ):** Calcd: 261.5572; Found: 261.5575

**UV/Vis ( $\epsilon$  [ $\mu M^{-1}cm^{-1}$ ] MeCN):**  $\lambda_{max}$  (195):  $0.050 \pm 0.002$ ;  $\lambda_{sh}$  (210):  $0.044 \pm 0.002$ ;

$\lambda_{max}$  (264):  $0.0203 \pm 0.0009$ ;  $\lambda_{sh}$  (392):  $0.00144 \pm 0.00005$ ;  $\lambda_{max}$  (621):  $0.00020 \pm 0.00005$

### 3.8 Synthesis of (6)



#### Procedure:

A modified literature procedure was used.<sup>81</sup>

Methyl 4-Bromo-3-hydroxybenzoate (2.3 g, 10.0 mmol, 1.0 equiv.), 4-methoxycarbonyl-2-nitrophenylboronic acid (2.3 g, 10.4 mmol, 1.0 equiv.) and freshly powdered  $\text{KF}\cdot 2\text{H}_2\text{O}$  (3.1 g, 33.2 mmol, 3.3 equiv.) were mixed with THF (20 mL) in a 50 mL round-bottom flask. The suspension was bubbled with Ar for 20 minutes, before adding  $\text{Pd}_2\text{dba}_3$  (2.5 mol %) and  $\text{HBF}_4\cdot \text{P}(\text{t-Bu})_3$  (6.2 mol %). The bubbling was continued for 2-3 minutes after which a reflux condenser was attached to the flask. The reaction mixture was then heated at 80 °C for one hour under Ar. After cooling to room temperature, the reaction was extracted with  $\text{CH}_2\text{Cl}_2$  (100 mL). Subsequently, the solvent was removed under reduced pressure. The residue was purified by flash chromatography (gradient: first: half DCM / half 5% EtOAc in Hexane, then: half DCM / half 15% EtOAc in Hexane).

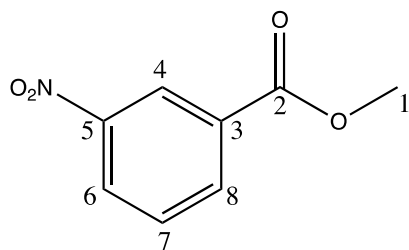
Yield: 1.5 g, 4.5 mmol, 45%

**$^1\text{H}$  NMR (400MHz, DMSO- $d_6$ ):**  $\delta$  3.85 (s, 3H, H-1), 3.93 (s, 3H, H-16), 7.45 (d,  $J = 1.36$  Hz, 1H, H-4), 7.47 (d,  $J = 7.92$  Hz, 1H, H-6), 7.54 (dd,  $J = 1.36$  and 7.88 Hz, 1H, H-5), 7.67 (d,  $J = 8.0$  Hz, 1H, H-10), 8.28 (dd,  $J = 1.08$  and 7.88 Hz, 1H, H-11), 8.43 (d,  $J = 1.56$  Hz, 1H, H-13), 10.4 (s (br), 1H, OH)

**$^{13}\text{C}$  NMR (400 MHz, DMSO- $d_6$ ):**  $\delta$  52.2 (C-16), 52.8 (C-1), 115.2 (C-4), 120.4 (C-5), 124.4 (C-13), 128.7 (C-8), 130.01 (C-14), 130.06 (C-6), 131.2 (C-3), 133.2 (C-10), 133.4 (C-11), 136.1 (C-9), 149.0 (C-7), 154.1 (C-12), 164.4 (C-15), 165.8 (C-2)

**HRMS (ESI)  $m/z$  [ $\text{M}-\text{H}^+$ ]** ( $\text{C}_{16}\text{H}_{12}\text{NO}_7$ ): Calcd: 330.0619; Found: 330.0619

### 3.8.1 Sideproduct (6a)

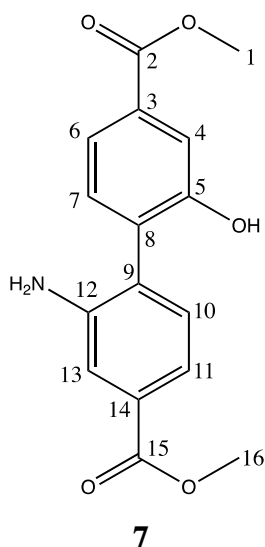


**6a**

**$^1\text{H NMR}$  (400MHz, DMSO- $d_6$ ):**  $\delta$  3.93 (s, 3H, H-1), 7.84 (t,  $J = 8.04$  Hz, 1H, H-7), 8.37 (dt,  $J = 7.8$  and  $1.2$  Hz, 1H, H-8), 8.50 (ddd,  $J = 1.04$ ,  $2.38$  and  $8.34$  Hz, 1H, H-6), 8.63 (t,  $J = 2.04$  Hz, 1H, H-4)

**$^{13}\text{C NMR}$  (400 MHz, DMSO- $d_6$ ):**  $\delta$  52.8 (C-1), 123.5 (C-4), 127.7 (C-6), 130.7 (C-7), 131.1 (C-3), 135.1 (C-8), 147.8 (C-5), 164.5 (C-2)

### 3.9 Synthesis of (7)



#### Procedure:

Compound **6** (500 mg, 1.50 mmol, 1.0 equiv.) was suspended in AcOH (50 mL), and Fe powder (1.3 g, 0.03 mmol, 15 equiv.) was added in one portion. The reaction mixture was flushed with Ar for 2 hours, and then stirred at rt under Ar atmosphere for 15 hours. The reaction mixture was poured into a beaker containing ice (ca. 100 mL), and concentrated ammonia solution (28% aq., ca. 100 mL) was added in portions of 25 mL. More ice was added to the neutralization if the the mixture warmed up significantly. After all ammonia had been added, the resulting suspension was stirred for 5 minutes, the solids were then collected through filtration and washed with water (3×100 mL). The solids were then dissolved in warm EtOAc (ca. 50-60 °C, 300 mL) under stirring. The warm EtOAc solution was filtrated through celite to remove undissolved material and the celite was rinsed with additional EtOAc (ca. 200 mL). The filtrate was dried over Na<sub>2</sub>SO<sub>4</sub>, before the solvent was removed under reduced pressure. After recrystallization from acetonitrile a yellow solid was obtained.

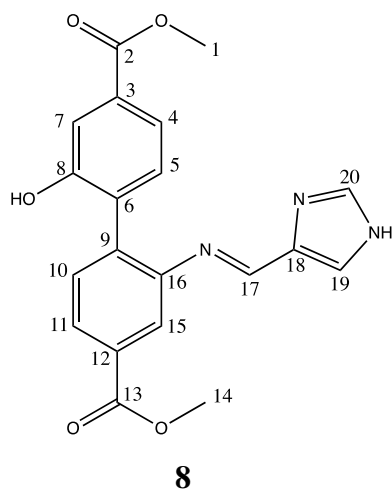
Yield: 210.4 mg, 0.698 mmol, 46%

**<sup>1</sup>H NMR (400MHz, DMSO-d<sub>6</sub>):** δ 3.82 (s, 3H, H-16), 3.85 (s, 3H, H-1), 4.97 (s(br), 2H, NH<sub>2</sub>), 7.08 (d, J = 7.88 Hz, 1H, H-10), 7.21 (dd, J = 1.6 and 7.92 Hz, 1H, H-11) 7.26 (d, J = 7.88 Hz, 1H, H-7), 7.40 (d, J = 1.56 Hz, 1H, H-13), 7.47 (dd, J = 1.52 and 7.88 Hz, 1H, H-6), 7.56 (d, J = 1.48 Hz, 1H, H-4), 10.1 (s(br), OH)

**<sup>13</sup>C NMR (400 MHz, DMSO-d<sub>6</sub>):** δ 51.9 (C-16), 52.1 (C-1), 115.7 (C-13), 116.4 (C-4), 116.9 (C-11), 120.1 (C-6), 127.6 (C-14), 129.4 (C-9), 130.0 (C-8), 130.7 (C-3), 130.9 (C-10), 131.4 (C-7), 146.0 (C-12), 154.5 (C-5), 166.0 (C-2), 166.5 (C-15)

**HRMS (ESI) *m/z* [M+H<sup>+</sup>]** (C<sub>16</sub>H<sub>15</sub>NO<sub>5</sub> + H<sup>+</sup>): Calcd: 302.1023; Found: 302.1022

## 3.10 Synthesis of Ligand (8)



**8**

### Procedure:

Compound **7** (509 mg, 1.66 mmol, 1.00 equiv.) and 1H-imidazole-4-carbaldehyde (162 mg, 1.69 mmol, 1.00 equiv.) were suspended in dry EtOH. 3 drops of formic acid were added. The mixture was stirred for 21 hours, and the precipitated product was collected through filtration. The product was washed with dry EtOH and dried in vacuum oven at 60 °C overnight. The crude was then recrystallized from acetonitrile, resulting in an airy/puffy white solid.

Yield: 439 mg, 1.15 mmol, 68%

**<sup>1</sup>H NMR (400 MHz, DMSO-*d*<sub>6</sub>):** δ 3.83 (s, 3H, H-1), 3.88 (s, 3H, H-14), 7.31 (d, *J* = 7.88 Hz, 1H, H-5), 7.43 (dd, *J* = 1.52 and 7.88 Hz, 1H, H-4), 7.46 (d, *J* = 1.52 Hz, 1H, H-7), 7.49 (d, *J* = 8.00 Hz, 1H, H-10), 7.60 (s, 1H, H-15), 7.64 (s(br), 1H, H-20), 7.78 (s, 1H, H-19), 7.83 (dd, *J* = 1.64 and 8.00 Hz, 1H, H-11), 8.41 (s, 1H, H-17 (imine)), 10.29 (s(br), 1H, OH), 12.62 (s(br), 1H, NH imidazole)

**<sup>13</sup>C NMR (400 MHz, DMSO-*d*<sub>6</sub>):** δ 52.1 (C-1), 52.2 (C-4), 116.8 (found from HSQC correlation, C-7), 119.5 (C-4), 119.6 (C-15), 125.3 (C-11), 130.0 (C-3), 130.1 (C-12), 131.0 (found from DEPT135, C-6), 131.4 (C-10), 131.7 (C-5), 136.3 (C-16), 138.3 (weak signal, found from HSQC correlation, C-19), 150.7 (C-17), 154.8 (C-8), 165.9 (C-13), 166.0 (C-2)  
Signals C-9, C-18 and C-20 are missing

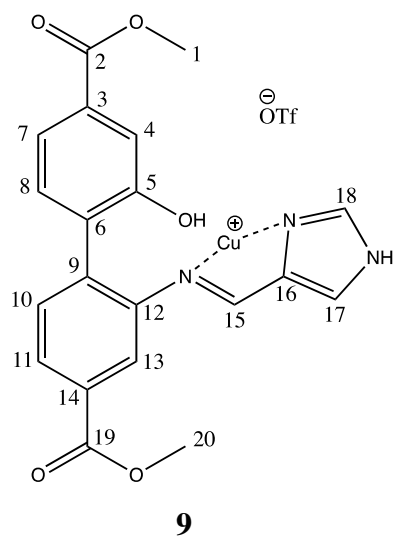
**<sup>15</sup>N NMR (600 MHz, DMSO-*d*<sub>6</sub>):** δ -209 (NH<sub>imidazole</sub>), -118 (N<sub>imidazole</sub>), -79 (N<sub>imine</sub>)

**HRMS (ESI) *m/z* [M+Na<sup>+</sup>] (C<sub>20</sub>H<sub>17</sub>N<sub>3</sub>NaO<sub>5</sub><sup>+</sup>):** Calcd: 402.1060; Found: 402.1060

**UV/Vis (ε [μM<sup>-1</sup>cm<sup>-1</sup>] MeCN):** λ<sub>sh</sub> (210): 0.032 ± 0.006; λ<sub>max</sub> (276): 0.0391 ± 0.007; λ<sub>max</sub> (311): 0.023 ± 0.004



### 3.11 Synthesis of Complex (9)



#### Procedure:

A mixture of **8** (155.2 mg, 0.40 mmol, 1.00 equiv.) and Cu(OTf) (87 mg, 0.40 mmol, 1.00 equiv.) were stirred in acetonitrile (4.5 mL) overnight. The reaction mixture was precipitated with diethyl ether. Solids were collected through filtrated and washed with diethyl ether. After letting the residual solvent to evaporate overnight, a brown/red solid was obtained.

Yield: 85 mg, 0.14 mmol, 35%

**<sup>1</sup>H NMR (400MHz, DMSO-d<sub>6</sub>):** δ 3.83 (s, 3H, H-1), 3.88 (s, 3H, H-20), 6.7 (s, 1H, H-4), 6.84 (s, 1H, H-7), 6.90 (s, 1H, H-8), 6.95 (s, 1H, H-10), 7.28 (s, 1H, H-13), 7.40 (s, 1H, H-18), 7.54 (s, 1H, H-11), 7.80 (s, 1H, H-17), 8.36 (s, 1H, imine), 9.61 (s, 1H, OH), 12.97 (s, 1H, NH (imidazole))

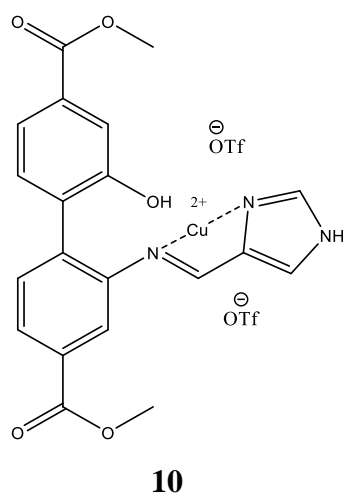
**<sup>13</sup>C NMR (400 MHz, DMSO-d<sub>6</sub>):** δ 51.8 (C-20), 52.0 (C-1), 115.0 (C-10), 118.0 (C-7), 118.2 (C-7), 119.9 (C-8), 121.9 (C-17), 125.2 (C-11), 128.9 (C-6), 129.1 (C-14), 129.6 (C-3), 130.4 (C-13), 131.1 (C-4), 136.0 (C-9), 136.4 (C-18), 138.0 (C-16), 147.5 (C-12), 152.5 (C-15), 154.2 (C-5), 165.3 (C-19), 165.9 (C-2)

**<sup>15</sup>N NMR (600 MHz, DMSO-d<sub>6</sub>):** δ -207 (NH<sub>imidazole</sub>), -170 (N<sub>imidazole</sub>), -91 (N<sub>imine</sub>)

**<sup>19</sup>F NMR (400 MHz, DMSO-d<sub>6</sub>):** δ -79.6 (CF<sub>3</sub>)

**HRMS (ESI) *m/z* [M-H<sup>+</sup>]** (C<sub>20</sub>H<sub>16</sub>CuN<sub>3</sub>O<sub>5</sub><sup>+</sup>): Calcd: 441.0386; Found: 441.0380

## 3.12 Synthesis of Complex (10)



### Procedure:

A mixture of **8** (123.1 mg, 0.32 mmol, 1.00 equiv.) and Cu(OTf)<sub>2</sub> (117.8 mg, 0.32 mmol, 1.00 equiv) were stirred in acetonitrile (5 mL) overnight. The solvent was removed under reduced pressure. After drying in vacuum oven at 50 °C overnight, a black solid was obtained.

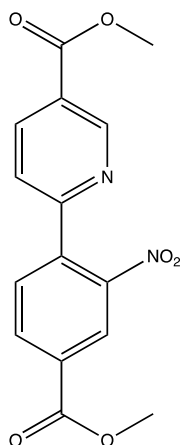
Yield: 222 mg, 0.299 mmol, 92%

**HRMS (ESI) [M-H<sup>+</sup>] *m/z* (C<sub>20</sub>H<sub>16</sub>CuN<sub>3</sub>O<sub>5</sub><sup>+</sup>):** Calcd: 441.0380; Found: 441.0380

**UV/Vis (ε [μM<sup>-1</sup>cm<sup>-1</sup>] MeCN):** λ<sub>max</sub> (208): 0.04 ± 0.01; λ<sub>max</sub> (269): 0.035 ± 0.008;

λ<sub>max</sub> (731): 0.00018 ± 0.00009

### 3.13 Synthesis of (11)



**11**

#### Procedure:

Methyl 6-Bromo-3-pyridine carboxylate (800 mg, 3.70 mmol, 1.00 equiv.), 4-methoxycarbonyl-2-nitrophenylboronic acid (833 mg, 3.70 mmol, 1.00 equiv.) and freshly powdered  $\text{KF}\cdot 2\text{H}_2\text{O}$  (1.15 g, 12.23 mmol, 3.3 equiv.) were mixed with dry THF (20 mL) in a 100 mL two-neck round flask. The suspension was bubbled with argon for 15 minutes, before  $\text{Pd}_2\text{dba}_3$  (2.5 mol%) and  $\text{HBF}_4\cdot \text{P}(\text{t-Bu})_3$  (6 mol%) were added. The bubbling was continued for 3-4 minutes after which a reflux condenser was attached to the flask. The reaction mixture was then stirred at reflux temperature for 1 hour under Ar. After cooling to room temperature, the reaction mixture was diluted with  $\text{CH}_2\text{Cl}_2$  (60 mL). The reaction mixture was then filtrated, and the solvent was then removed under reduced pressure. The crude was purified with flash chromatography (half  $\text{CH}_2\text{Cl}_2$ / half 5% EtOAc in Hexane, to half  $\text{CH}_2\text{Cl}_2$ / half 15% EtOAc in Hexane) resulting in orange powder.

Yield: 819 mg, 2.59 mmol, 70%

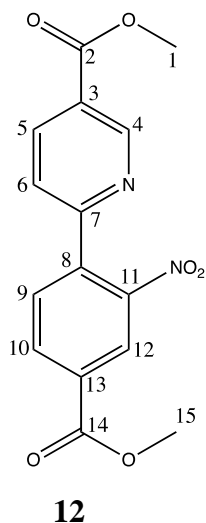
$^1\text{H NMR}$  (400MHz,  $\text{CDCl}_3$ ):  $\delta$  3.95 (s, 3H), 3.97 (s, 3H), 7.56 (dd,  $J = 0.72$  and 8.16 Hz, 1H), 7.69 (d,  $J = 8.00$  Hz, 1H), 8.30 (dd,  $J = 1.64$  and 8.00 Hz, 1H), 8.39 (dd,  $J = 2.12$  and 8.16 Hz, 1H), 8.53 (d,  $J = 1.52$  Hz, 1H), 9.21 (dd,  $J = 0.68$  and 2.00 Hz, 1H)

$^{13}\text{C NMR}$  (400 MHz,  $\text{CDCl}_3$ ):  $\delta$  52.5, 52.8, 122.3, 125.5, 125.6, 131.4, 131.8, 133.1, 138.1(2), 138.1(6), 149.1, 150.8, 158.1, 164.5, 165.2

**HRMS (ESI)** [ $\text{M}+\text{Na}^+$ ]  $m/z$  ( $\text{C}_{15}\text{H}_{12}\text{N}_2\text{NaO}_6^+$ ): Calcd: 339.0588; Found: 339.0587

The spectroscopic data is in accordance with that reported in the literature.<sup>78</sup>

## 3.14 Synthesis of (12)



### Procedure:

Compound **11** (3.106 mg, 9.820 mmol, 1.00 equiv.) and Fe powder (8.22 g, 0.15 mol, 15 equiv.) were suspended in acetic acid. The reaction mixture was flushed with argon for 2 hours, and then stirred at room temperature for 20 hours. The reaction mixture was poured into a beaker containing ice (ca. 200 mL), with another ice bath surrounding it, and concentrated ammonia solution (28% aq., ca. 150 mL) was added in portion of 25 mL. After all ammonia had been added, the resulting suspension was stirred for 5 minutes, then the solids were collected through filtration and washed with water (3×100 mL). The solids were then dissolved in warm EtOAc (ca. 50-60 °C, 300 mL) under stirring. The warm EtOAc solution was filtrated through celite to remove undissolved material. The filtrate was dried over Na<sub>2</sub>SO<sub>4</sub>, before the solvent was removed under pressure.

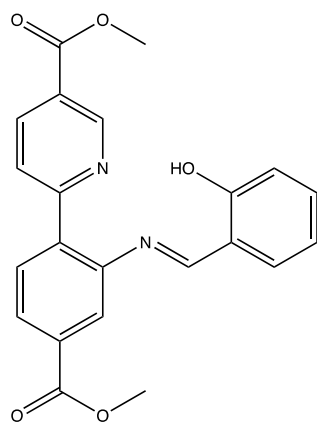
Yield: 2.76 g, 9.65 mmol, 98%

**<sup>1</sup>H NMR (400MHz, CDCl<sub>3</sub>):** δ 3.88 (s, 3H, H-15), 3.94 (s, 3H, H-1), 6.02 (s, 2H, NH<sub>2</sub>), 7.36 (dd, J = 1.6 and 8.2 Hz, 1H, H-9), 7.41 (d, J = 1.52 Hz, H-12), 7.60 (d, J = 8.24 Hz, 1H, H-10), 7.76 (d, J = 8.44 Hz, 1H, H-6), 8.33 (dd, J = 2.24 and 8.44 Hz, 1H, H-5), 9.18 (d, J = 1.72 Hz, 1H, H-4)

**<sup>13</sup>C NMR (400 MHz, CDCl<sub>3</sub>):** δ 52.1 (C-15), 52.3 (C-1), 118.0 (C-9), 118.5 (C-12), 121.7 (C-6), 123.4 (C-7), 123.8 (C-13), 129.5 (C-10), 131.9 (C-11), 137.7 (C-5), 147.2 (C-8), 149.3 (C-4), 162.0 (C-3), 165.5 (C-2), 166.8 (C-14)

**HRMS (ESI) [M+Na<sup>+</sup>] m/z (C<sub>15</sub>H<sub>14</sub>N<sub>2</sub>NaO<sub>4</sub><sup>+</sup>):** Calcd: 309.0845; Found: 309.0846

### 3.15 Synthesis of (13)



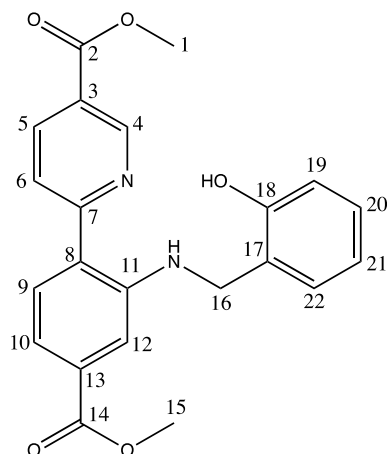
**13**

#### **Procedure:**

Methyl 6-(2-amino-4-(methoxycarbonyl) phenyl) nicotinate (**12**) (210 mg, 0.733 mmol, 1.00 equiv.) and Salicylaldehyde (76  $\mu$ L, 0.728 mmol, 1.00 equiv.) were suspended in dry EtOH. 2 drops of formic acid were added. The mixture stirred for 19 hours, and the precipitated product was collected through filtration. The product was then washed with dry EtOH and dried in vacuum oven for 3 hours.

Not isolated, conversion: 75%

## 3.16 Synthesis of Ligand (14)



**14**

### Procedure:

A mixture of **12** (179 mg, 0.62 mmol, 1.00 equiv.), salicylaldehyde (65  $\mu$ L, 0.62 mmol, 1.00 equiv.) and 1 drop of formic acid were stirred in dry MeOH overnight. The reaction mixture was cooled with an ice bath, and NaBH<sub>4</sub> (259 mg, 6.84 mmol, 11.04 equiv.) was added portion wise over the course of 5 minutes. Under addition of NaBH<sub>4</sub>, color change was observed from yellow to orange. The ice bath was then removed, and the reaction was stirred at ambient temperature for two more hours. The reaction mixture was diluted with NaHCO<sub>3</sub> (aq., sat., 26 mL). The aqueous phase was extracted with CH<sub>2</sub>Cl<sub>2</sub> (3 $\times$ 50 mL). The combined organic phase was dried over Na<sub>2</sub>SO<sub>4</sub>. The solvent was then removed under reduced pressure. The crude was purified with flash chromatography (gradient: first: 20% EtOAc / 80% Hexane, then: 50% EtOAc / 50% Hexane).

Yield: 137.5 mg, 0.31 mmol, 31%

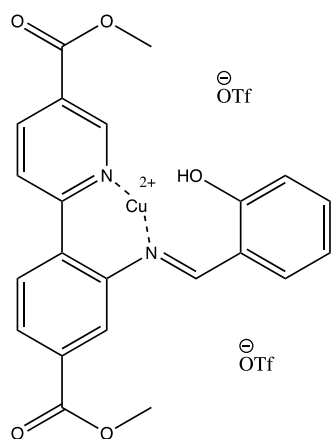
**<sup>1</sup>H NMR (400MHz, DMSO-d<sub>6</sub>):**  $\delta$  3.82 (s, 3H, H-1), 3.90 (s, 3H, H-15), 4.40 (d, J = 5.72 Hz, 2H, H-16), 6.73 (t, J = 7.36 Hz, 1H, H-21), 6.85 (d, J = 7.92 Hz, 1H, H-22), 7.07 (td, J = 7.52 and 1.32 Hz, 1H, H-20), 7.16 (dd, J = 7.68 and 0.92 Hz, 1H, H-19), 7.22 (dd, J = 8.24 and 1.36 Hz, 1H, H-10), 7.30 (d, J = 1.08 Hz, 1H, H-12), 7.84 (d, 8.24 Hz, 1H, H-9), 8.08 (d, J = 8.56 Hz, 1H, H-6), 8.36 (dd, J = 8.4 and 2.24 Hz, 1H, H-5), 9.08 (t, J = 5.76 Hz, 1H, NH (sec. amine)), 9.11 (d, J = 1.96 Hz, 1H, H-4), 9.66 (s, 1H, OH)

**<sup>13</sup>C NMR (400 MHz, DMSO-d<sub>6</sub>):**  $\delta$  41.4 (C-16), 52.1 (C-15), 52.4 (C-1), 112.0 (C-12), 114.9 (C-22), 115.6 (C-10), 118.8 (C-21), 122.3 (C-6), 122.8 (C-13), 122.9 (C-3), 124.7

(C-17), 127.8 (C-20), 127.9 (C-19), 130.1 (C-9), 131.6 (C-8), 137.6 (C-5), 147.8 (C-11),  
148.3 (C-4), 155.1 (C-18), 161.3 (C-7), 164.9 (C-2), 166.2 (C-14)

**HRMS (ESI)  $m/z$  [M+Na<sup>+</sup>] (C<sub>22</sub>H<sub>20</sub>N<sub>2</sub>O<sub>5</sub> + Na<sup>+</sup>):** Calcd:415.1264; Found: 415.1264

### 3.17 Synthesis of Complex (15)



**15**

#### Procedure:

A mixture of **12** (178 mg, 0.62 mmol, 1.00 equiv.), Cu(OTf)<sub>2</sub> (224 mg, 0.62 mmol, 1.00 equiv.) and salicylaldehyde (64  $\mu$ L, 0.62 mmol, 1.00 equiv.) were stirred in MeOH (3 mL) overnight. The solvent was removed under reduced pressure and dried in the vacuum oven at 50 °C overnight, resulting in a green solid.

Yield: 45 mg, 0.059 mmol, 10%

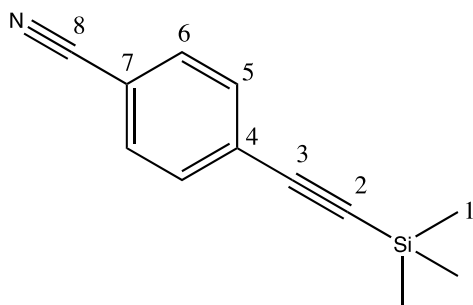
**HRMS** (ESI)  $m/z$  [M-H<sup>+</sup>] (C<sub>22</sub>H<sub>17</sub>CuN<sub>2</sub>O<sub>5</sub><sup>+</sup>): Calcd: 452.0428; Found: 452.0428

**UV/Vis** ( $\epsilon$  [ $\mu$ M<sup>-1</sup>cm<sup>-1</sup>] MeCN):  $\lambda_{\max}$  (246): 0.040  $\pm$  0.009;  $\lambda_{\max}$  (289): 0.005  $\pm$  0.01;

$\lambda_{\text{sh}}$  (302): 0.04  $\pm$  0.01;  $\lambda_{\max}$  (423): 0.012  $\pm$  0.002;  $\lambda_{\max}$  (668): 0.00025  $\pm$  0.00006



### 3.18 Synthesis of (16)



**16**

#### Procedure:

To a 50 mL round bottomed flask 4-Bromobenzonitrile (1.00 g, 5.49 mmol, 1.00 equiv), Pd(PPh<sub>3</sub>)<sub>4</sub> (127.7 mg, 0.11 mmol, 0.02 equiv), and CuI (69.9 mg, 0.367 mmol, 0.06 equiv) were added. The flask was closed with a rubber septum and backfilled with argon to create an inert atmosphere. Dry THF (7 mL) and diisopropylamine (3.13 mL, 22.33 mmol, 4.06 equiv) were added under argon at room temperature (under addition of diisopropylamine, the solution turned green/brown). The mixture was cooled down to 0°C before adding Trimethylsilyl acetylene (0.83 mL, 6.04 mmol, 1.1 equiv) dropwise and leaving it to stir for 43 h, while allowing the temperature to slowly reach room temperature. Under addition of Trimethylsilyl acetylene, the solution first turned yellow, then brown/black at the end of addition. The dark brown solution was concentrated under reduced pressure. Then it was filtrated through celite with pentane as solvent, and at last concentrated again under reduced pressure, resulting in pink/brown solid.

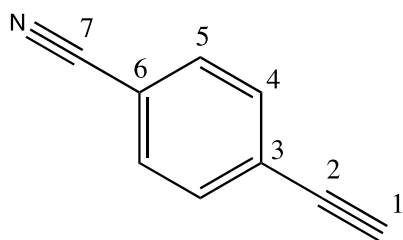
Yield: 572mg, 2.87 mmol, 52%

<sup>1</sup>H NMR (400 MHz, CDCl<sub>3</sub>): δ 7.55-7.57 (dd, J = 2.1 and 8.6 Hz, 2H, H-6), 7.49-7.51 (dd, J = 1.7 and 8.4 Hz, 2H, H-5), 0.23 (s, 9H, H-1)

<sup>13</sup>C NMR (400 MHz, CDCl<sub>3</sub>): δ -0.3 (C-1), 99.5 (C-2), 102.9 (C-3), 111.7 (C-7), 118.3 (C-8), 127.9 (C-4), 131.8 (C-5), 132.3 (C-6)

HRMS (ESI) *m/z* [M+Na<sup>+</sup>] (C<sub>12</sub>H<sub>13</sub>NNaSi<sup>+</sup>): Calcd: 222.0715; Found: 222.071

### 3.19 Synthesis of (17)



**17**

#### Procedure:

In a 50 mL round bottomed flask **16** (572.3 mg, 2.87 mmol, 1.00 equiv) was dissolved in methanol (13 mL), followed by addition of  $K_2CO_3$  (504 mg, 3.6 mmol, 1.27 equiv). A color change was observed after addition of  $K_2CO_3$ , from pink/brown to dark brown. The reaction mixture was stirred at room temperature for 2 hours. Saturated NaCl (30 mL) was added, followed by extraction with ethyl acetate (3×30 mL) and drying over  $Na_2SO_4$ . Then the solution was concentrated under reduced pressure, resulting in 383.7 mg of dark orange solid. The crude was purified with flash chromatography (EtOAc/Hexane, 6:4).

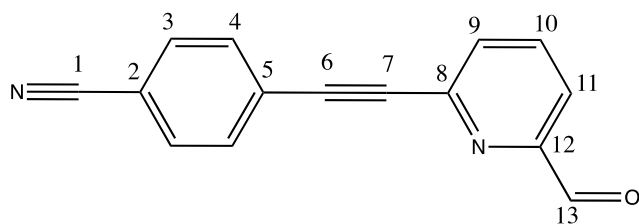
Yield: 107.8 mg, 0.847 mmol, 30%

$^1H$  NMR (400 MHz,  $CDCl_3$ ):  $\delta$  3.2 (s, 1H, H-1), 7.54-7.56 (dd,  $J = 2$  and 4.8 Hz, 2H, H-4), 7.59-7.61 (dd,  $J = 2$  and 4.8 Hz, 2H, H-5)

$^{13}C$  NMR (400 MHz,  $CDCl_3$ ):  $\delta$  81.5 (C-1), 81.8 (C-3), 112.3 (C-6), 118.2 (C-7), 126.9 (C-3), 132.0 (C-4), 132.6 (C-5)

HRMS (ESI)  $m/z$  [ $M+Na^+$ ] ( $C_9H_5NNa^+$ ): Calcd: 150.0320; Found: 150.031

## 3.20 Synthesis of (18)



**18**

### Procedure:

To a 50 mL round bottomed flask 6-Bromo-2-formylpyridine (149.3 mg, 0.8 mmol, 1.00 equiv), Pd(PPh<sub>3</sub>)<sub>4</sub> (21.6 mg, 0.018 mmol, 0.02 equiv) and CuI (8.8 mg, 0.0462 mmol, 0.057 equiv) were added. The flask was closed with a rubber septum and backfilled with argon to create an inert atmosphere. Dry THF (1.5 mL) and diisopropylamine (0.45 mL, 0.33 mmol, 4.07 equiv) were added under argon at room temperature. Under addition of diisopropylamine, the solution first turned green from yellow, and then brown at the end. The solution was cooled down to 0°C before adding **17** (107.8 mg, 0.847 mmol, 1.05 equiv) dropwise and leaving it to stir for 18 h, while allowing the temperature to slowly reach room temperature. The solution color got darker (dark brown) right after the addition of 4-ethynylbenzonitrile. The solution was concentrated under reduced pressure. Then it was filtrated through celite with pentane as solvent, and at last concentrated again under reduced pressure, resulting in a light brown solid. The crude was purified with flash chromatography (EtOAc/Hexane, 6:4), resulting in a brown/yellow solid.

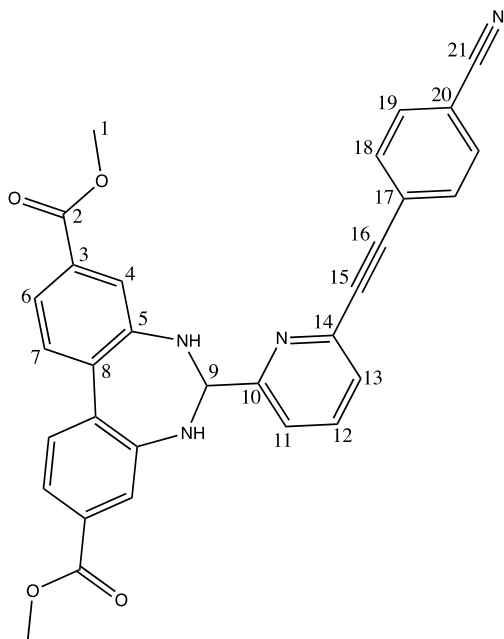
Yield: 67.2 mg, 0.28 mmol, 36%

**<sup>1</sup>H NMR (400 MHz, CDCl<sub>3</sub>):** δ 7.64-7.67 (dd, J = 2.06 and 4.52 Hz, 2H, H-3), 7.69-7.71 (dd, J = 2.06 and 4.56 Hz, 2H, H-4), 7.73-7.76 (dd, J = 1.56 and 5.84 Hz, 1H, H-9), 7.88-7.92 (td, J = 0.6, 7.2 and 6.84 Hz, 1H, H-10), 7.93-7.95 (dd, J = 1.48 and 6.28 Hz, 1H, H-11), 10.07 (s, 1H, H-13)

**<sup>13</sup>C NMR (400 MHz, CDCl<sub>3</sub>):** δ 88 (C-6), 91 (C-7), 112 (C-2), 118(C-1), 121 (C-11), 126 (C-5), 131 (C-9), 132.1 (C-4), 132.6 (C-3), 137 (C-10), 143 (C-8), 153 (C-12), 192 (C-13)

**HRMS (ESI) *m/z* [M+Na<sup>+</sup>] (C<sub>15</sub>H<sub>8</sub>N<sub>2</sub>NaO<sup>+</sup>):** Calcd: 255.0534; Found: 255.053

## 3.21 Synthesis of (19)



**19**

### Procedure:

To a 50 mL round bottom flask **18** (22.4 mg, 0.0965 mmol, 1.00 equiv.), **2** (28.3 mg, 0.0943 mmol, 0.97 equiv.) and MeOH (3 mL) were added. The flask was closed with a rubber septum, and the reaction mixture was left to stir for 18 h. The crude was collected through filtration, resulting in a yellow solid.

Yield: 25.9 mg, 0.0533mmol, 53%

**<sup>1</sup>H NMR (400 MHz, CDCl<sub>3</sub>):**  $\delta$  3.81 (s, 6H, H-1), 5.66 (t,  $J = 3.56$  Hz, 1H, H-9), 6.70 (d,  $J = 3.6$  Hz, 2H, NH), 7.36 (d,  $J = 7.72$  Hz, 1H, H-11), 7.47 (dd,  $J = 1.6$  Hz and 8.2 Hz, 2H, H-6), 7.55 (d,  $J = 1.64$  Hz, 2H, H-4), 7.58 (d,  $J = 8.28$  Hz, 2H, H-7), 7.62 (d,  $J = 7.32$  Hz, 1H, H-13), 7.80 (t,  $J = 7.6$  Hz, 1H, H-12), 7.81 (d,  $J = 8.36$  Hz, 2H, H-19), 7.94 (d,  $J = 8.36$  Hz, 2H, H-18)

**<sup>13</sup>C NMR (400 MHz, CDCl<sub>3</sub>):**  $\delta$  52.0 (C-1), 78.5 (C-9), 86.7 (C-21), 92.3 (C-15), 111.6 (C-16), 118.2 (C-20), 120.8 (C-6), 121.2 (C-4), 121.4 (C-11), 126.1 (C-8), 127.0 (C-13), 128.8 (C-3), 130.1 (C-7), 132.3 (C-19), 132.4 (C-5), 132.7 (C-18), 137.3 (C-12), 140.5 (C-17), 146.6 (C-10), 161.3 (C-14), 166.1 (C-2)

**HRMS (ESI)  $m/z$  [M+Na<sup>+</sup>] (C<sub>31</sub>H<sub>22</sub>N<sub>4</sub>NaO<sub>4</sub><sup>+</sup>):** Calcd: 537.1539; Found: 537.1533

## 4 Conclusion

During the two years of this project, five new copper-complexes, three copper(II)- and two copper(I)-complexes, were successfully synthesized and characterized. Three synthetic routes were developed and discussed for synthesizing ligands incorporating specific functional groups to imitate the active site of the LPMO enzyme.

Crystal structure of complex **5** was obtained, revealing its five-coordinated environment and square pyramidal geometry. By  $^1\text{H}$ - $^{15}\text{N}$  HMBC, the nitrogen coordination shifts ( $\delta^{15}\text{N}_{\text{complex}}$ - $\delta^{15}\text{N}_{\text{ligand}}$ ) of complex **9** were calculated and compared to a similar complex from literature,<sup>77</sup> confirming it being a bidentate complex. Furthermore, UV-vis experiments were employed on all copper(II) complexes, showing d-d transition.

Due to time limitation, ligand **14** could not be metalated. The synthesized complexes, **4**, **5**, **9** and **10** were sent to Max Planck Institute for Chemical Energy Conversion, Mülheim an der Ruhr, Germany for Electron Paramagnetic Resonance (EPR) and X-ray Absorption Near Edge Spectroscopy (XANES). XANES results have been received and discussed, giving an insight into the oxidation state of the complex and structure around the copper.

Future study should focus on catalytic testing of the synthesized complexes, to investigate the potential impact of incorporating oxygen atom in the ligand on the reactivity of the complex. This evaluation will further help in possibly adjusting the ligand design for better reactivity. Additionally, the focus should also be on incorporating the synthesized complexes into MOFs. Lastly, more ligands should be synthesized, with resemblance even more pronounced to the active site.

## 5 Bibliography

- (1) Eijsink, V. G. H.; Petrovic, D.; Forsberg, Z.; Mekasha, S.; Røhr, Å. K.; Várnai, A.; Bissaro, B.; Vaaje-Kolstad, G. On the Functional Characterization of Lytic Polysaccharide Monooxygenases (LPMOs). *Biotechnol. Biofuels* **2019**, *12*, 58. <https://doi.org/10.1186/s13068-019-1392-0>.
- (2) *The Direct Catalytic Oxidation of Methane to Methanol—A Critical Assessment - Ravi - 2017 - Angewandte Chemie International Edition - Wiley Online Library*. <https://onlinelibrary-wiley-com.ezproxy.uio.no/doi/full/10.1002/anie.201702550> (accessed 2023-05-29).
- (3) Cutsail, G. E.; Ross, M. O.; Rosenzweig, A. C.; DeBeer, S. Towards a Unified Understanding of the Copper Sites in Particulate Methane Monooxygenase: An X-Ray Absorption Spectroscopic Investigation. *Chem. Sci.* **2021**, *12* (17), 6194–6209. <https://doi.org/10.1039/D1SC00676B>.
- (4) Ravishankara, A. R.; Kuylenstierna, J. C. I.; Michalopoulou, E.; Höglund-Isaksson, L.; Zhang, Y.; Seltzer, K.; Ru, M.; Castelino, R.; Faluvegi, G.; Naik, V.; Horowitz, L.; He, J.; Lamarque, J.-F.; Sudo, K.; Collins, W. J.; Malley, C.; Harmsen, M.; Stark, K.; Junkin, J.; Li, G.; Glick, A.; Borgford-Parnell, N. *Global Methane Assessment: Benefits and Costs of Mitigating Methane Emissions*. UNEP - UN Environment Programme. <http://www.unep.org/resources/report/global-methane-assessment-benefits-and-costs-mitigating-methane-emissions> (accessed 2023-04-13).
- (5) Black, S.; Parry, I.; Vernon, N. *Methane Emissions Must Fall for World to Hit Temperature Targets*. <https://www.imf.org/en/Blogs/Articles/2022/11/02/methane-emissions-must-fall-for-world-to-hit-temperature-targets> (accessed 2023-06-03).
- (6) Zhen, X.; Wang, Y. An Overview of Methanol as an Internal Combustion Engine Fuel. *Renew. Sustain. Energy Rev.* **2015**, *52*, 477–493. <https://doi.org/10.1016/j.rser.2015.07.083>.
- (7) Wang, B.; Albarracín-Suazo, S.; Pagán-Torres, Y.; Nikolla, E. Advances in Methane Conversion Processes. *Catal. Today* **2017**, *285*, 147–158. <https://doi.org/10.1016/j.cattod.2017.01.023>.
- (8) Nandy, A.; Duan, C.; Goffinet, C.; Kulik, H. J. New Strategies for Direct Methane-to-Methanol Conversion from Active Learning Exploration of 16 Million Catalysts. *JACS Au* **2022**, *2* (5), 1200–1213. <https://doi.org/10.1021/jacsau.2c00176>.
- (9) Bissaro, B.; Eijsink, V. G. H. Lytic Polysaccharide Monooxygenases: Enzymes for Controlled and Site-Specific Fenton-like Chemistry. *Essays Biochem.* **2023**, *67* (3), 575–584. <https://doi.org/10.1042/EBC20220250>.
- (10) Signorile, M.; Borfecchia, E.; Bordiga, S.; Berlier, G. Influence of Ion Mobility on the Redox and Catalytic Properties of Cu Ions in Zeolites. *Chem. Sci.* **2022**, *13* (35), 10238–10250. <https://doi.org/10.1039/D2SC03565K>.
- (11) Centrella, B.; Deplano, G.; Damin, A.; Signorile, M.; Tortora, M.; Barolo, C.; Bonomo, M.; Bordiga, S. A Multi-Technique Approach to Unveil the Redox Behaviour and Potentiality of Homoleptic CuI Complexes Based on Substituted Bipyridine Ligands in Oxygenation Reactions. *Dalton Trans.* **2022**, *51* (38), 14439–14451. <https://doi.org/10.1039/D2DT01234K>.

- (12) Frandsen, K. E. H.; Lo Leggio, L. Lytic Polysaccharide Monooxygenases: A Crystallographer's View on a New Class of Biomass-Degrading Enzymes. *IUCrJ* **2016**, *3* (Pt 6), 448–467. <https://doi.org/10.1107/S2052252516014147>.
- (13) Moreau, C.; Tapin-Lingua, S.; Grisel, S.; Gimbert, I.; Le Gall, S.; Meyer, V.; Petit-Conil, M.; Berrin, J.-G.; Cathala, B.; Villares, A. Lytic Polysaccharide Monooxygenases (LPMOs) Facilitate Cellulose Nanofibrils Production. *Biotechnol. Biofuels* **2019**, *12* (1), 156. <https://doi.org/10.1186/s13068-019-1501-0>.
- (14) McEvoy, A.; Creutzberg, J.; Singh, R. K.; Bjerrum, M. J.; Hedegård, E. D. The Role of the Active Site Tyrosine in the Mechanism of Lytic Polysaccharide Monooxygenase. *Chem. Sci.* **12** (1), 352–362. <https://doi.org/10.1039/d0sc05262k>.
- (15) Kamaraj, K.; Kim, E.; Galliker, B.; Zakharov, L. N.; Rheingold, A. L.; Zuberbühler, A. D.; Karlin, K. D. Copper(I) and Copper(II) Complexes Possessing Cross-Linked Imidazole-Phenol Ligands: Structures and Dioxygen Reactivity. *J. Am. Chem. Soc.* **2003**, *125* (20), 6028–6029. <https://doi.org/10.1021/ja034263f>.
- (16) Paradisi, A.; Johnston, E. M.; Tovborg, M.; Nicoll, C. R.; Ciano, L.; Dowle, A.; McMaster, J.; Hancock, Y.; Davies, G. J.; Walton, P. H. Formation of a Copper(II)–Tyrosyl Complex at the Active Site of Lytic Polysaccharide Monooxygenases Following Oxidation by H<sub>2</sub>O<sub>2</sub>. *J. Am. Chem. Soc.* **2019**, *141* (46), 18585–18599. <https://doi.org/10.1021/jacs.9b09833>.
- (17) Fukatsu, A.; Morimoto, Y.; Sugimoto, H.; Itoh, S. Modelling a 'Histidine Brace' Motif in Mononuclear Copper Monooxygenases. *Chem. Commun.* **2020**, *56* (38), 5123–5126. <https://doi.org/10.1039/D0CC01392G>.
- (18) Dolphin, D.; McKenna, C.; Murakami, Y.; Tabushi, I. *Biomimetic Chemistry*; 1980. <https://doi.org/10.1021/ba-1980-0191>.
- (19) Silva, A. R.; Mourão, T.; Rocha, J. Oxidation of Cyclohexane by Transition-Metal Complexes with Biomimetic Ligands. *Catal. Today* **2013**, *203*, 81–86. <https://doi.org/10.1016/j.cattod.2012.07.043>.
- (20) Kumar, S.; Mohan, B.; Tao, Z.; You, H.; Ren, P. Incorporation of Homogeneous Organometallic Catalysts into Metal–Organic Frameworks for Advanced Heterogenization: A Review. *Catal. Sci. Technol.* **2021**, *11* (17), 5734–5771. <https://doi.org/10.1039/D1CY00663K>.
- (21) *Zeolites*; Król, M., Florek, P., Eds.; MDPI - Multidisciplinary Digital Publishing Institute, 2022. <https://doi.org/10.3390/books978-3-0365-3411-4>.
- (22) *Zeolites and Metal-Organic Frameworks: From Lab to Industry*. In *Zeolites and Metal-Organic Frameworks*; Amsterdam University Press, 2018. <https://doi.org/10.1515/9789048536719>.
- (23) Alezi, D.; Belmabkhout, Y.; Suyetin, M.; Bhatt, P. M.; Weseliński, Ł. J.; Solovyeva, V.; Adil, K.; Spanopoulos, I.; Trikalitis, P. N.; Emwas, A.-H.; Eddaoudi, M. MOF Crystal Chemistry Paving the Way to Gas Storage Needs: Aluminum-Based Soc-MOF for CH<sub>4</sub>, O<sub>2</sub>, and CO<sub>2</sub> Storage. *J. Am. Chem. Soc.* **2015**, *137* (41), 13308–13318. <https://doi.org/10.1021/jacs.5b07053>.
- (24) Vincent Blay, Luis Francisco Bobadilla and Alejandro Cabrera. *Zeolites and Metal-Organic Frameworks*; Amsterdam University Press, 2018.
- (25) van Leeuwen, P. W. N. M. Decomposition Pathways of Homogeneous Catalysts. *Appl. Catal. Gen.* **2001**, *212* (1), 61–81. [https://doi.org/10.1016/S0926-860X\(00\)00844-9](https://doi.org/10.1016/S0926-860X(00)00844-9).

- (26) Najafpour, M. M.; Feizi, H. A New Decomposition Mechanism for Metal Complexes under Water-Oxidation Conditions. *Sci. Rep.* **2019**, *9*, 7483. <https://doi.org/10.1038/s41598-019-43953-6>.
- (27) Crabtree, R. H. The Stability of Organometallic Ligands in Oxidation Catalysis. *J. Organomet. Chem.* **2014**, *751*, 174–180. <https://doi.org/10.1016/j.jorganchem.2013.07.061>.
- (28) Hailu, S. L.; Nair, B. U.; Redi-Abshiro, M.; Diaz, I.; Tessema, M. COMPUTATIONAL STUDIES ON HETEROGENIZATION OF HOMOGENEOUS CATALYST OF IRON(III), NICKEL(II) AND COPPER(II) N,N'-DISALICYLIDENE-1,2-PHENYLENEDIAMINE COMPLEX. *Bull. Chem. Soc. Ethiop.* **2019**, *33* (1), 91–103. <https://doi.org/10.4314/bcse.v33i1.9>.
- (29) Thomas, S. J. M. The Advantages of Exploring the Interface Between Heterogeneous and Homogeneous Catalysis. *ChemCatChem* **2010**, *2* (2), 127–132. <https://doi.org/10.1002/cctc.200900275>.
- (30) Lu, W.; Wei, Z.; Gu, Z.-Y.; Liu, T.-F.; Park, J.; Park, J.; Tian, J.; Zhang, M.; Zhang, Q.; Ili, T. G.; Bosch, M.; Zhou, H.-C. Tuning the Structure and Function of Metal–Organic Frameworks via Linker Design. *Chem. Soc. Rev.* **2014**, *43* (16), 5561–5593. <https://doi.org/10.1039/C4CS00003J>.
- (31) Yuan, S.; Feng, L.; Wang, K.; Pang, J.; Bosch, M.; Lollar, C.; Sun, Y.; Qin, J.; Yang, X.; Zhang, P.; Wang, Q.; Zou, L.; Zhang, Y.; Zhang, L.; Fang, Y.; Li, J.; Zhou, H.-C. Stable Metal–Organic Frameworks: Design, Synthesis, and Applications. *Adv. Mater.* **2018**, *30* (37), 1704303. <https://doi.org/10.1002/adma.201704303>.
- (32) Cavka, J. H.; Jakobsen, S.; Olsbye, U.; Guillou, N.; Lamberti, C.; Bordiga, S.; Lillerud, K. P. A New Zirconium Inorganic Building Brick Forming Metal Organic Frameworks with Exceptional Stability. *J. Am. Chem. Soc.* **2008**, *130* (42), 13850–13851. <https://doi.org/10.1021/ja8057953>.
- (33) Vahabi, A. H.; Norouzi, F.; Sheibani, E.; Rahimi-Nasrabadi, M. Functionalized Zr-UiO-67 Metal–Organic Frameworks: Structural Landscape and Application. *Coord. Chem. Rev.* **2021**, *445*, 214050. <https://doi.org/10.1016/j.ccr.2021.214050>.
- (34) Gutzler, R.; Stepanow, S.; Grumelli, D.; Lingenfelder, M.; Kern, K. Mimicking Enzymatic Active Sites on Surfaces for Energy Conversion Chemistry. *Acc. Chem. Res.* **2015**, *48* (7), 2132–2139. <https://doi.org/10.1021/acs.accounts.5b00172>.
- (35) *Which Metals are Green for Catalysis? Comparison of the Toxicities of Ni, Cu, Fe, Pd, Pt, Rh, and Au Salts - Egorova - 2016 - Angewandte Chemie International Edition - Wiley Online Library.* <https://onlinelibrary-wiley-com.ezproxy.uio.no/doi/full/10.1002/anie.201603777> (accessed 2023-05-20).
- (36) Trammell, R.; Rajabimoghadam, K.; Garcia-Bosch, I. Copper-Promoted Functionalization of Organic Molecules: From Biologically Relevant Cu/O<sub>2</sub> Model Systems to Organometallic Transformations. *Chem. Rev.* **2019**, *119* (4), 2954–3031. <https://doi.org/10.1021/acs.chemrev.8b00368>.
- (37) *Copper Active Sites in Biology | Chemical Reviews.* <https://pubs-acsc-org.ezproxy.uio.no/doi/full/10.1021/cr400327t> (accessed 2023-05-20).
- (38) Mir, A. R.; Pichtel, J.; Hayat, S. Copper: Uptake, Toxicity and Tolerance in Plants and Management of Cu-Contaminated Soil. *BioMetals* **2021**, *34* (4), 737–759. <https://doi.org/10.1007/s10534-021-00306-z>.
- (39) *Nondestructive Evaluation Physics : Magnetism.* <https://www.nde-ed.org/Physics/Magnetism/ferromagmaterials.shtml> (accessed 2023-05-20).



- (40) Singh, O. I.; Damayanti, M.; Singh, N. R.; Singh, R. K. H.; Mohapatra, M.; Kadam, R. M. Synthesis, EPR and Biological Activities of Bis(1-n-Butylamidino-O-Alkylurea)Copper(II)Chloride Complexes: EPR Evidence for Binuclear Complexes in Frozen DMF Solution. *Polyhedron* **2005**, *24* (8), 909–916. <https://doi.org/10.1016/j.poly.2005.02.014>.
- (41) Spessard, G. O.; Miessler, G. L. *Organometallic Chemistry*, 3rd edition.; Oxford University Press, 2015.
- (42) Czeakański, Ł.; Hoffmann, S. K.; Barczyński, P.; Gąsowska, A.; Bregier-Jarzębowska, R.; Zalewska, A.; Goslar, J.; Ratajczak-Sitarz, M.; Katrusiak, A. Crystal Structure and Physical Properties of 1-Methyl-3-(Carboxymethyl)Benzimidazolium Betaine·CuBr<sub>2</sub> in Crystal and Water Solution. *New J. Chem.* **2016**, *40* (12), 10526–10535. <https://doi.org/10.1039/C6NJ03192G>.
- (43) Popova, T. V.; Aksenova, N. V. Complexes of Copper in Unstable Oxidation States. *Russ. J. Coord. Chem.* **2003**, *29* (11), 743–765. <https://doi.org/10.1023/B:RUCO.00000003432.39025.cc>.
- (44) *Advances in Cross-Coupling Reactions*; Pérez Sestelo, J., Sarandeses, L. A., Eds.; MDPI - Multidisciplinary Digital Publishing Institute, 2020. <https://doi.org/10.3390/books978-3-03943-568-5>.
- (45) D'Alterio, M. C.; Casals-Cruañas, È.; Tzouras, N. V.; Talarico, G.; Nolan, S. P.; Poater, A. Mechanistic Aspects of the Palladium-Catalyzed Suzuki-Miyaura Cross-Coupling Reaction. *Chem. – Eur. J.* **2021**, *27* (54), 13481–13493. <https://doi.org/10.1002/chem.202101880>.
- (46) Echavarren, A. M.; Homs, A. Mechanistic Aspects of Metal-Catalyzed C,C- and C,X-Bond Forming Reactions. In *Metal-Catalyzed Cross-Coupling Reactions and More*; John Wiley & Sons, Ltd, 2014; pp 1–64. <https://doi.org/10.1002/9783527655588.ch1>.
- (47) Schaub, T. A.; Kivala, M. Cross-Coupling Reactions to Sp Carbon Atoms. In *Metal-Catalyzed Cross-Coupling Reactions and More*; John Wiley & Sons, Ltd, 2014; pp 665–762. <https://doi.org/10.1002/9783527655588.ch9>.
- (48) Raczuk, E.; Dmochowska, B.; Samaszko-Fiertek, J.; Madaj, J. Different Schiff Bases—Structure, Importance and Classification. *Molecules* **2022**, *27* (3), 787. <https://doi.org/10.3390/molecules27030787>.
- (49) Ali, S. S.; Kenawy, E.-R.; Sonbol, F. I.; Sun, J.; Al-Etewy, M.; Ali, A.; Huizi, L.; El-Zawawy, N. A. Pharmaceutical Potential of a Novel Chitosan Derivative Schiff Base with Special Reference to Antibacterial, Anti-Biofilm, Antioxidant, Anti-Inflammatory, Hemocompatibility and Cytotoxic Activities. *Pharm. Res.* **2018**, *36* (1), 5. <https://doi.org/10.1007/s11095-018-2535-x>.
- (50) Abuamer, K. M.; Maihub, A. A.; El-Ajaily, M. M.; Etoriki, A. M.; Abou-Krishna, M. M.; Almagani, M. A. The Role of Aromatic Schiff Bases in the Dyes Techniques. *Int. J. Org. Chem.* **2014**, *2014*. <https://doi.org/10.4236/ijoc.2014.41002>.
- (51) More, M. S.; Joshi, P. G.; Mishra, Y. K.; Khanna, P. K. Metal Complexes Driven from Schiff Bases and Semicarbazones for Biomedical and Allied Applications: A Review. *Mater. Today Chem.* **2019**, *14*, 100195. <https://doi.org/10.1016/j.mtchem.2019.100195>.
- (52) Hanson, J. Synthesis and Use of Jacobsen's Catalyst: Enantioselective Epoxidation in the Introductory Organic Laboratory. *J. Chem. Educ.* **2001**, *78* (9), 1266. <https://doi.org/10.1021/ed078p1266>.
- (53) Cubillos, J.; Hölderich, W. Jacobsens Catalyst Anchored on Al-MCM-41 and NH<sub>2</sub> Group Modified Si-MCM-41 as Heterogeneous Enantioselective Epoxidation Catalyst

- Using in Situ Generated Dimethyldioxirane as Oxidant. *Rev. Fac. Ing. Univ. Antioquia* **2007**, *41*, 31–47.
- (54) da Silva, C. M.; da Silva, D. L.; Modolo, L. V.; Alves, R. B.; de Resende, M. A.; Martins, C. V. B.; de Fátima, Â. Schiff Bases: A Short Review of Their Antimicrobial Activities. *J. Adv. Res.* **2011**, *2* (1), 1–8. <https://doi.org/10.1016/j.jare.2010.05.004>.
- (55) Prakash, A.; Adhikari, D. Application of Schiff Bases and Their Metal Complexes-A Review. **2011**.
- (56) Meena, R.; Meena, P.; Kumari, A.; Sharma, N.; Fahmi, N. Schiff Bases and Their Metal Complexes: Synthesis, Structural Characteristics and Applications; 2023. <https://doi.org/10.5772/intechopen.108396>.
- (57) Urbansky, E. T. Carbinolamines and Geminal Diols in Aqueous Environmental Organic Chemistry. *J. Chem. Educ.* **2000**, *77* (12), 1644. <https://doi.org/10.1021/ed077p1644>.
- (58) *Reductive Amination in the Synthesis of Pharmaceuticals | Chemical Reviews*. <https://pubs-acs-org.ezproxy.uio.no/doi/full/10.1021/acs.chemrev.9b00383> (accessed 2023-05-25).
- (59) Ashenhurst, J. *Nucleophilic Addition To Carbonyls*. Master Organic Chemistry. <https://www.masterorganicchemistry.com/2022/09/09/nucleophilic-addition/> (accessed 2023-05-25).
- (60) Simpson, A. J.; Simpson, M. J.; Soong, R. Nuclear Magnetic Resonance Spectroscopy and Its Key Role in Environmental Research. *Environ. Sci. Technol.* **2012**, *46* (21), 11488–11496. <https://doi.org/10.1021/es302154w>.
- (61) Stolarski, R.; Dudycz, L.; Shugar, D. NMR Studies in the Syn-Anti Dynamic Equilibrium in Purine Nucleosides and Nucleotides. *Eur. J. Biochem.* **1980**, *108* (1), 111–121. <https://doi.org/10.1111/j.1432-1033.1980.tb04701.x>.
- (62) Fan, T. W.-M.; Lane, A. N. Applications of NMR Spectroscopy to Systems Biochemistry. *Prog. Nucl. Magn. Reson. Spectrosc.* **2016**, *92–93*, 18–53. <https://doi.org/10.1016/j.pnmrs.2016.01.005>.
- (63) Zloh, M. NMR Spectroscopy in Drug Discovery and Development: Evaluation of Physico-Chemical Properties. *ADMET DMPK* **2019**, *7* (4), 242–251. <https://doi.org/10.5599/admet.737>.
- (64) Claridge, T. D. W. *High-Resolution NMR Techniques in Organic Chemistry*, 3rd edition.; Elsevier, 2016. <https://doi.org/10.1016/B978-0-08-099986-9.00001-4>.
- (65) Pavia, D. L.; Lampman, G. M.; Kriz, G. S.; Vyvyan, J. R. *Introduction to Spectroscopy*, 5TH edition.; CENGAGE Learning, 2015.
- (66) Sheehy, K. J.; Bateman, L. M.; Flosbach, N. T.; Breugst, M.; Byrne, P. A. Identification of N- or O-Alkylation of Aromatic Nitrogen Heterocycles and N-Oxides Using <sup>1</sup>H–<sup>15</sup>N HMBC NMR Spectroscopy. *Eur. J. Org. Chem.* **2020**, *2020* (22), 3270–3281. <https://doi.org/10.1002/ejoc.202000329>.
- (67) *Nuclear Overhauser Effect - an overview | ScienceDirect Topics*. <https://www.sciencedirect.com/topics/medicine-and-dentistry/nuclear-overhauser-effect> (accessed 2023-06-07).
- (68) Yano, J.; Yachandra, V. K. X-Ray Absorption Spectroscopy. *Photosynth. Res.* **2009**, *102* (2), 241. <https://doi.org/10.1007/s11120-009-9473-8>.
- (69) Yano, J.; Yachandra, V. K. Where Water Is Oxidized to Dioxygen: Structure of the Photosynthetic Mn<sub>4</sub>Ca Cluster from X-Ray Spectroscopy. *Inorg. Chem.* **2008**, *47* (6), 1711–1726. <https://doi.org/10.1021/ic7016837>.

- (70) Sherborne, G. J.; Nguyen, B. N. Recent XAS Studies into Homogeneous Metal Catalyst in Fine Chemical and Pharmaceutical Syntheses. *Chem. Cent. J.* **2015**, *9* (1), 37. <https://doi.org/10.1186/s13065-015-0103-6>.
- (71) Bonino, F.; Groppo, E.; Prestipino, C.; Agostini, G.; Piovano, A.; Gianolio, D.; Mino, L.; Gallo, E.; Lamberti, C. Catalyst Characterization by XAS and XES Spectroscopies: In Situ and Operando Experiments. In *Synchrotron Radiation: Basics, Methods and Applications*; Mobilio, S., Boscherini, F., Meneghini, C., Eds.; Springer: Berlin, Heidelberg, 2015; pp 717–736. [https://doi.org/10.1007/978-3-642-55315-8\\_28](https://doi.org/10.1007/978-3-642-55315-8_28).
- (72) Bordiga, S.; Groppo, E.; Agostini, G.; van Bokhoven, J. A.; Lamberti, C. Reactivity of Surface Species in Heterogeneous Catalysts Probed by In Situ X-Ray Absorption Techniques. *Chem. Rev.* **2013**, *113* (3), 1736–1850. <https://doi.org/10.1021/cr2000898>.
- (73) Lamberti, C.; Bokhoven, J. A. van; Margaritondo, G.; Kas, J. J.; Jorisson, K.; Rehr, J. J.; Joly, Y.; Grenier, S.; Gianolio, D.; Glatzel, P.; Alonsi-Mori, R.; Sokaras, D. *X-Ray Absorption and X-Ray Emission Spectroscopy: Theory and Applications*; John Wiley & Sons, Ltd, 2016.
- (74) *X-Ray Absorption Spectroscopy of Semiconductors*; Schnohr, C. S., Ridgway, M. C., Eds.; Springer Series in Optical Sciences; Springer: Berlin, Heidelberg, 2015; Vol. 190. <https://doi.org/10.1007/978-3-662-44362-0>.
- (75) *Scattering Methods for Condensed Matter Research: Towards Novel Applications at Future Sources*; Angst, M., Forschungszentrum Jülich, Eds.; Lecture notes of the ... IFF spring school; Forschungszentrum Jülich: Jülich, 2012.
- (76) Geoghegan, B. L.; Liu, Y.; Peredkov, S.; Dechert, S.; Meyer, F.; DeBeer, S.; Cutsail, G. E. I. Combining Valence-to-Core X-Ray Emission and Cu K-Edge X-Ray Absorption Spectroscopies to Experimentally Assess Oxidation State in Organometallic Cu(I)/(II)/(III) Complexes. *J. Am. Chem. Soc.* **2022**, *144* (6), 2520–2534. <https://doi.org/10.1021/jacs.1c09505>.
- (77) Gerz, I.; Jannuzzi, S. A. V.; Hylland, K. T.; Negri, C.; Wragg, D. S.; Øien-Ødegaard, S.; Tilset, M.; Olsbye, U.; DeBeer, S.; Amedjkouh, M. Structural Elucidation, Aggregation, and Dynamic Behaviour of N,N,N,N-Copper(I) Schiff Base Complexes in Solid and in Solution: A Combined NMR, X-Ray Spectroscopic and Crystallographic Investigation. *Eur. J. Inorg. Chem.* **2021**, *2021* (46), 4762–4775. <https://doi.org/10.1002/ejic.202100722>.
- (78) Hylland, K. T.; Øien-Ødegaard, S.; Tilset, M. The Suzuki–Miyaura Cross-Coupling as the Key Step in the Synthesis of 2-Aminobiphenyls and 2,2'-Diaminobiphenyls: Application in the Synthesis of Schiff Base Complexes of Zn. *Eur. J. Org. Chem.* **2020**, *2020* (27), 4208–4226. <https://doi.org/10.1002/ejoc.202000599>.
- (79) Hylland, K. T.; Øien-Ødegaard, S.; Heyn, R. H.; Tilset, M. Zinc Schiff Base Complexes Derived from 2,2'-Diaminobiphenyls: Solution Behavior and Reactivity towards Nitrogen Bases. *Eur. J. Inorg. Chem.* **2020**, *2020* (38), 3627–3643. <https://doi.org/10.1002/ejic.202000589>.
- (80) Ko, N.; Hong, J.; Sung, S.; Cordova, K. E.; Park, H. J.; Yang, J. K.; Kim, J. A Significant Enhancement of Water Vapour Uptake at Low Pressure by Amine-Functionalization of UiO-67. *Dalton Trans.* **2015**, *44* (5), 2047–2051. <https://doi.org/10.1039/C4DT02582B>.
- (81) Hylland, K. *The Suzuki–Miyaura Cross-Coupling as the Key Step in the Synthesis of 2-Aminobiphenyls and 2,2'-Diaminobiphenyls: Application in the Synthesis of Schiff Base Complexes of Zn - Hylland - 2020 - European Journal of Organic Chemistry - Wiley Online Library*. <https://chemistry-europe.onlinelibrary.wiley.com/doi/10.1002/ejoc.202000599> (accessed 2022-03-06).

- (82) Protodeboronation of Heteroaromatic, Vinyl, and Cyclopropyl Boronic Acids: pH–Rate Profiles, Autocatalysis, and Disproportionation | *Journal of the American Chemical Society*. <https://pubs-acsc-org.ezproxy.uio.no/doi/full/10.1021/jacs.6b03283> (accessed 2023-05-12).
- (83) Hall, D. G. Structure, Properties, and Preparation of Boronic Acid Derivatives. In *Boronic Acids*; John Wiley & Sons, Ltd, 2011; pp 1–133. <https://doi.org/10.1002/9783527639328.ch1>.
- (84) Vonlanthen, D. *Biphenyl-Cyclophanes: The Molecular Control over the Conductivity of Single-Molecule Junctions*; 2010.
- (85) Mazzanti, A.; Lunazzi, L.; Minzoni, M.; Anderson, J. E. Rotation in Biphenyls with a Single Ortho-Substituent. *J. Org. Chem.* **2006**, *71* (15), 5474–5481. <https://doi.org/10.1021/jo060205b>.
- (86) Joule, J. A.; Mills, K. *Heterocyclic Chemistry, Fifth Edition*. **2010**.
- (87) *Overview of Schiff Bases* | *IntechOpen*. <https://www.intechopen.com/chapters/84305> (accessed 2023-05-13).
- (88) Zito, S. W.; Martinez-Carrion, M. Stereospecificity of Sodium Borohydride Reduction of Schiff Bases at the Active Site of Aspartate Aminotransferase. *J. Biol. Chem.* **1980**, *255* (18), 8645–8649. [https://doi.org/10.1016/S0021-9258\(18\)43548-X](https://doi.org/10.1016/S0021-9258(18)43548-X).
- (89) Orpen, A. . G.; Brammer, L.; Allen, F. H.; Kennard, O.; Watson, D. G.; Taylor, R. Appendix A: Typical Interatomic Distances in Organic Compounds and Organometallic Compounds and Coordination Complexes of the d- and f-Block Metals. In *Structure Correlation*; John Wiley & Sons, Ltd, 1994; pp 752–858. <https://doi.org/10.1002/9783527616091.app1>.
- (90) *IR Spectrum Table*. <https://www.sigmaaldrich.com/NO/en/technical-documents/technical-article/analytical-chemistry/photometry-and-reflectometry/ir-spectrum-table> (accessed 2023-06-04).
- (91) Niccoli Asabella, A.; Cascini, G. L.; Altini, C.; Paparella, D.; Notaristefano, A.; Rubini, G. The Copper Radioisotopes: A Systematic Review with Special Interest to <sup>64</sup>Cu. *BioMed Res. Int.* **2014**, *2014*, 786463. <https://doi.org/10.1155/2014/786463>.
- (92) Sangeetha, N. R.; Pal, S. Syntheses and Structures of Square-Pyramidal Acetonitrile Coordinated Copper(II) Complexes with N-(Aroyl)-N'-(5-Nitrosalicylidene)Hydrazines. *J. Chem. Crystallogr.* **1999**, *29* (3), 287–293. <https://doi.org/10.1023/A:1009517716964>.
- (93) Pazderski, L. 15N NMR Coordination Shifts in Pd(II), Pt(II), Au(III), Co(III), Rh(III), Ir(III), Pd(IV), and Pt(IV) Complexes with Pyridine, 2,2'-Bipyridine, 1,10-Phenanthroline, Quinoline, Isoquinoline, 2,2'-Biquinoline, 2,2':6', 2'-Terpyridine and Their Alkyl or Aryl Derivatives. *Magn. Reson. Chem.* **2008**, *46* (S1), S3–S15. <https://doi.org/10.1002/mrc.2301>.
- (94) Kleinmaier, R.; Arenz, S.; Karim, A.; Carlsson, A.-C. C.; Erdélyi, M. Solvent Effects on 15N NMR Coordination Shifts. *Magn. Reson. Chem.* **2013**, *51* (1), 46–53. <https://doi.org/10.1002/mrc.3907>.
- (95) Giorgetti, M.; Pelli, M.; Lobbia, G. G.; Santini, C. XAFS Studies on Copper(I) Complexes Containing Scorpionate Ligands. *J. Phys. Conf. Ser.* **2009**, *190* (1), 012146. <https://doi.org/10.1088/1742-6596/190/1/012146>.
- (96) Kau, L. S.; Spira-Solomon, D. J.; Penner-Hahn, J. E.; Hodgson, K. O.; Solomon, E. I. X-Ray Absorption Edge Determination of the Oxidation State and Coordination Number of Copper. Application to the Type 3 Site in *Rhus Vernicifera* Laccase and Its Reaction with

- Oxygen. *J. Am. Chem. Soc.* **1987**, *109* (21), 6433–6442.  
<https://doi.org/10.1021/ja00255a032>.
- (97) Hahn, J. E.; Scott, R. A.; Hodgson, K. O.; Doniach, S.; Desjardins, S. R.; Solomon, E. I. Observation of an Electric Quadrupole Transition in the X-Ray Absorption Spectrum of a Cu(II) Complex. *Chem. Phys. Lett.* **1982**, *88* (6), 595–598. [https://doi.org/10.1016/0009-2614\(82\)85016-1](https://doi.org/10.1016/0009-2614(82)85016-1).
- (98) Gaur, A.; Klysubun, W.; Soni, B.; Shrivastava, B. D.; Prasad, J.; Srivastava, K. Identification of Different Coordination Geometries by XAFS in Copper(II) Complexes with Trimesic Acid. *J. Mol. Struct.* **2016**, *1121*, 119–127.  
<https://doi.org/10.1016/j.molstruc.2016.05.066>.
- (99) Seidler, G. T.; Mortensen, D. R.; Remesnik, A. J.; Pacold, J. I.; Ball, N. A.; Barry, N.; Styczinski, M.; Hoidn, O. R. A Laboratory-Based Hard x-Ray Monochromator for High-Resolution x-Ray Emission Spectroscopy and x-Ray Absorption near Edge Structure Measurements. *Rev. Sci. Instrum.* **2014**, *85* (11), 113906.  
<https://doi.org/10.1063/1.4901599>.
- (100) Jahrman, E. P.; Holden, W. M.; Ditter, A. S.; Mortensen, D. R.; Seidler, G. T.; Fister, T. T.; Kozimor, S. A.; Piper, L. F. J.; Rana, J.; Hyatt, N. C.; Stennett, M. C. An Improved Laboratory-Based x-Ray Absorption Fine Structure and x-Ray Emission Spectrometer for Analytical Applications in Materials Chemistry Research. *Rev. Sci. Instrum.* **2019**, *90* (2), 024106. <https://doi.org/10.1063/1.5049383>.

# 6 Appendix

## 6.1 A.1 NMR data

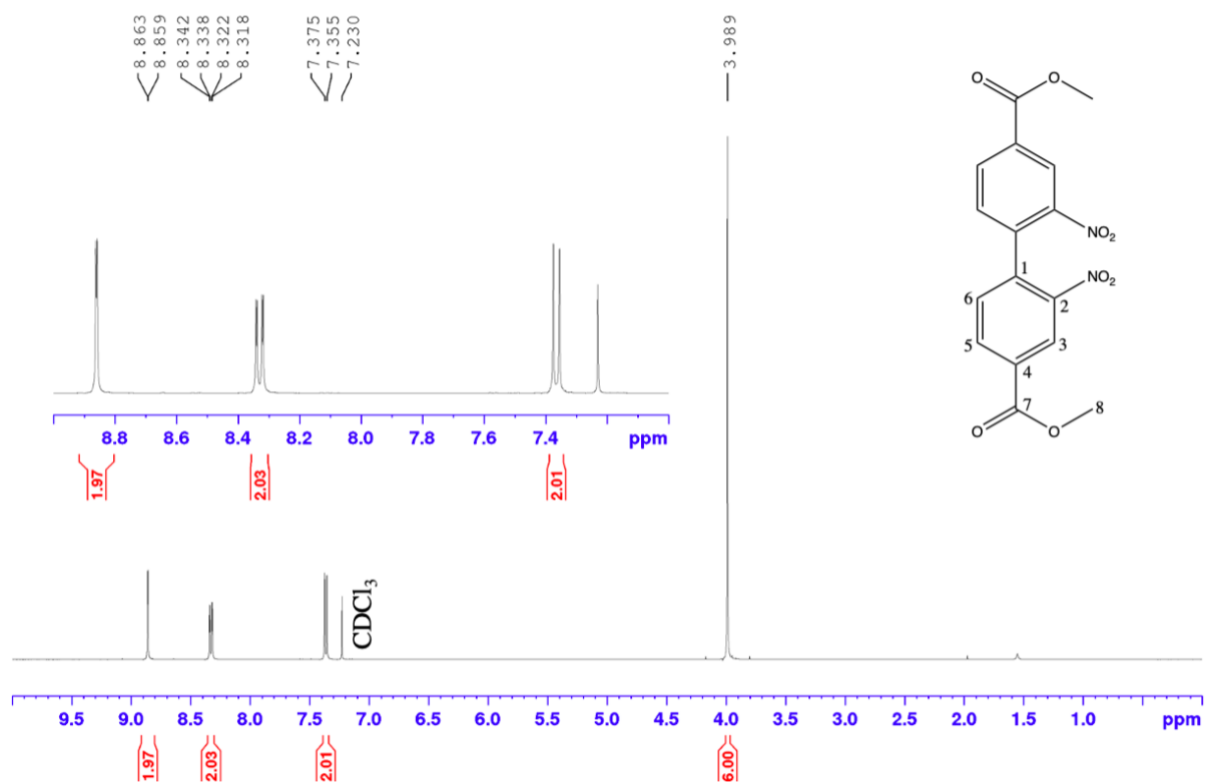


Figure 29: <sup>1</sup>H NMR (400 MHz, CDCl<sub>3</sub>) spectrum for compound **1**.

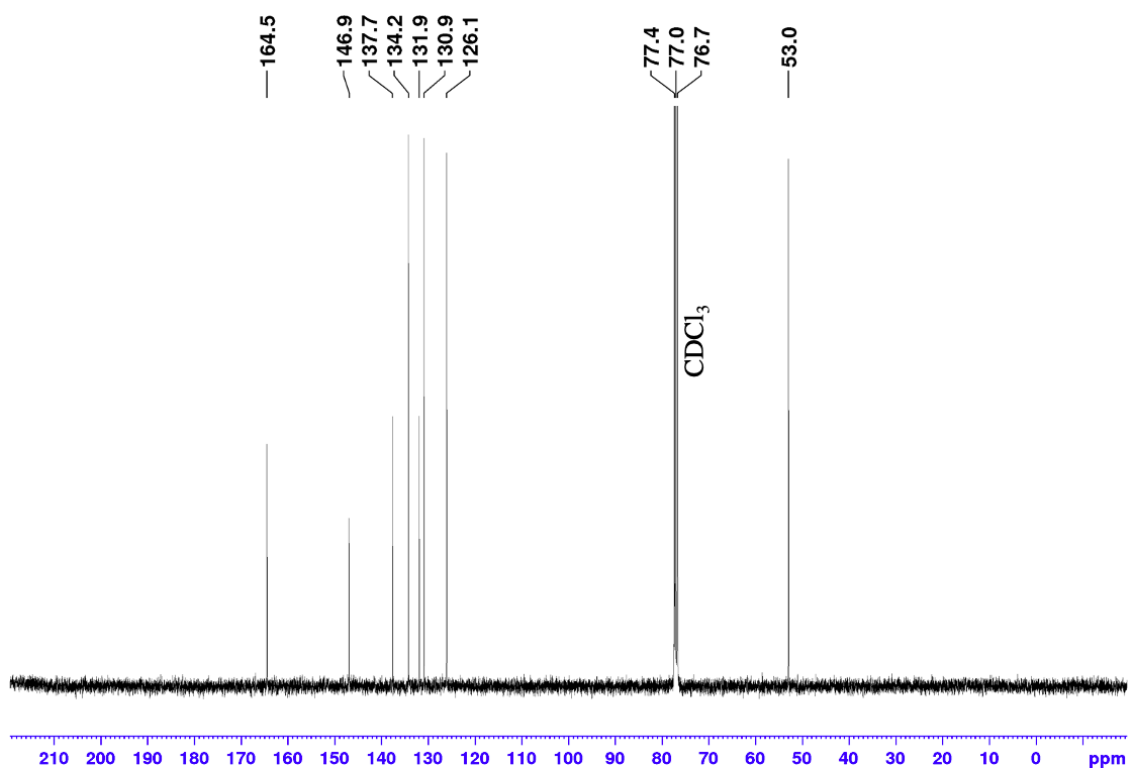


Figure 30:  $^{13}\text{C}$  NMR (400 MHz,  $\text{CDCl}_3$ ) spectrum for compound **1**.

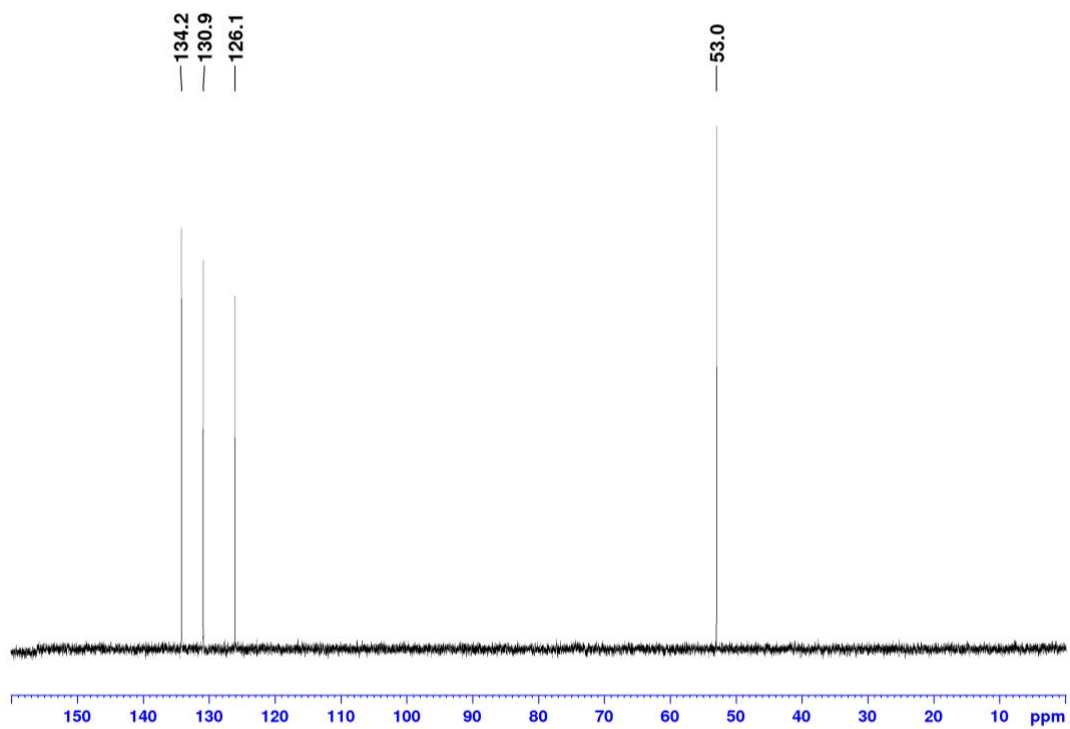


Figure 31: DEPT135 (400 MHz,  $\text{CDCl}_3$ ) spectrum of compound **1**, CH,  $\text{CH}_3$  phased positive and  $\text{CH}_2$  phased negative.

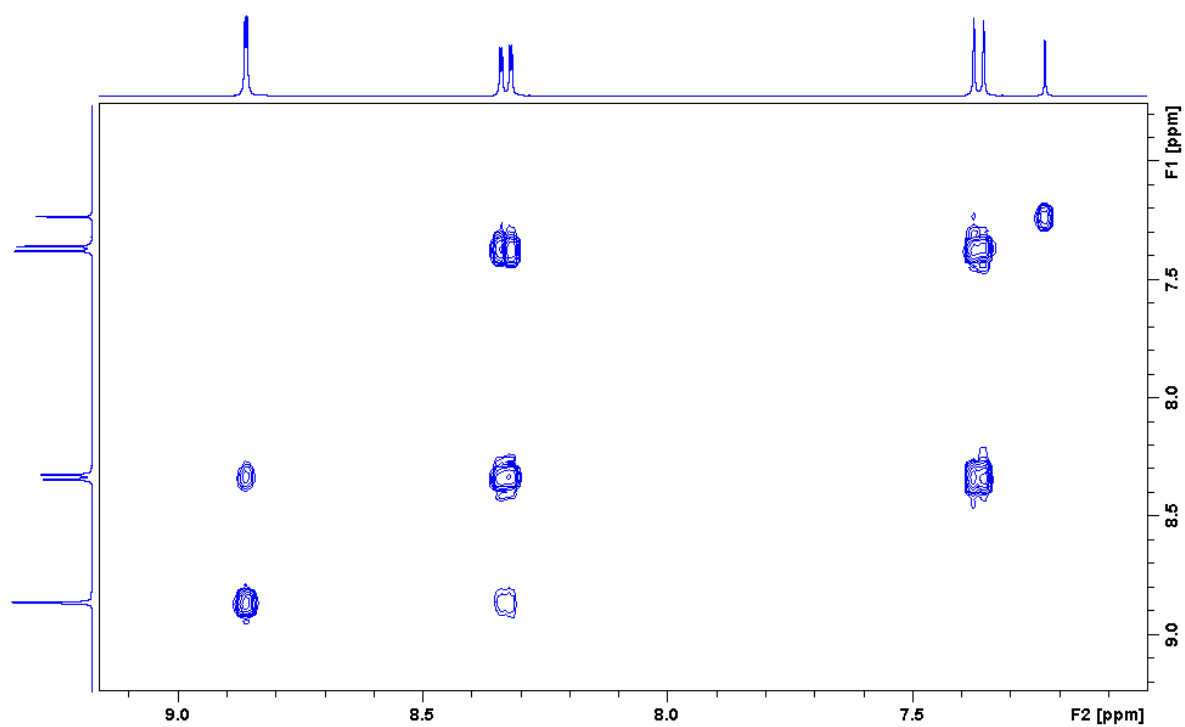


Figure 32: COSY (400 MHz, CDCl<sub>3</sub>) spectrum of compound **1** (zoomed in at aromatic region).

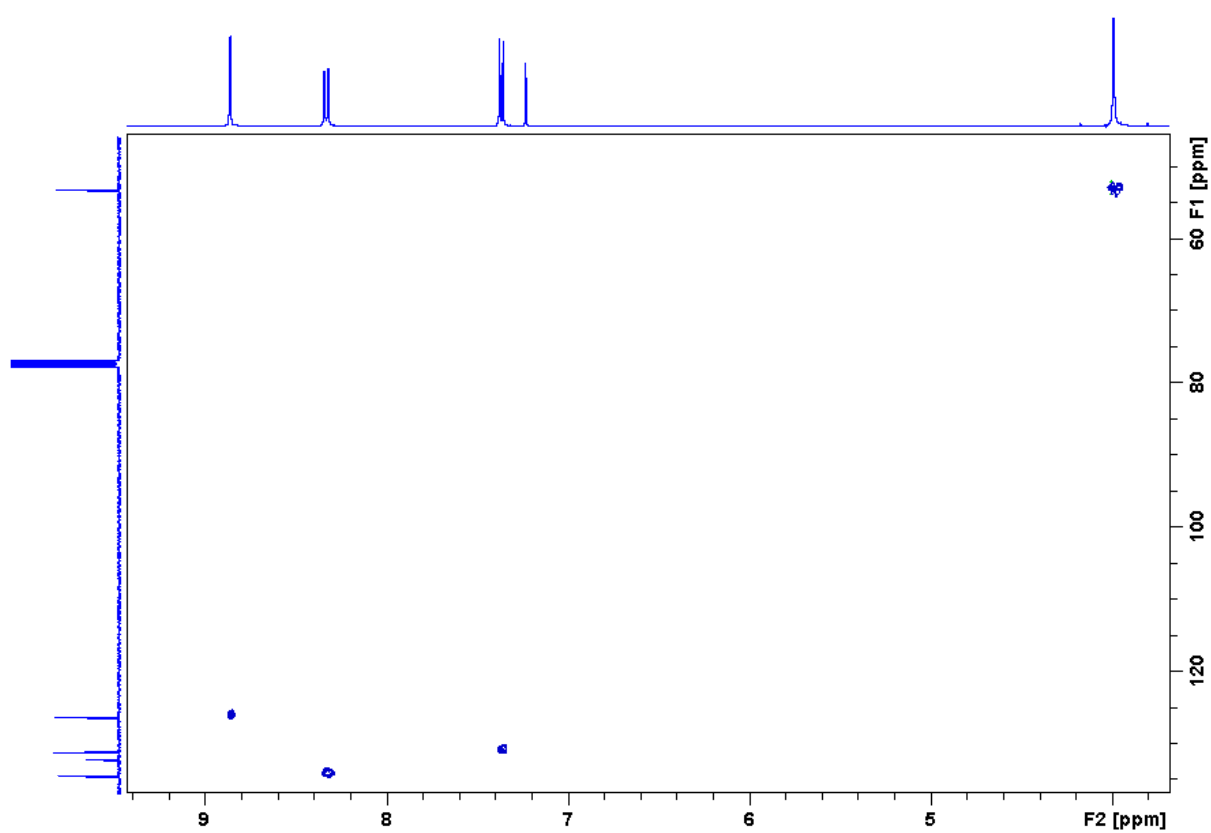


Figure 33: HSQC (400 MHz, CDCl<sub>3</sub>) spectrum of compound **1**.



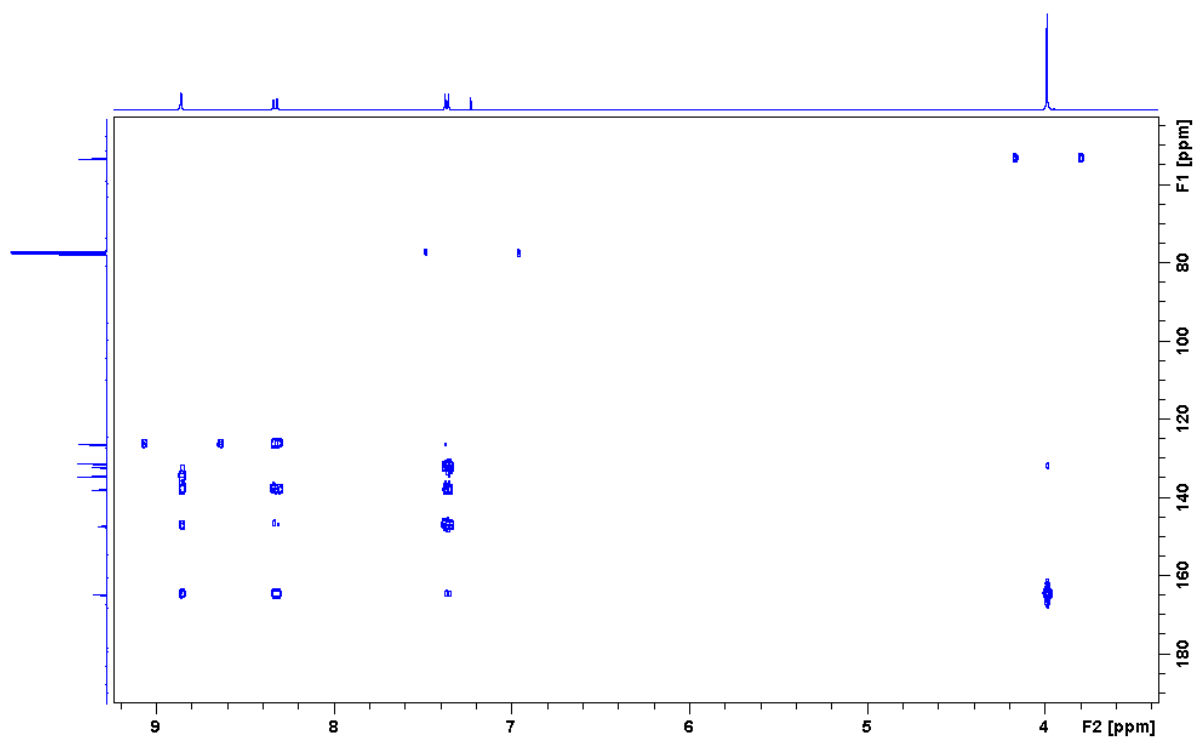


Figure 34: HMBC (400 MHz,  $\text{CDCl}_3$ ) spectrum of compound **1**.

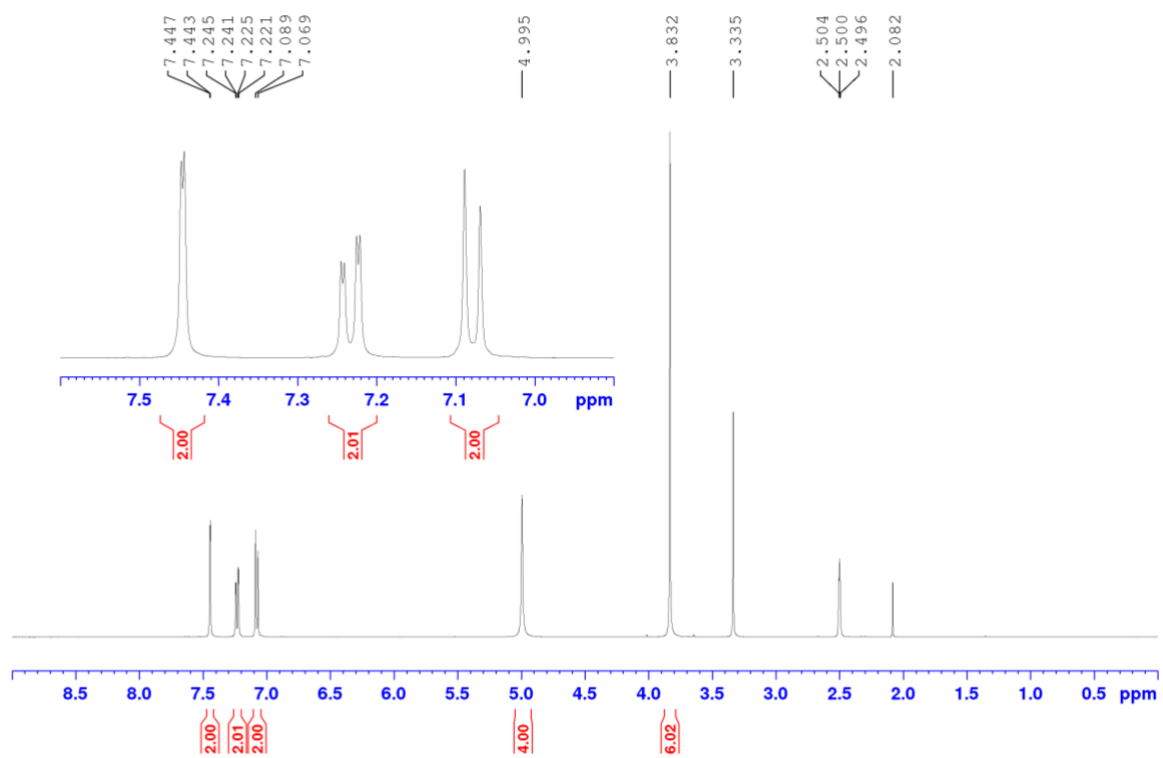


Figure 35:  $^1\text{H}$  NMR (400 MHz,  $\text{DMSO-d}_6$ ) spectrum for compound 2.

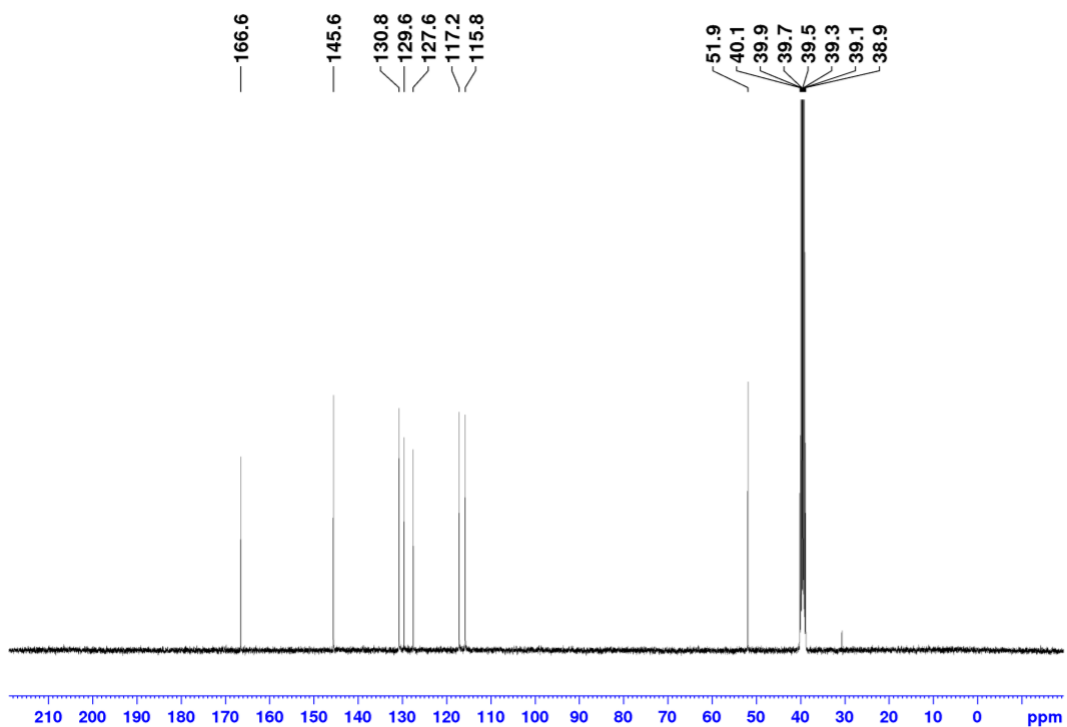


Figure 36:  $^{13}\text{C}$  NMR (400 MHz,  $\text{DMSO-d}_6$ ) spectrum of compound 2.

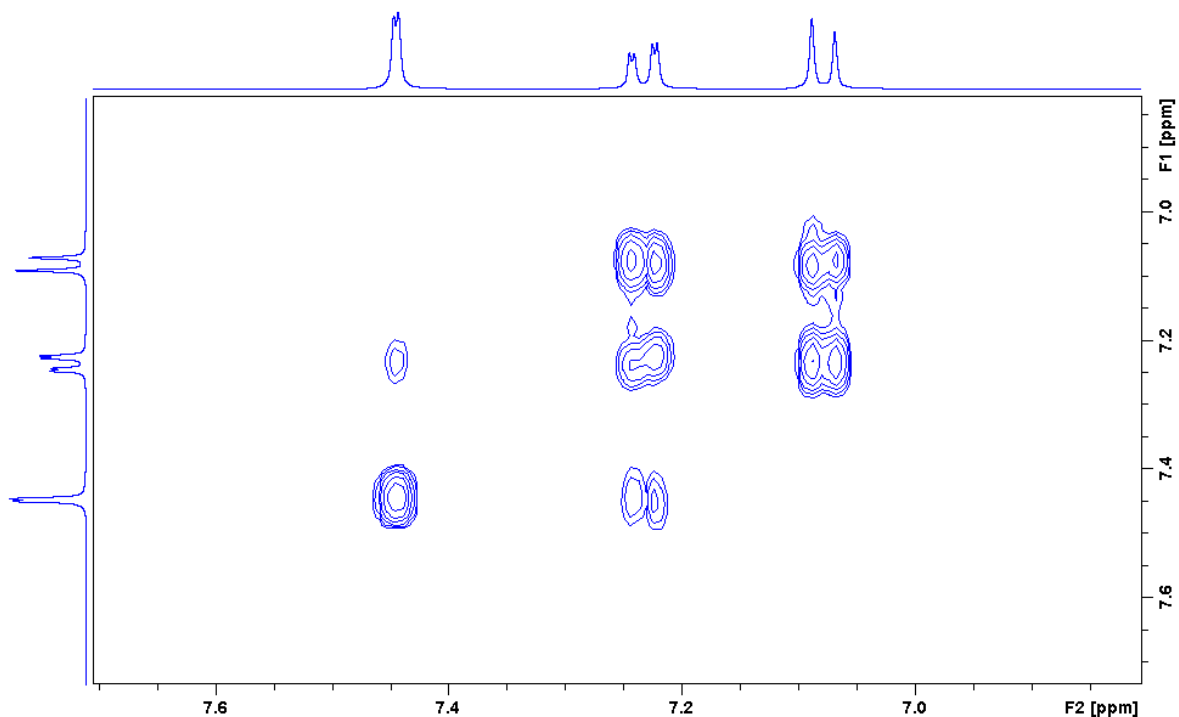


Figure 37: COSY (400 MHz, DMSO-d<sub>6</sub>) spectrum of compound **2** (zoomed at aromatic region).

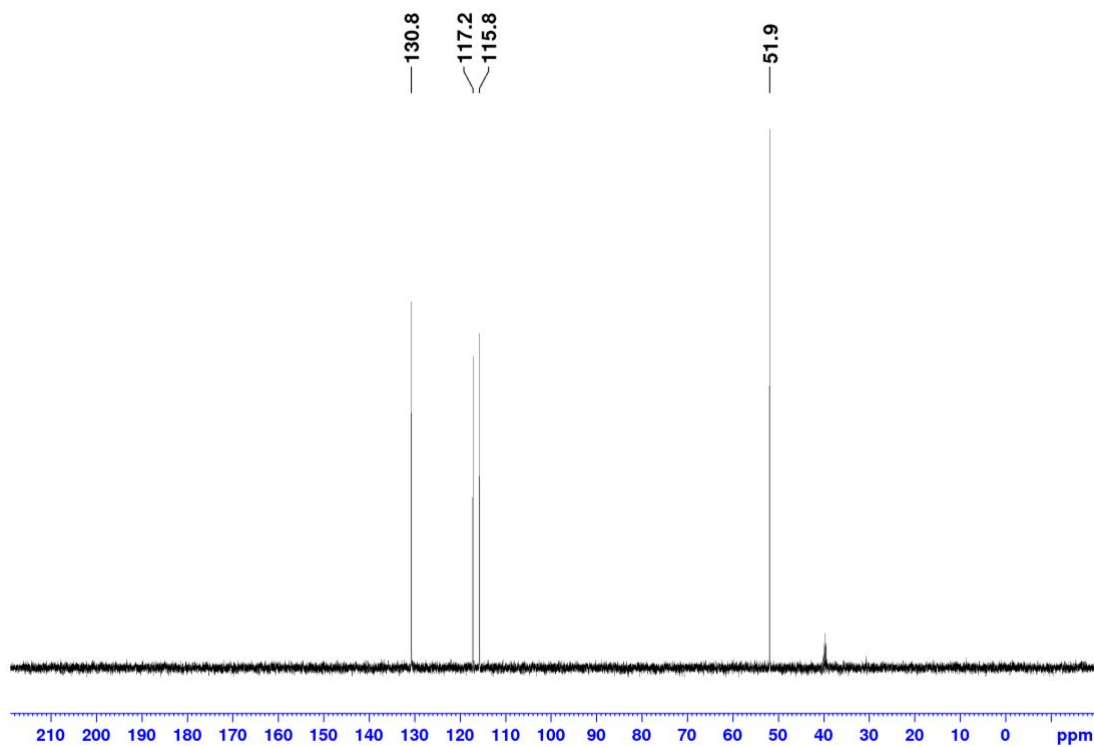


Figure 38: DEPT135 (400 MHz, DMSO-d<sub>6</sub>) spectrum of compound **2**, CH and CH<sub>3</sub> phased positive, and CH<sub>2</sub> phased negative.

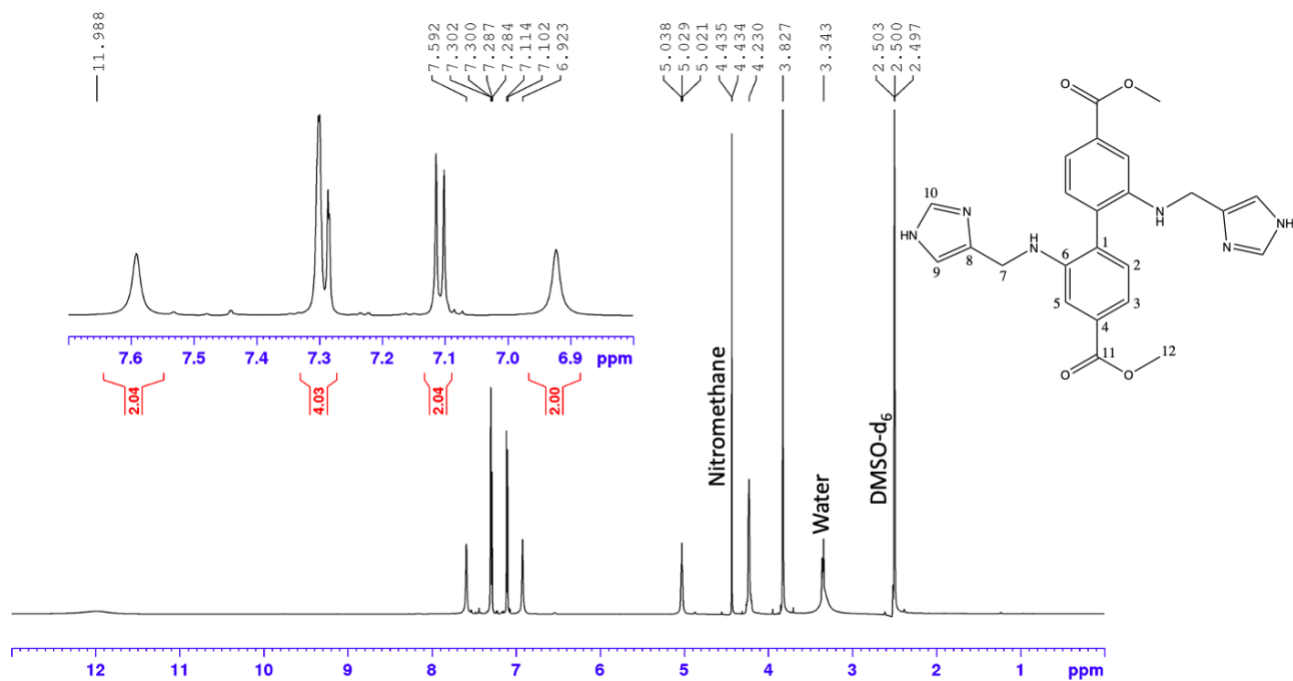


Figure 39:  $^1\text{H}$  NMR (600 MHz,  $\text{DMSO-d}_6$ ) spectrum for compound **3**.

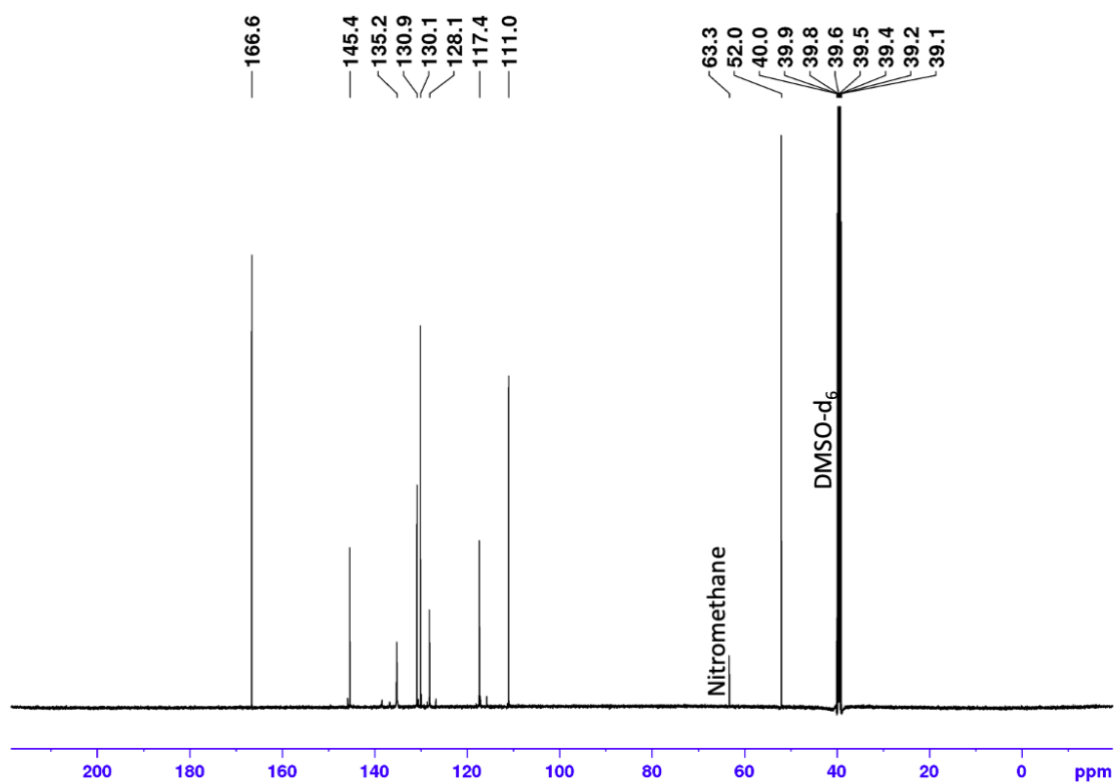


Figure 40:  $^{13}\text{C}$  NMR (600 MHz,  $\text{DMSO-d}_6$ ) spectrum of compound **3**.

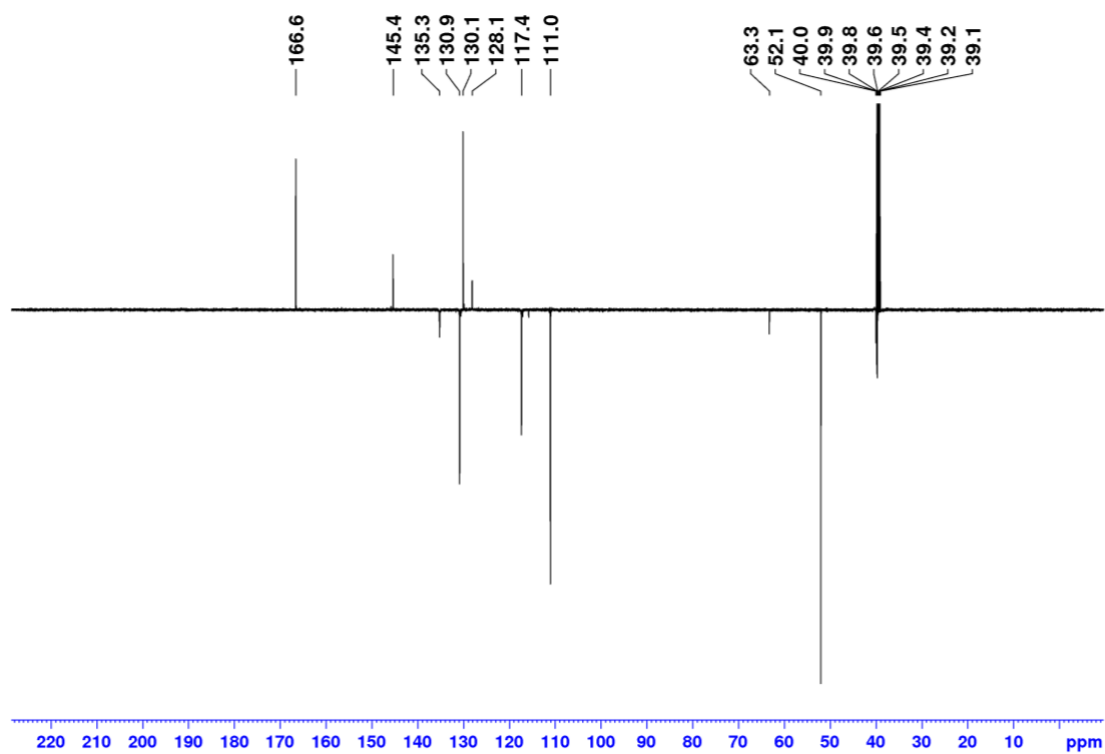


Figure 41: DEPT135Q (600 MHz, DMSO- $d_6$ ) NMR spectrum of compound **3**, CH, CH<sub>3</sub> and CH<sub>2</sub> negative, and C positive.

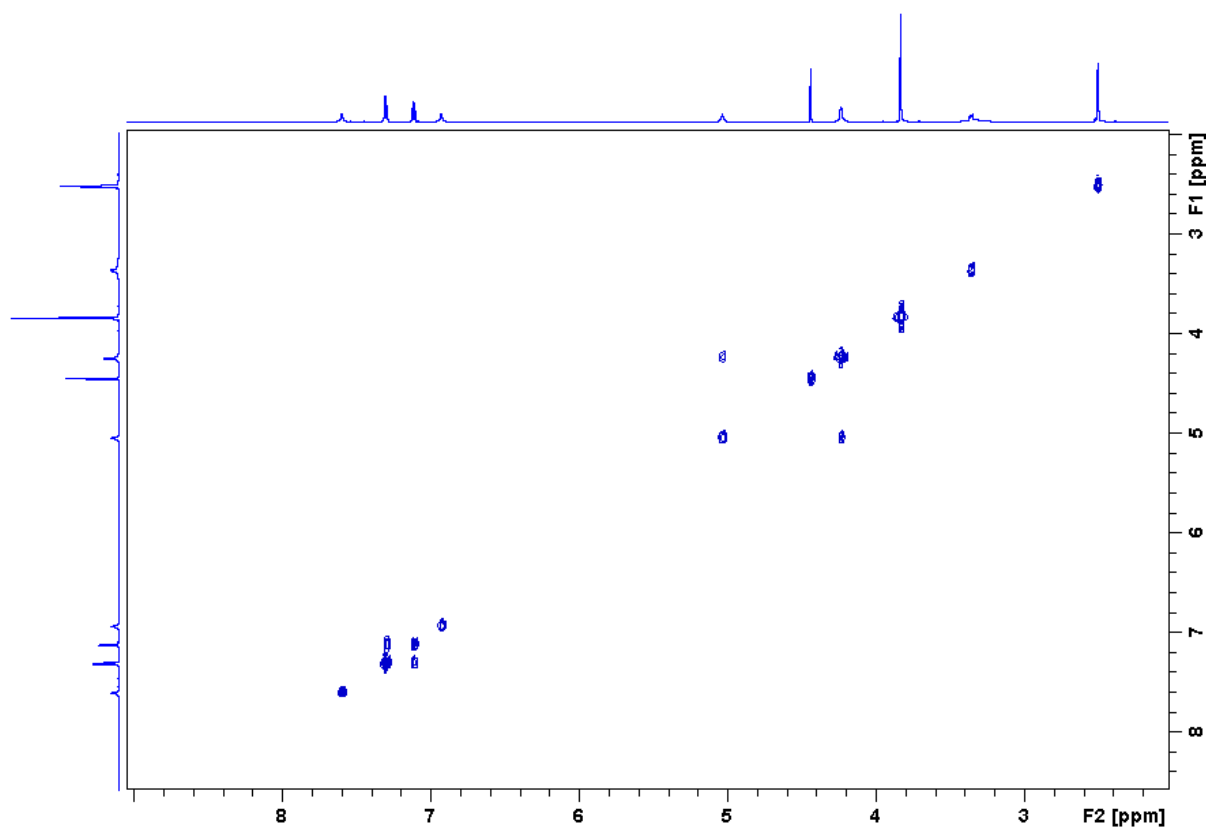


Figure 42: COSY (600 MHz, DMSO- $d_6$ ) spectrum of compound **3**.

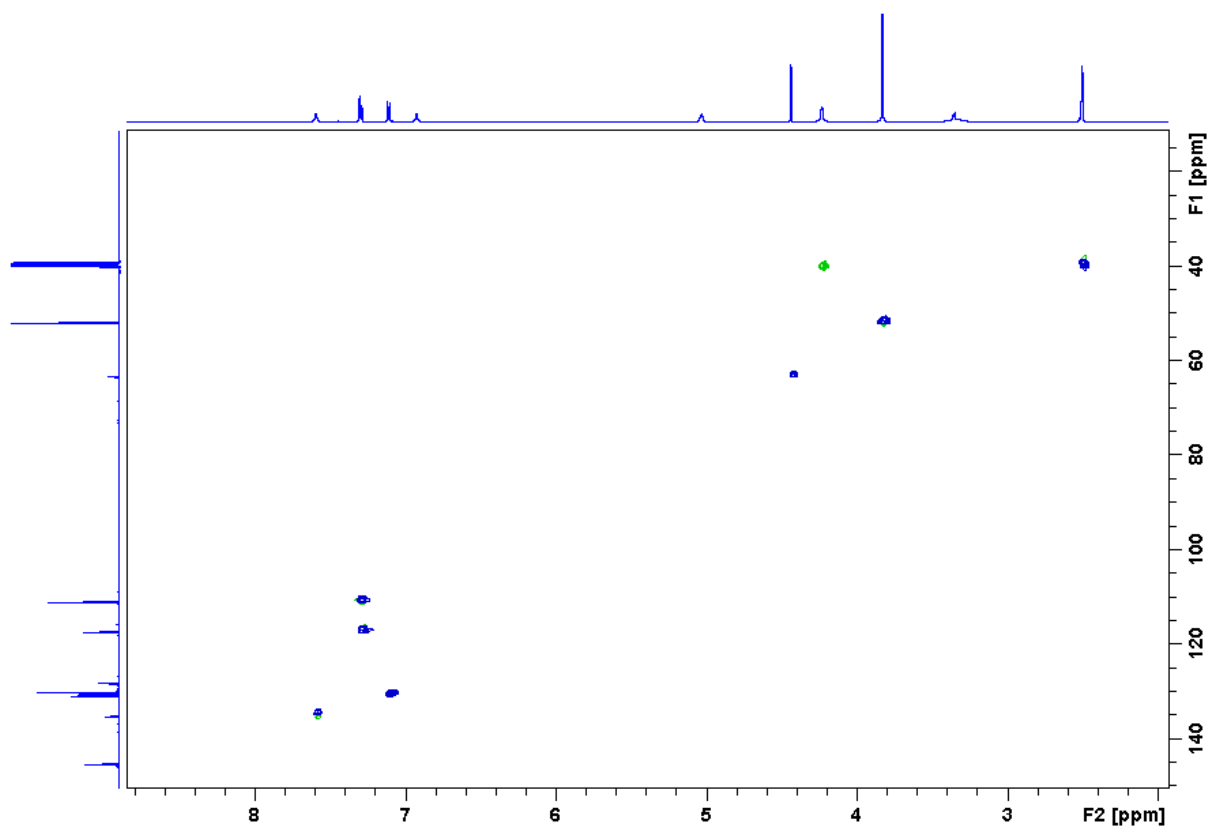


Figure 43: HSQC (600 MHz, DMSO-d<sub>6</sub>) spectrum of compound **3**.

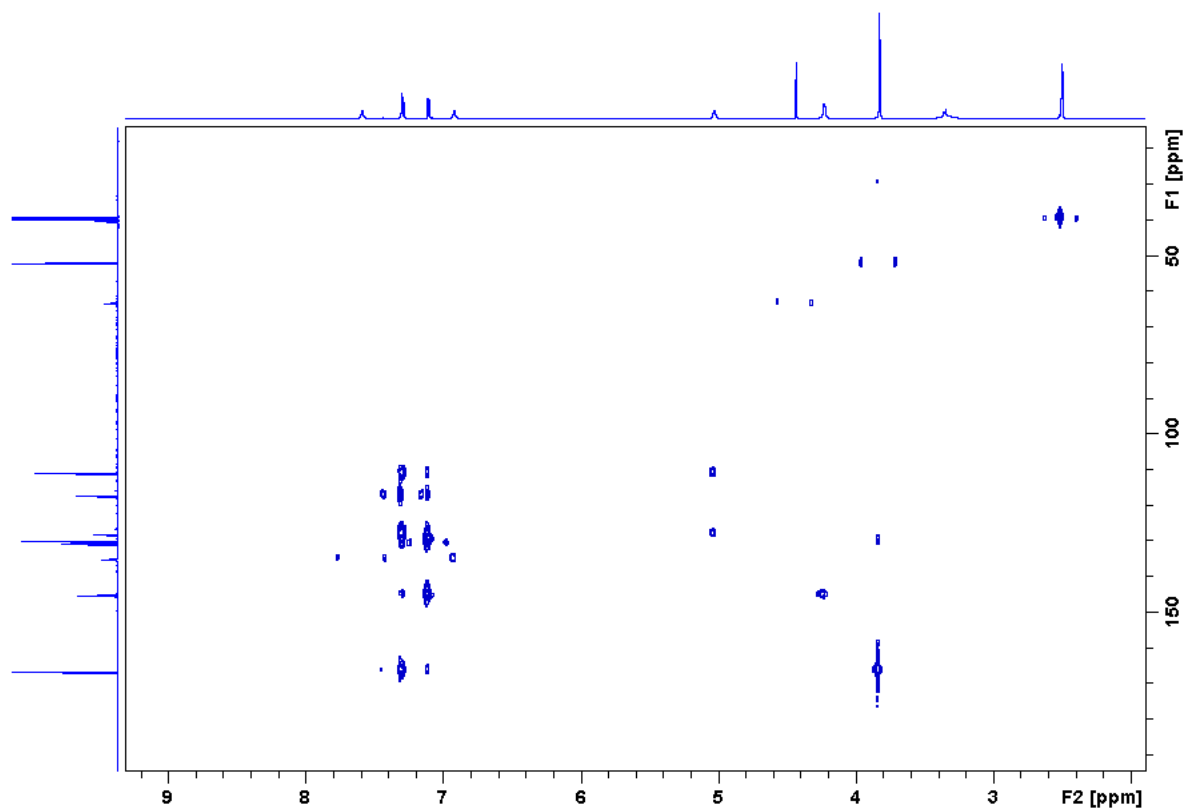


Figure 44: HMBC (600 MHz, DMSO-d<sub>6</sub>) spectrum of compound **3**.

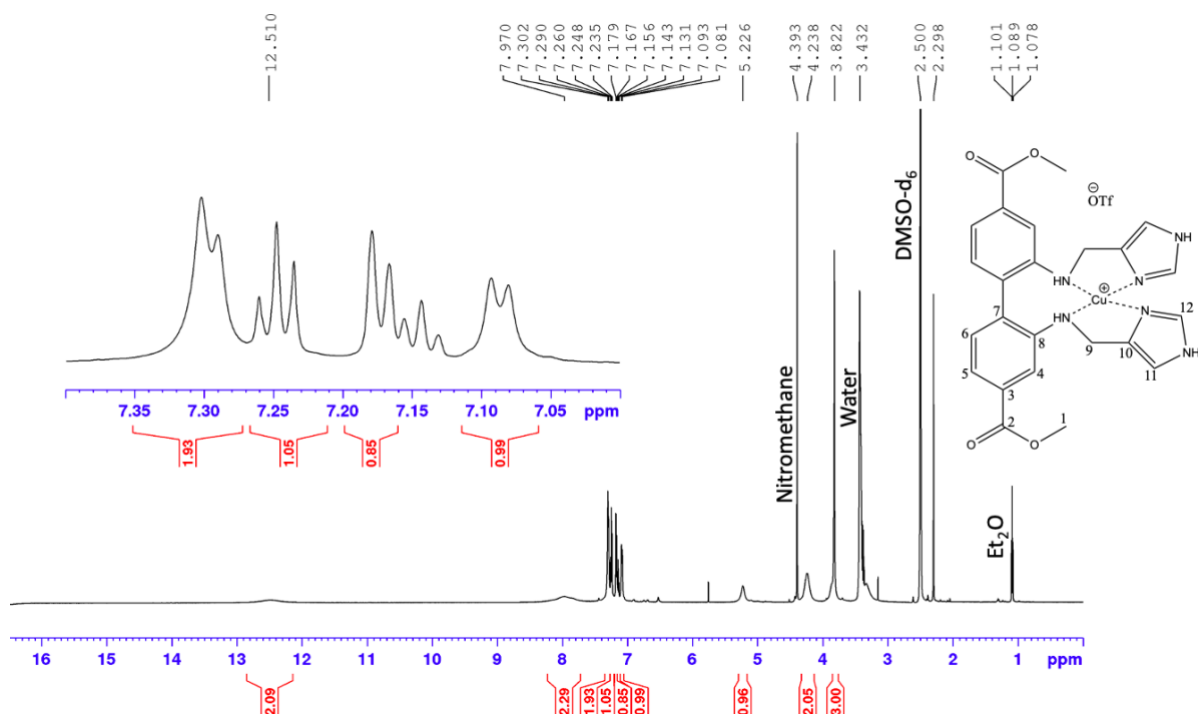


Figure 45: <sup>1</sup>H NMR (600 MHz, DMSO-d<sub>6</sub>) spectrum of compound 4 with nitromethane and hexafluorobenzene as external standards.

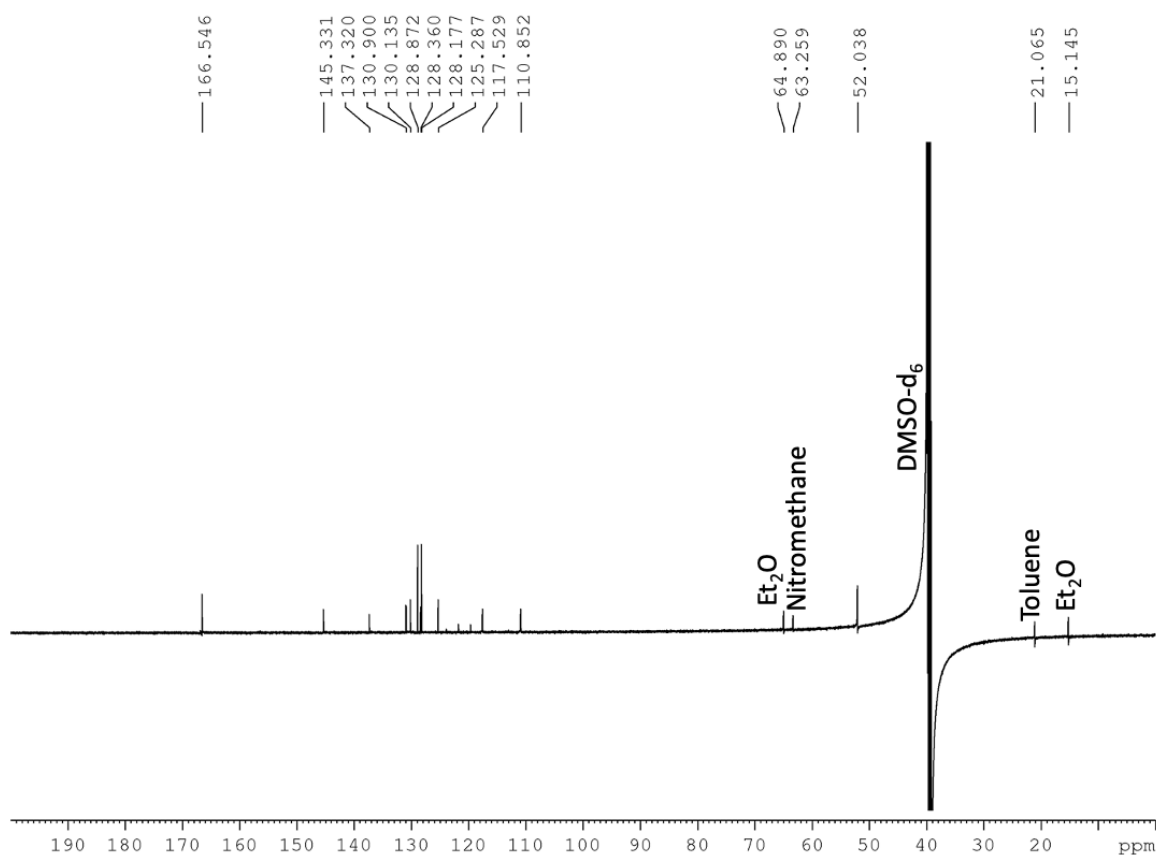


Figure 46: <sup>13</sup>C NMR (600 MHz, DMSO-d<sub>6</sub>) spectrum of compound 4 with nitromethane and hexafluorobenzene as external standards.

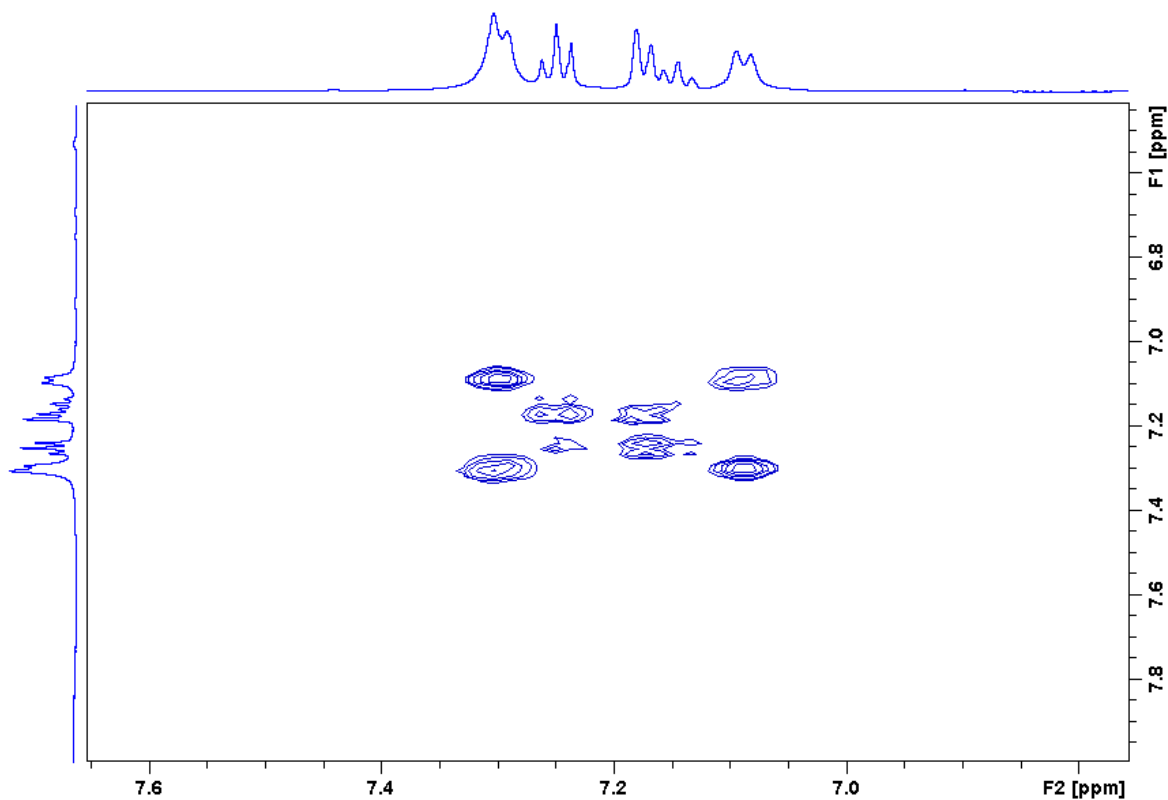


Figure 47: COSY (600 MHz, DMSO-d<sub>6</sub>) spectrum of compound **4** (zoomed at aromatic region).

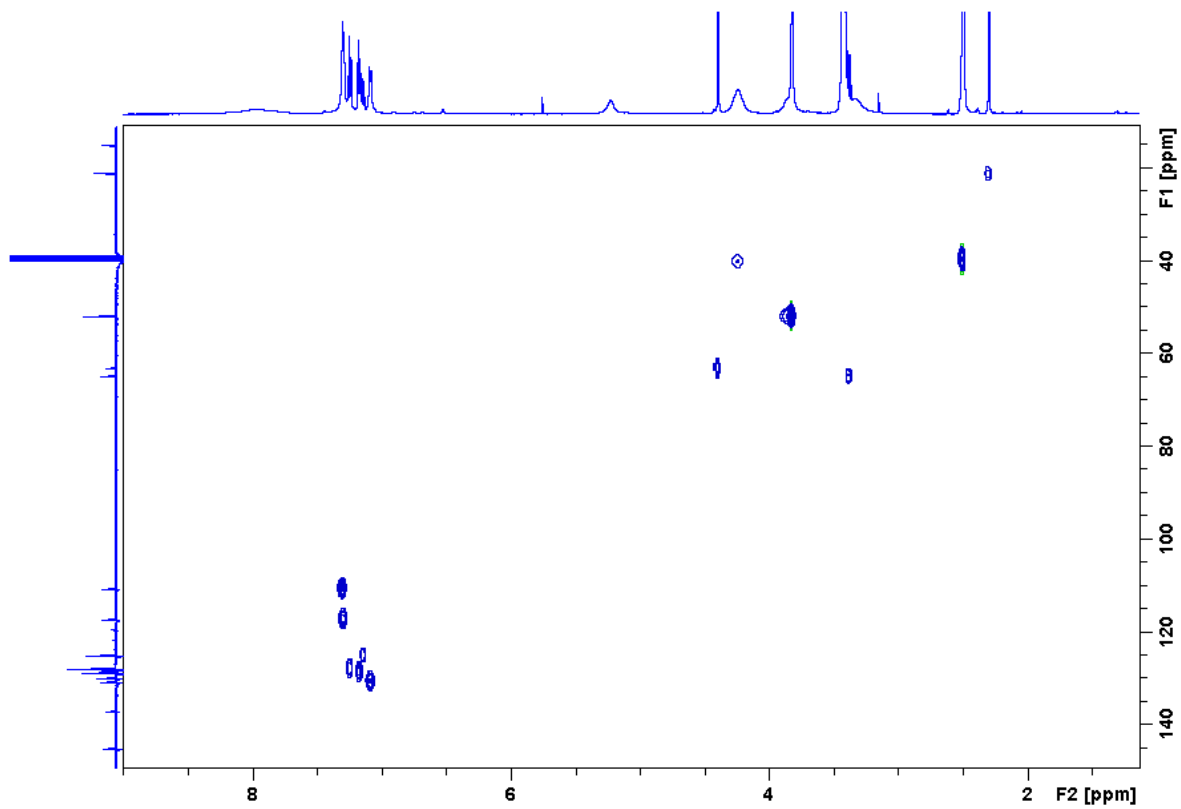


Figure 48: HSQC (600 MHz, DMSO-d<sub>6</sub>) spectrum of compound **4**.



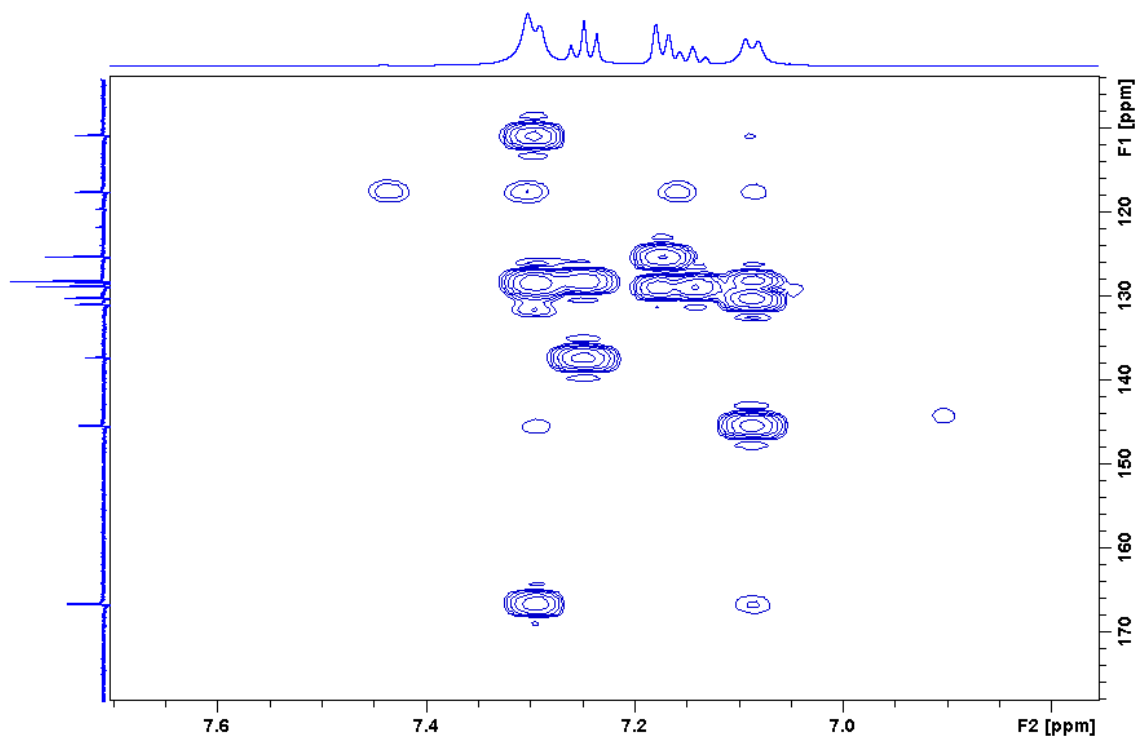


Figure 49: HMBC (600 MHz, DMSO- $d_6$ ) spectrum of compound **4** (zoomed at aromatic region).

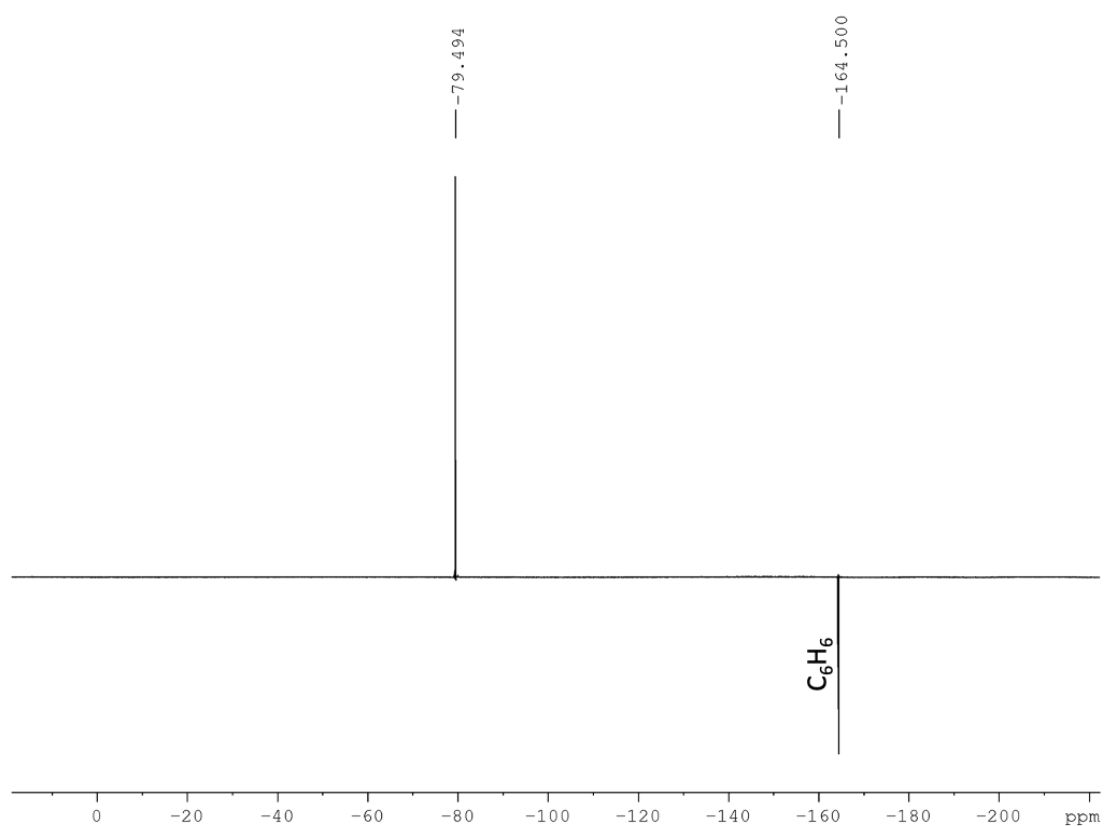


Figure 50:  $^{19}\text{F}$  NMR (400 MHz, DMSO- $d_6$ ) spectrum of compound **4** with hexafluorobenzene as external standard.

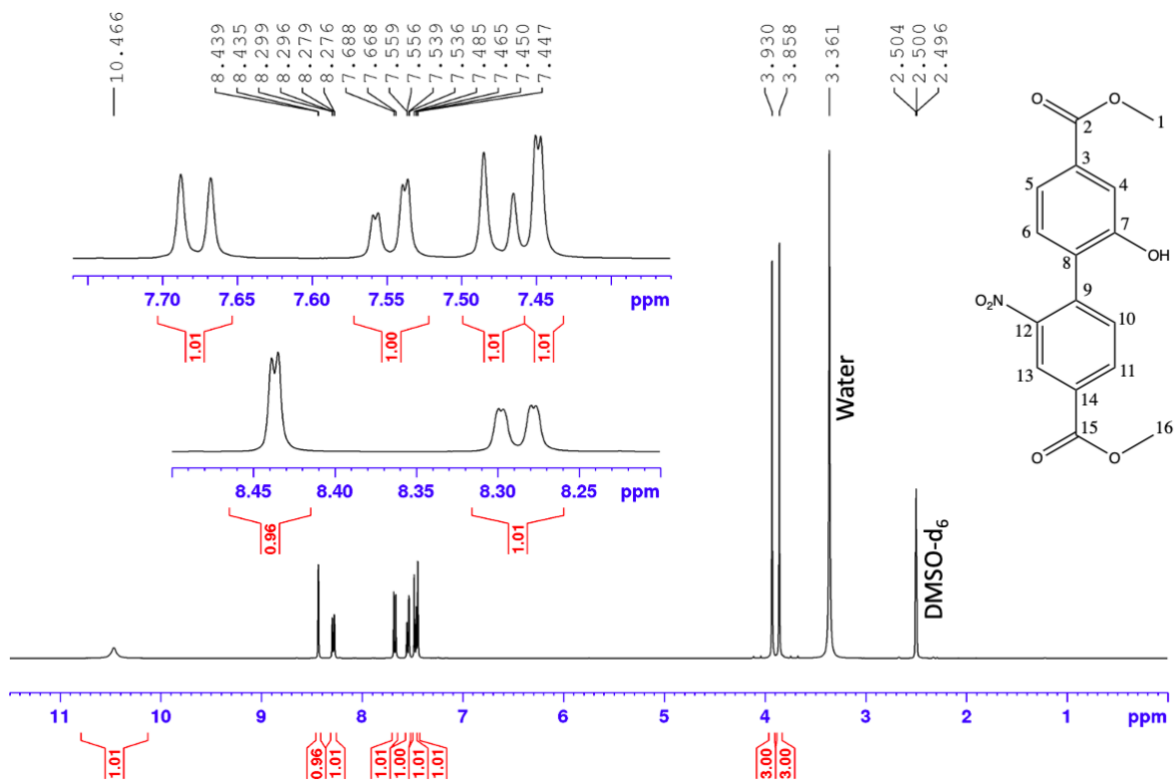


Figure 51: <sup>1</sup>H NMR (400 MHz, DMSO-d<sub>6</sub>) spectrum of compound 6.

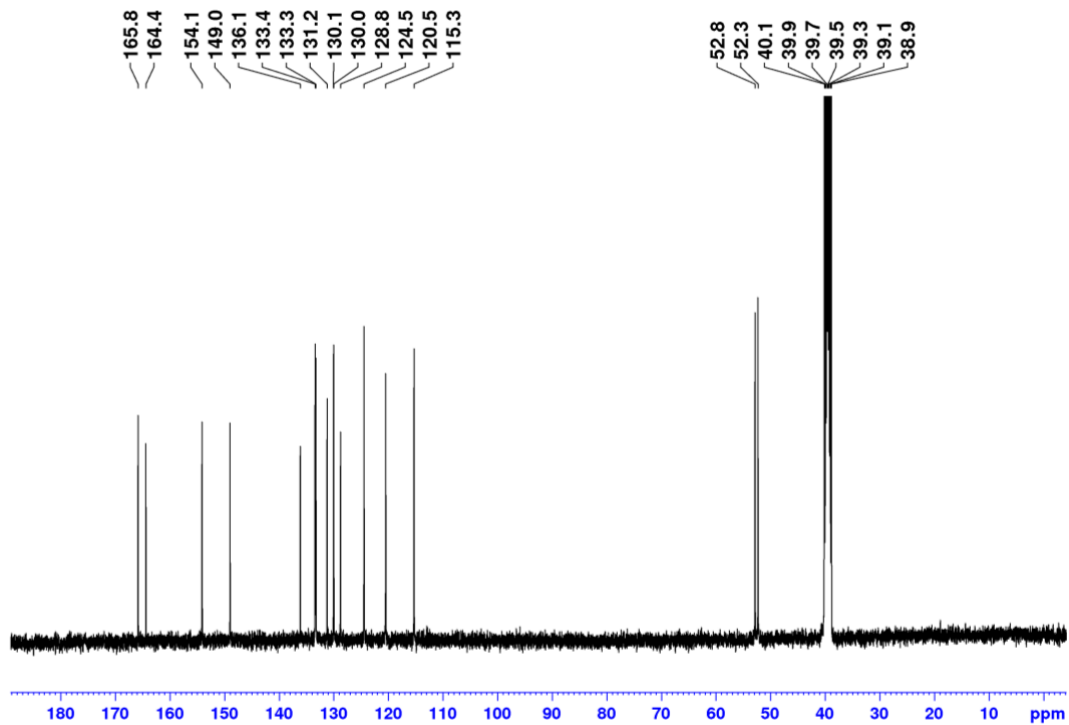


Figure 52: <sup>13</sup>C NMR (400 MHz, DMSO-d<sub>6</sub>) spectrum of compound 6.

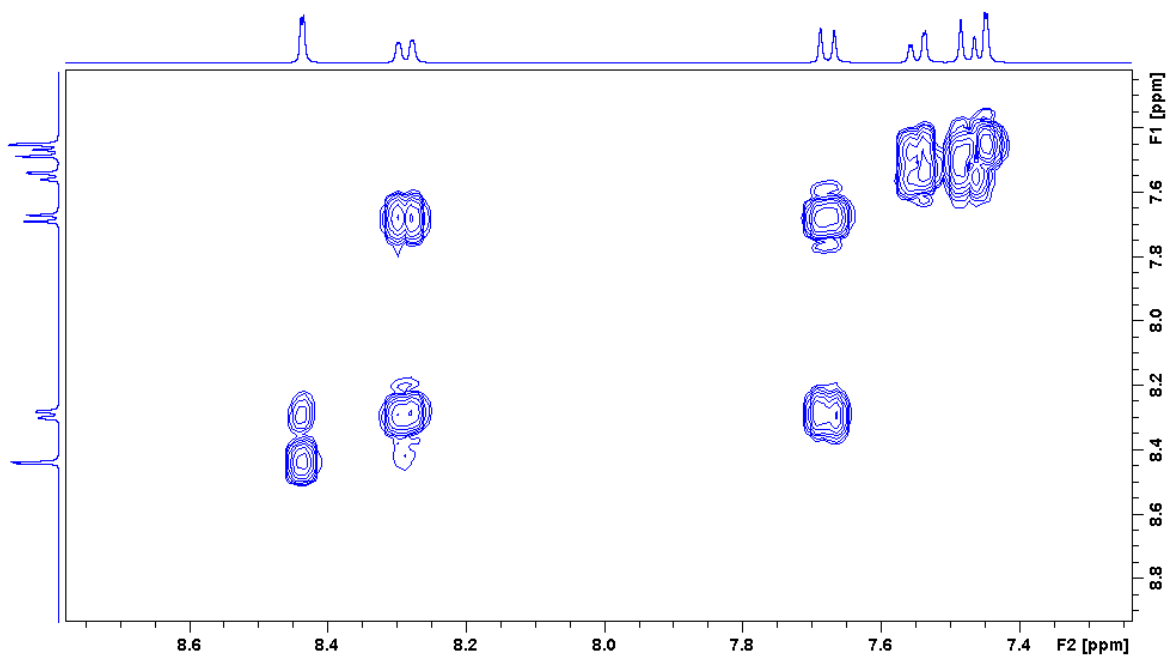


Figure 53: COSY (400 MHz, DMSO-d<sub>6</sub>) spectrum of compound **6** (zoomed at aromatic region).

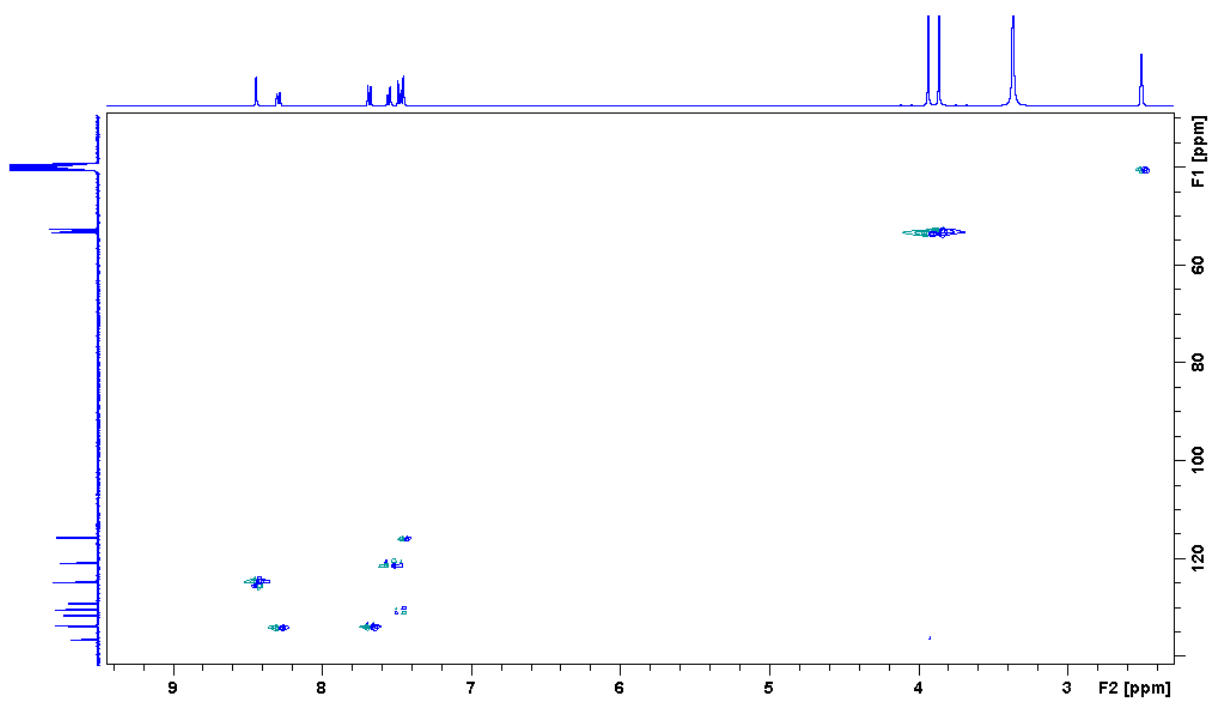


Figure 54: HSQC (400 MHz, DMSO-d<sub>6</sub>) spectrum of compound **6**.

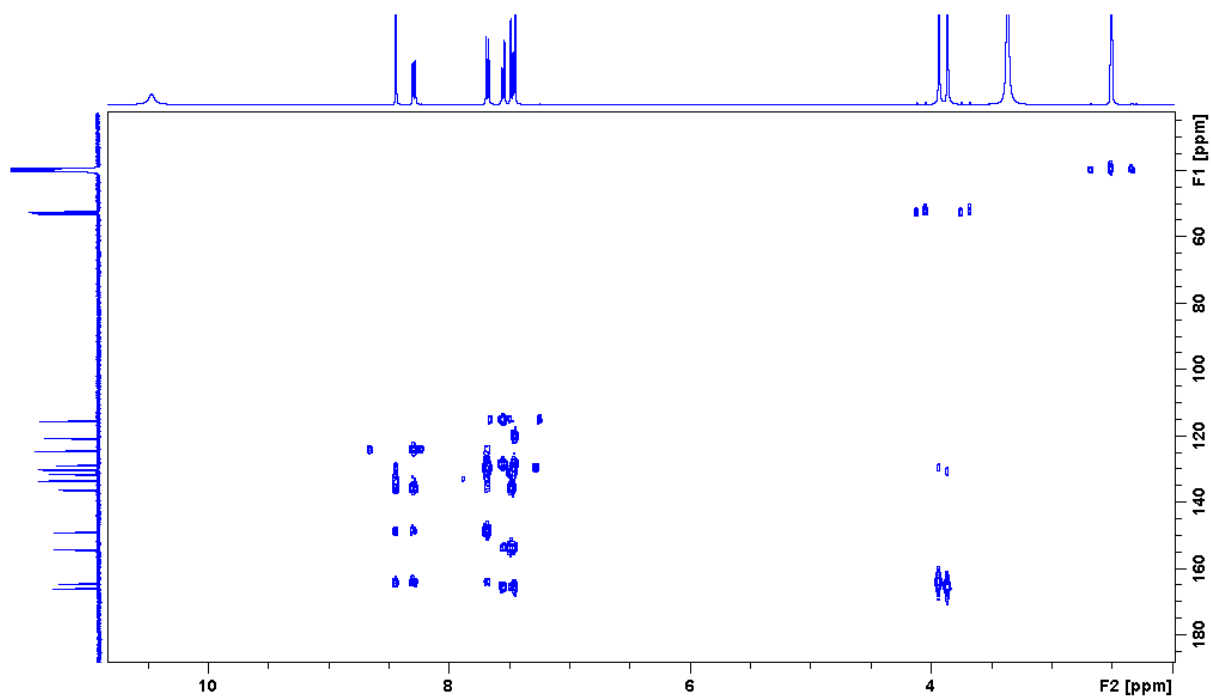


Figure 55: HMBC (400 MHz, DMSO- $d_6$ ) spectrum of compound **6**.

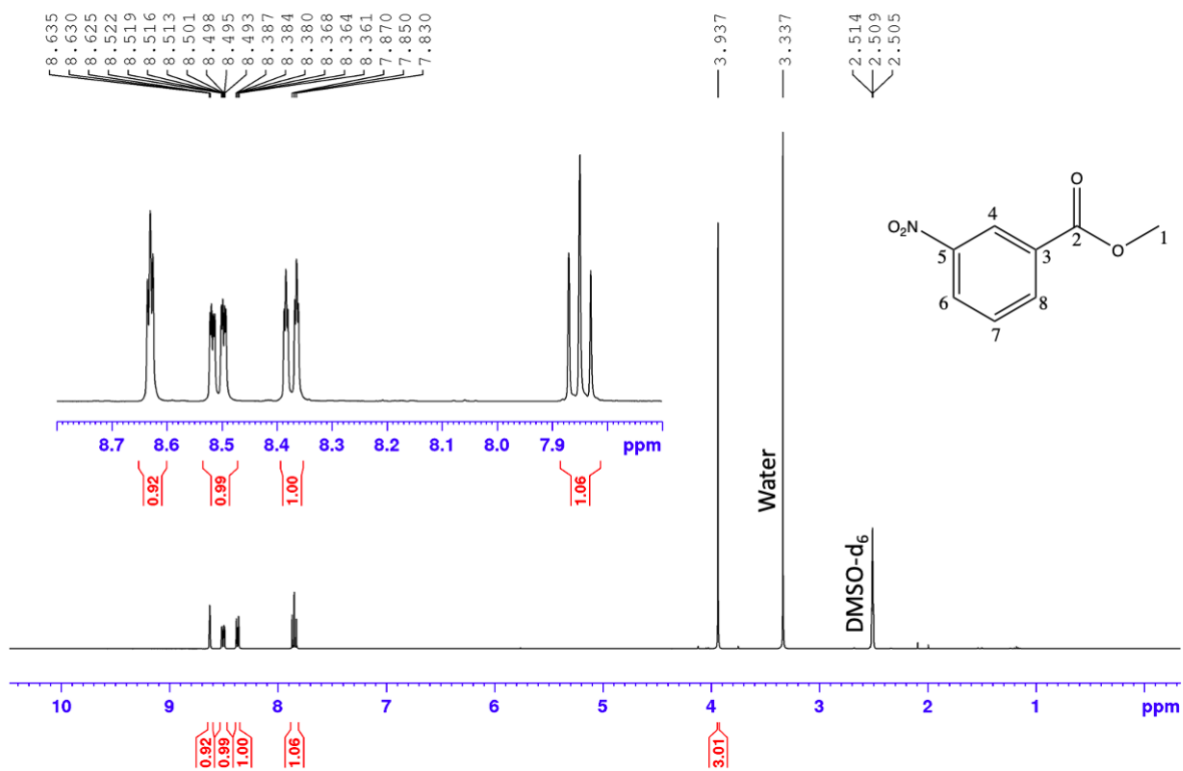


Figure 56: <sup>1</sup>H NMR (400 MHz, DMSO-d<sub>6</sub>) spectrum of compound **6a**.

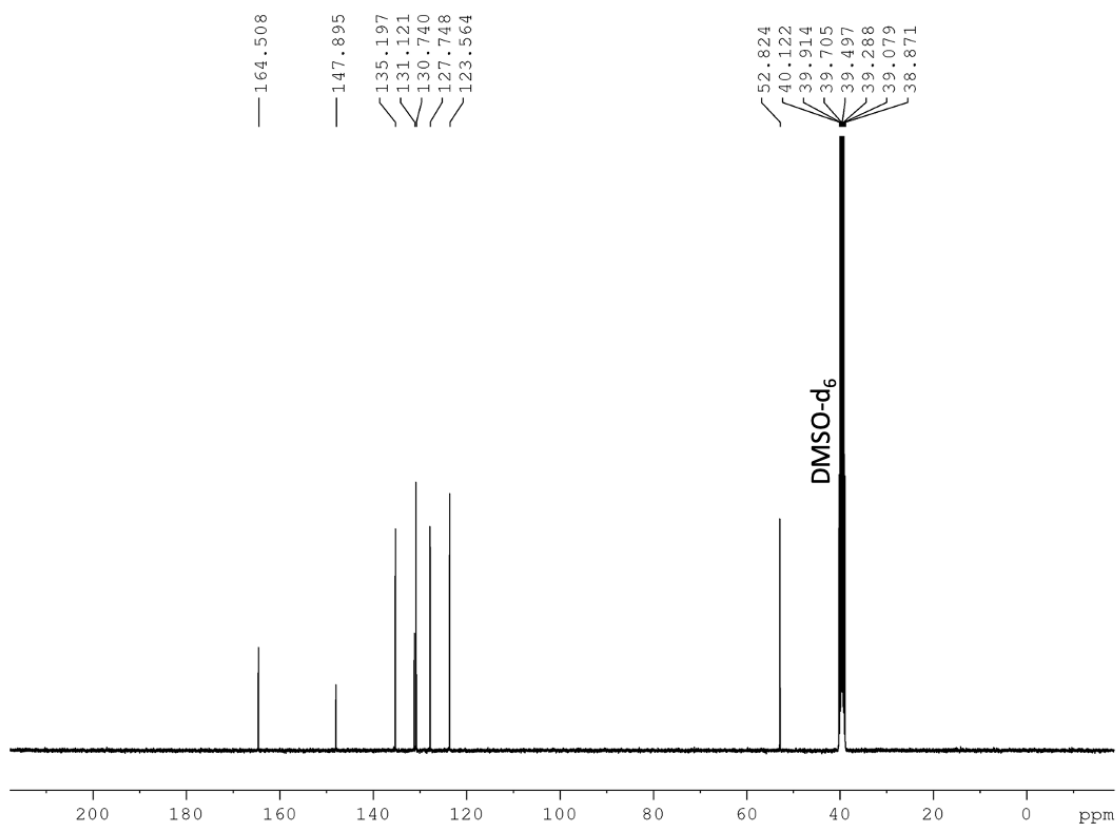


Figure 57: <sup>13</sup>C NMR (400 MHz, DMSO-d<sub>6</sub>) spectrum of compound **6a**.

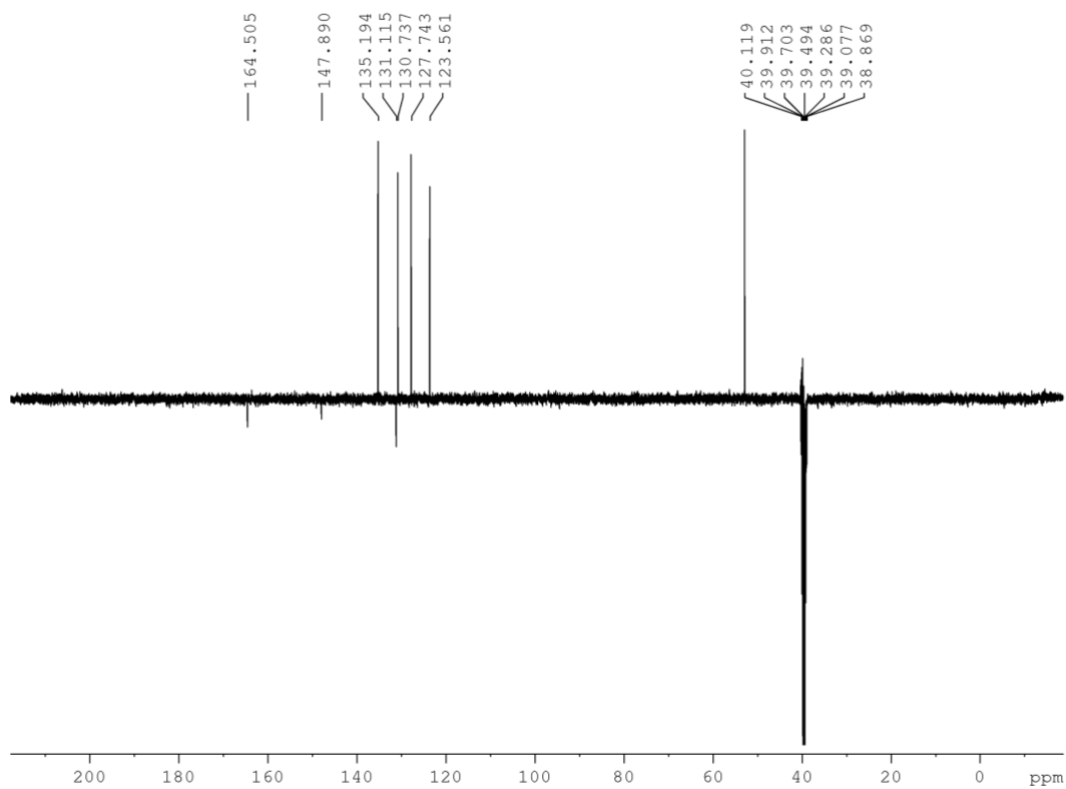


Figure 58: DEPT135Q (400 MHz, DMSO-d<sub>6</sub>) NMR spectrum of compound **6a**, CH<sub>3</sub> and CH phased positive, and C phased negative.

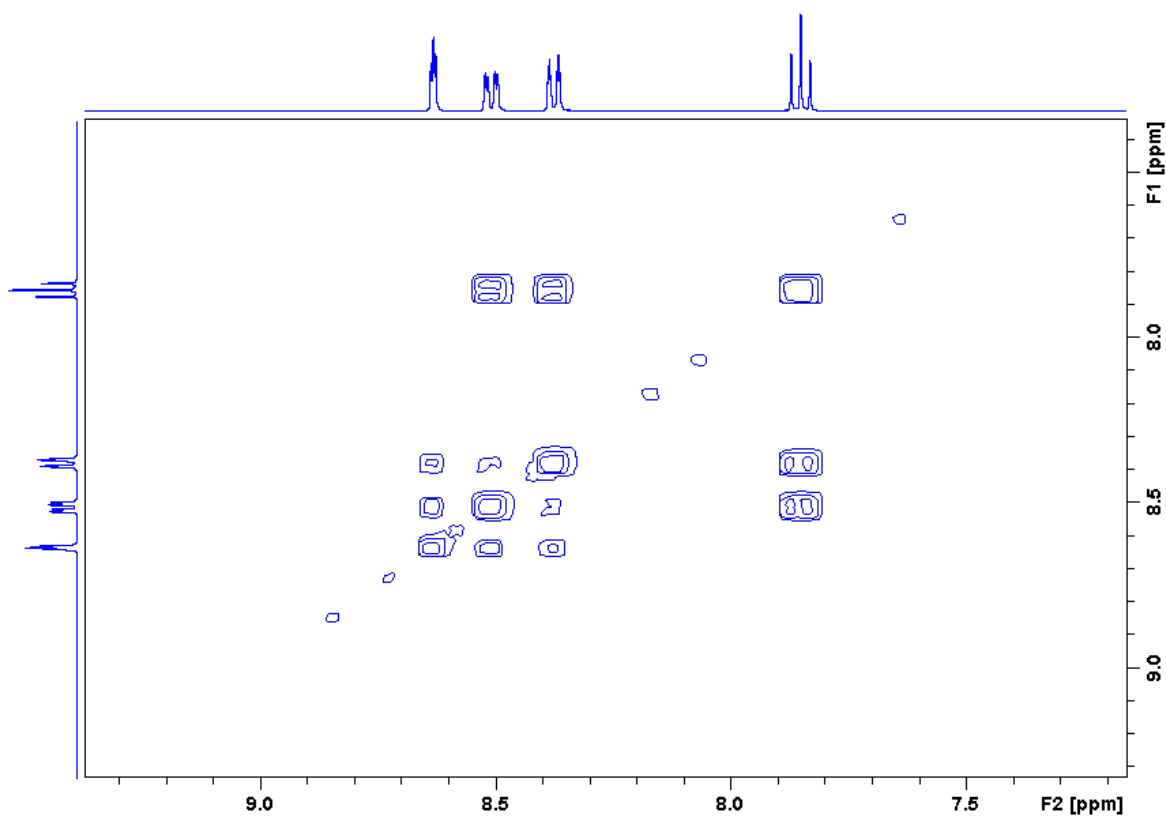


Figure 59: COSY (400 MHz, DMSO-d<sub>6</sub>) spectrum of compound **6a** (zoomed at aromatic region).

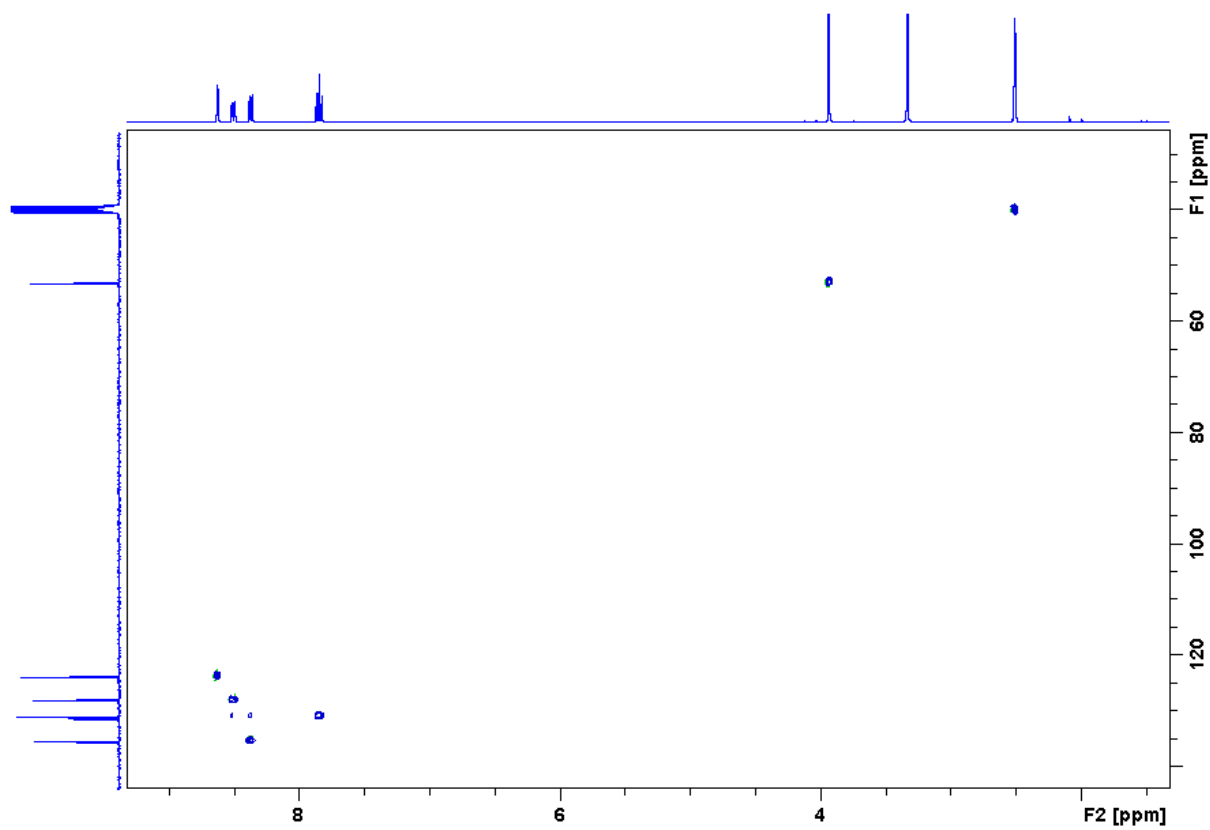


Figure 60: HSQC (400 MHz, DMSO-d<sub>6</sub>) spectrum of compound **6a**.

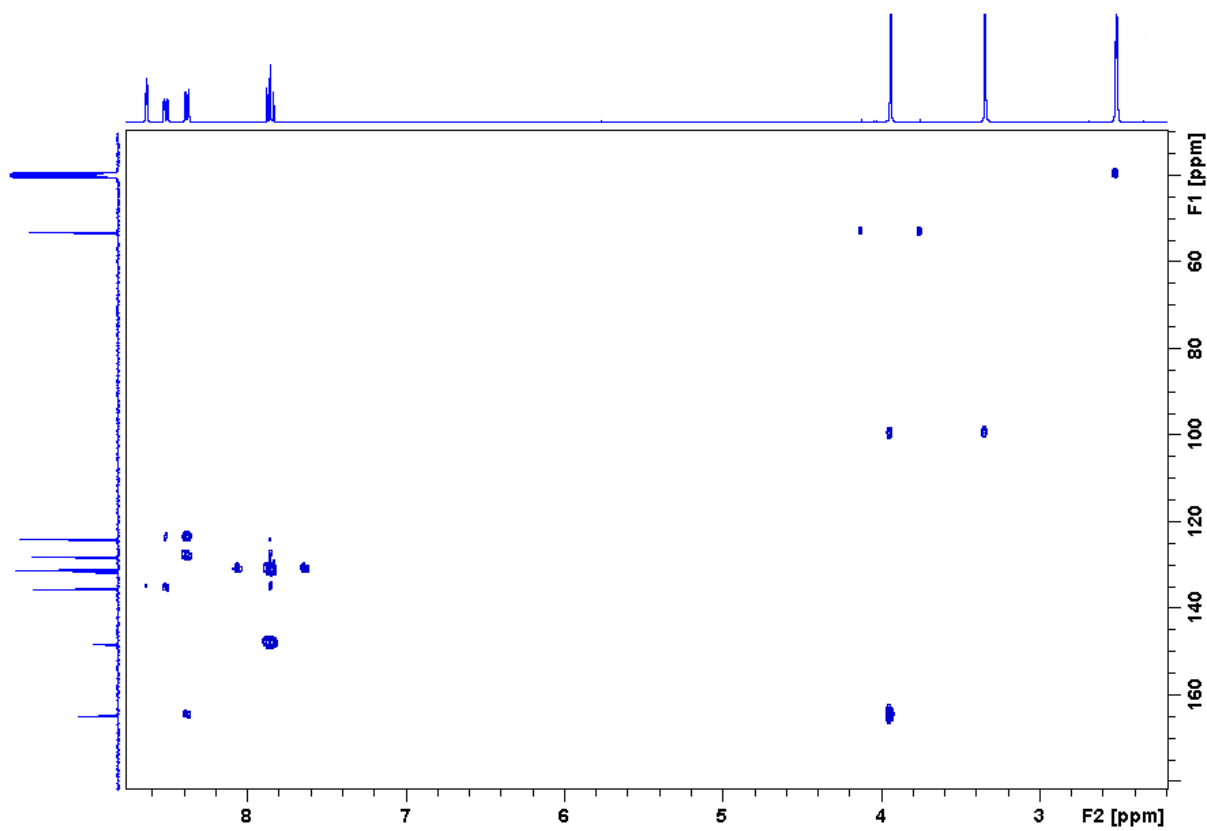


Figure 61: HMBC (400 MHz, DMSO-d<sub>6</sub>) spectrum of compound **6a**.

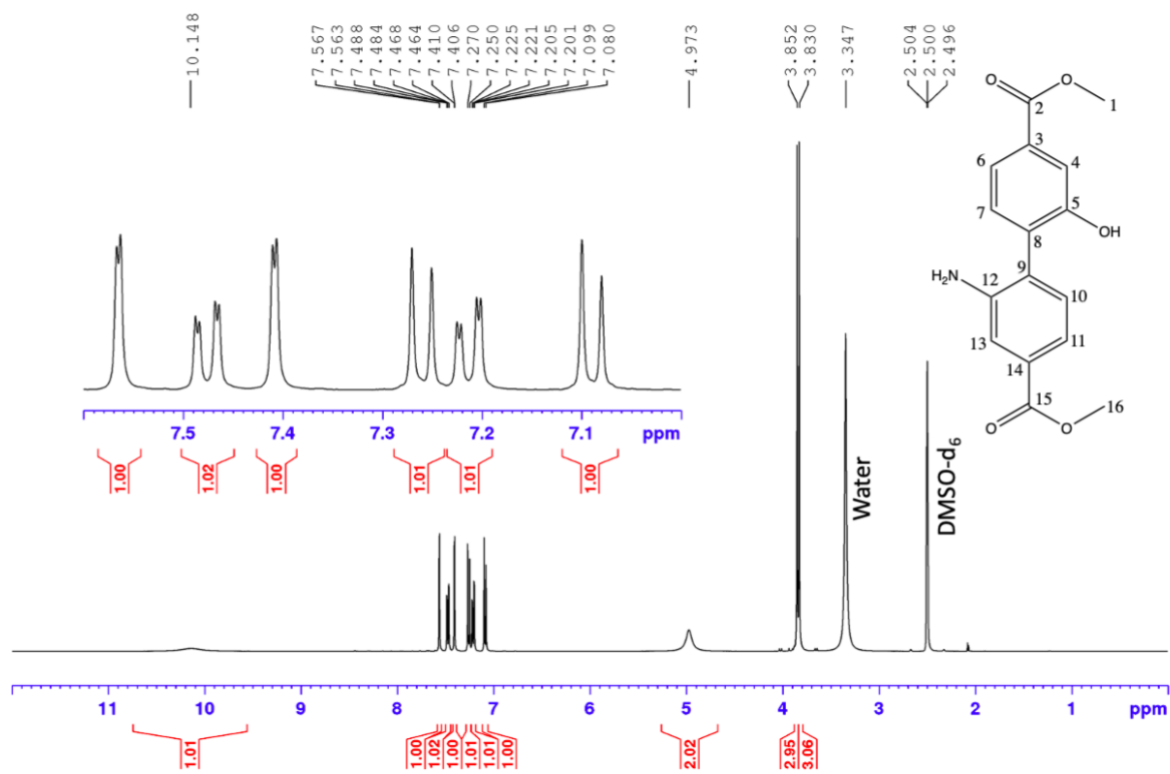


Figure 62: <sup>1</sup>H NMR (400 MHz, DMSO-d<sub>6</sub>) spectrum of compound 7.

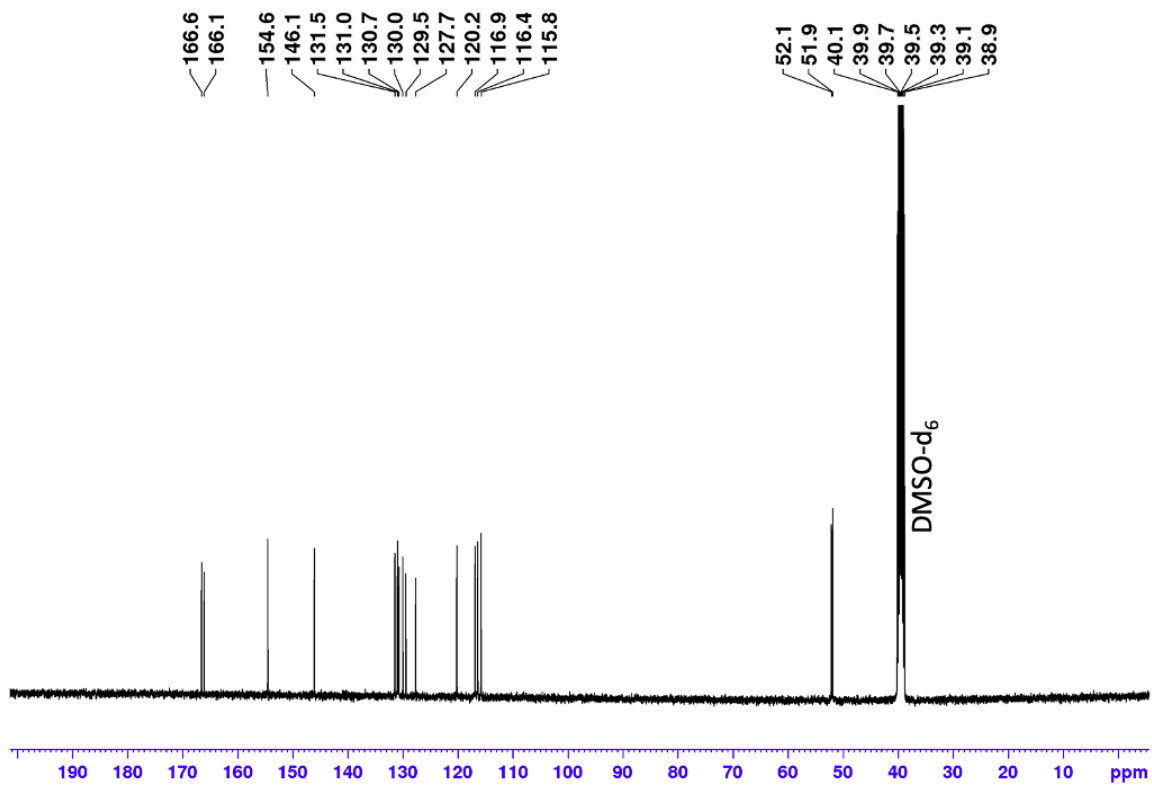


Figure 63: <sup>13</sup>C NMR (400 MHz, DMSO-d<sub>6</sub>) spectrum of compound 7.



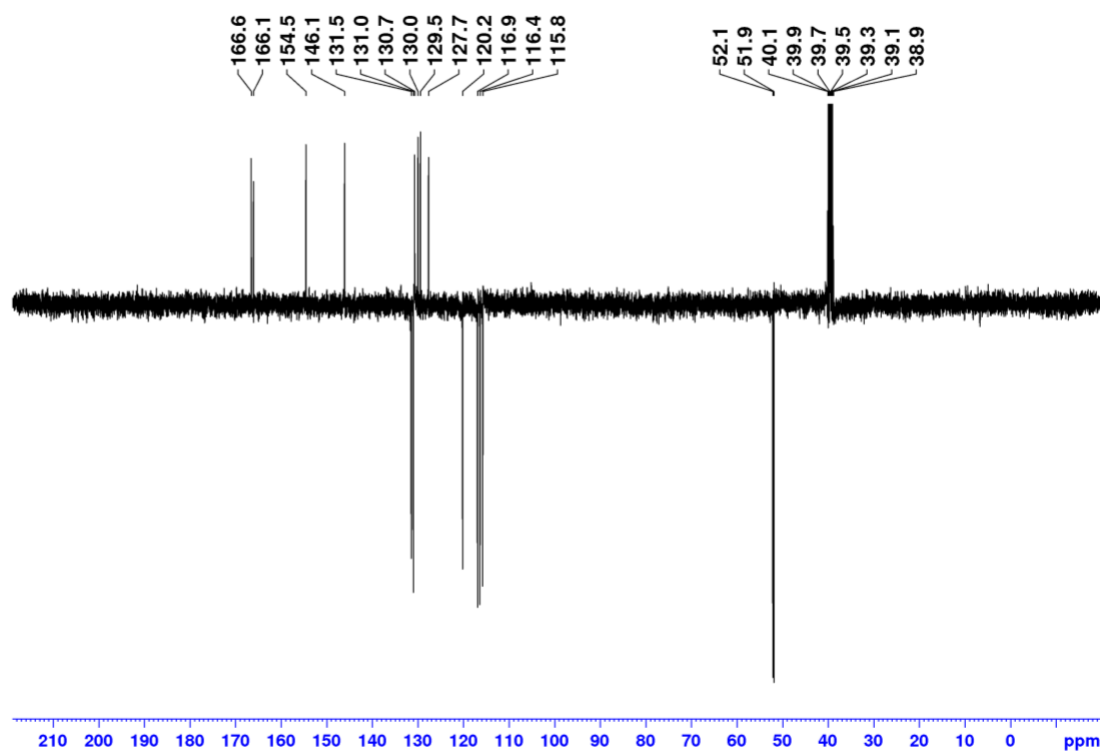


Figure 64: DEPT135Q (400 MHz, DMSO-d<sub>6</sub>) NMR spectrum of compound **7**, CH<sub>3</sub> and CH phased negative, and C phased positive.

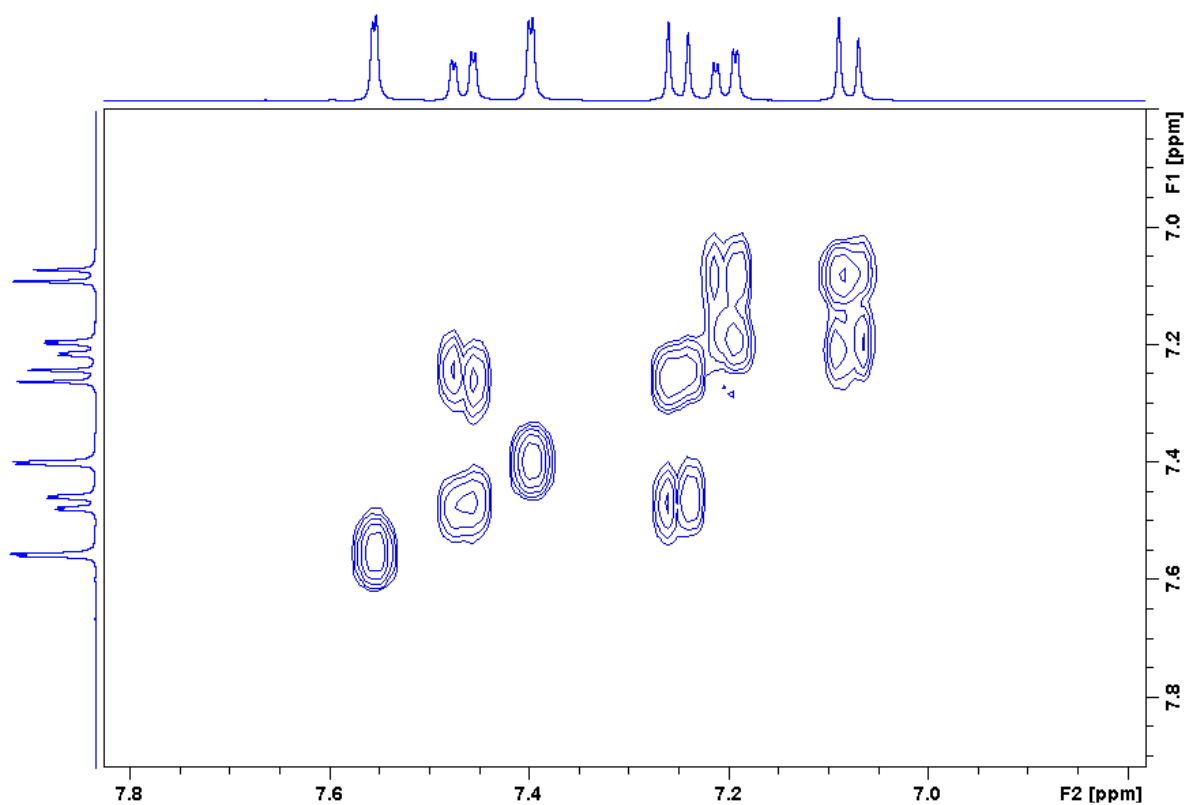


Figure 65: COSY (400 MHz, DMSO-d<sub>6</sub>) spectrum of compound **7** (zoomed at aromatic region).

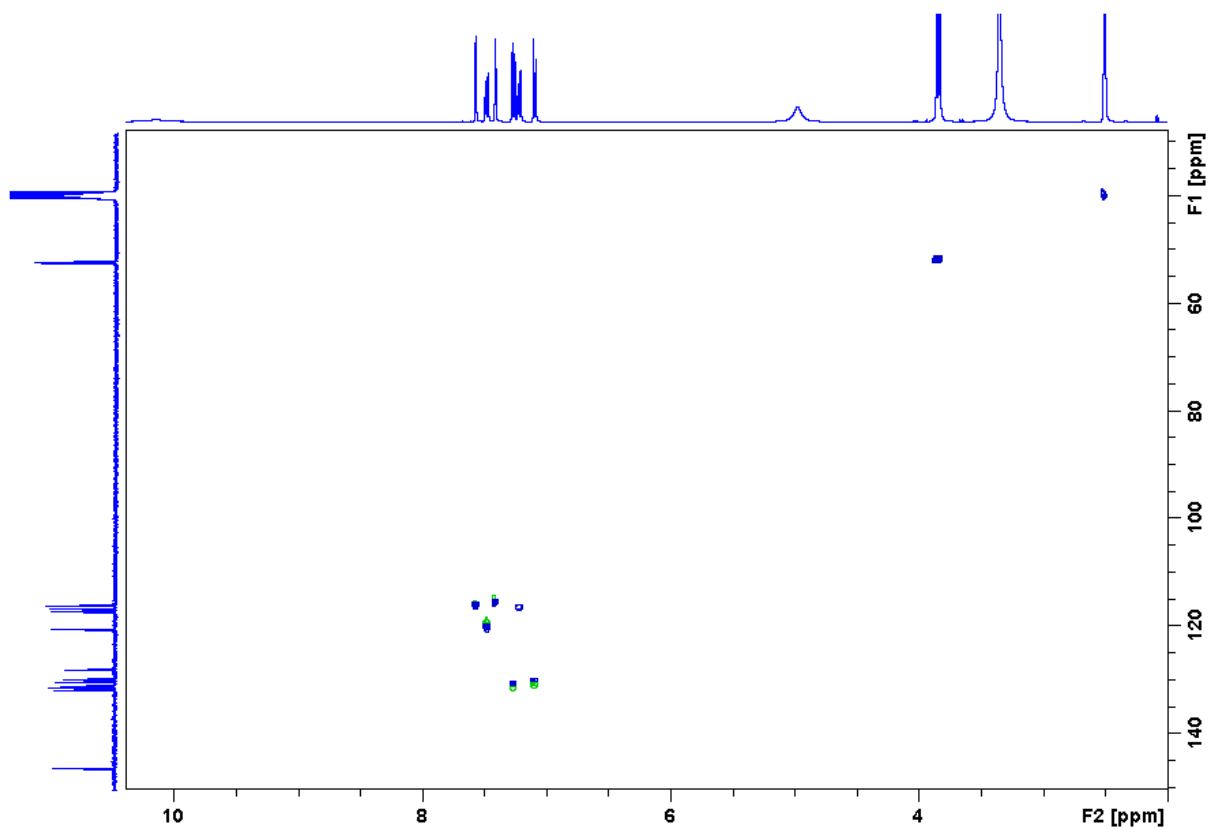


Figure 66: HSQC (400 MHz, DMSO-d<sub>6</sub>) spectrum of compound 7.

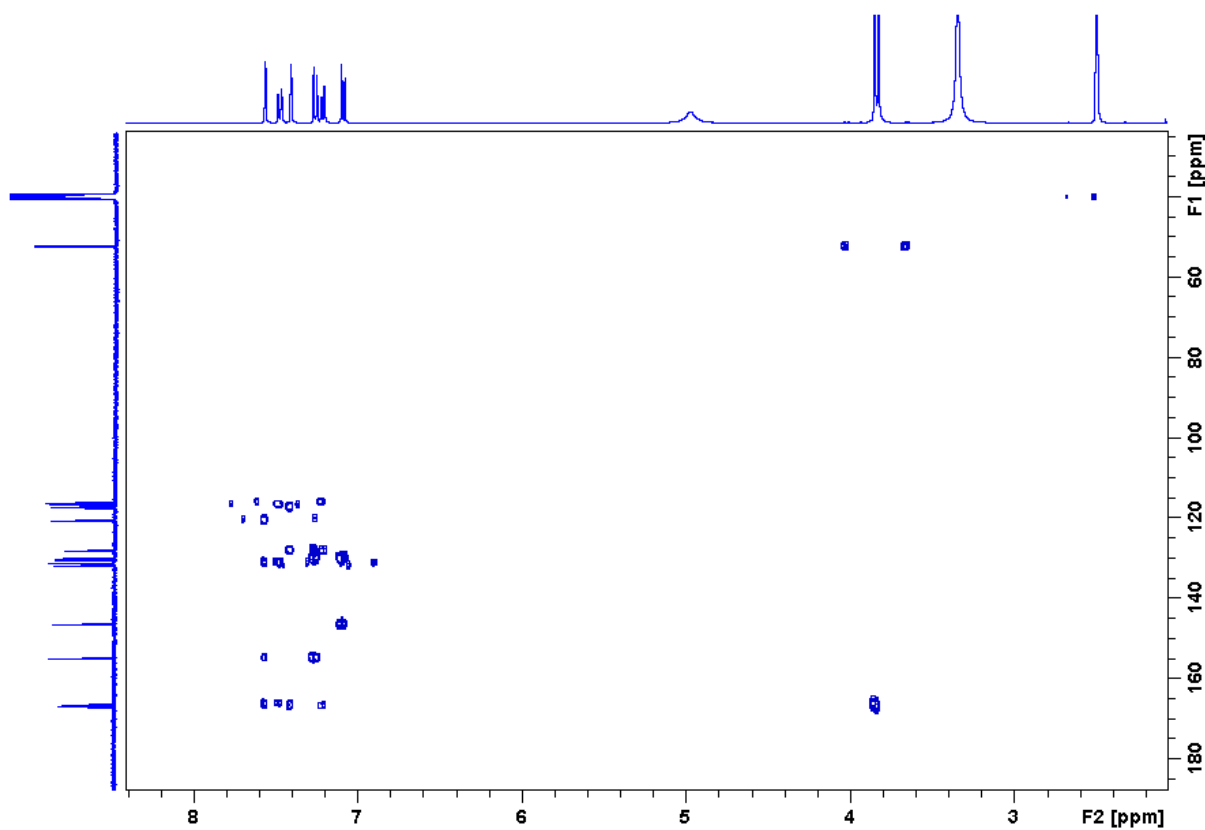


Figure 67: HMBC (400 MHz, DMSO-d<sub>6</sub>) spectrum of compound 7.

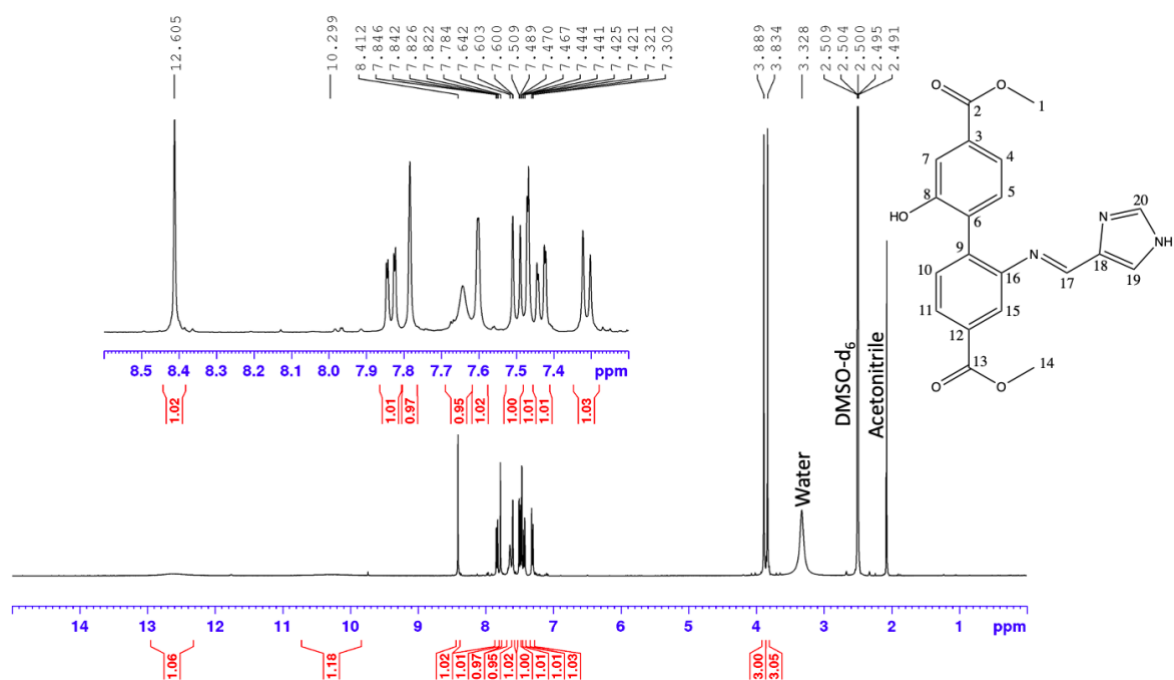


Figure 68:  $^1\text{H}$  NMR (400 MHz,  $\text{DMSO-d}_6$ ) spectrum of compound **8**.

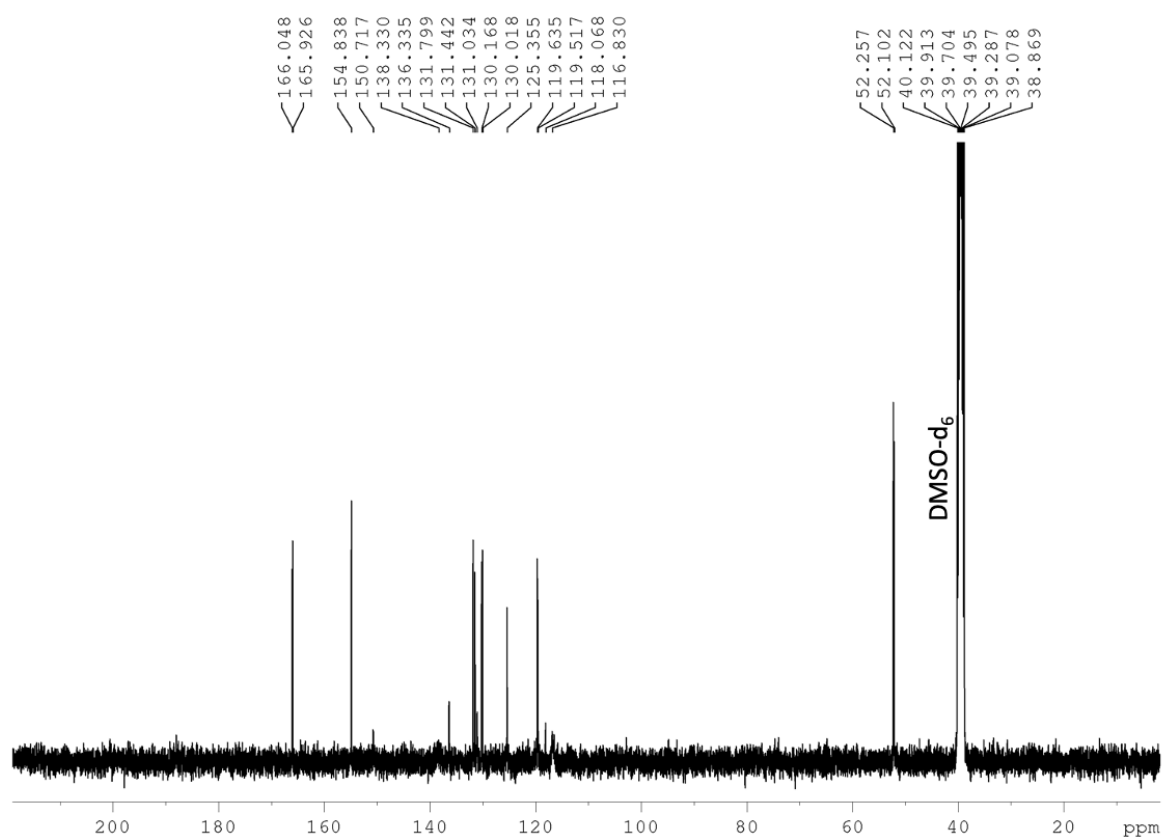


Figure 69:  $^{13}\text{C}$  NMR (400 MHz,  $\text{DMSO-d}_6$ ) spectrum of compound **8**.

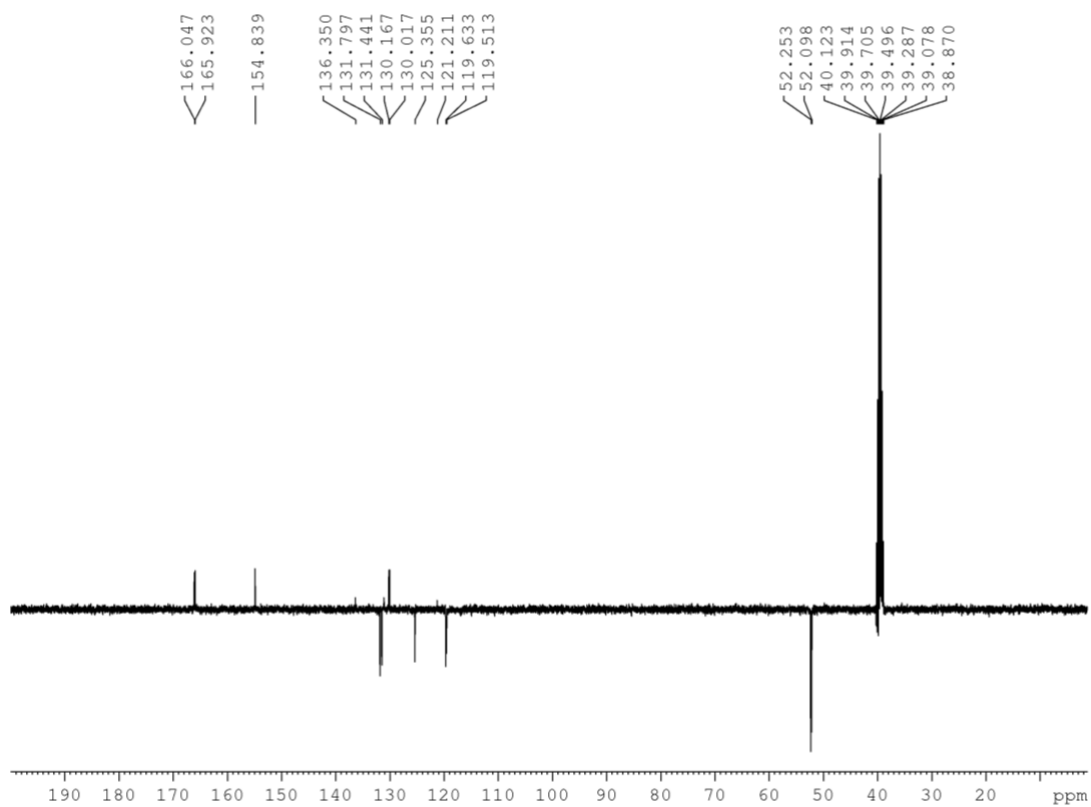


Figure 70: DEPT135Q (400 MHz, DMSO-d<sub>6</sub>) NMR spectrum of compound **8**, CH<sub>3</sub> and CH phased negative, and C phased positive.

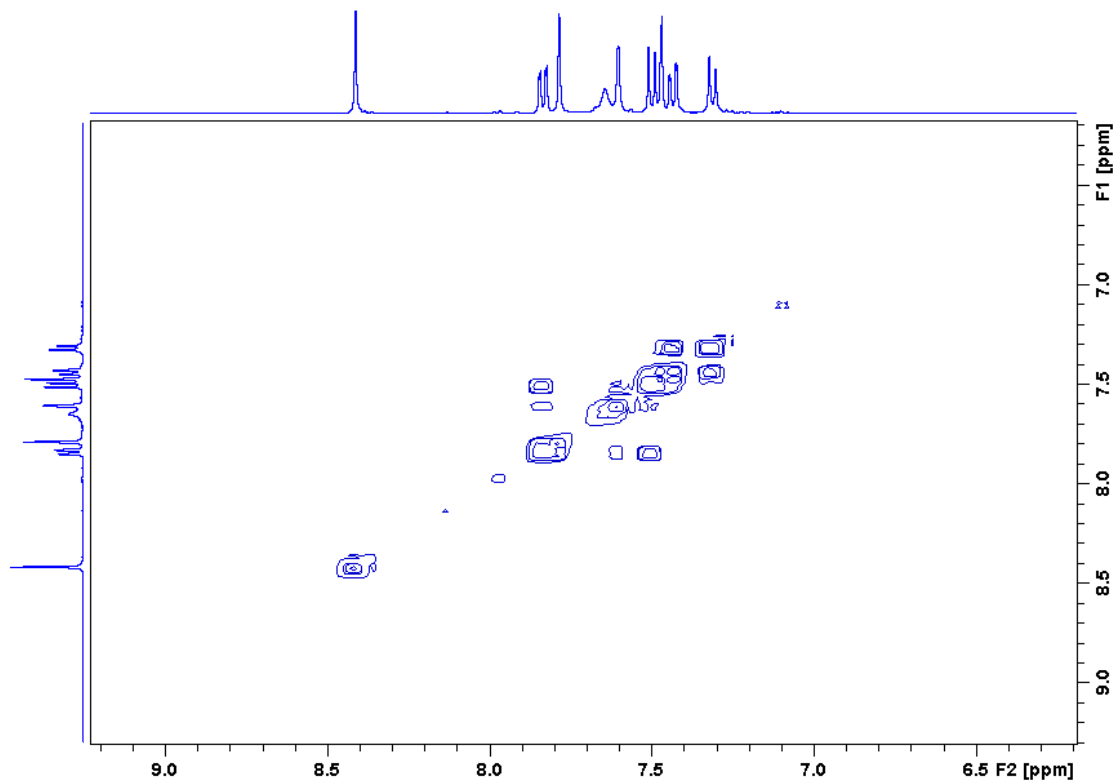


Figure 71: COSY (400 MHz, DMSO-d<sub>6</sub>) spectrum of compound **8** (zoomed at aromatic region).

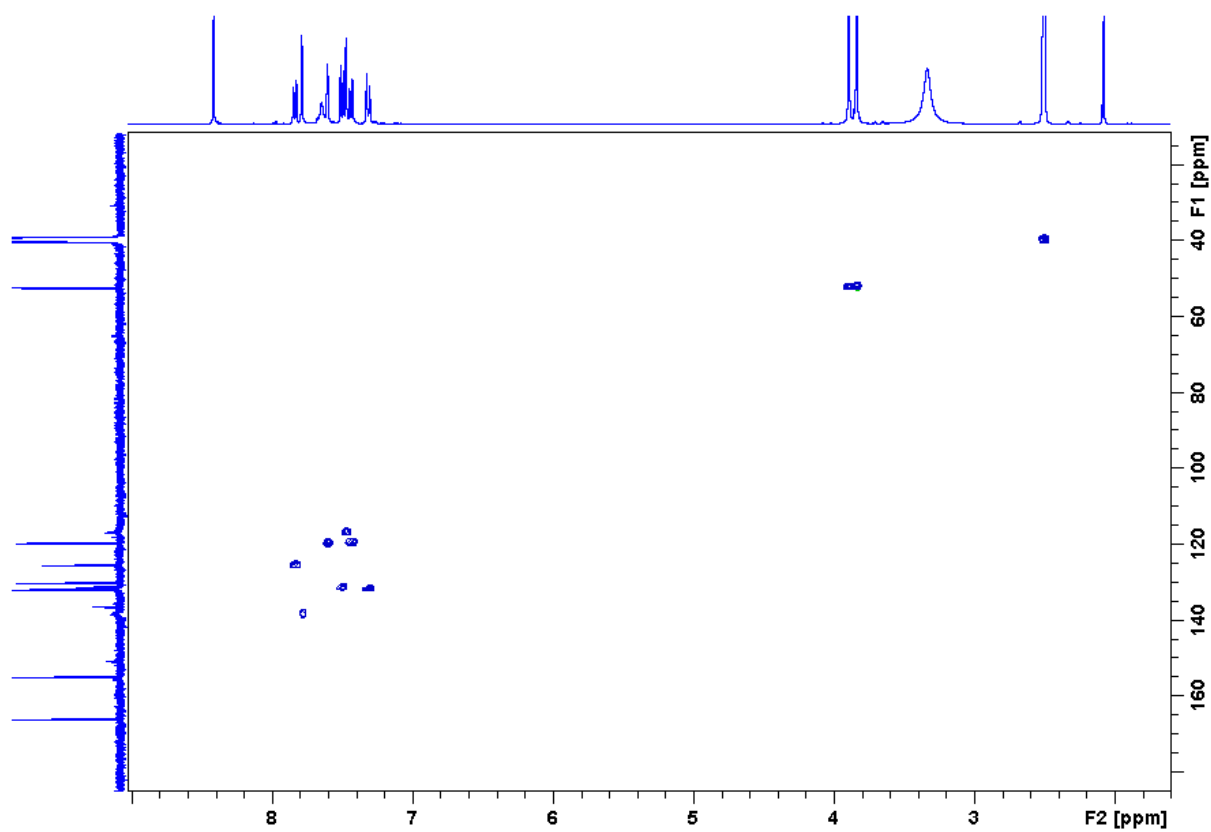


Figure 72: HSQC (400 MHz, DMSO- $d_6$ ) spectrum of compound **8**.

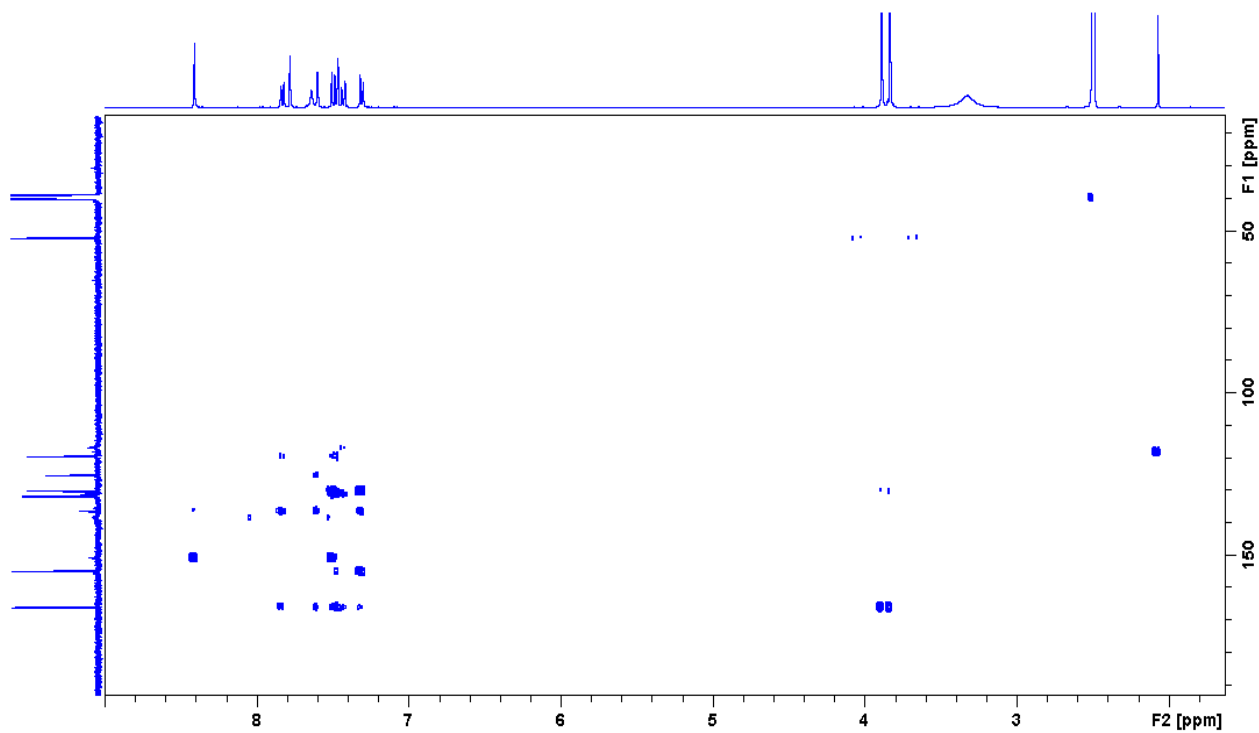


Figure 73: HMBC (400 MHz, DMSO- $d_6$ ) spectrum of compound **8**.

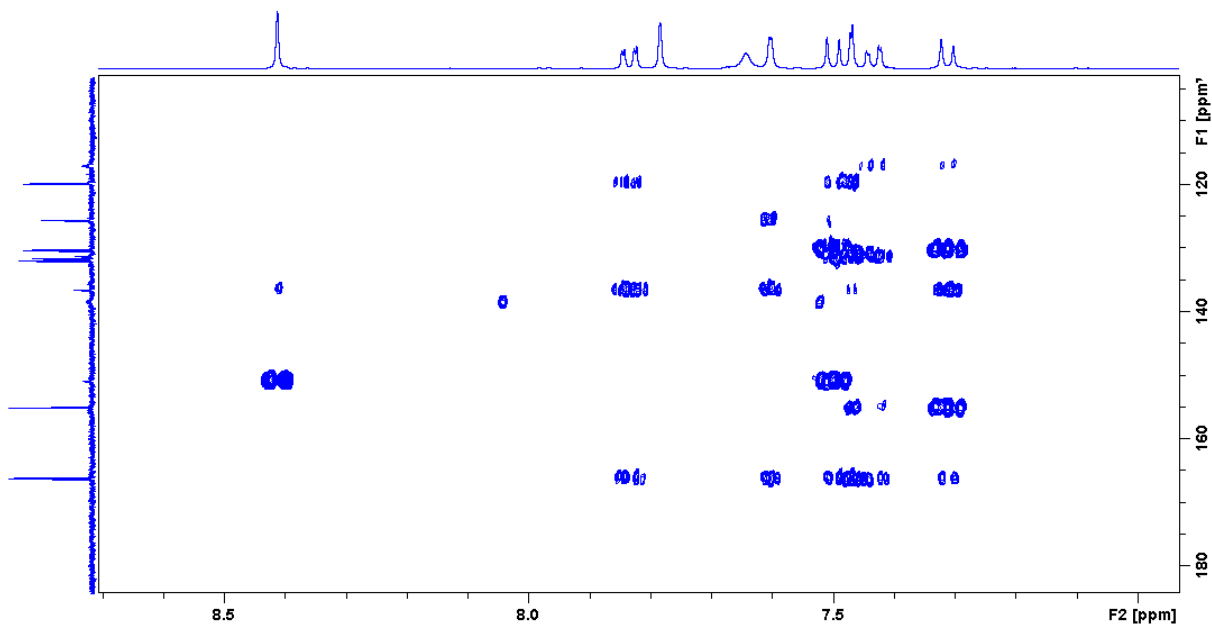


Figure 74: HMBC (400 MHz, DMSO-d<sub>6</sub>) spectrum of compound **8** (zoomed at aromatic region).

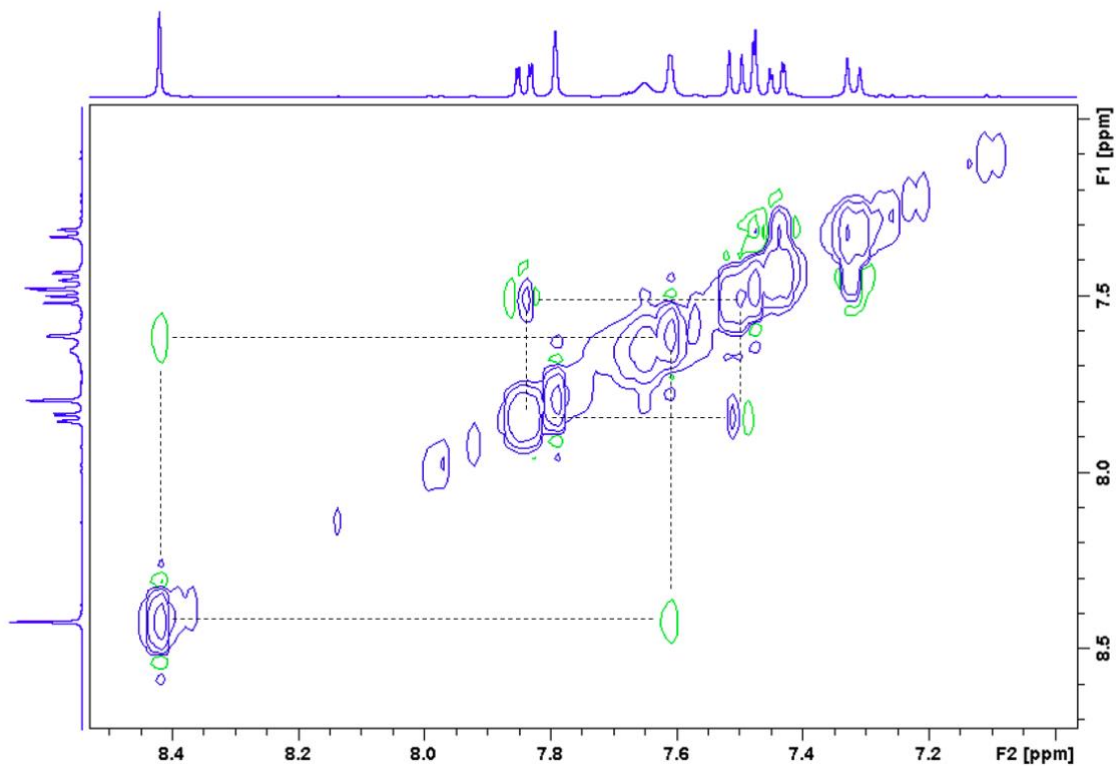


Figure 75: NOESY (400 MHz, DMSO-d<sub>6</sub>) spectrum of compound **8** (zoomed at aromatic region).

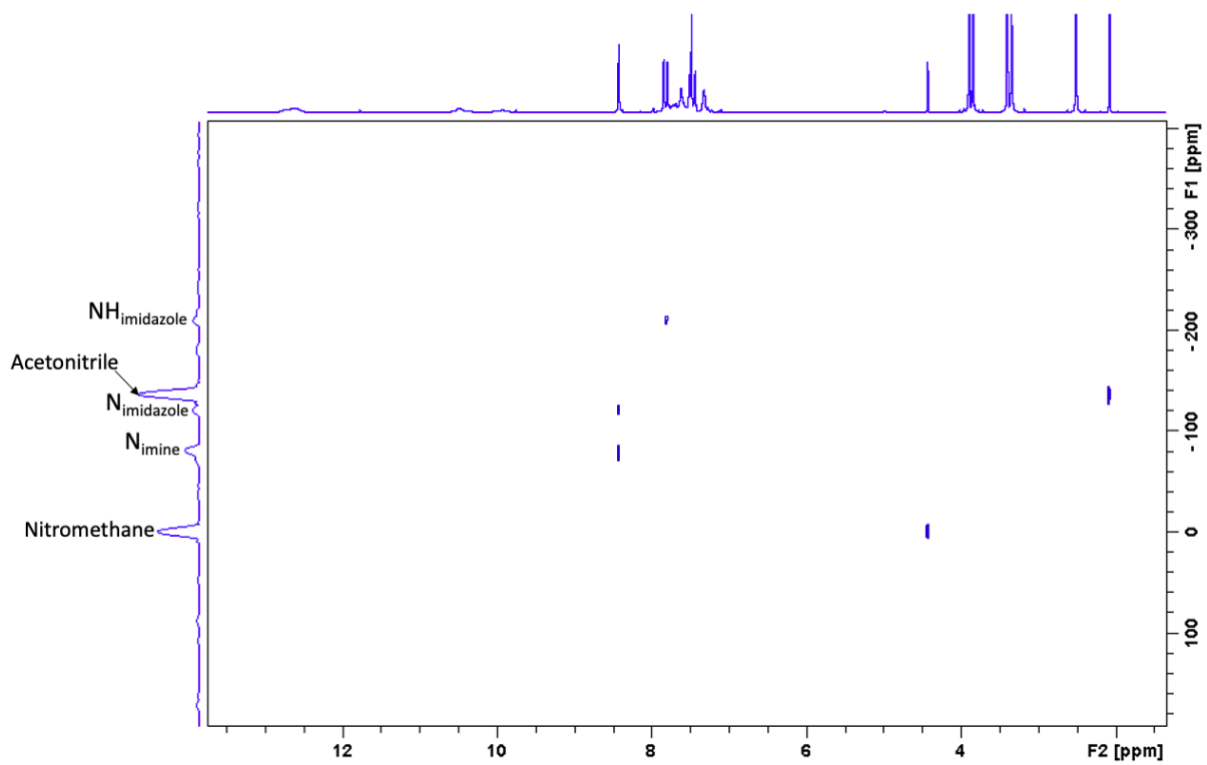


Figure 76:  $^{15}\text{N}$ - $^1\text{H}$  HMBC (600 MHz,  $\text{DMSO-d}_6$ ) spectrum of compound **8** with nitromethane as external standard.

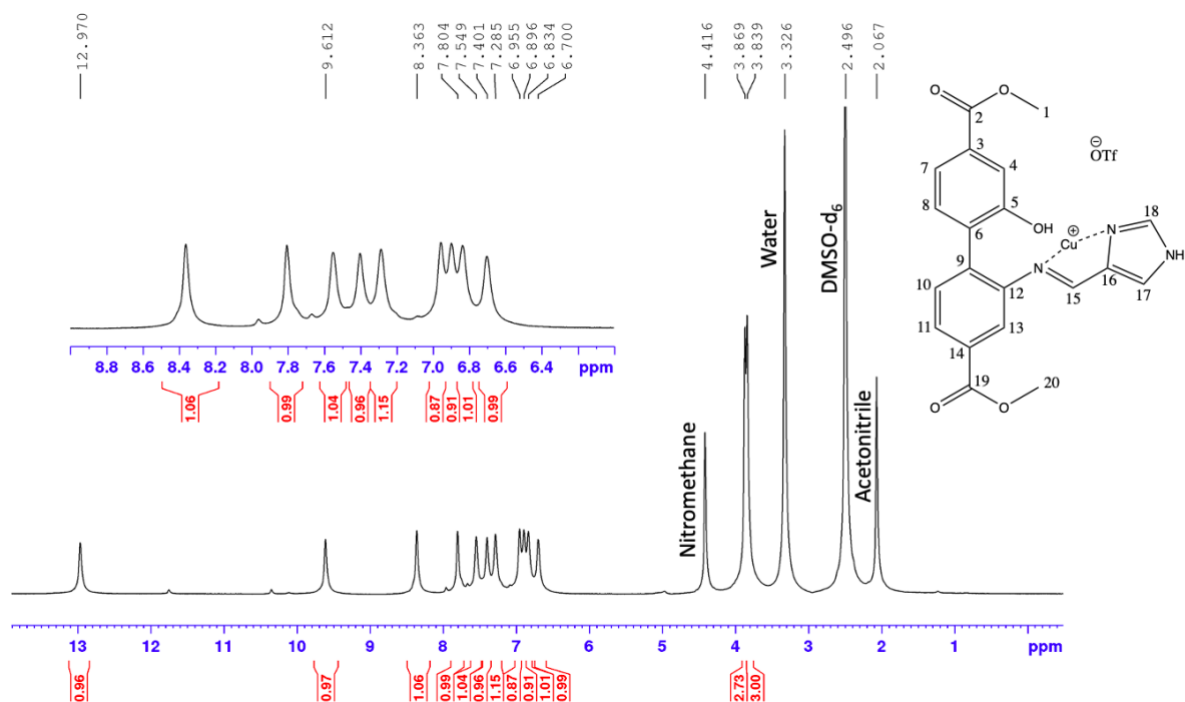


Figure 77:  $^1\text{H}$  NMR (600 MHz,  $\text{DMSO-d}_6$ ) spectrum of compound **9** with nitromethane and hexafluorobenzene as external standards.

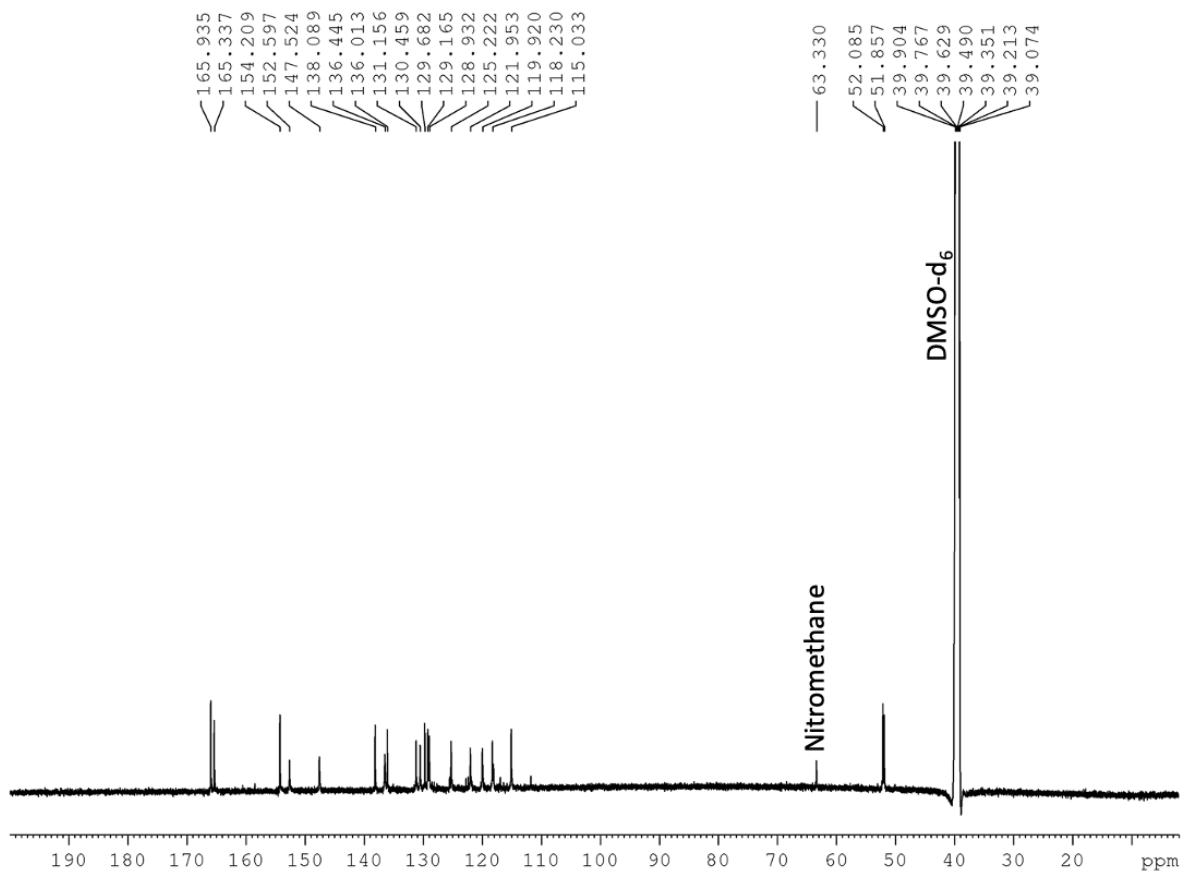


Figure 78:  $^{13}\text{C}$  NMR (600 MHz,  $\text{DMSO-d}_6$ ) spectrum of compound **9** with nitromethane and hexafluorobenzene as external standards.



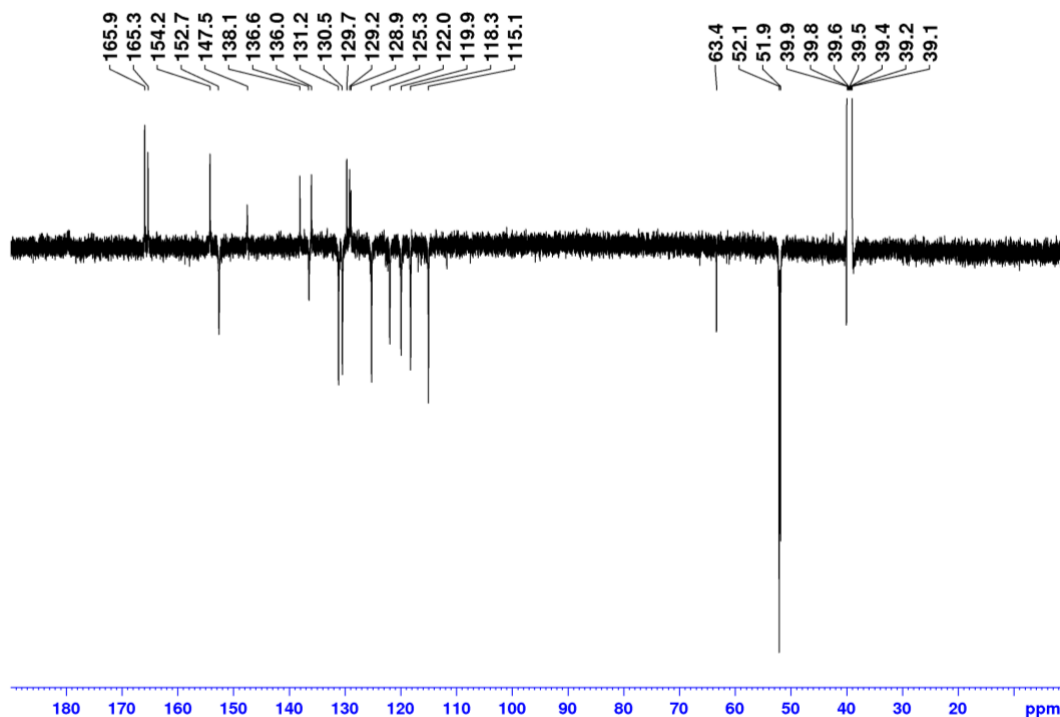


Figure 79: DEPT135Q (600 MHz, DMSO- $d_6$ ) NMR spectrum of compound **9**, CH<sub>3</sub> and CH phased negative, and C phased positive.

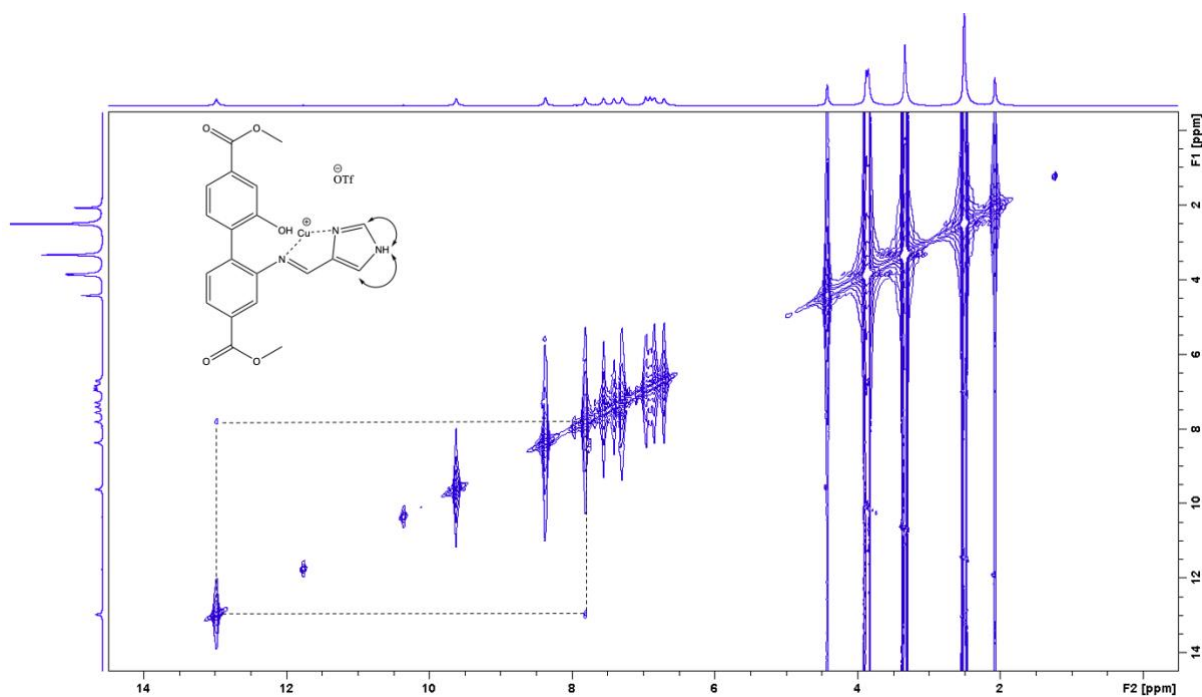


Figure 80: COSY (600 MHz, DMSO- $d_6$ ) spectrum of compound **9**.

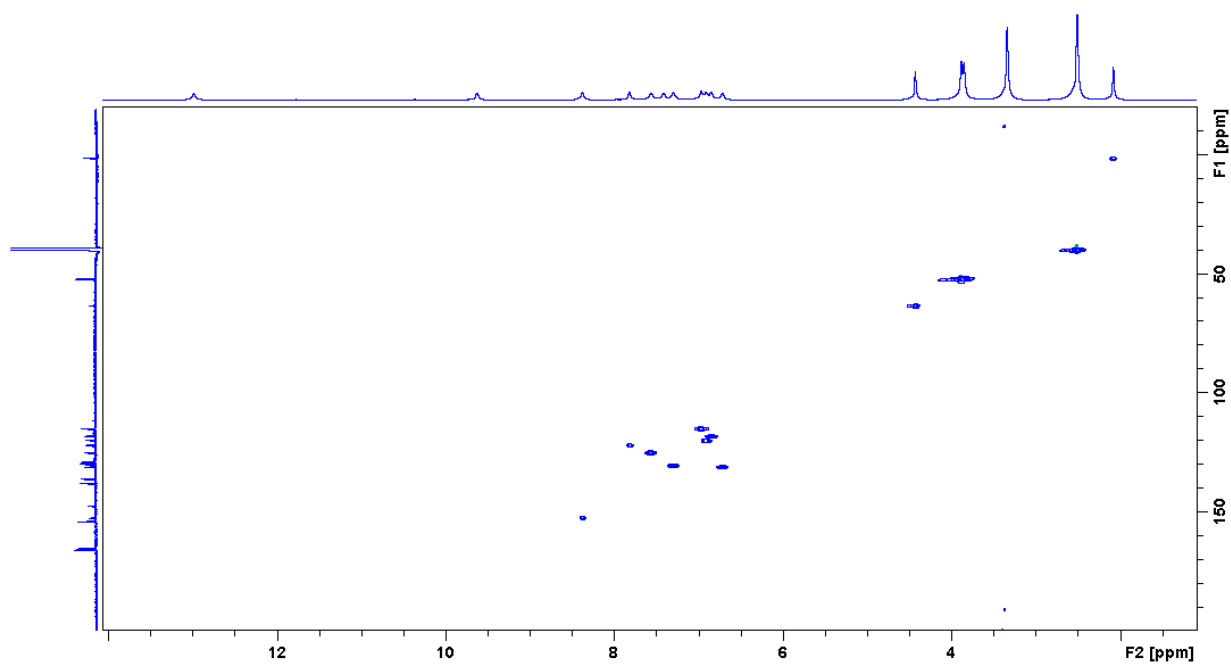


Figure 81: HSQC (600 MHz, DMSO-d<sub>6</sub>) spectrum of compound **9**.

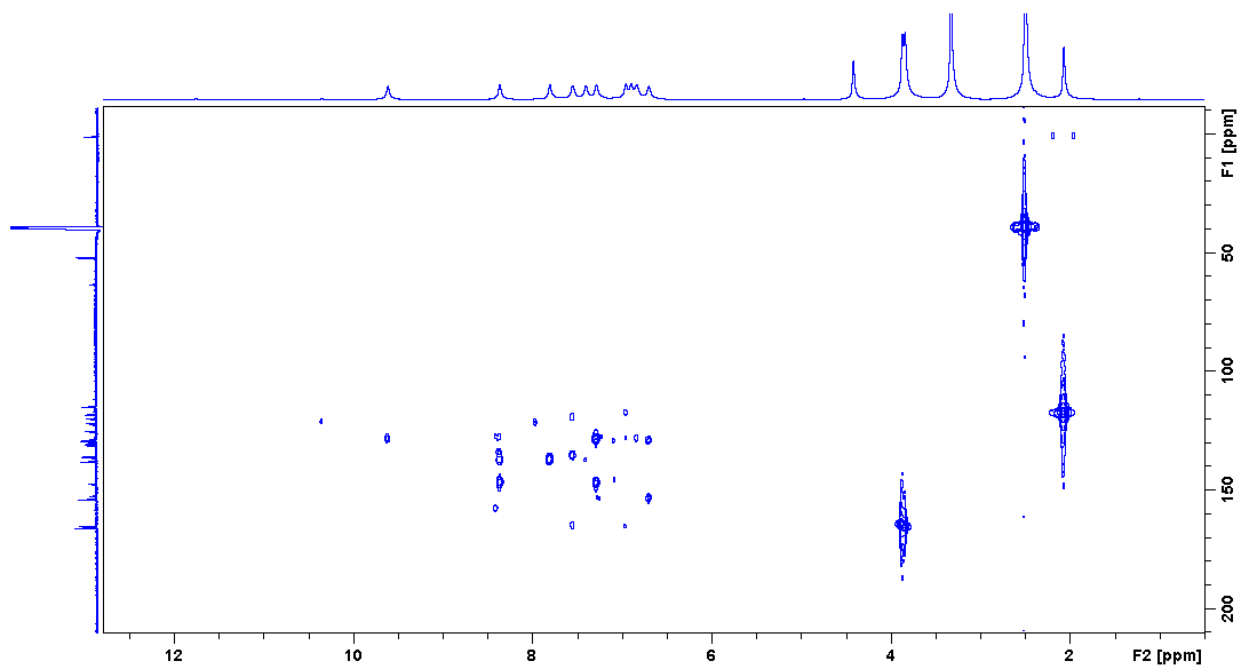


Figure 82: HMBC (600 MHz, DMSO-d<sub>6</sub>) spectrum of compound **9**.

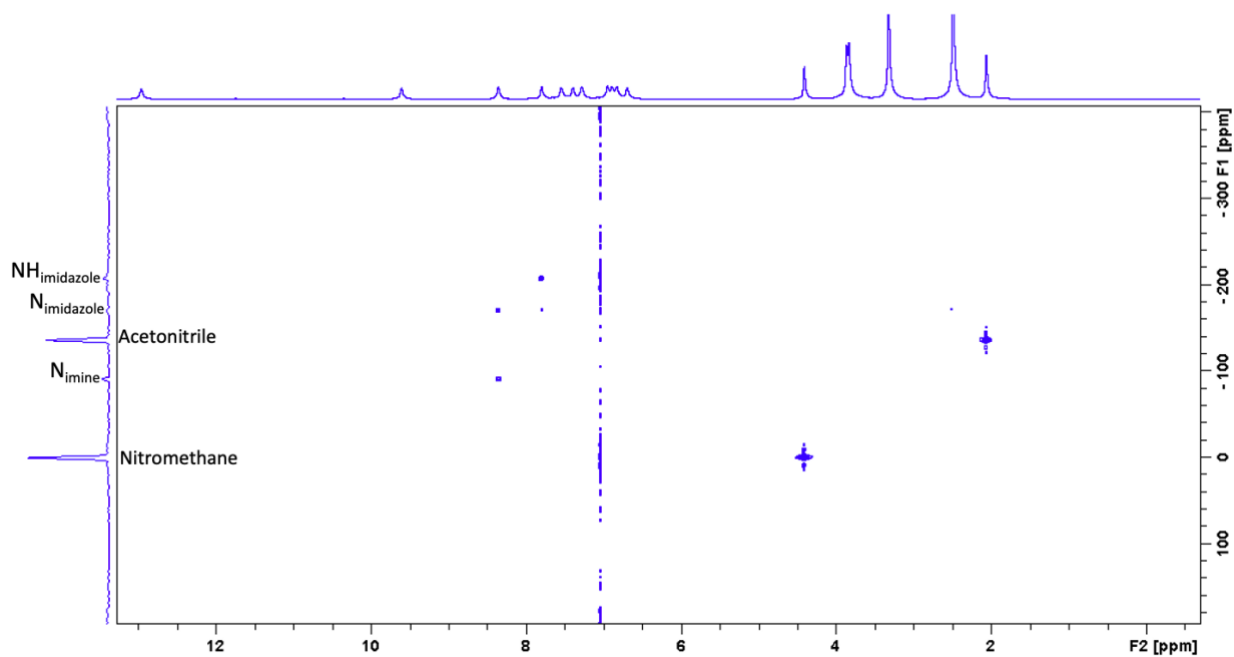


Figure 83:  $^{15}\text{N}$ - $^1\text{H}$  HMBC (600 MHz,  $\text{DMSO-d}_6$ ) spectrum of compound **9** with nitromethane as external standards.

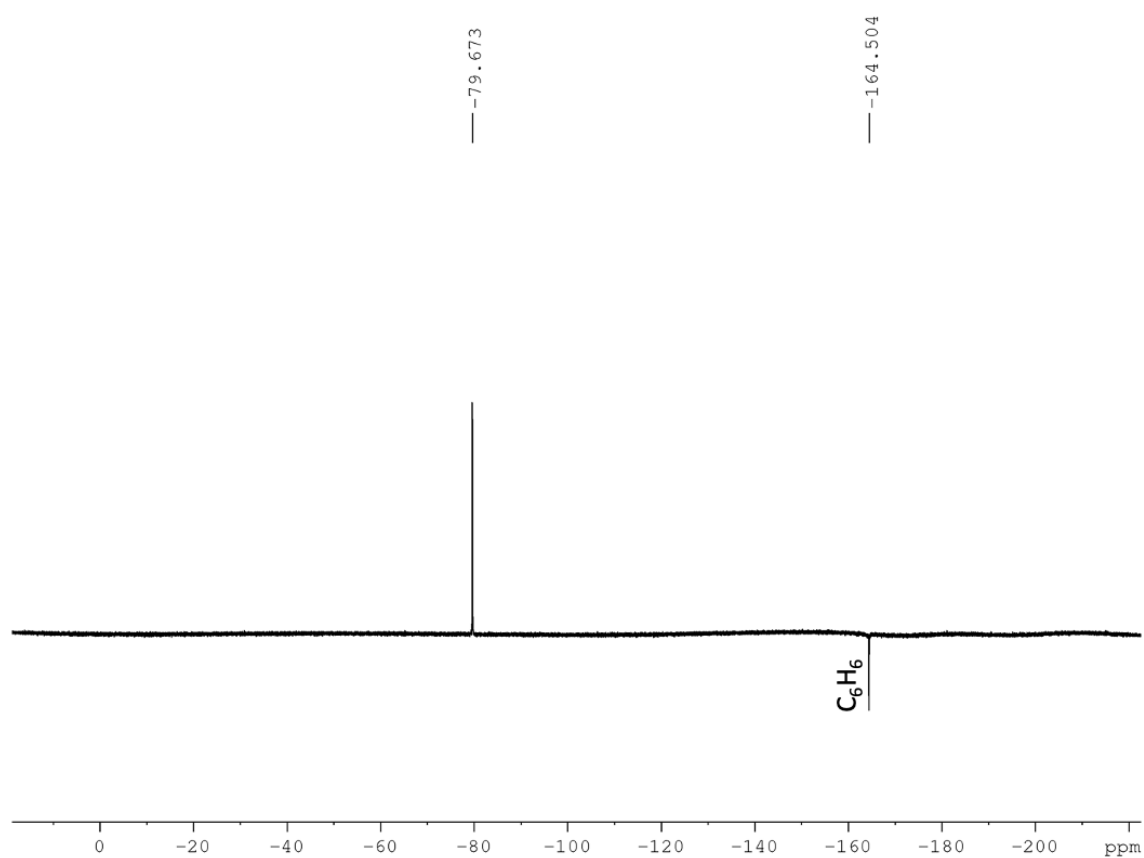


Figure 84:  $^{19}\text{F}$  NMR (400 MHz,  $\text{DMSO-d}_6$ ) spectrum of compound **9** with hexafluorobenzene as external standard.

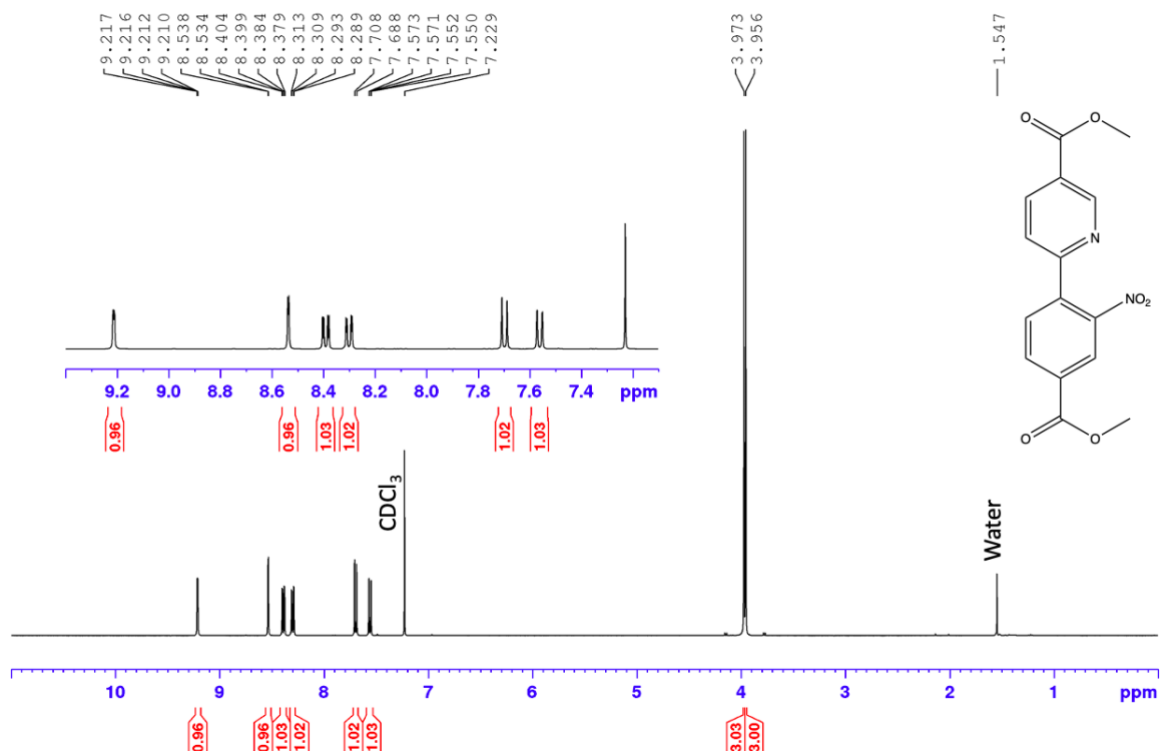


Figure 85: <sup>1</sup>H NMR (400 MHz, CDCl<sub>3</sub>) spectrum of compound 11.

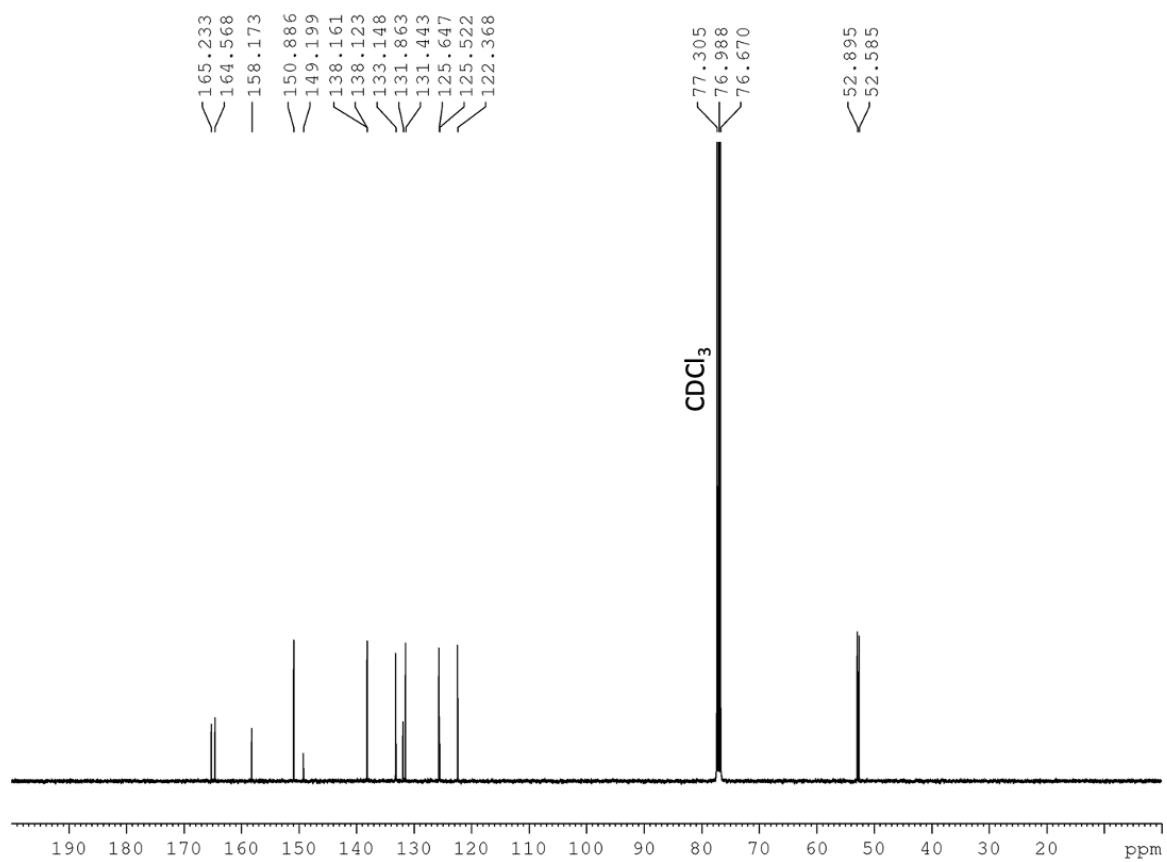


Figure 86: <sup>13</sup>C NMR (400 MHz, CDCl<sub>3</sub>) spectrum of compound 11.

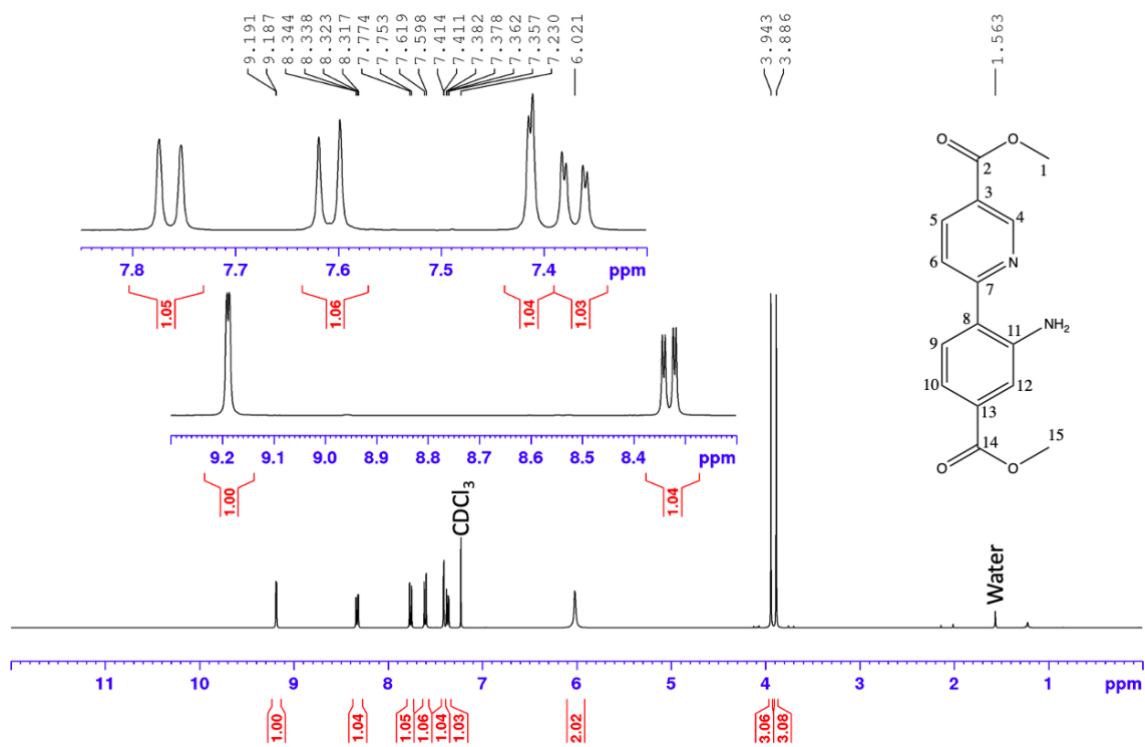


Figure 87: <sup>1</sup>H NMR (400 MHz, CDCl<sub>3</sub>) spectrum of compound 12.

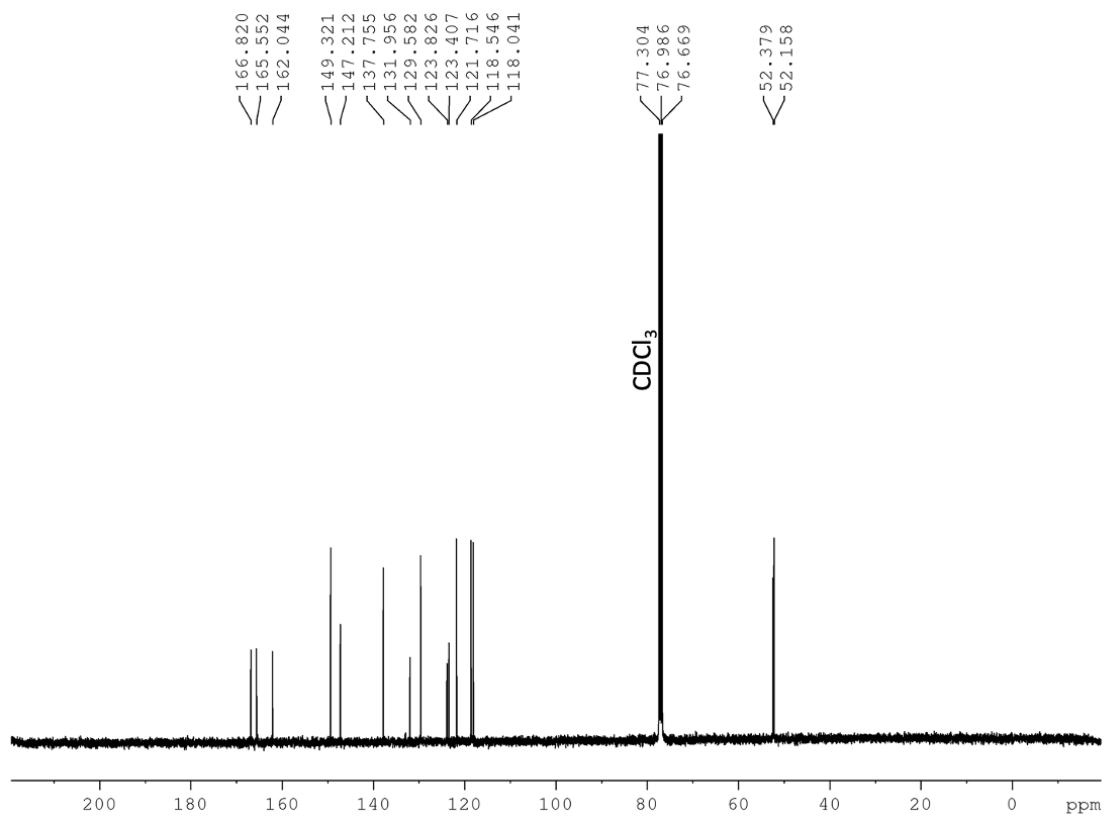


Figure 88: <sup>13</sup>C NMR (400 MHz, CDCl<sub>3</sub>) spectrum of compound 12.

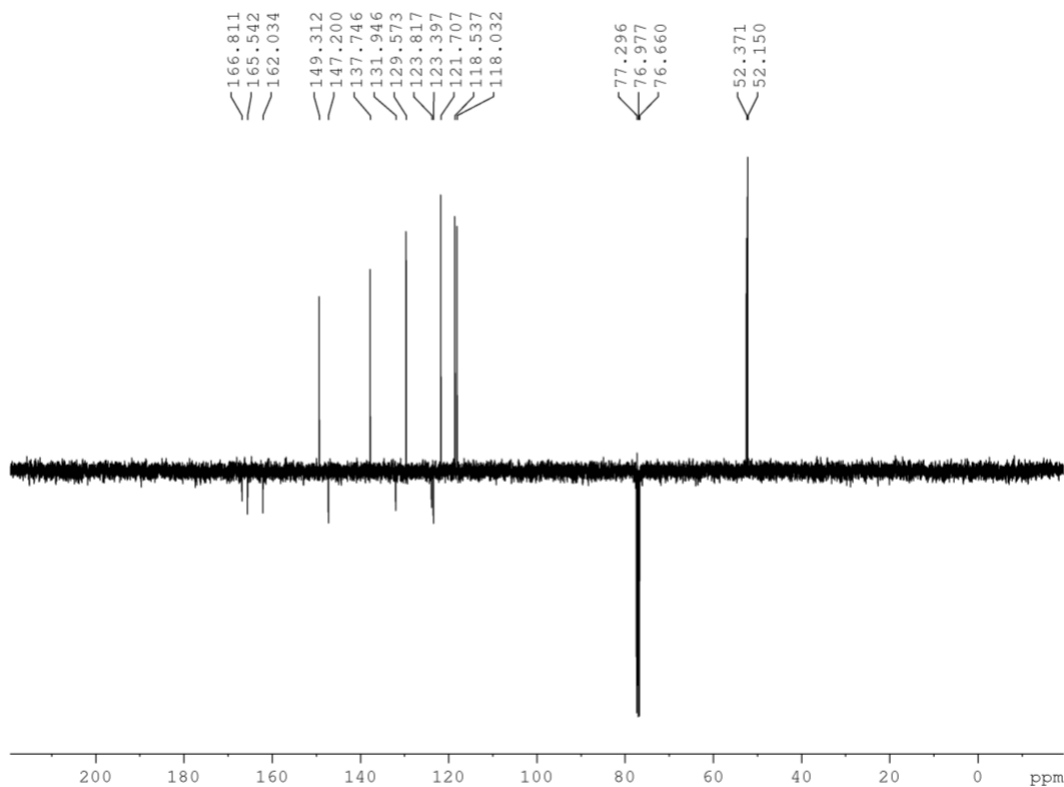


Figure 89: DEPT135Q (400 MHz, CDCl<sub>3</sub>) NMR spectrum of compound **12**, CH<sub>3</sub> and CH phased positive, and C phased negative.

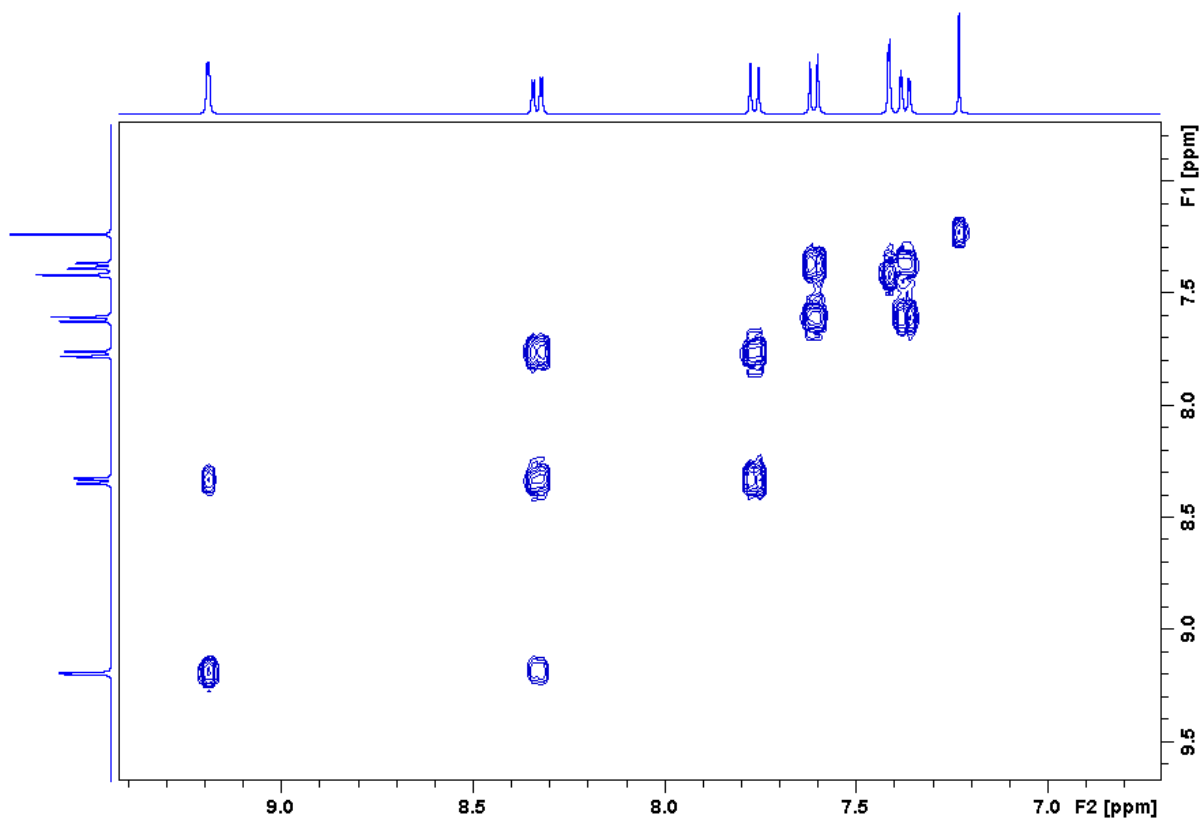


Figure 90: COSY (400 MHz, CDCl<sub>3</sub>) spectrum of compound **12** (zoomed at aromatic region).

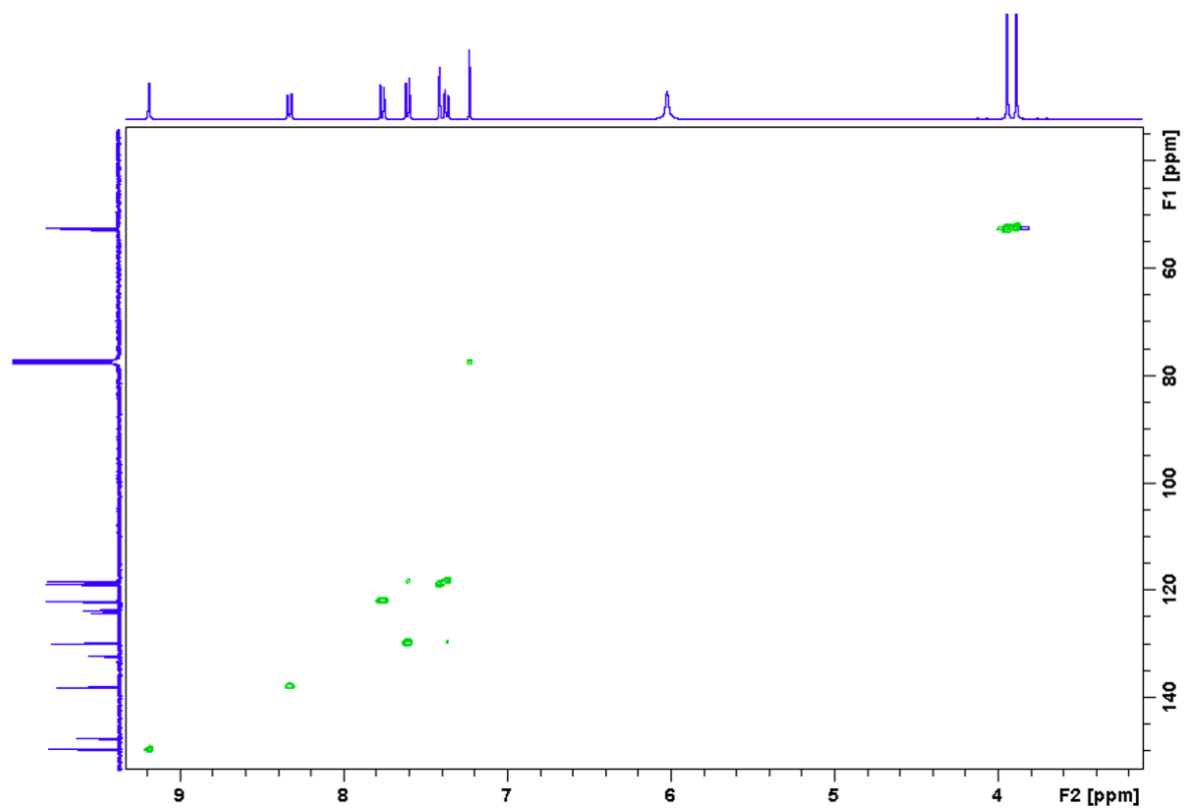


Figure 91: HSQC (400 MHz, CDCl<sub>3</sub>) spectrum of compound **12**.

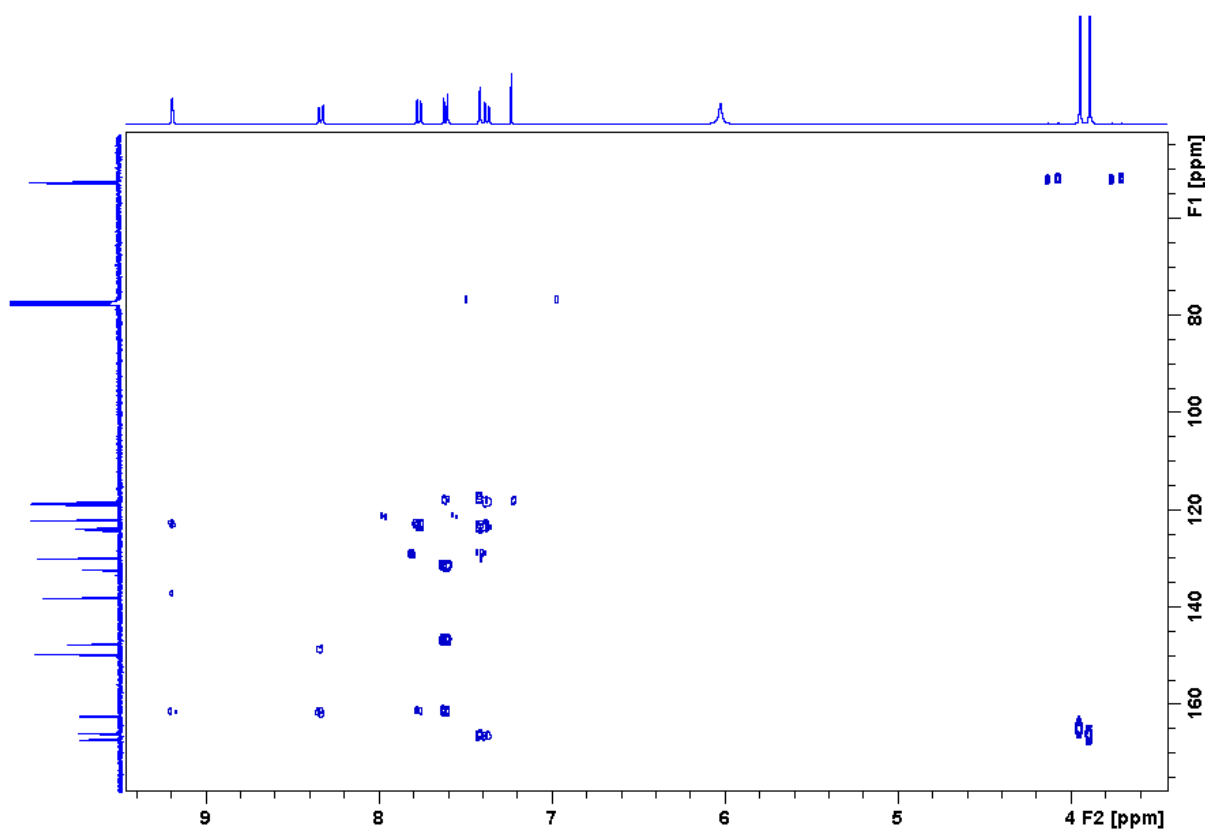


Figure 92: HMBC (400 MHz, CDCl<sub>3</sub>) spectrum of compound **12**.

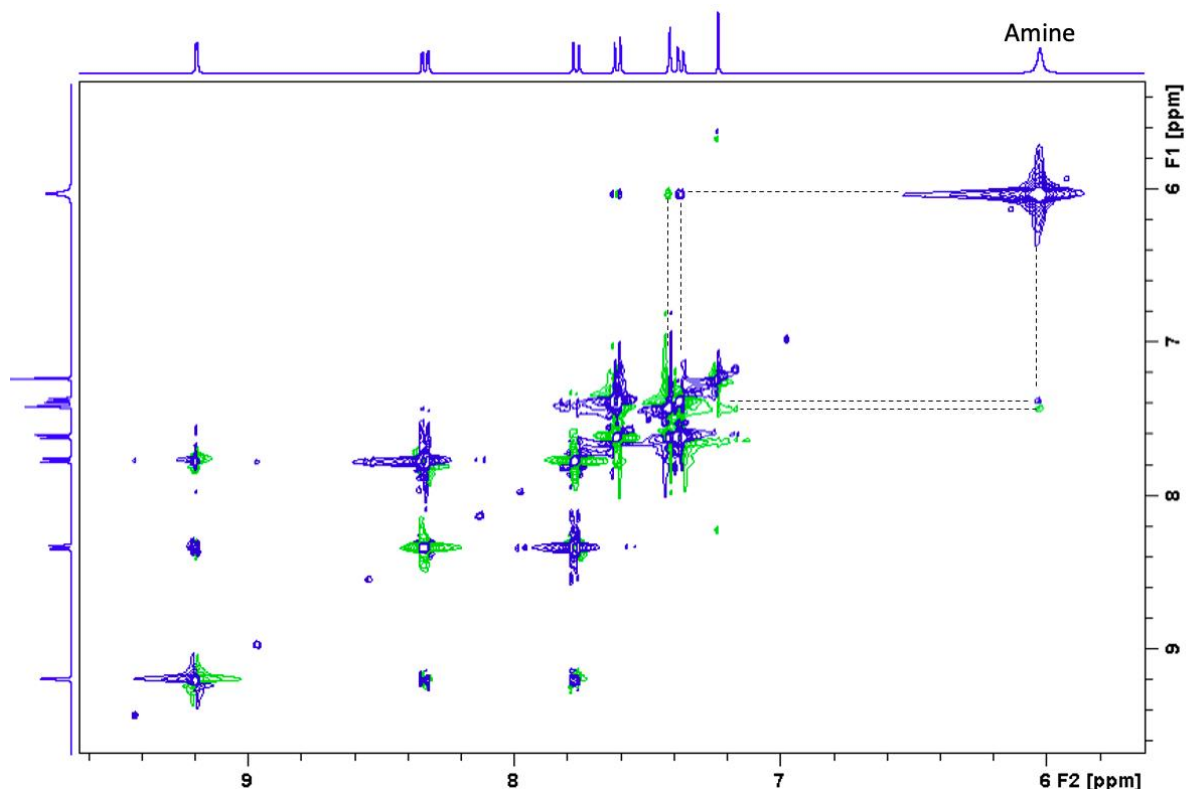


Figure 93: TOCSY (400 MHz,  $\text{CDCl}_3$ ) spectrum of compound **12**.

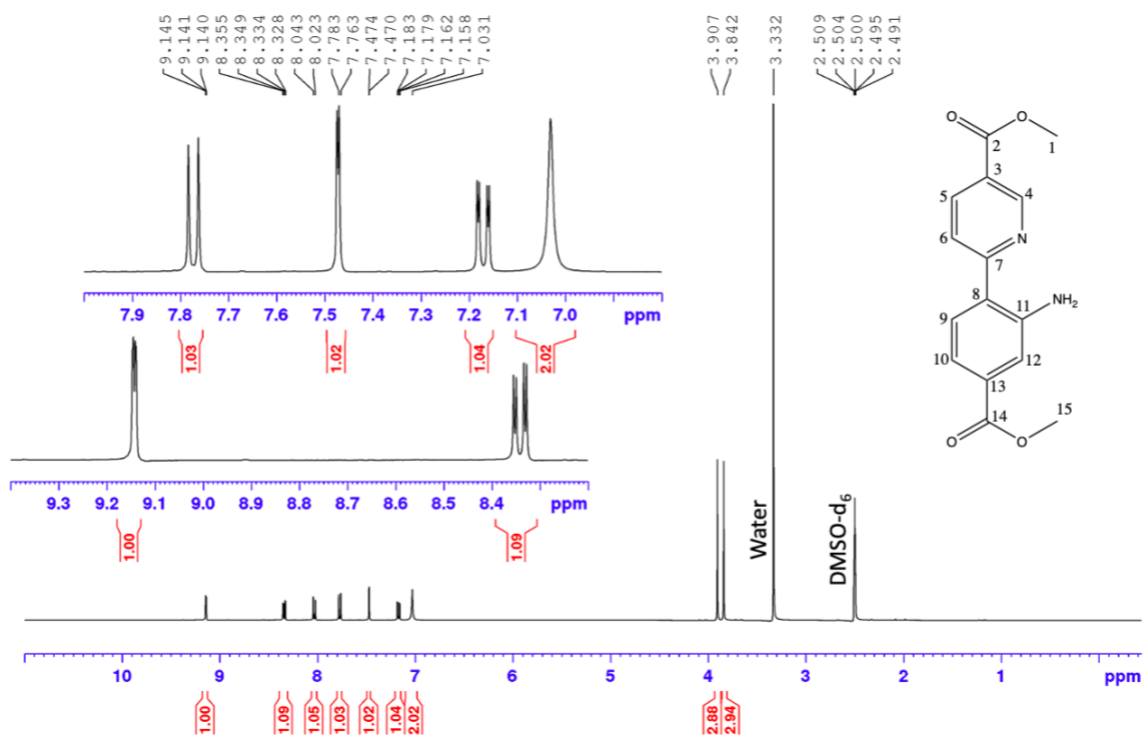


Figure 94:  $^1\text{H}$  NMR (400 MHz,  $\text{DMSO-d}_6$ ) spectrum of compound **12**.



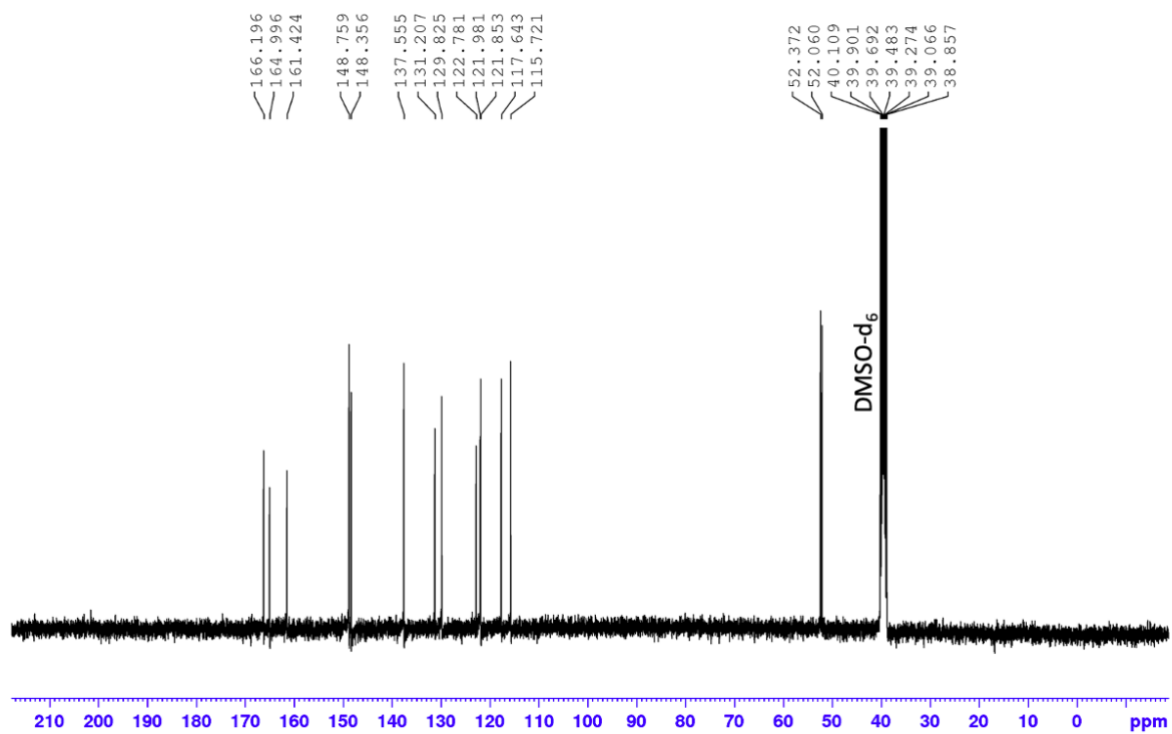


Figure 95:  $^{13}\text{C}$  NMR (400 MHz,  $\text{DMSO-d}_6$ ) spectrum of compound **12**.

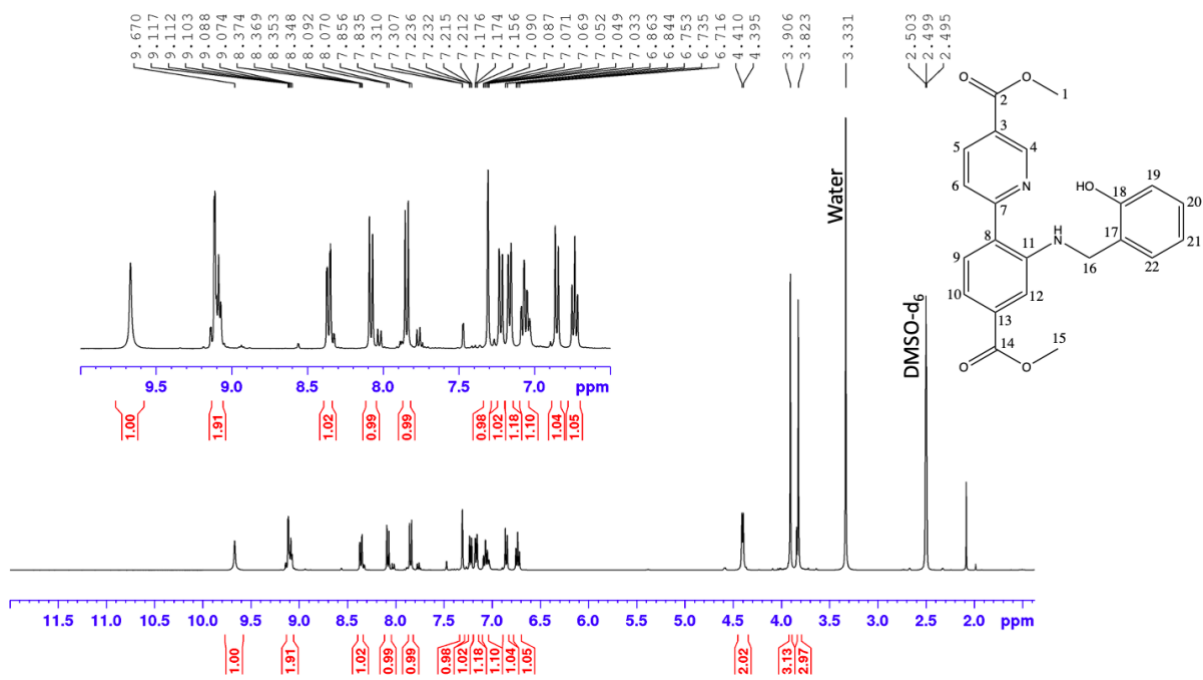


Figure 96: <sup>1</sup>H NMR (400 MHz, DMSO-d<sub>6</sub>) spectrum of compound 14.

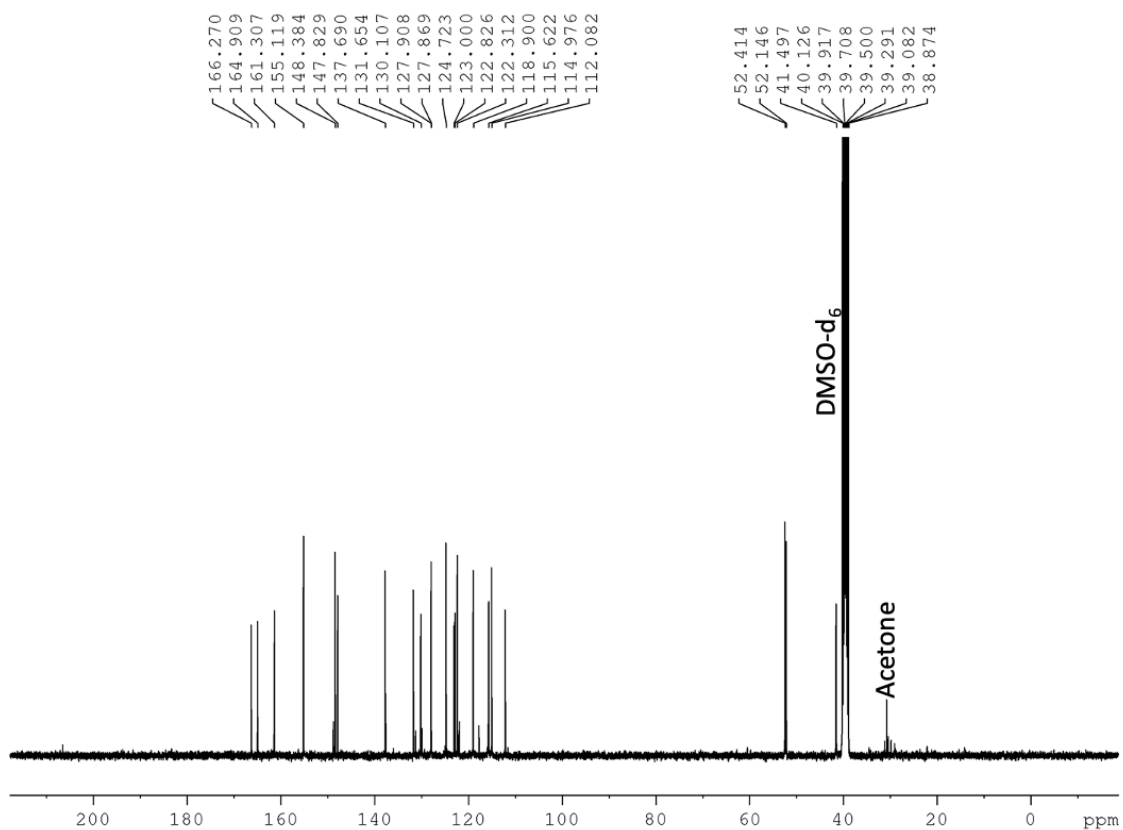


Figure 97: <sup>13</sup>C NMR (400 MHz, DMSO-d<sub>6</sub>) spectrum of compound 14.

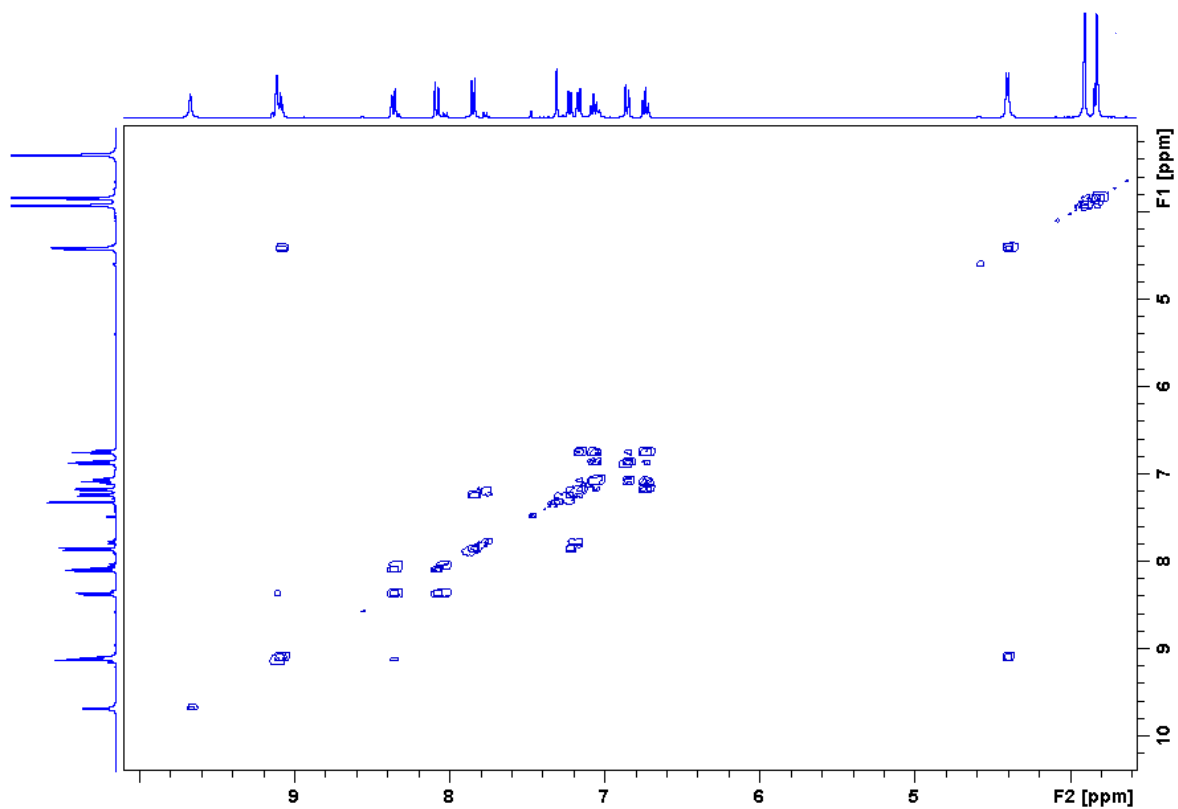


Figure 98: COSY (400 MHz, DMSO-d<sub>6</sub>) spectrum of compound **14**.

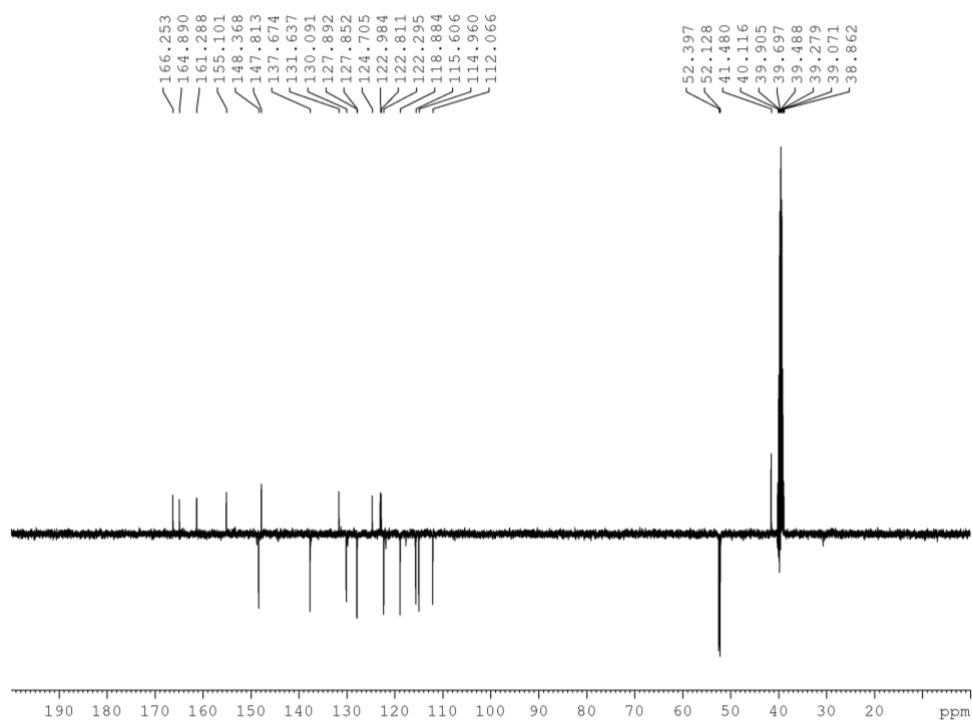


Figure 99: DEPT135Q (400 MHz, DMSO-d<sub>6</sub>) NMR spectrum of compound **14**, CH<sub>3</sub> and CH phased negative, and C and CH<sub>2</sub> phased negative .

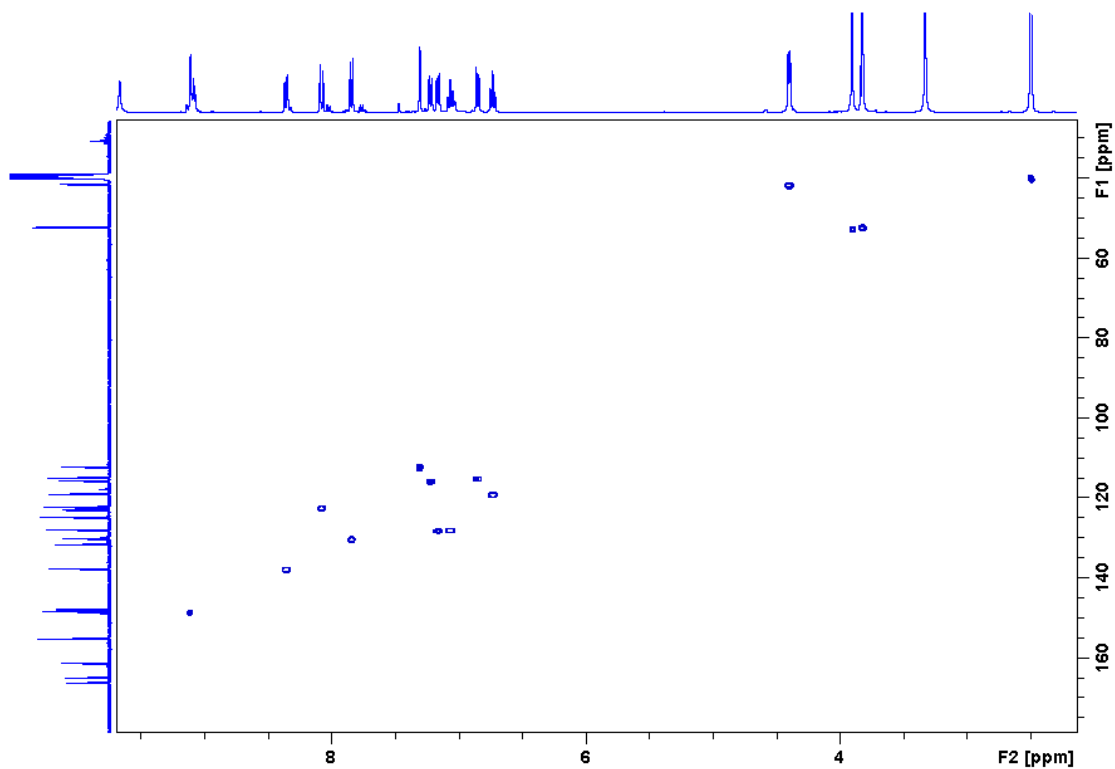


Figure 100: HSQC (400 MHz, DMSO-d<sub>6</sub>) spectrum of compound **14**.

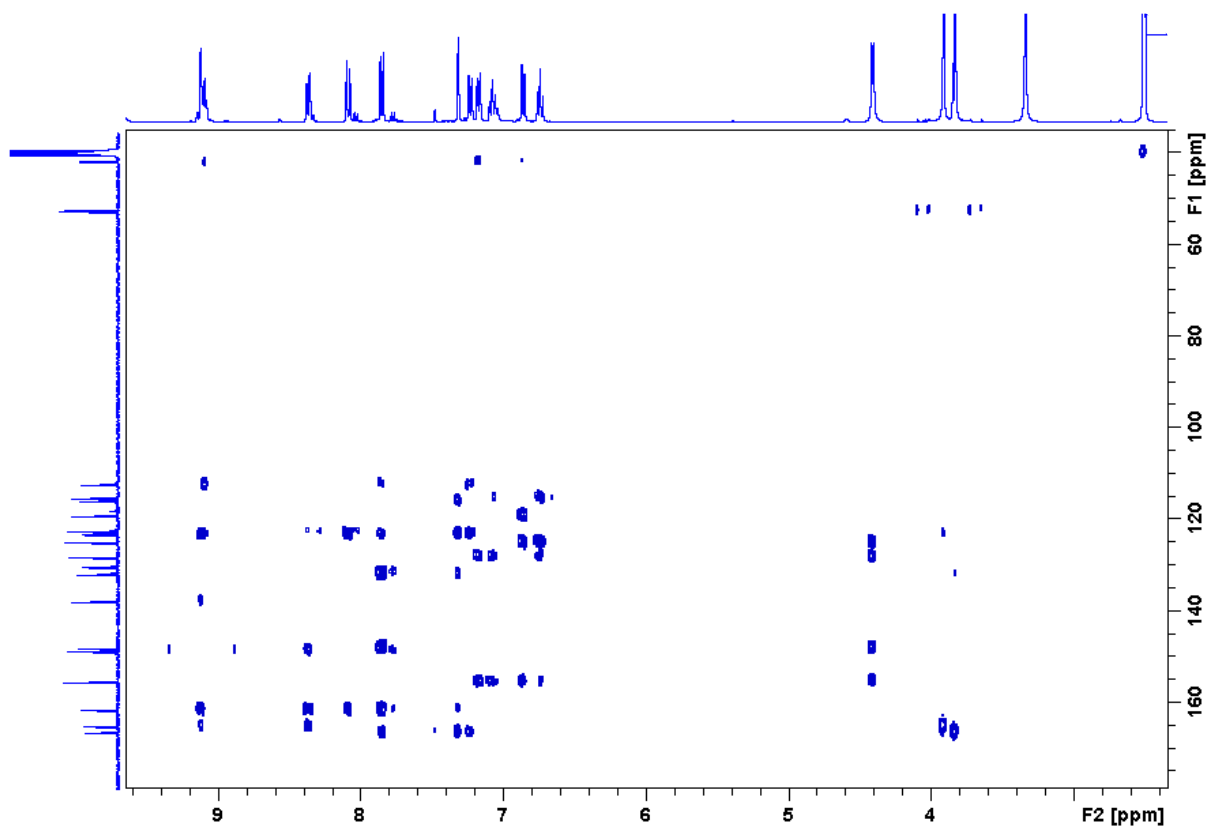


Figure 101: HMBC (400 MHz, DMSO-d<sub>6</sub>) spectrum of compound **14**.

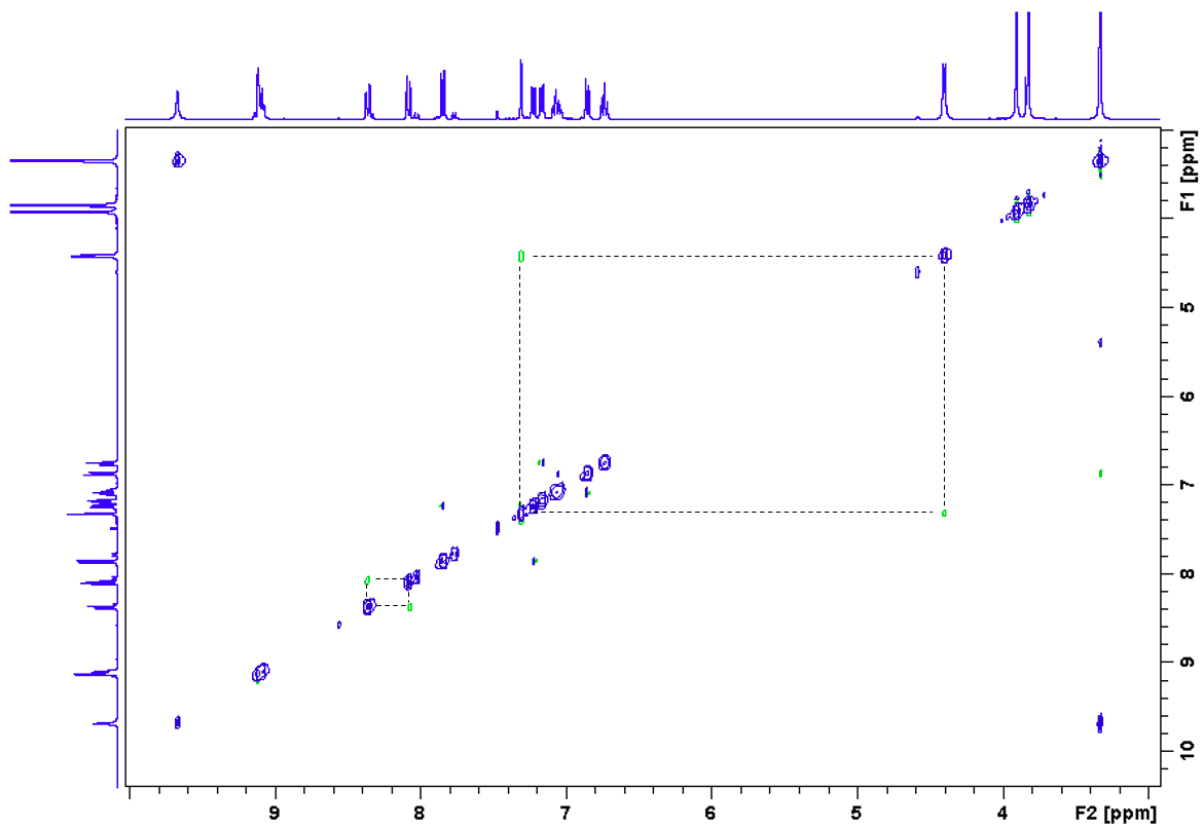


Figure 102: NOESY (400 MHz, DMSO-d<sub>6</sub>) spectrum of compound **14**.

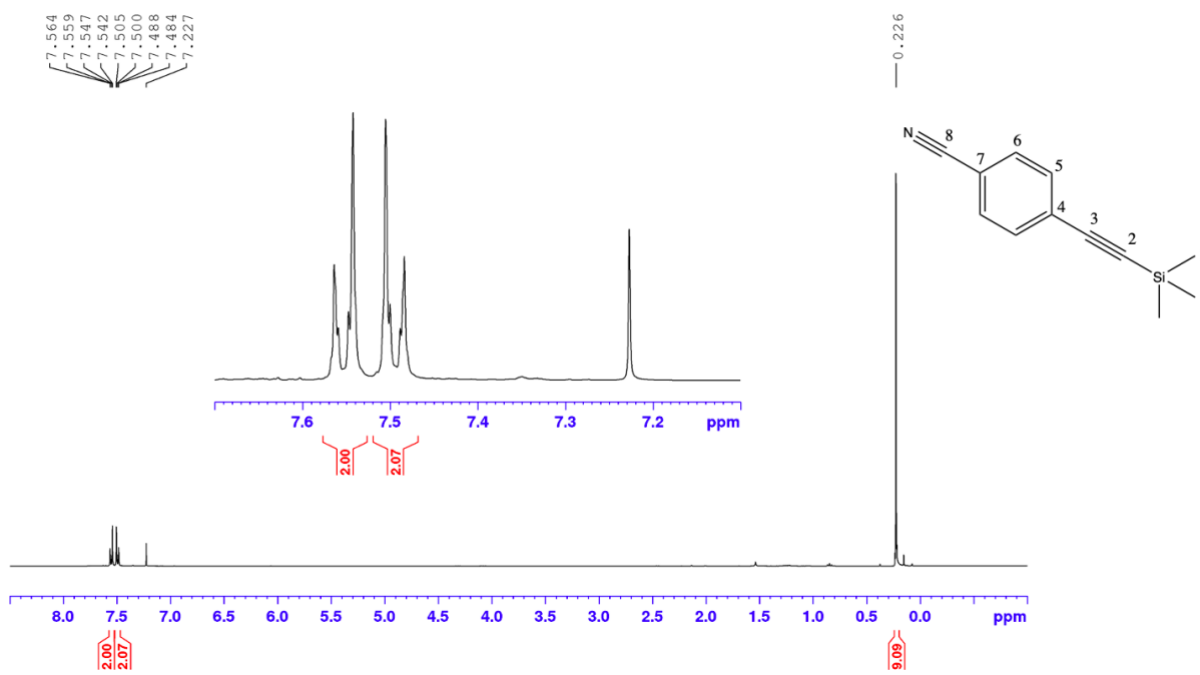


Figure 103: <sup>1</sup>H NMR (400 MHz, CDCl<sub>3</sub>) spectrum of compound **16**.

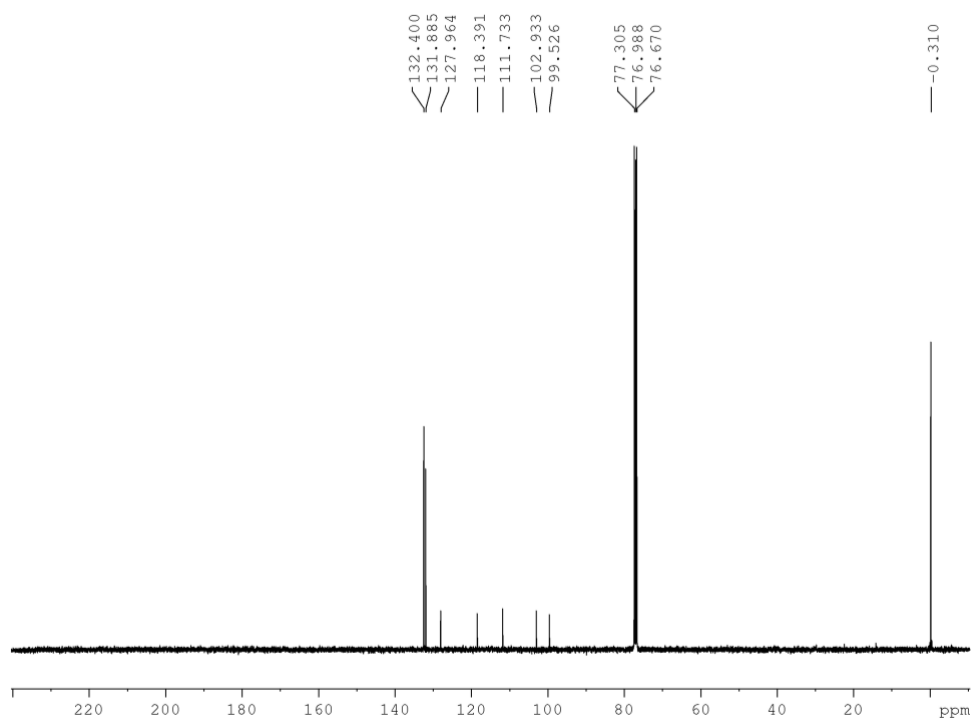


Figure 104: <sup>13</sup>C NMR (400 MHz, CDCl<sub>3</sub>) spectrum of compound **16**.

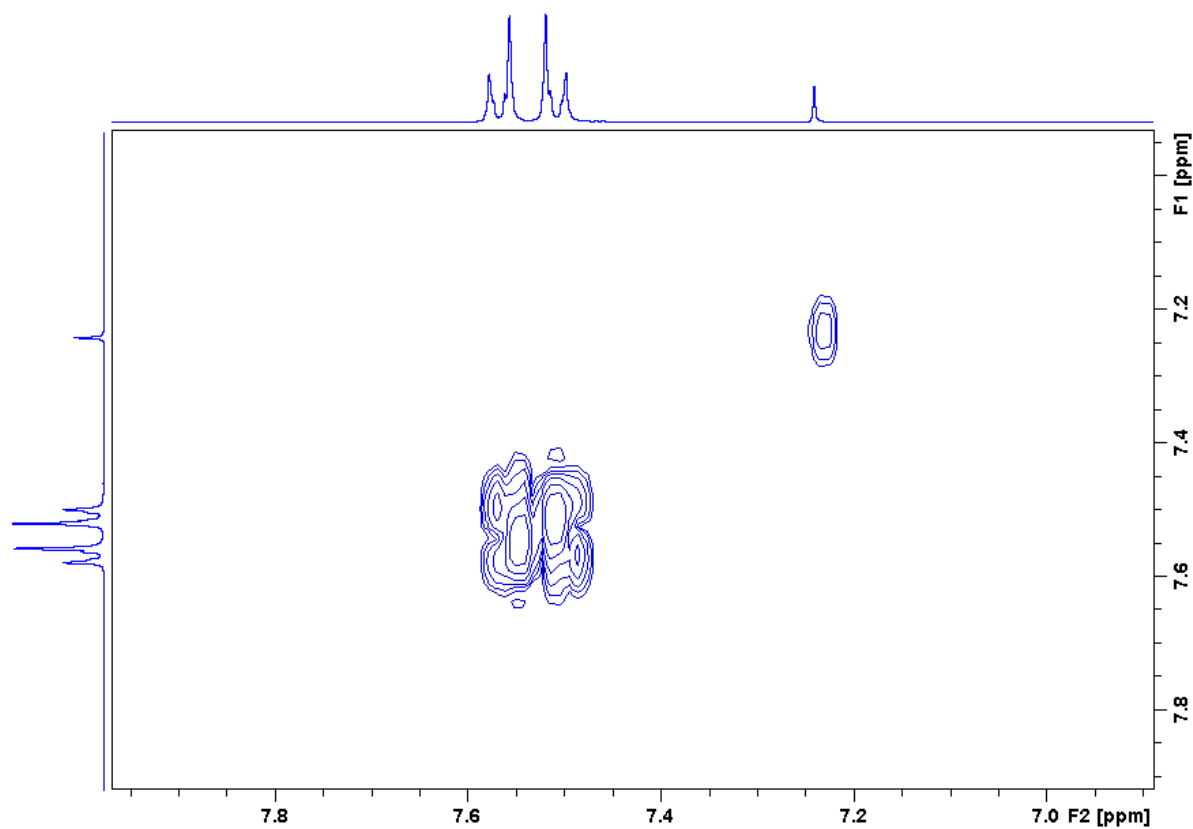


Figure 105: COSY (400 MHz,  $\text{CDCl}_3$ ) spectrum of compound **16**.

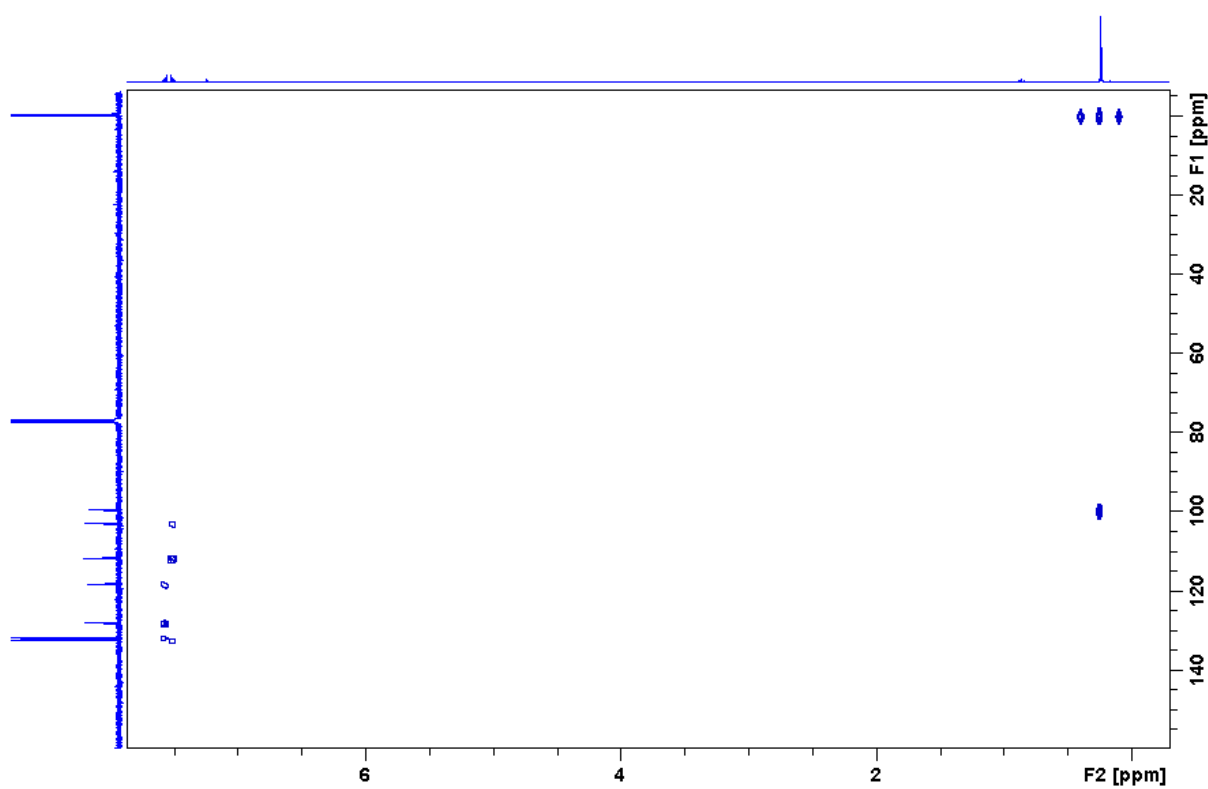


Figure 106: HMBC (400 MHz,  $\text{CDCl}_3$ ) spectrum of compound **16**.

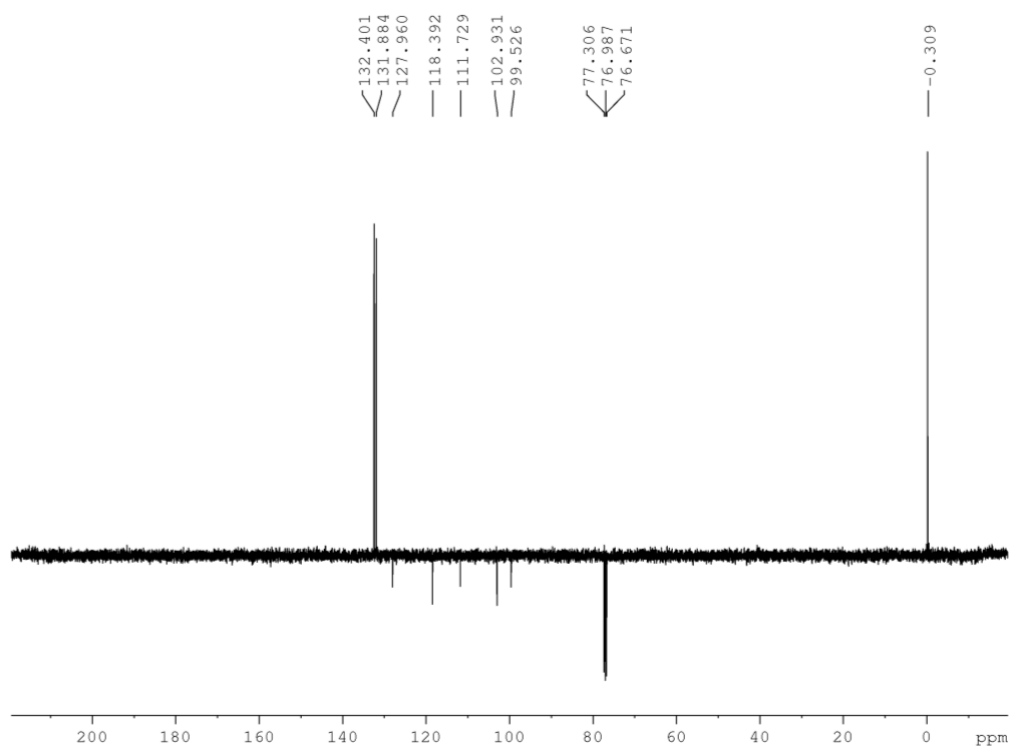


Figure 107: DEPT135Q (400 MHz,  $\text{CDCl}_3$ ) NMR spectrum of compound **16**, with CH,  $\text{CH}_3$  phased positive, and C phased negative.



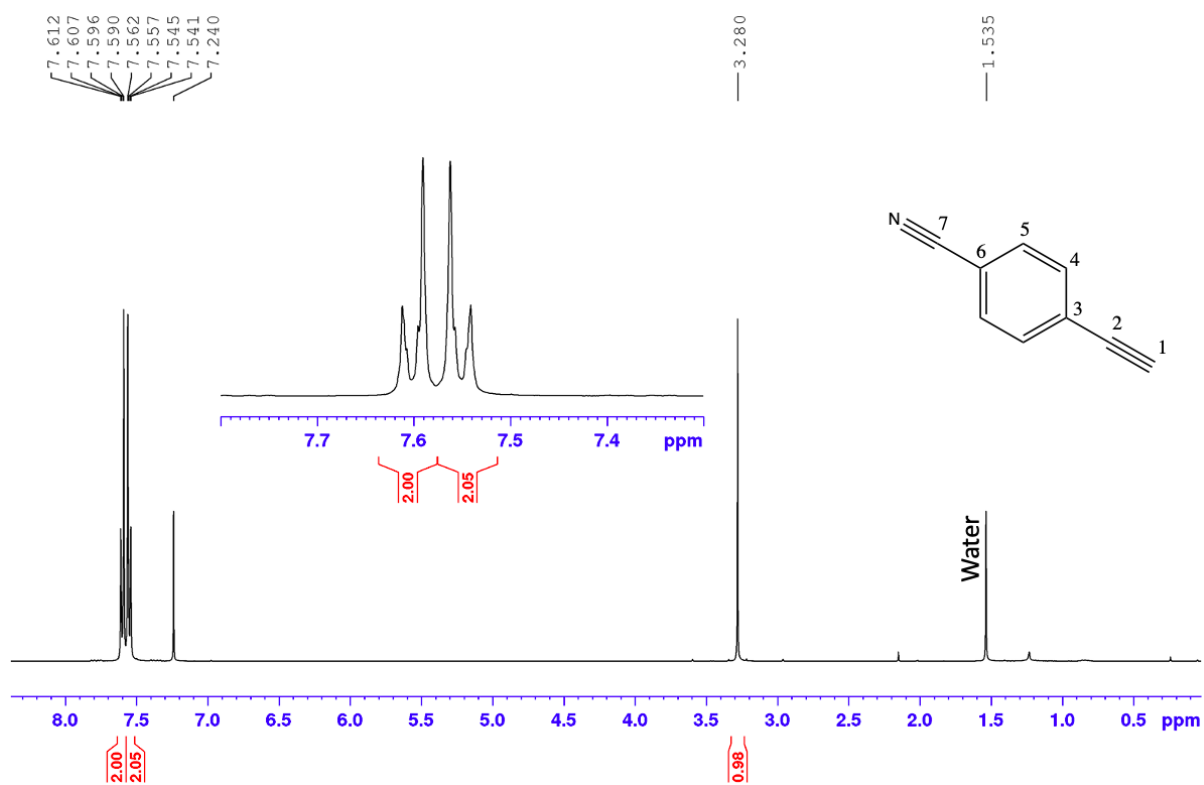


Figure 108: <sup>1</sup>H NMR (400 MHz, CDCl<sub>3</sub>) spectrum of compound **17**.

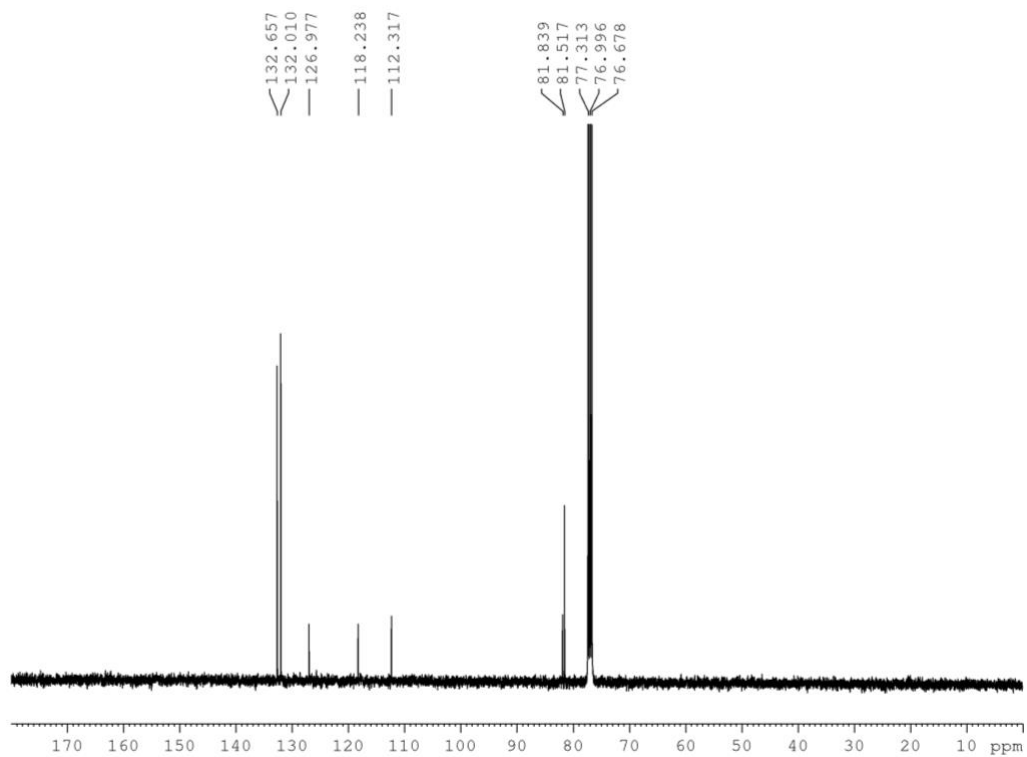


Figure 109: <sup>13</sup>C NMR (400 MHz, CDCl<sub>3</sub>) spectrum of compound **17**.

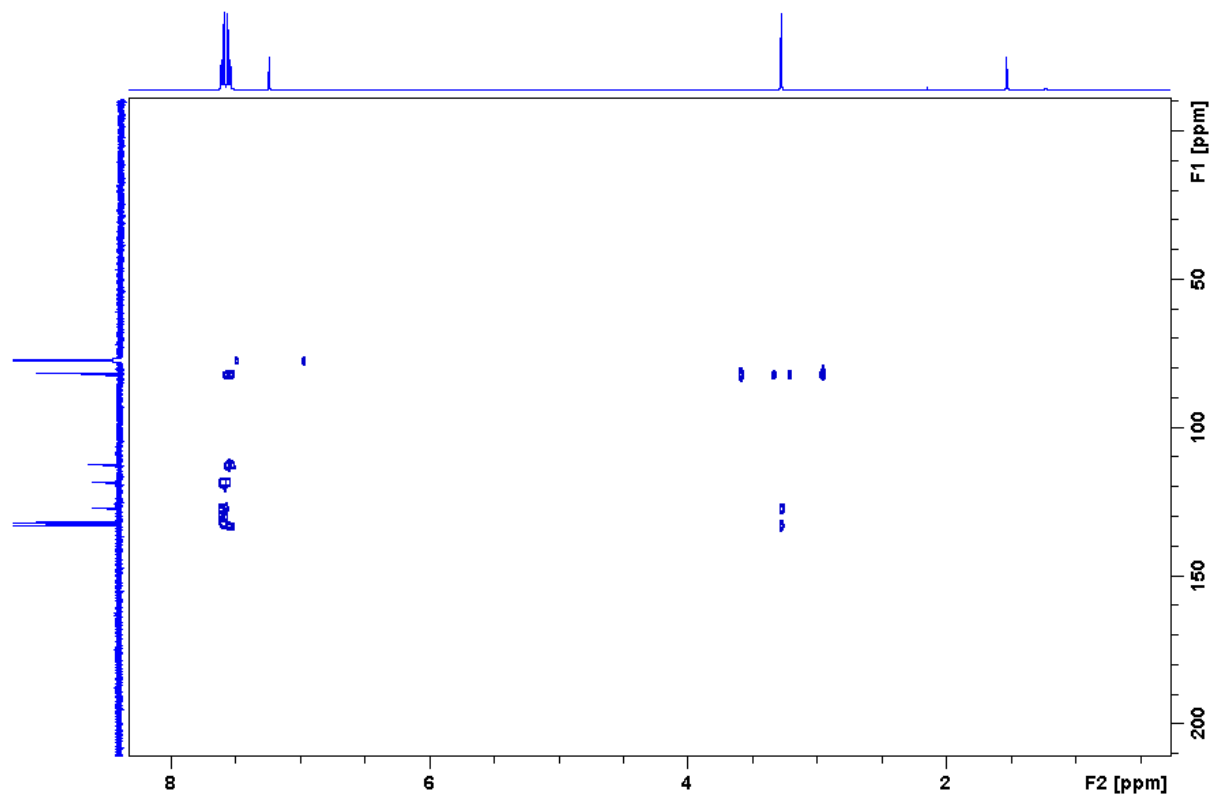


Figure 110: HMBC (400 MHz, CDCl<sub>3</sub>) spectrum of compound **17**.

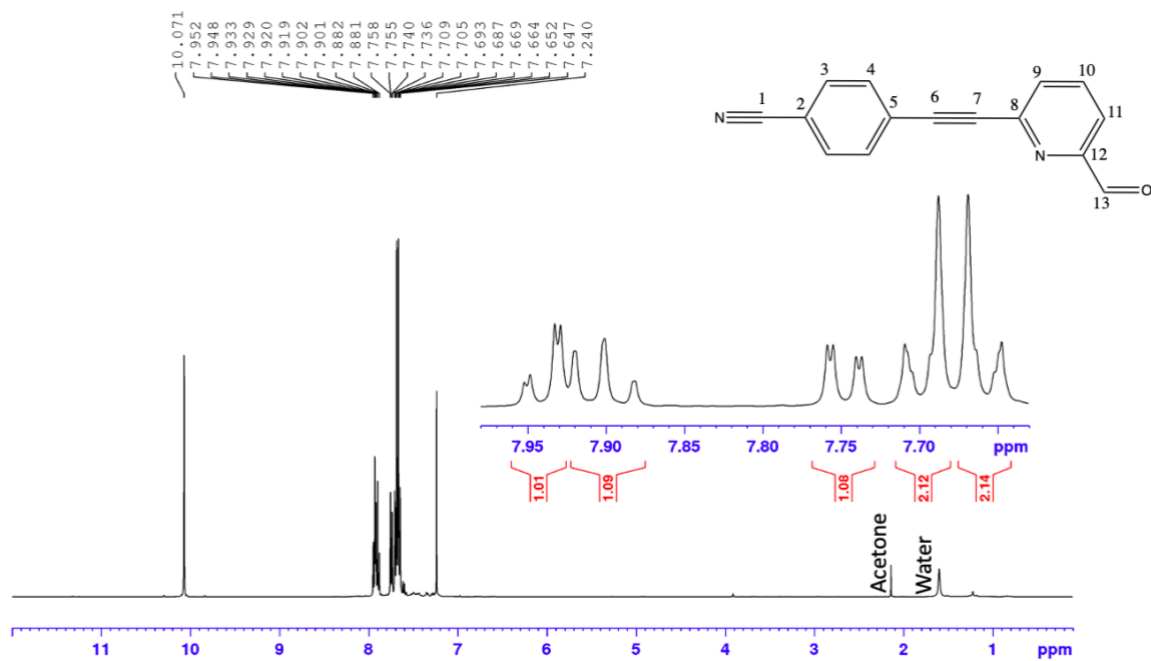


Figure 111: <sup>1</sup>H NMR (400 MHz, CDCl<sub>3</sub>) spectrum of compound **18**.

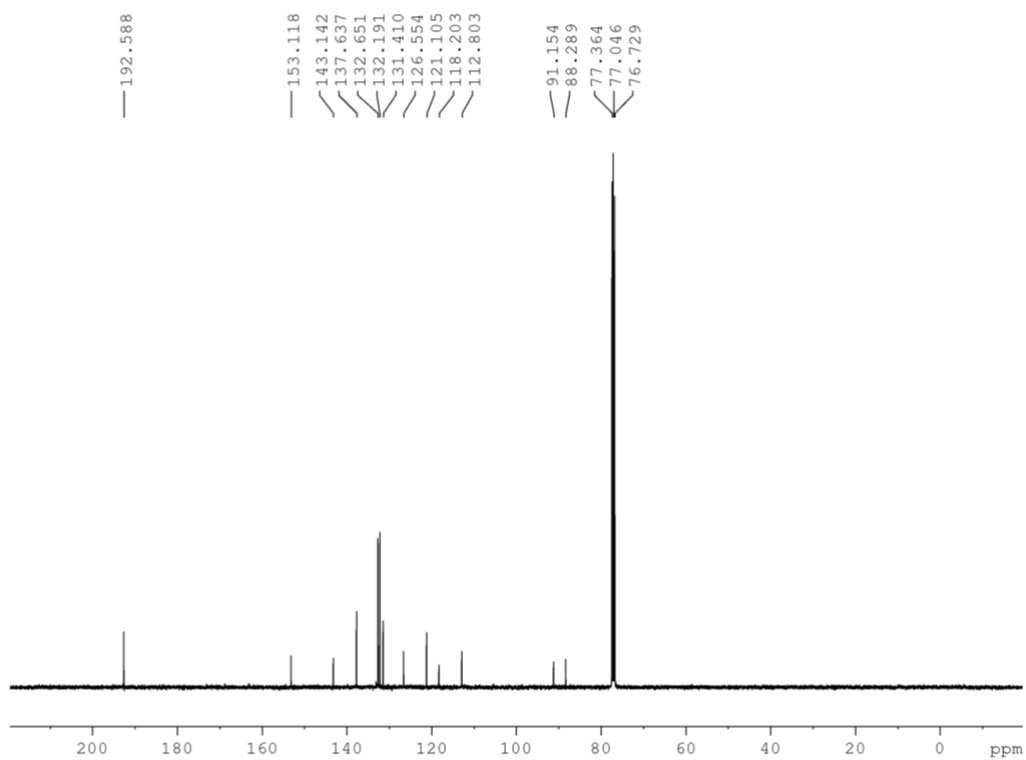


Figure 112: <sup>13</sup>C NMR (400 MHz, CDCl<sub>3</sub>) spectrum of compound **18**.

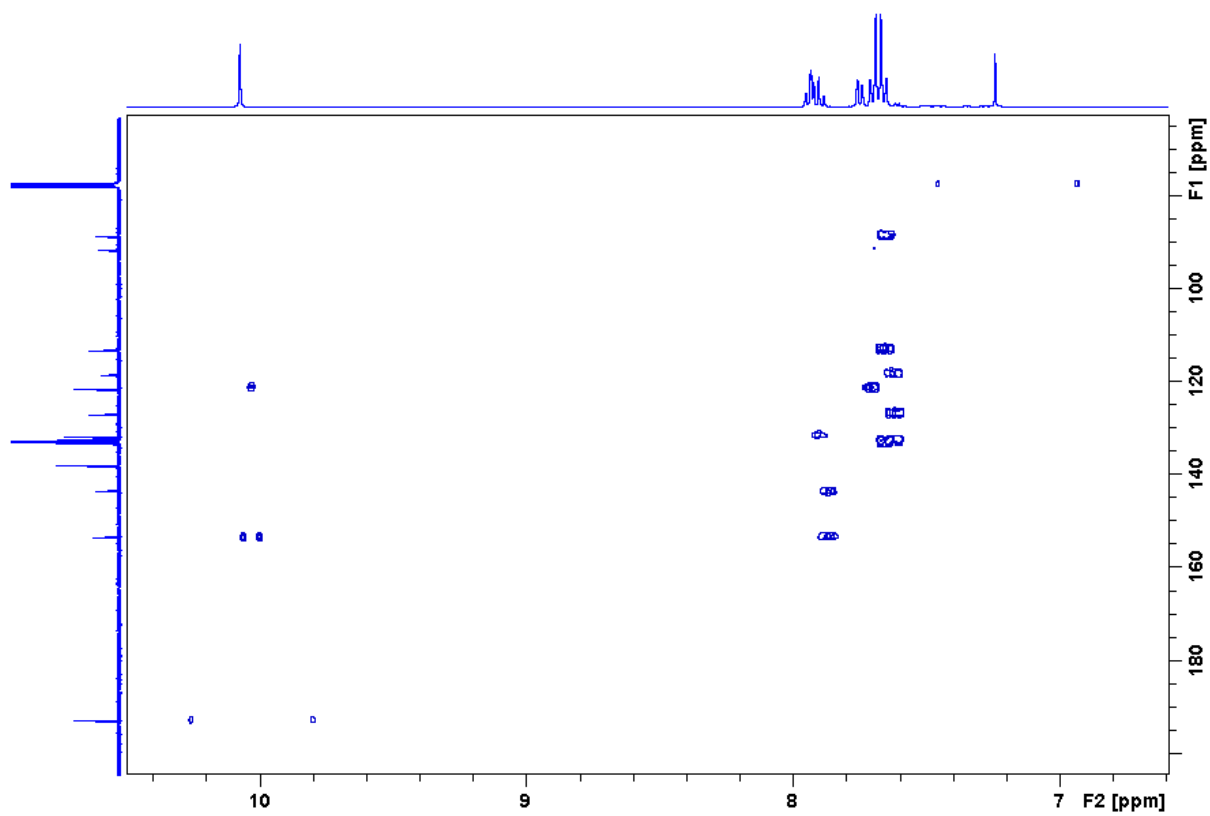


Figure 113: HMBC (400 MHz, CDCl<sub>3</sub>) spectrum of compound **18** (zomed at the aromatic region).

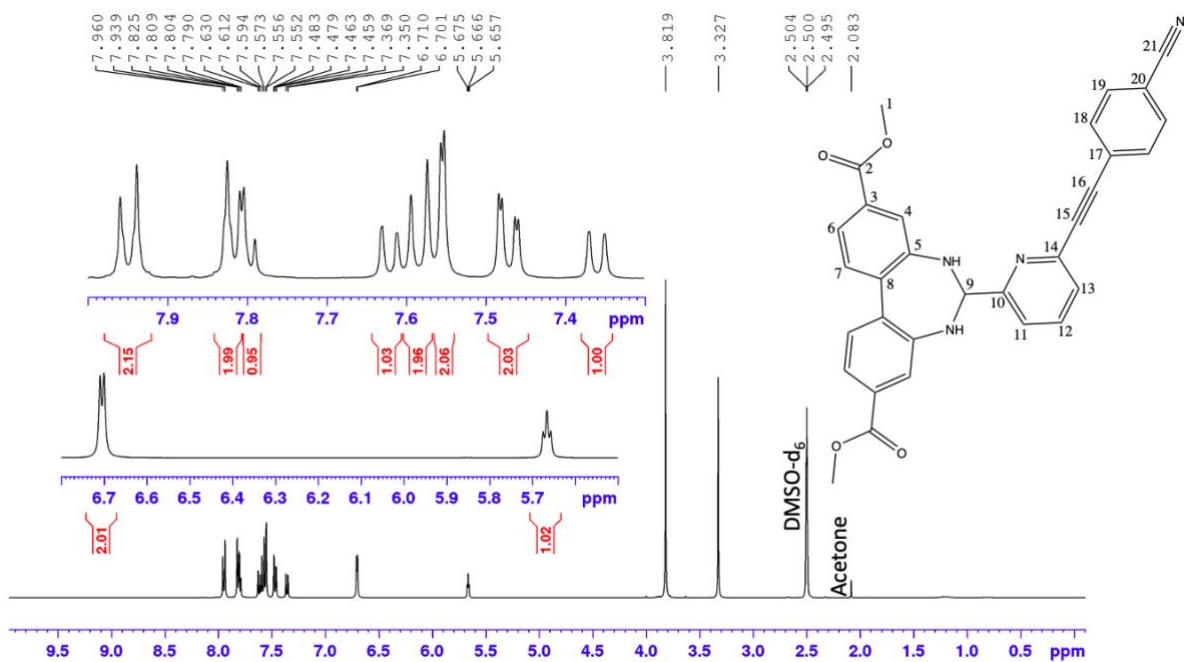


Figure 114: <sup>1</sup>H NMR (400 MHz, DMSO-d<sub>6</sub>) spectrum of compound 19.

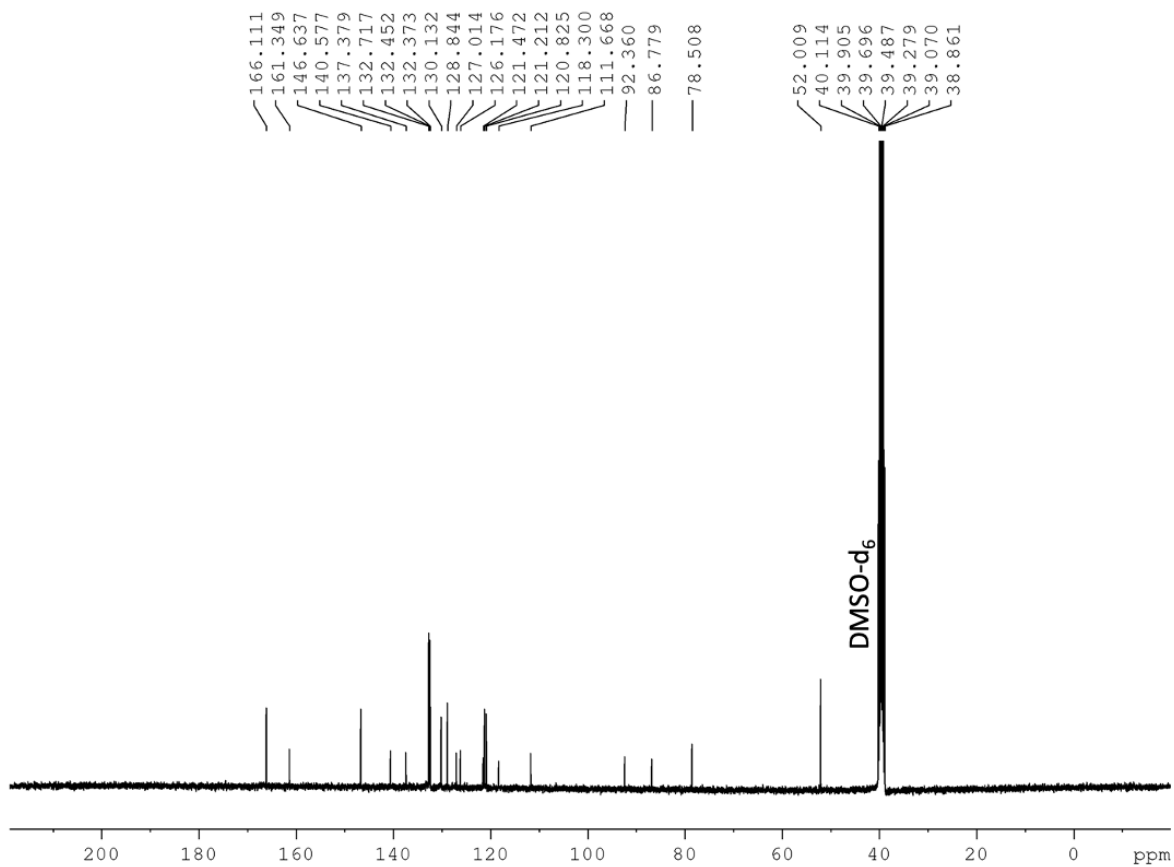


Figure 115: <sup>13</sup>C NMR (400 MHz, DMSO-d<sub>6</sub>) spectrum of compound 19.

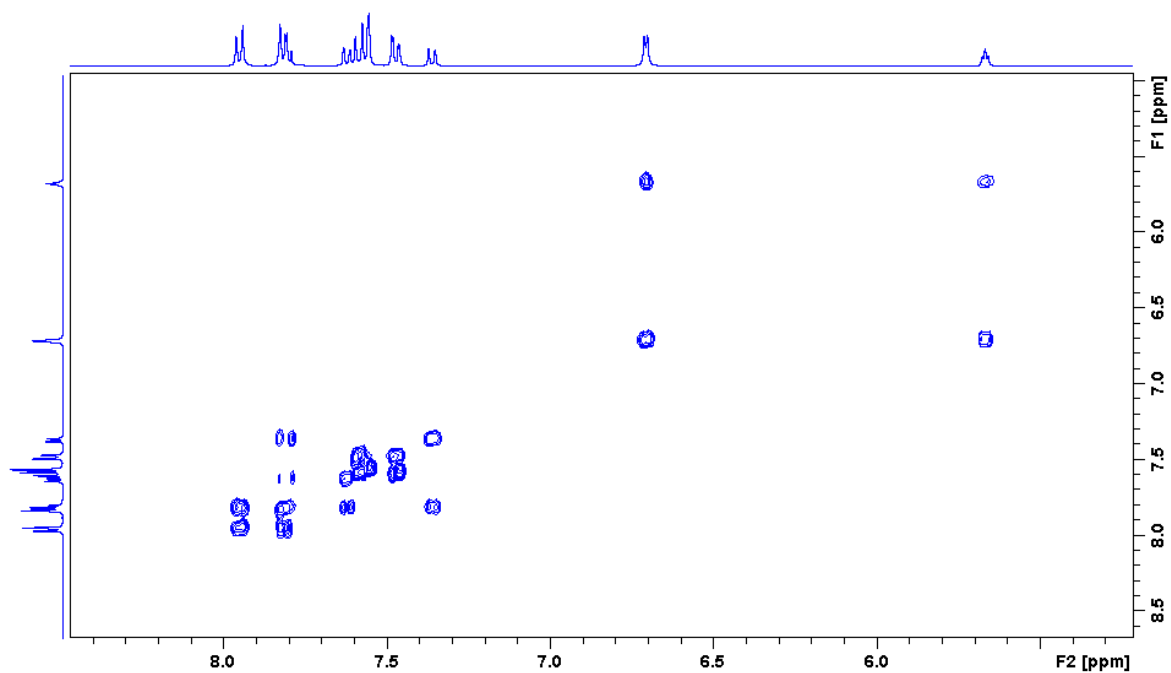


Figure 116: COSY (400 MHz, DMSO-d<sub>6</sub>) spectrum of compound **19**.

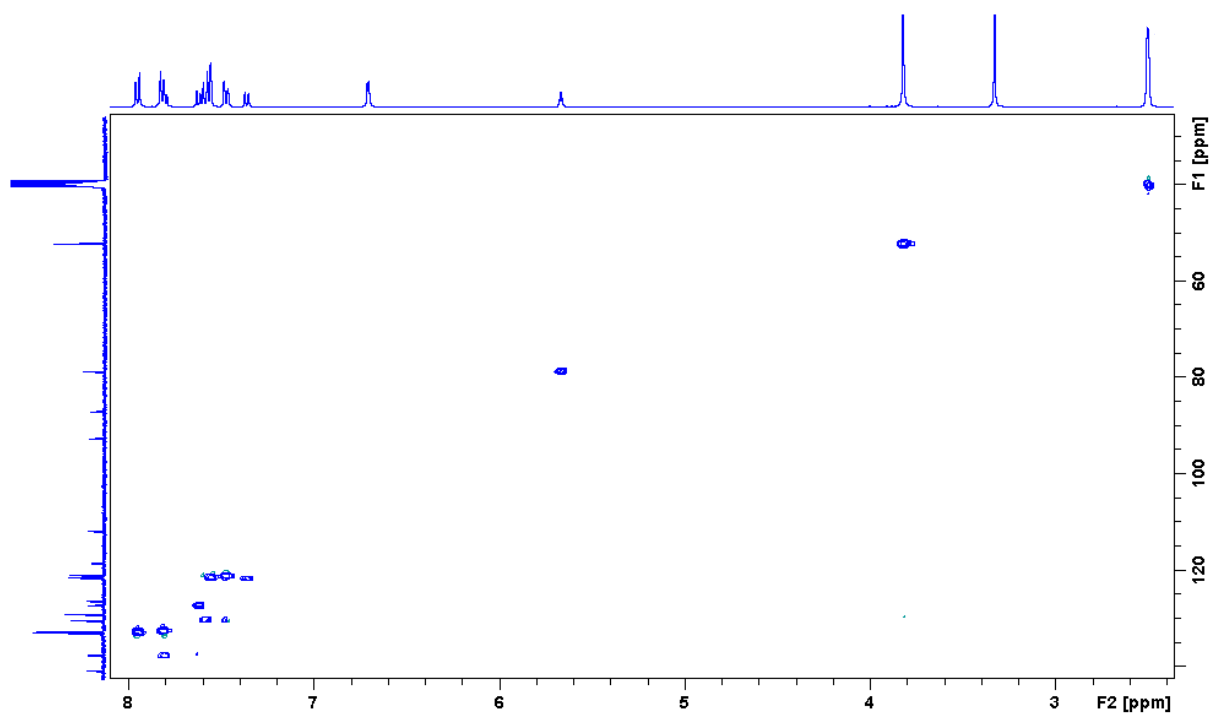


Figure 117: HSQC (400 MHz, DMSO-d<sub>6</sub>) spectrum of compound **19**.

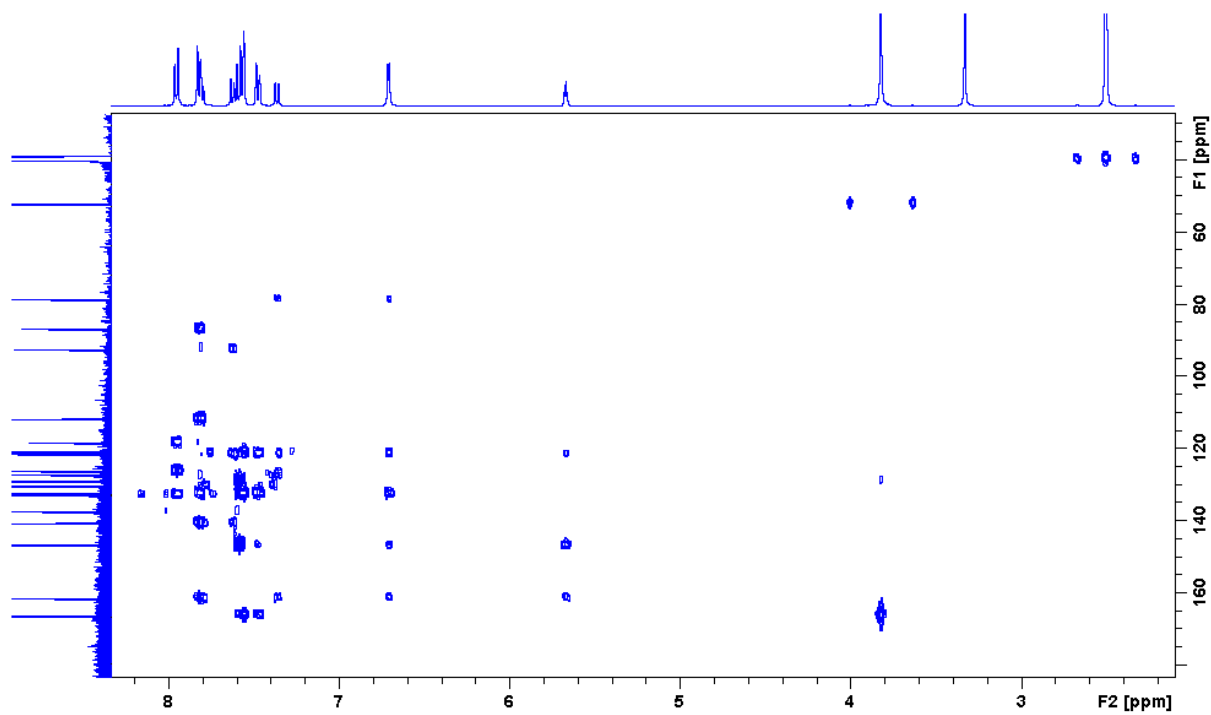


Figure 118: HMBC (400 MHz, DMSO- $d_6$ ) spectrum of compound **19**.

## 6.2 A.2 UV-Vis data

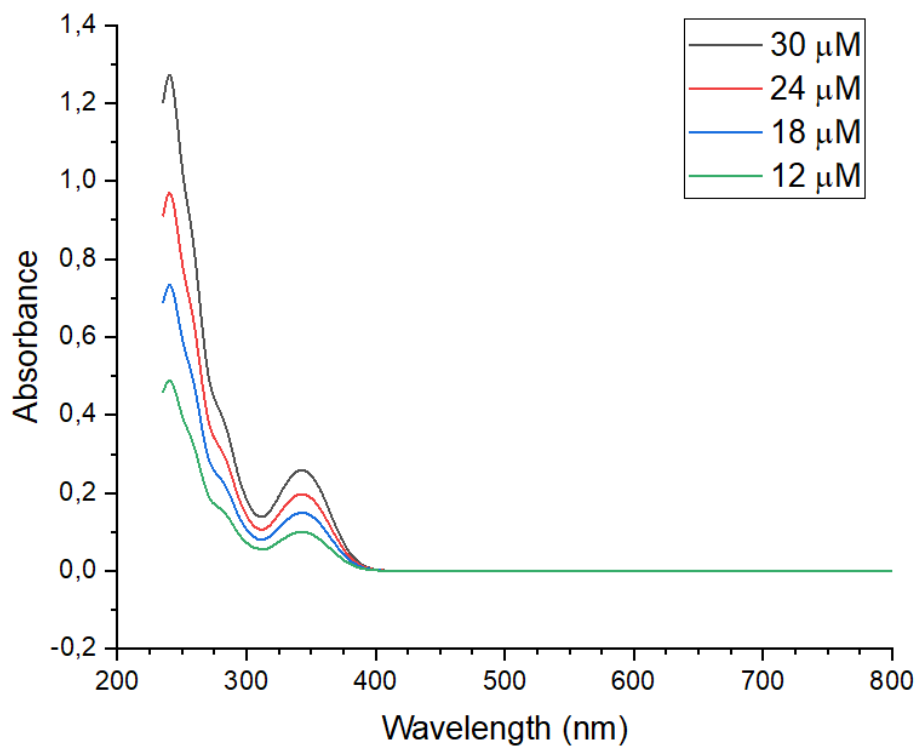


Figure 119: UV-vis spectrum of **3** at different concentrations in CH<sub>2</sub>Cl<sub>2</sub>.



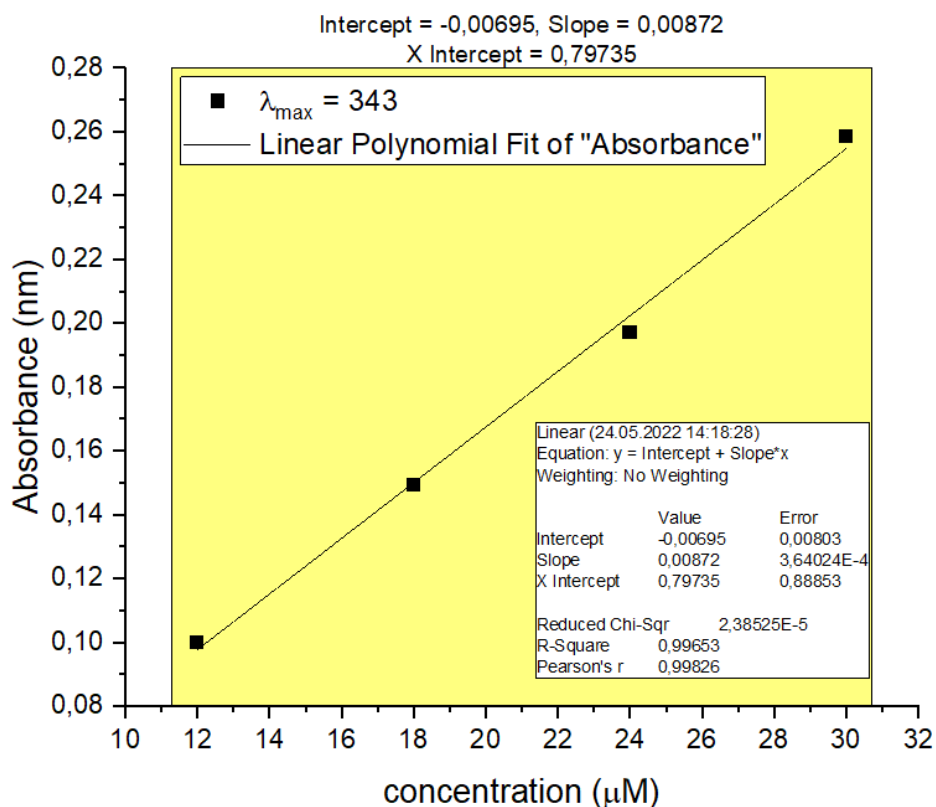


Figure 120: UV-vis linear regression for compound **3** in  $\text{CH}_2\text{Cl}_2$  at 343 nm,  $\epsilon = 8720 \text{ M}^{-1}\text{cm}^{-1}$ .

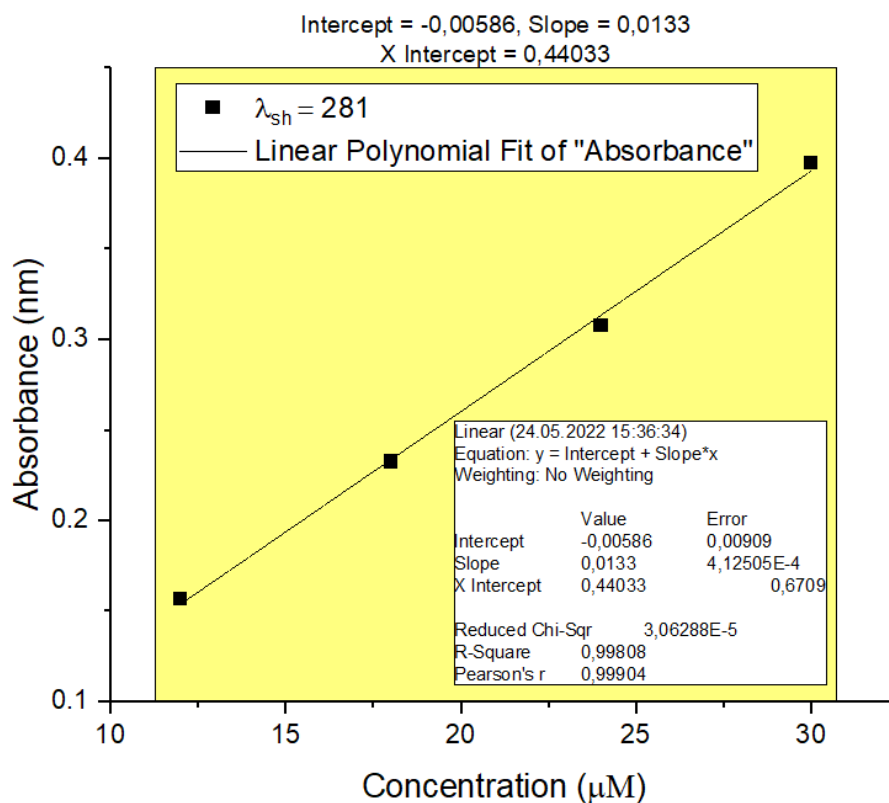


Figure 121: UV-vis linear regression for compound **3** in  $\text{CH}_2\text{Cl}_2$  at 281 nm,  $\epsilon = 13300 \text{ M}^{-1}\text{cm}^{-1}$ .

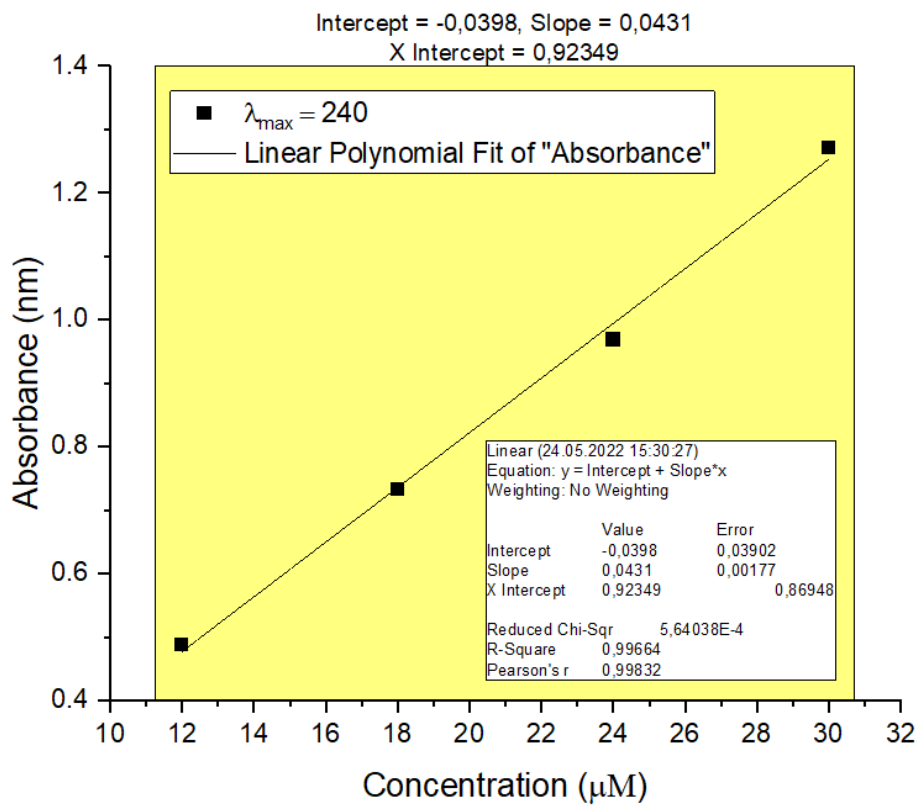


Figure 122: UV-vis linear regression for compound **3** in  $\text{CH}_2\text{Cl}_2$  at 240 nm,  $\epsilon = 43100 \text{ M}^{-1}\text{cm}^{-1}$ .

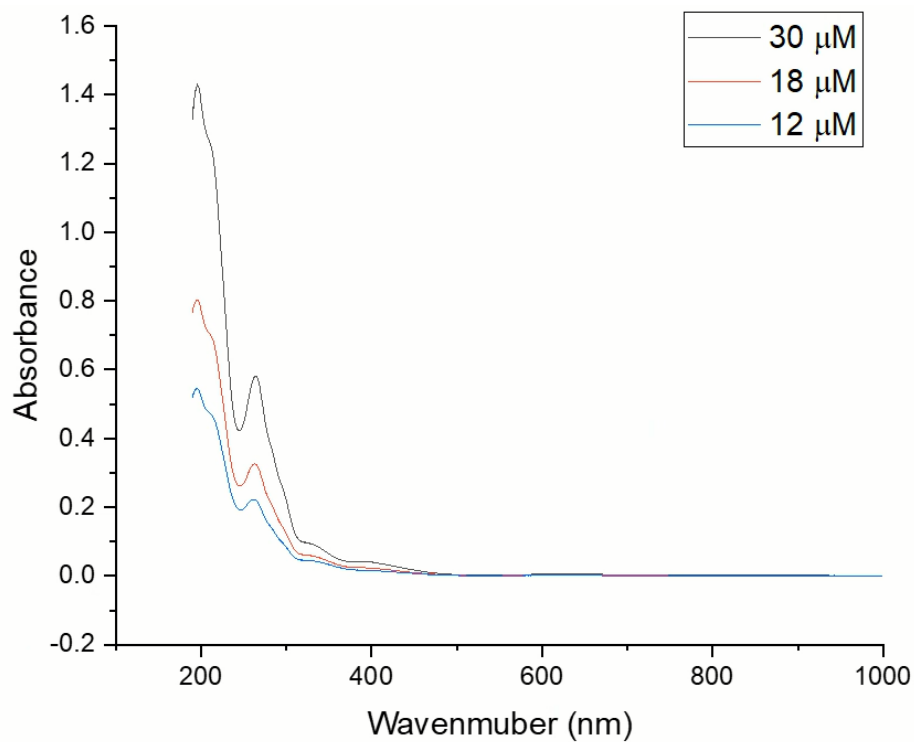


Figure 123: UV-vis spectrum of **5** at different concentrations in MeCN.

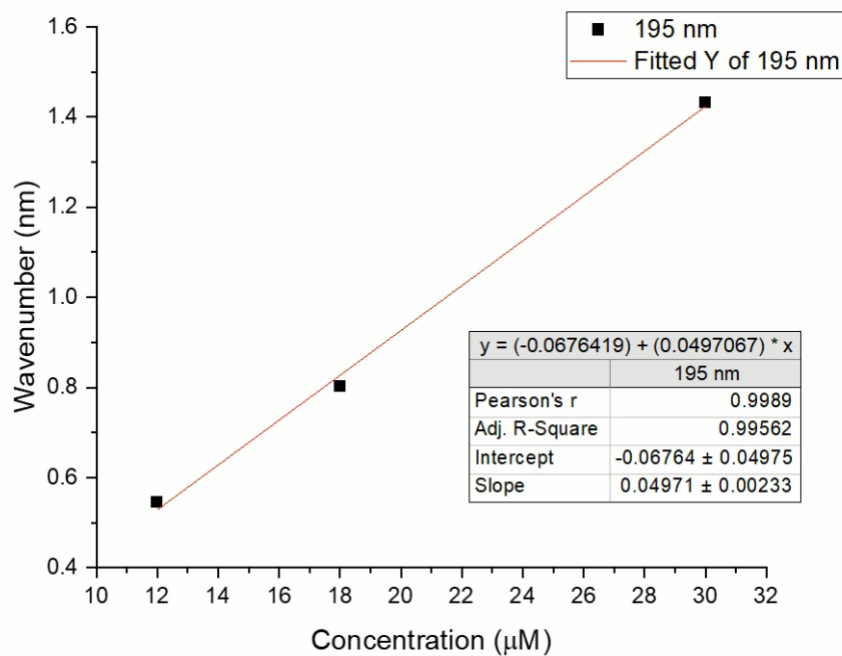


Figure 124: UV-vis linear regression for compound **5** in MeCN at 195 nm,  $\epsilon = 49710 \text{ M}^{-1}\text{cm}^{-1}$ .

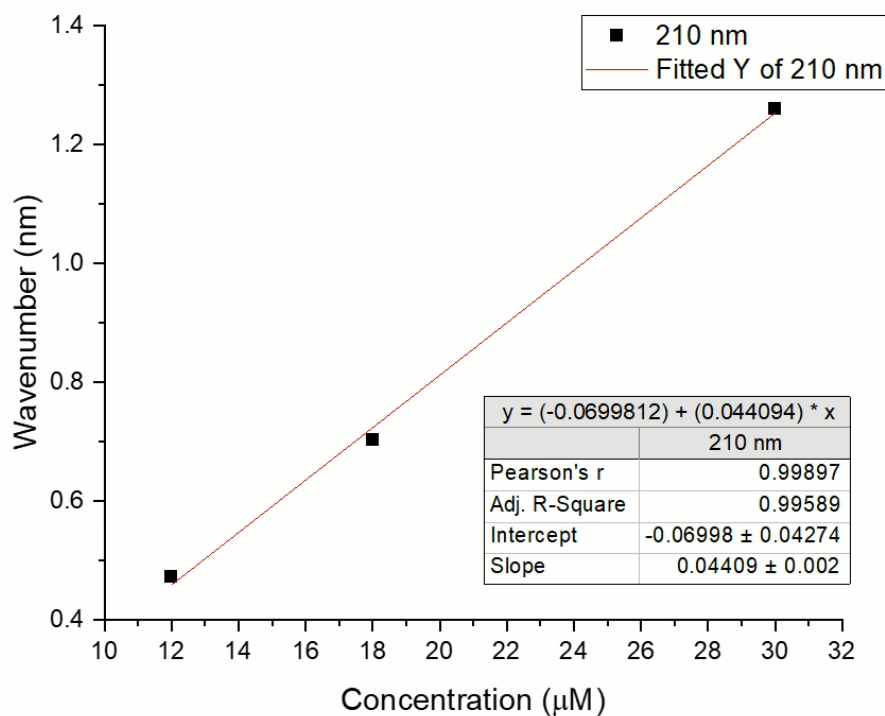


Figure 125: UV-vis linear regression for compound **5** in MeCN at 210 nm,  $\epsilon = 44090 \text{ M}^{-1}\text{cm}^{-1}$ .

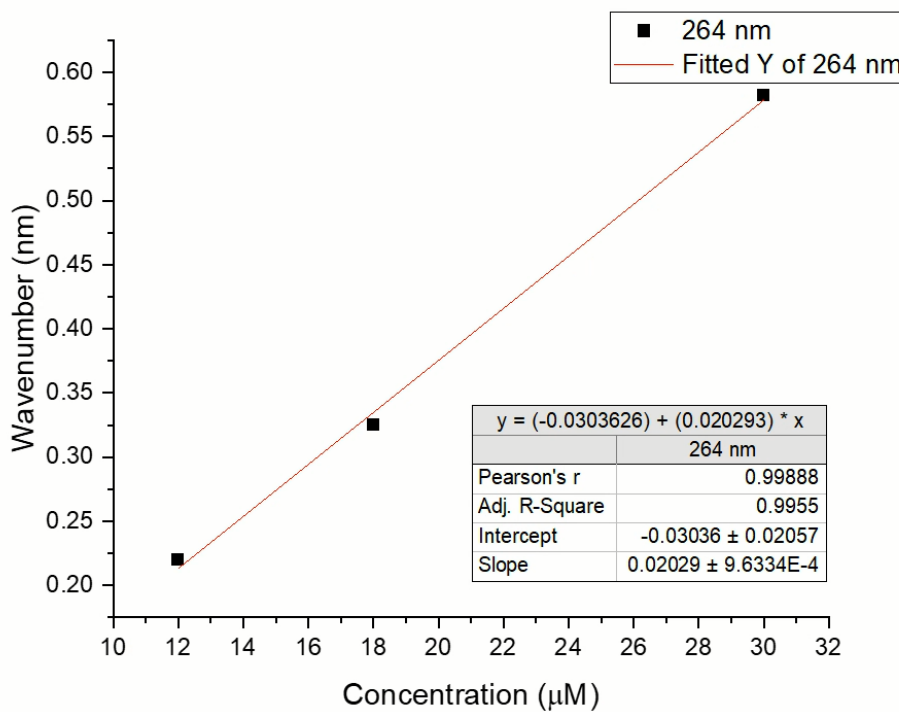


Figure 126: UV-vis linear regression for compound **5** in MeCN at 264 nm,  $\epsilon = 20290 \text{ M}^{-1}\text{cm}^{-1}$ .

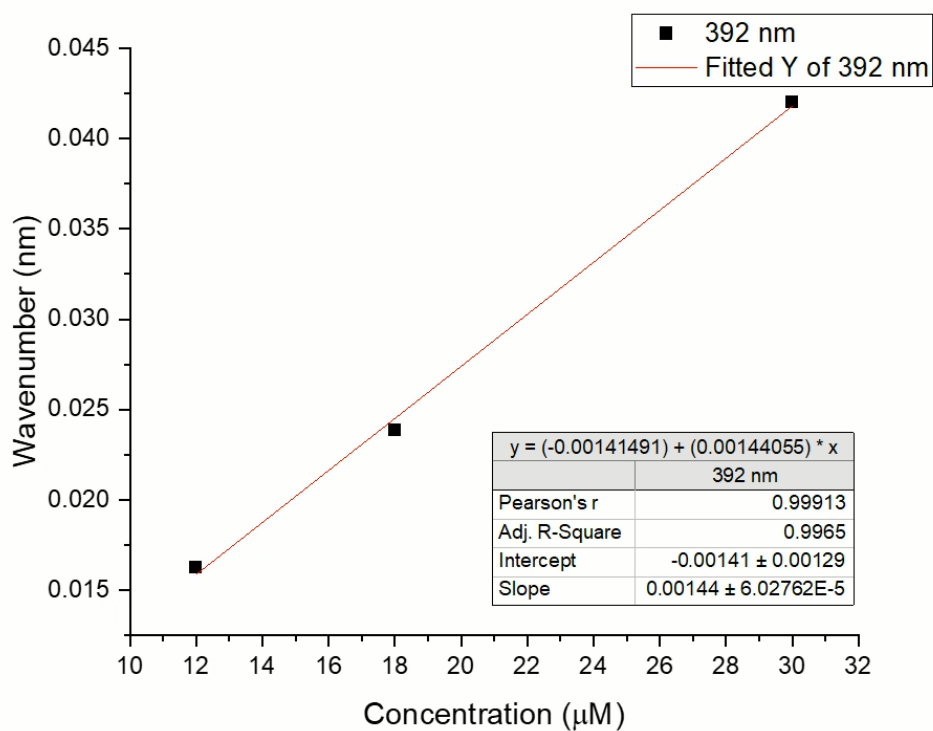


Figure 127: UV-vis linear regression for compound **5** in MeCN at 392 nm,  $\epsilon = 1440 \text{ M}^{-1}\text{cm}^{-1}$ .

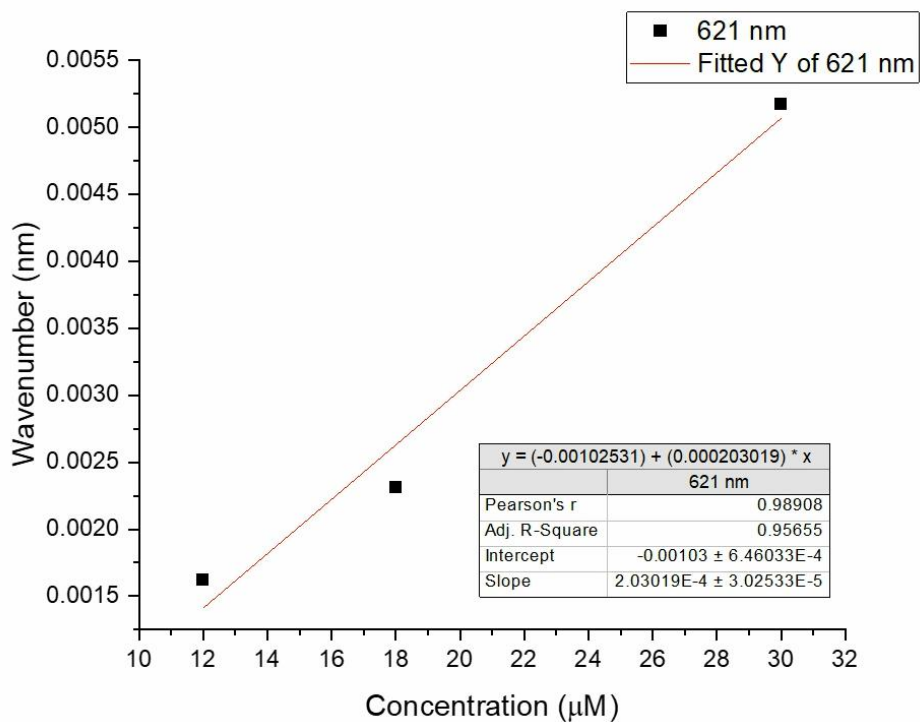


Figure 128: UV-vis linear regression for compound **5** in MeCN at 621 nm,  $\epsilon = 1440 \text{ M}^{-1}\text{cm}^{-1}$ .

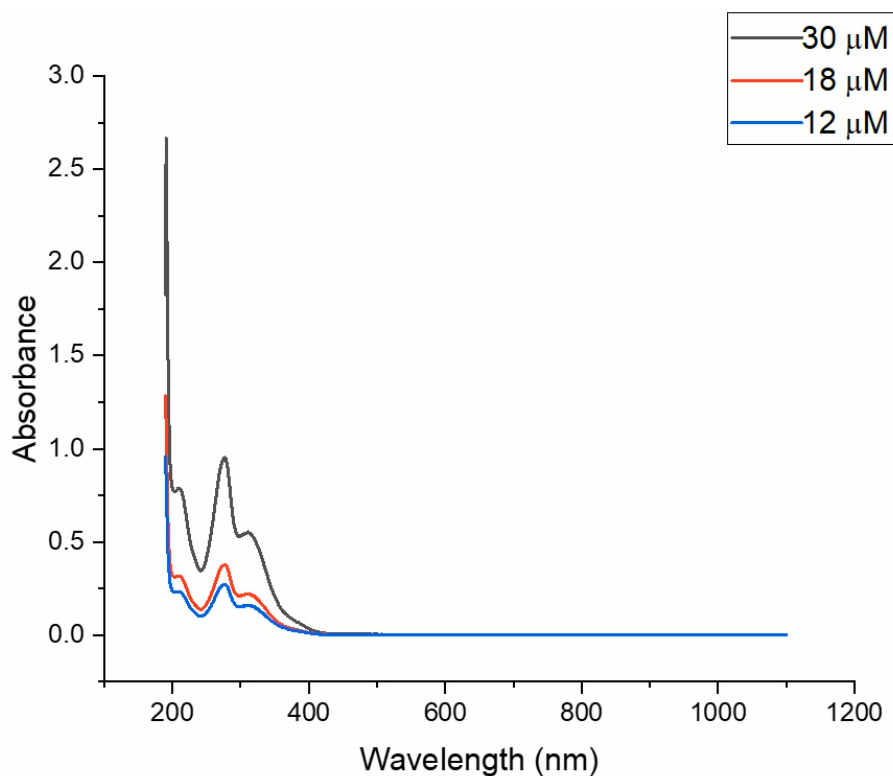


Figure 129: UV-vis spectrum of **8** at different concentrations in MeCN.

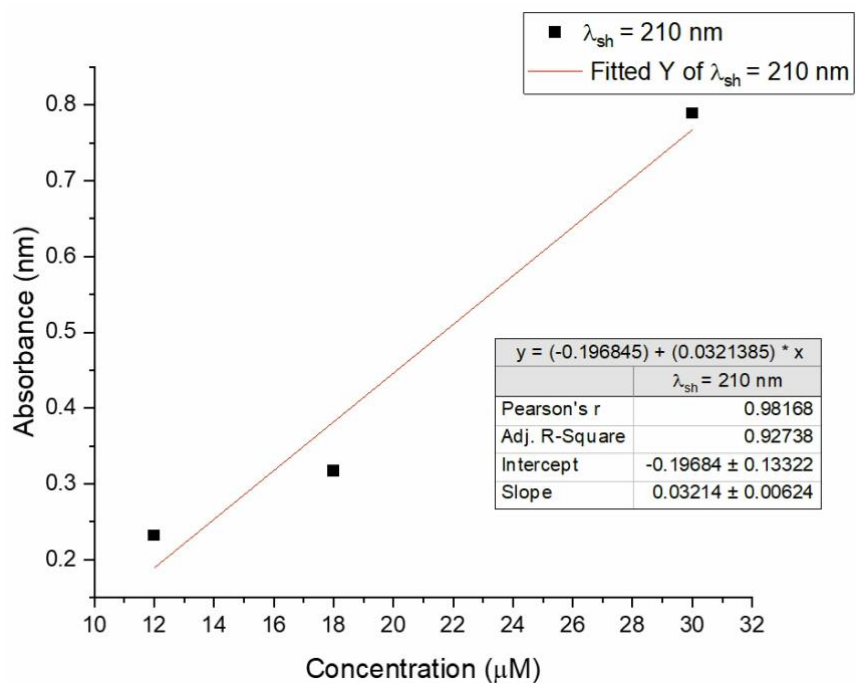


Figure 130: UV-vis linear regression for compound **8** in MeCN at 210 nm,  $\epsilon = 32140 \text{ M}^{-1}\text{cm}^{-1}$ .

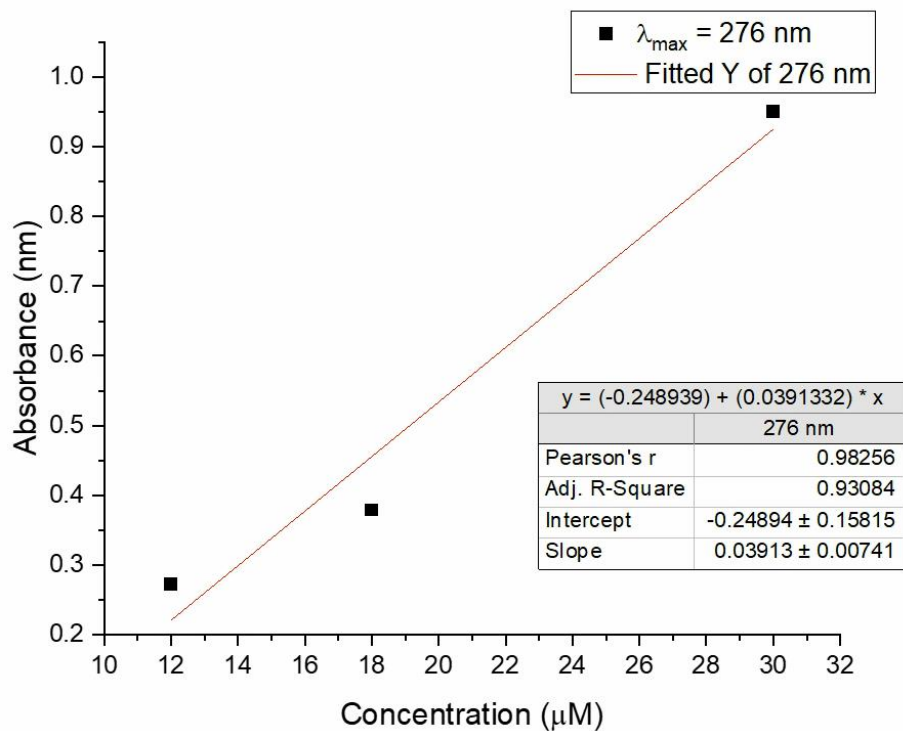


Figure 131: UV-vis linear regression for compound **8** in MeCN at 276 nm,  $\epsilon = 39130 \text{ M}^{-1}\text{cm}^{-1}$ .

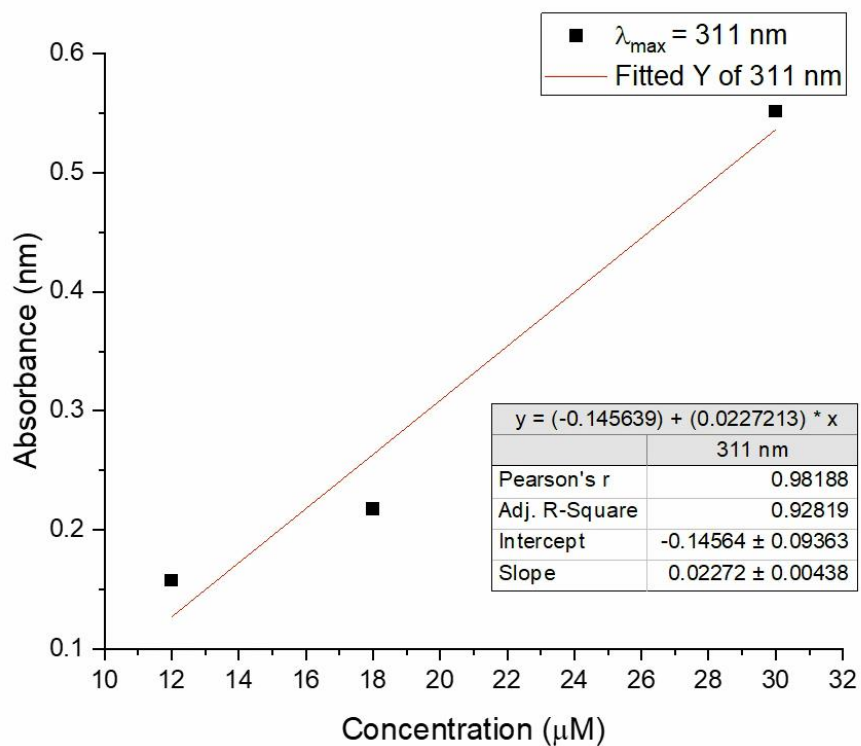


Figure 132: UV-vis linear regression for compound **8** in MeCN at 311 nm,  $\epsilon = 22720 \text{ M}^{-1}\text{cm}^{-1}$ .

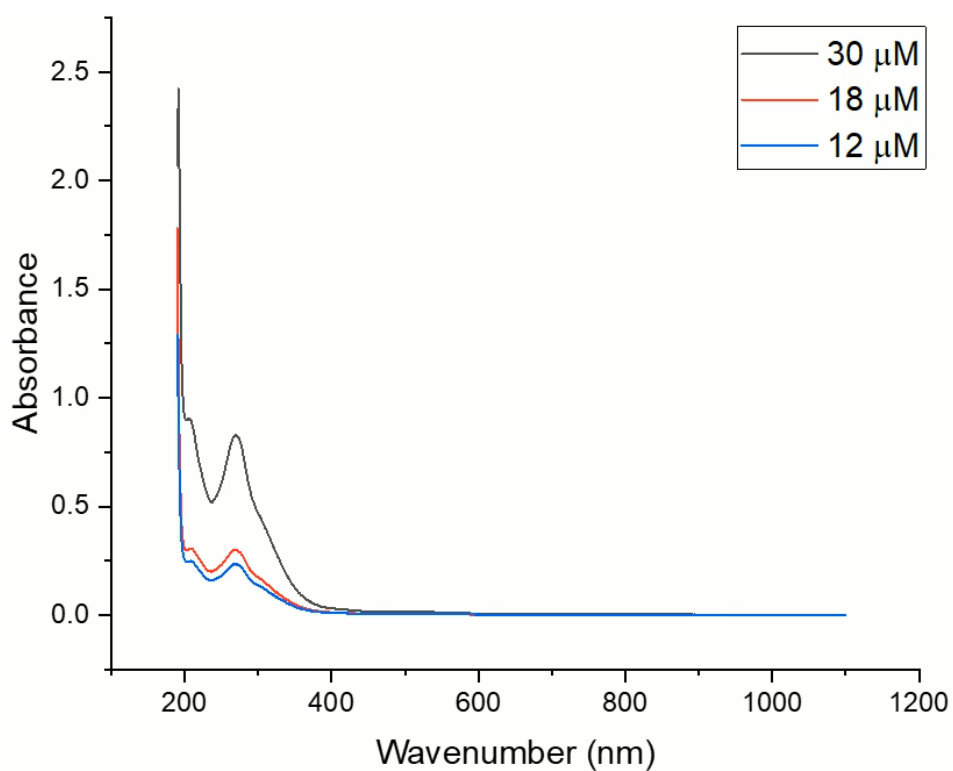


Figure 133: UV-vis spectrum of **10** at different concentrations in MeCN.

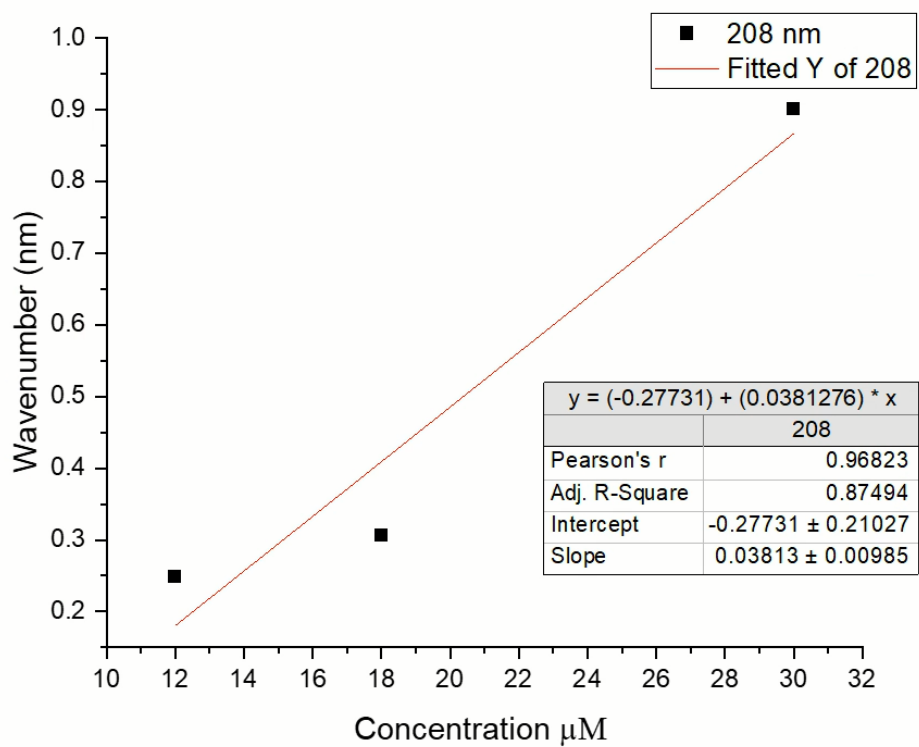


Figure 134: UV-vis linear regression for compound **10** in MeCN at 208 nm,  $\epsilon = 38130 \text{ M}^{-1}\text{cm}^{-1}$ .



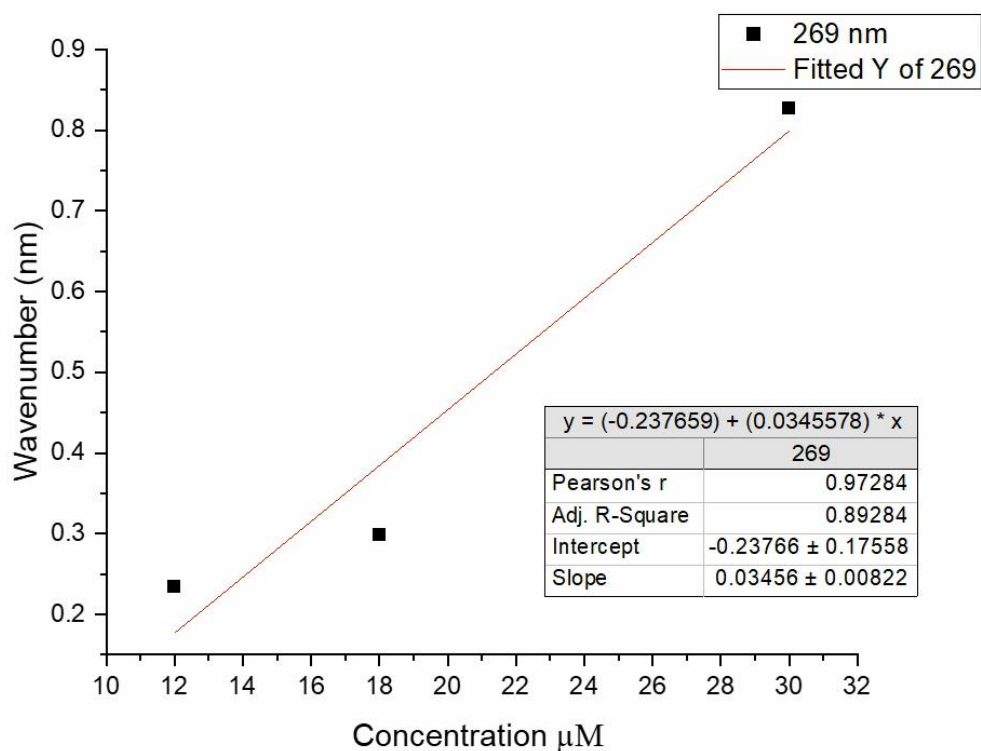


Figure 135: UV-vis linear regression for compound **10** in MeCN at 269 nm,  $\epsilon = 34560 \text{ M}^{-1}\text{cm}^{-1}$ .

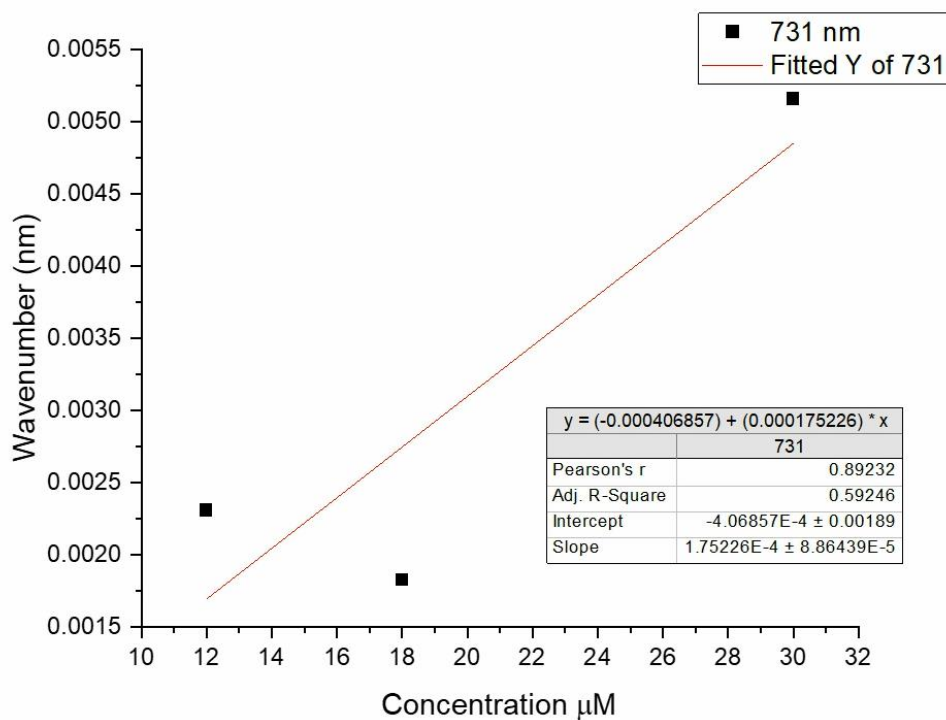


Figure 136: UV-vis linear regression for compound **10** in MeCN at 731 nm,  $\epsilon = 175 \text{ M}^{-1}\text{cm}^{-1}$ .

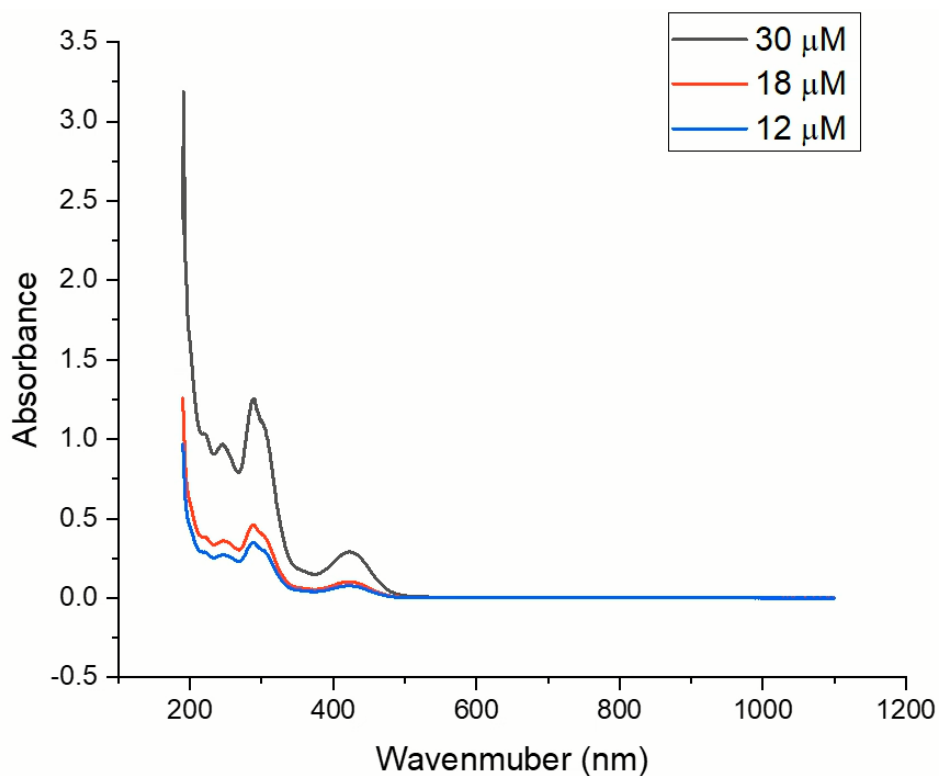


Figure 137: UV-vis spectrum of **15** at different concentrations in MeCN.

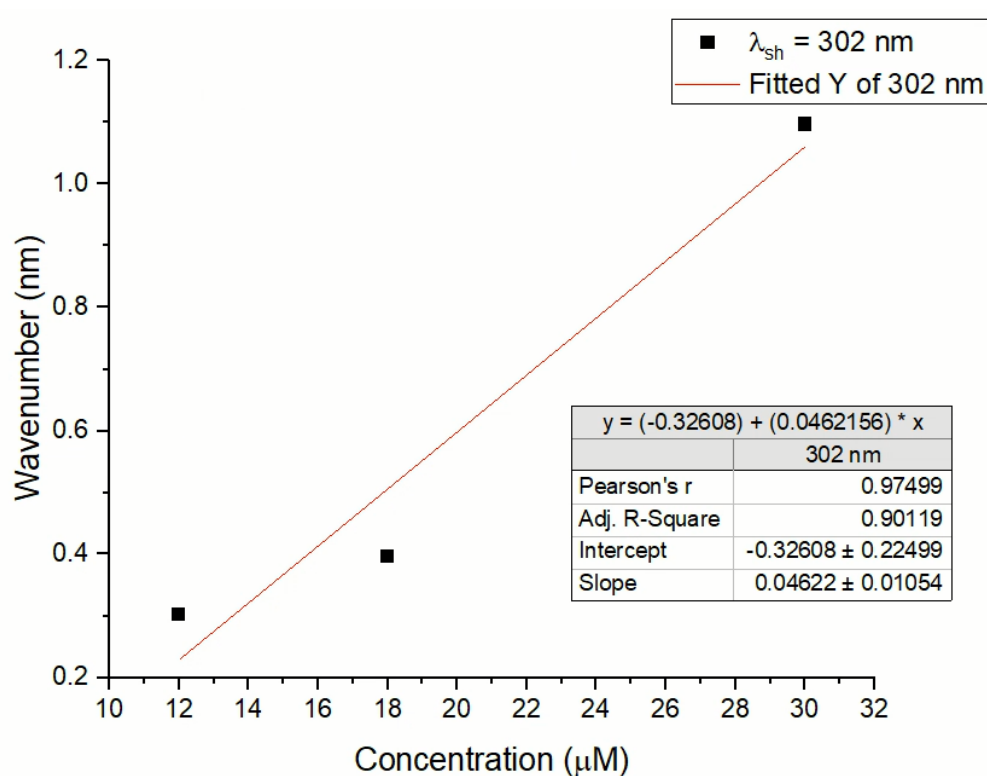


Figure 138: UV-vis linear regression for compound **15** in MeCN at 302 nm,  $\epsilon = 46220 \text{ M}^{-1}\text{cm}^{-1}$ .

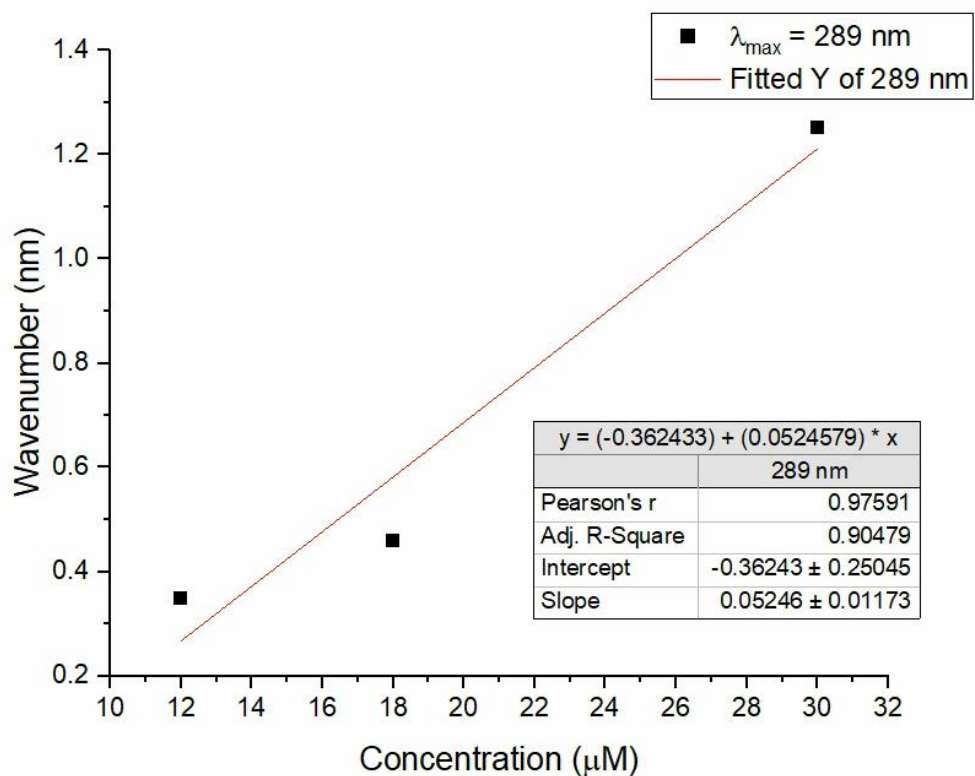


Figure 139: UV-vis linear regression for compound **15** in MeCN at 289 nm,  $\epsilon = 52460 \text{ M}^{-1}\text{cm}^{-1}$ .

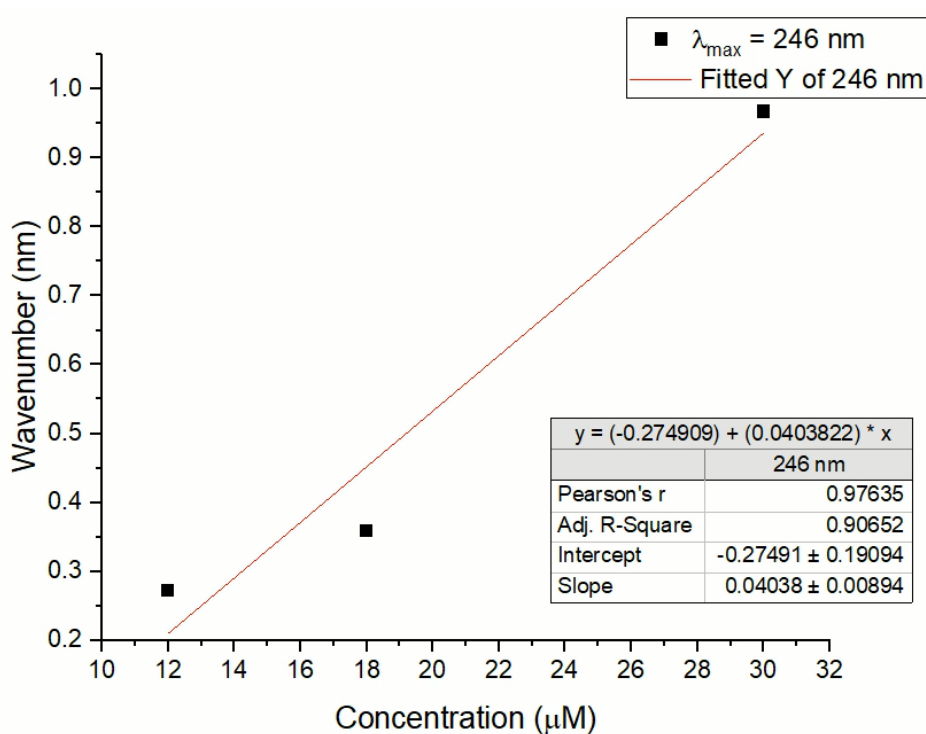


Figure 140: UV-vis linear regression for compound **15** in MeCN at 246 nm,  $\epsilon = 40380 \text{ M}^{-1}\text{cm}^{-1}$ .

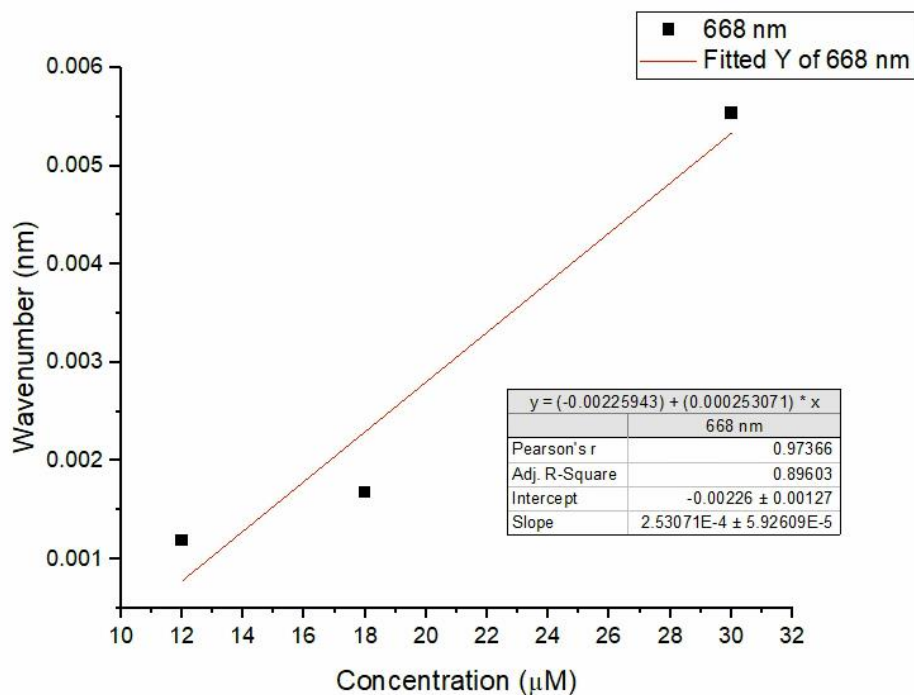


Figure 141: UV-vis linear regression for compound **15** in MeCN at 668 nm,  $\epsilon = 253 \text{ M}^{-1}\text{cm}^{-1}$ .

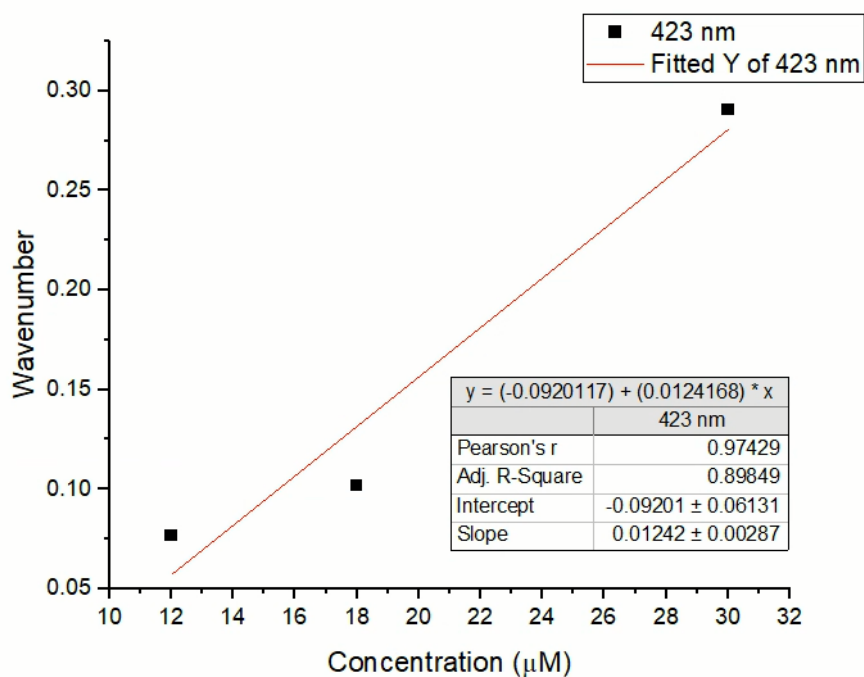


Figure 142: UV-vis linear regression for compound **15** in MeCN at 423 nm,  $\epsilon = 12420 \text{ M}^{-1}\text{cm}^{-1}$ .

### 6.3 IR data

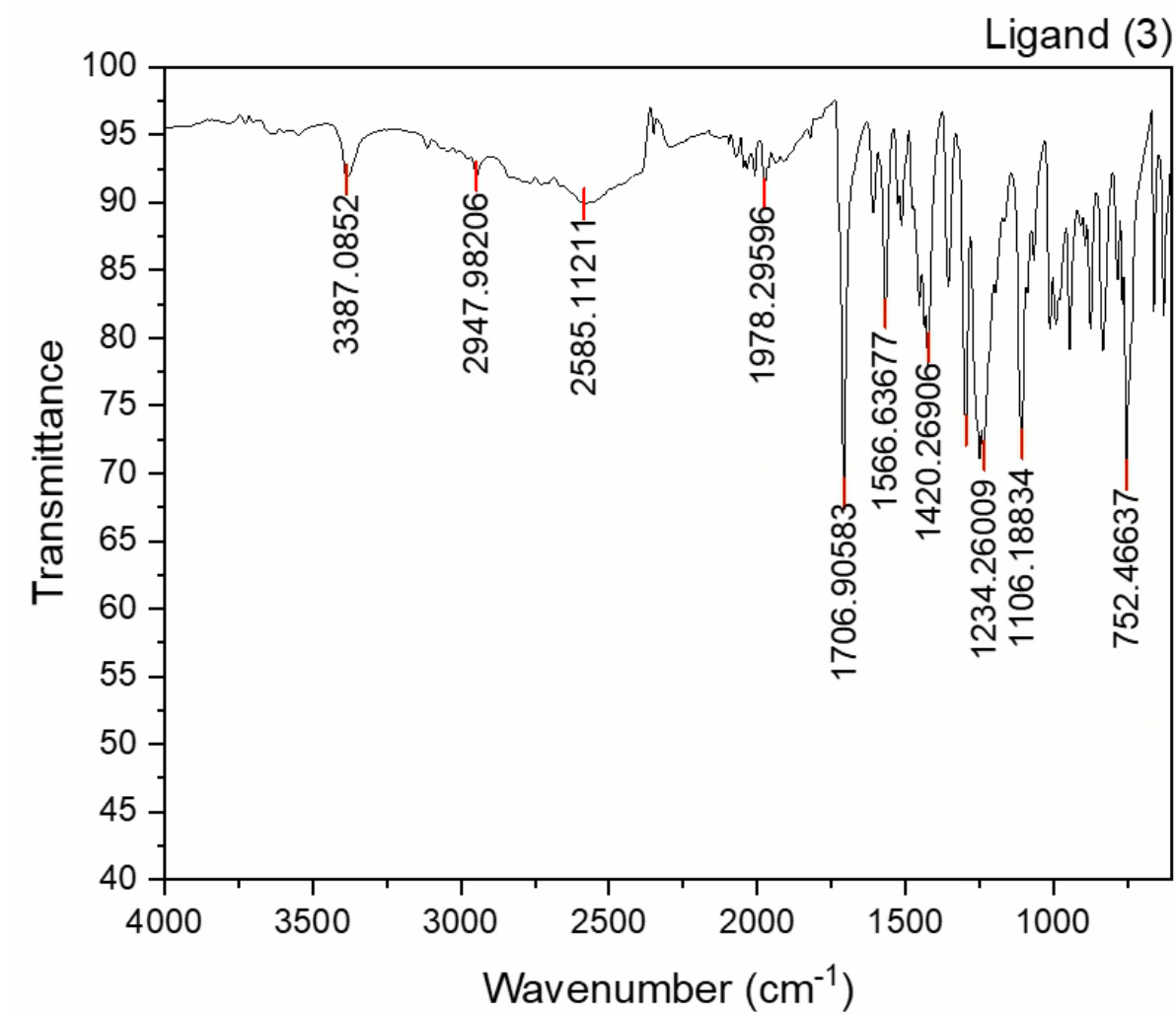


Figure 143: FTIR spectrum of Ligand 3.

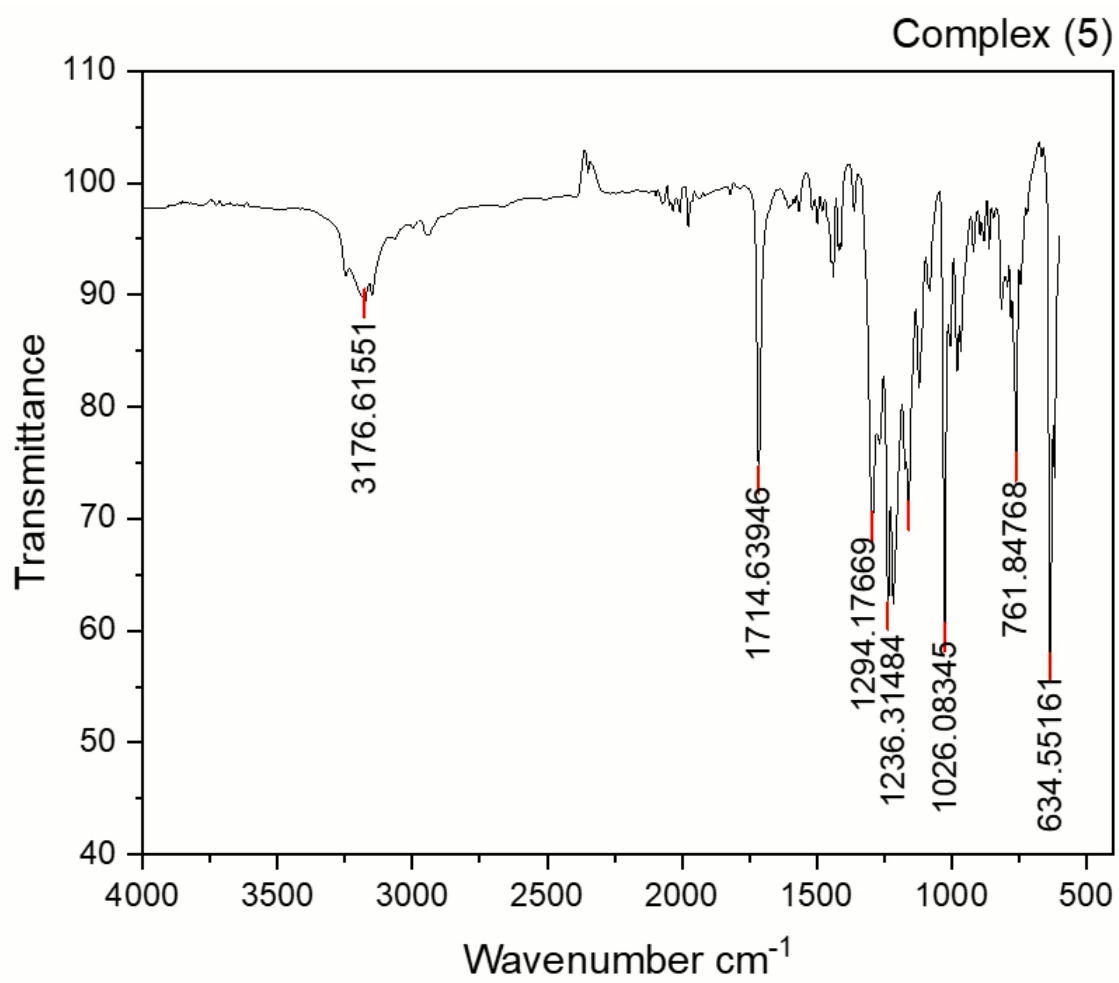


Figure 144: FTIR spectrum of Complex 5.

## 6.4 SC-XRD data

Table 2: Crystal and refinement data for compound **5**.

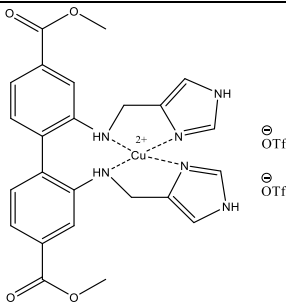
<b>Crystal data</b>	
Identification	<b>mo_aaa54_0m_a</b>
Empirical formula	<b>C<sub>28</sub>H<sub>27</sub>CuF<sub>6</sub>N<sub>7</sub>O<sub>10</sub>S<sub>2</sub></b>
Formula weight	863.22
Crystal system, space group	Triclinic, P-1
Temperature (K)	100
a/Å	7.9898(8)
b/Å	13.5191(14)
c/Å	16.3310(17)
β (°)	89.244(4)
Volume (Å <sup>3</sup> )	1734.8(3)
Z	2
Radiation type	MoKα
μ (mm <sup>-1</sup> )	0.848
Crystal size (mm <sup>3</sup> )	1.74 × 1.33 × 0.46
Diffractometer	Bruker D8 Venture diffractometer
Absorption correction	MULTI-SCAN
T <sub>min</sub> , T <sub>max</sub>	0.638, 0.744
No. of measured, independent and observed [I > 2σ(I)] reflections	2838, 19701
R <sub>int</sub>	0.0748
<b>Refinement</b>	
R[F <sup>2</sup> > 2σ(F <sup>2</sup> )], wR(F <sup>2</sup> ), S	0.0642(2292), 0.1720(2838), 1.204
No. of reflections	2838
No. of parameters	488
No. of restraints	1
Δ ρ <sub>max</sub> , Δ ρ <sub>min</sub> , (e Å <sup>-3</sup> )	0.86/-0.50

Table 3: Coordination bond angles of complex **5**.

<b>Atom1</b>	<b>Atom2</b>	<b>Atom3</b>	<b>Angle(°)</b>
N2	Cu1	N5	101.7(4)
N5	Cu1	N4	83.0(3)
N4	Cu1	N1	91.5(3)
N2	Cu1	N1	82.9(3)
O6	Cu1	N5	88.9(3)
O6	Cu1	N2	105.3(3)
O6	Cu1	N1	96.9(3)
O6	Cu1	N4	81.7(3)